INVESTIGATIONS ON PROCESSING OF CARBON FOAMS FROM SUCROSE AND REINFORCING CARBON ADDITIVES

A Thesis submitted

in partial fulfillment for the Degree of

Doctor of Philosophy

by

R. NARASIMMAN

Department of Chemistry

INDIAN INSTITUTE OF SPACE SCIENCE AND TECHNOLOGY

Thiruvananthapuram – 695 547

MARCH 2015

CERTIFICATE

This is to certify that the thesis entitled **Investigations on Processing of Carbon Foams from Sucrose and Reinforcing Carbon Additives,** submitted by **R. Narasimman,** to the Indian Institute of Space Science and Technology, Thiruvananthapuram, in partial fulfillment for the award of the degree of **Doctor of Philosophy,** is a *bona fide* record of research work carried out by him under my supervision. The contents of this thesis, in full or in parts, have not been submitted to any other Institution or University for the award of any degree or diploma.

Dr. K. Prabhakaran
Supervisor
Associate Professor
Department of Chemistry

Thiruvananthapuram
March, 2015

Counter signature of HOD with seal

DECLARATION

I declare that this thesis entitled **Investigations on Processing of Carbon Foams from Sucrose and Reinforcing Carbon Additives** submitted in partial fulfillment of the degree of **Doctor of Philosophy** is a record of original work carried out by me under the supervision of Dr. K. Prabhakaran, and has not formed the basis for the award of any other degree or diploma, in this or any other Institution or University. In keeping with the ethical practice in reporting scientific information, due acknowledgements have been made wherever the findings of others have been cited.

R. Narasimman
SC11D008

Thiruvananthapuram - 695 547
March, 2015

ACKNOWLEDGEMENTS

I would like to thank all people who have helped and encouraged me during my study at Indian Institute of Space Science and Technology.

First and foremost I would like to express my heartfelt gratitude towards my supervisor Dr. K. Prabhakaran for giving me the opportunity to work under his supervision and also for his academic guidance, continuous support and encouragement throughout this research work. I have been extremely lucky to have a supervisor who cared so much about my work, and who responded to my questions and queries so promptly by providing with his precious time.

I take this opportunity to thank Dr. K.S. Das Gupta, Director, IIST for providing me with all the necessary facilities. It is my pleasure to extent my deep gratitude to the Dean (Student Activities) and the Head of the Department of Chemistry, Prof. Kuruvilla Joseph for his continuous support and encouragement during my stay. Financial assistance from IIST is gratefully appreciated.

I have to extent my heartfelt thanks to doctoral committee members, Dr. K. N. Ninan, Prof. Sabu Thomas, Dr. C. P. Reghunathan Nair, Prof. Parag Bhargav, Dr. K.Y. Sandhya and Dr. V.J. Rajesh. I am very grateful to their guidance, constructive criticism and enthusiastic support during my research. I am indebted to the faculty members of Department of Chemistry for their whole hearted support.

I am deeply indebted to members of VSSC, NIIST, SCTIMST, Amrita Institute, SAIF IIT and CESS for the characterization of my samples throughout my research. I also offer my sincere appreciation especially to Mr. Sujith Vijayan, who has shared lot of knowledge on experimental and also for the fruitful discussions during my thesis work. I am thankful to all my fellow scholars especially Mr. Raneesh Konnola, Ms. Jalaja, Mrs. Deepthi Sivadas, Mr. Mukthar,

Ms. Sarah, Mrs. Remya and Ms. Kavitha for their sincere help and support. I would like to thank sincerely Dr. Gigy J.Alex and Mr. Sreekumaran Nair for their effort to correct my thesis. I also take this opportunity to thank Mr. Dileep Kumar, Mr. Loveson, Mrs. Rehna and Mrs. Jayashree for their friendship and kind assistance. I would like to thank staffs of Library IIST for their assistance in setting and printing of this thesis.

Last but not least, I would like to thank my parents Rajaram and Usha and my brother Balaji for their constant love, support and help not only during the time of this thesis, but during all my life. They always cheered me up and kept me motivated. I would like to extend my sincere gratitude to each and every one who has rendered their help directly or indirectly during this research.

ABSTRACT

Carbon foams are advanced carbon materials with excellent properties like low density, ablative properties, tunable thermal conductivities, low thermal expansion coefficient, good electrical conductivity and relatively high mechanical strength. They find applications in thermal protection systems, light-weight fire resistant structures, heat exchangers, radiators, battery electrodes, electromagnetic interference (EMI) shielding and acoustic absorption. The carbon foams are mainly prepared from the fossil fuel-based pitches and synthetic organic polymers which leave large carbon residue on pyrolysis. The depletion of fossil fuels and other environmental concerns necessitate a shift to alternate and naturally renewable precursors for carbon foams. Sucrose is a widely available naturally renewable precursor studied for the preparation of carbon foam. However, the density and mechanical strength of the carbon foam prepared from sucrose is low due to the low carbon yield. The main objectives of the thesis are to prepare carbon foams from sucrose by easy and energy efficient alternative methods and to study the effect of various reinforcing carbon additives on the foaming characteristics of sucrose and properties of carbon foams.

Thermo-foaming of molten sucrose using an aluminium nitrate blowing agent followed by dehydration and carbonization was used for the preparation of carbon foams. The aluminium nitrate catalyzed the –OH to –OH condensation reactions responsible for the nucleation, growth and stabilization of bubbles which enabled the faster foaming and setting of molten sucrose. The carbon foams obtained had an interconnected cellular structure. The density and cell size obtained were in the ranges of 0.15 to 0.05 g/cm^3 and 1.62 to 0.83 mm, respectively, at aluminium nitrate concentrations in the range of 0 to 4 wt.%. The carbon foams showed a turbostratic graphitic structure. The alumina (~ 0.2 to 1.58 wt. %) produced from the aluminium nitrate concentrated more on the surfaces of cell walls, ligaments, and struts. The compressive strength (0.06 to 0.64 MPa), Young's modulus (2.9 to 22 MPa) and thermal conductivity (0.04 to 0.07 W/m/K) of the carbon foams depended on the aluminium nitrate concentration. The surface area and pore volume of the carbon foams increased with an increase in aluminum nitrate concentration. The mechanism of formation of micropore due to *in situ* activation and alumina pillaring was established. The CO_2 adsorption capacity (2.87 to 3.37 mmol/g at 0 ^oC and 760 mmHg) of the carbon foams increased with an increase in aluminium nitrate concentration due to the interaction of quadrupole of carbon dioxide with the alumina. The alumina formed from the aluminum nitrate blowing agent catalyzed the carbon oxidation due to its Lewis acid character.

The oxidation resistance of carbon foams was improved by using boric acid as blowing agent. The H^+ generated from boric acid due to the formation of sucrose-boric acid complex catalyzed the -OH to -OH condensation reactions leading to the faster foaming and setting of the molten sucrose. The char yield increased from 24 to 39 wt.% when the boric acid concentration increased from 0 to 8 wt.% due to the formation of the B-O-C cross-links between sucrose polymer by B-OH to C-OH condensation. The density (0.103–0.16 g/cm^3) and compressive strength (0.2-1.1 MPa) decreased and cell size (0.67-1.17 mm)

increased with an increase in boric acid concentration. The thermal conductivity of the boron-doped carbon foams obtained was in the range of 0.057 to 0.043 W/m/K at 25 ^{o}C. The surface area and pore volume increased with an increase in the boric acid concentration up to 6 wt.% and then decreased. The boron present (0.44 to 3.4 wt.%) retarded the oxidation of carbon foams as evidenced from the increase in the oxidation onset temperature and char residue at 900 ^{o}C with an increase in boric acid concentration.

Various reinforcing agents such as activated carbon powder (AC), carbon fiber, multi-walled carbon nanotube (MWNT) and graphene were incorporated in sucrose to increase the carbon yield and to improve the mechanical properties of the carbon foams. The carbon composite foams were prepared by thermo-foaming of dispersions of the reinforcing carbon additives in molten sucrose to form solid organic foams followed by dehydration and carbonization.

The dispersed AC powder induced the foaming of molten sucrose by stabilizing the bubbles by adsorbing on the molten sucrose-gas interface, accelerated the foaming and foam setting by catalyzing the –OH to –OH condensation and increased the char yield. The density, cell size, compressive strength and thermal conductivity of the carbon composite foams depended on the AC powder to sucrose weight ratio. The maximum compressive strength of the carbon composite foam achieved was 1.36 MPa at an AC powder to sucrose weight ratio of 0.05. The foams had a hierarchical pore structure with interconnected cells made up of carbon-containing micropores. The carbon composite foams showed relatively high (2.59 to 3.04 mmol/g) CO_2 adsorption capacity with very good CO_2/N_2 selectivity and excellent recyclability. The carbon composite foams selectively absorbed oil phase from oil-water mixtures and surfactant stabilized oil-in-water emulsion.

The density and compressive strength of the carbon fiber reinforced carbon composite foams at an average fiber length of 300 μm decreased with an increase in fiber concentration due to the agglomerations by bridging of longer fibers. The average fiber length was decreased by planetary ball milling of sucrose-carbon fiber mixtures. The compressive strength of carbon composite foams increased with a decrease in fiber length, reached a maximum at an average fiber length of 33 μm and then decreased. The maximum compressive strength of 3.86 MPa was achieved at an average fiber length of 33 μm and a fiber concentration of 2 wt.%. The maximum improvement in compressive strength and specific compressive strength obtained as a result of reinforcement with the carbon fiber was 125 % and 92 %, respectively.

The foaming time and foam setting time of molten sucrose were decreased with an increase in MWNT concentration due to the catalytic effect of MWNT towards –OH to –OH condensation. The density of the MWNT reinforced carbon composite foam obtained was in the range of 0.23 to 0.26 g/cm^3. The maximum compressive strength and specific compressive strength of 4.9 MPa and 21 MPa/g/cm^3, respectively, were obtained at an MWNT concentration of 0.5 wt.%. Beyond 0.5 wt.% MWNT, the compressive strength and specific strength were decreased due to the agglomeration of MWNT. The d-spacing of (002) plane decreased from 3.614 to 3.472 Å when the MWNT concentration increased from 0 to 2.5 wt.% due to the development of crystal structure parallel to MWNT axis. The electrical conductivity increased with an increase in the MWNT

concentration up to 1 wt.% and then marginally decreased due to MWNT agglomeration. The EMI shielding effectiveness (SE) of the carbon composite foams in the X-band region increased gradually with an increase in the MWNT concentration up to 1.5 wt.% and then rapidly. The pores created by the local shrinkage of sucrose polymer within the MWNT agglomerates contributed to the SE by acting as new interfaces for internal reflections which are responsible for rapid increase in EM absorption at MWNT concentrations higher than 2 wt.%. The highest SE achieved was 39 dB at an MWNT concentration of 2.5 wt.%. The highest specific shielding effectiveness (SSE) of the MWNT reinforced carbon composite foam obtained was 166 dB/g/cm^3.

The melting point of the sucrose decreased from 190 to 120 ^{o}C when the GO GO concentration increased from 0 to 1.25 wt.%. The viscosity of GO dispersions in molten sucrose increased gradually with GO concentration up to 0.75 wt.% and then rapidly with further increase in GO concentrations. The foaming time and foam setting time decreased drastically from 6 to 1 h and 34 to 9 h, respectively, when the GO concentration increased from 0.25 to 1.25 wt.% due to the catalytic effect of GO towards –OH to –OH condensation reactions. The density and cell size of the graphene-reinforced carbon composite foams depended on the GO concentrations. A maximum compressive strength and specific compressive strength of 5.2 MPa and 21.3 MPa/g/cm^3, respectively, were achieved at a very low GO concentration of 0.25 wt.%. The electrical conductivity and EMI SE of the graphene reinforced carbon composite foams increased with an increase in the GO concentration up to 0.15 wt.% and then decreased due to graphene agglomeration. The maximum SE achieved was 38.6 dB at a GO concentration of 0.15 wt.%. The maximum SSE of the graphene reinforced carbon composite foam obtained was 160 dB/g/cm^3.

Thermo-foaming of dispersions of various reinforcing carbon additives (AC powder, carbon fiber, MWNT, and graphene) in an aqueous resin prepared by acid-catalyzed polymerization of sucrose solution was studied for the preparation of carbon foams. Among the various reinforcing carbon additives, AC powder only produced solid organic foam with homogeneous foam structure. The dispersion of AC powder in the aqueous sucrose resin was due to the adsorption of sucrose polymer molecules on the AC powder. The dispersed AC powder retarded the –OH to –OH condensation reactions responsible for the cross-linking of the sucrose polymer. The mechanism of foaming of aqueous sucrose resin by stabilization of the bubbles by the adsorption of AC particles on the gas-resin interface was established. The foam volume increased with a decrease in the AC particle size due to the better stabilization of bubbles by the finer particles. The AC particle size had a marginal effect on the density and thermal conductivity of the carbon composite foams. The maximum compressive strength of 2.8 MPa was achieved at the AC powder to sucrose weight ratio of 0.05 and at an average particle size of 15 μm. The carbon composite foams showed low thermal conductivity in the range of 0.026 to 0.063 W/m/K. The carbon composite foams showed very good machinability characteristics and fire resistance.

TABLE OF CONTENTS

LIST OF FIGURES

LIST OF TABLES

ABBREVIATIONS

AC	Activated Carbon
AFM	Atomic Force Microscopy
BJH	Barrett-Joyner-Halenda
BET	Brunauer, Emmett and Teller
CNF	Carbon Nanofiber
CNT	Carbon Nanotube
CVD	Chemical Vapour Deposition
CVI	Chemical Vapour Infiltration
DFT	Density Functional Theory
DSC	Differential Scanning Calorimeter
DTG	Differential Thermogram
EMI	Electromagnetic Interference
EM	Electromagnetic Radiation
EDAX	Energy Dispersive Spectroscopy
FTIR	Fourier Transform Infrared Spectroscopy
GO	Graphene Oxide
HIPE	High Internal Phase Emulsion
ICP	Inductively Coupled Plasma
IUPAC	International Union of Pure and Applied Chemistry
MTPS	Modified Transient Plane Source
MSC	Molecular Sieving Carbon

MWNT	Multi-Walled Carbon Nanotube
PCM	Phase Change Material
PAN	Polyacrylonitrile
PU	Polyurethane
PSD	Pore Size Distribution
RVC	Reticulated Vitreous Carbon
RPM	Rotation Per Minute
SEM	Scanning Electron Microscopy
SAED	Selected Area Electron Diffraction
SE	Shielding Effectiveness
SWNT	Single-Walled Carbon Nanotube
SSE	Specific Shielding Effectiveness
TPS	Thermal Protection System
TGA	Thermogravimetric Analyzer
TEM	Transmission Electron Microscopy
XRD	X-Ray Diffractometer

NOTATIONS

θ	Angle of diffraction
Å	Angstrom
σ_f*	Compressive strength of the foam
σ_f	Compressive strength of the solid
[HCl]	Concentration of the acid added to the aliquot taken from the original solution
[B]	Concentration of the base mixed with the carbon
[NaOH]	Concentration of the titrant NaOH in the back titration
I	Current
ρ*	Density of the foam
ρ_s	Density of the solid
s	Distance between the pins
d	D-spacing
ρ	Electrical resistivity
P	Equilibrium pressure
n_{csf}	Number of moles of carbon surface functionality
n_{HCl}	Number of moles of hydrochloric acid
n_{NaOH}	Number of moles of sodium hydroxide
R*	Resistivity of the foam
R_s	Resistivity of the solid
P_o	Saturation pressure

λ_g	Thermal conduction of gas
λ_s	Thermal conduction of solid
λ	Thermal conductivity
V	Voltage drop
V_{HCl}	Volume of the acid added to the aliquot taken from the original solution
V_a	Volume of the aliquot taken from the V_B
V_B	Volume of the base mixed with the carbon
V_{NaOH}	Volume of the titrant NaOH in the back titration

CHAPTER 1

INTRODUCTION

The aim of this chapter is to introduce and provide the state-of-the-art literature survey on the preparation of carbon foams from various precursors, different reinforcement used to improve their physical and functional properties and applications of the carbon foams. This chapter introduces the motivation and objectives of the research work. At the end of the chapter, the organization of the whole thesis and a brief introduction for each chapter is provided.

1.1 Carbon

Carbon is a fascinating element having an electronic configuration of $1s^2$ $2s^2$ $2p^2$. Carbon atoms link each other and also with other elements through single and multiple bonds using their *sp*, sp^2 and sp^3 hybrid orbitals to form a large number of both simple and very complex organic molecules (Pierson, 1993). On the other hand, carbon atoms link each other through single and double bonds using sp^2 and sp^3 hybrid orbitals in a number of ways to form a variety of carbon-based materials. Among them, diamond and graphite are the naturally occurring carbon allotropes. The diamond is an insulating material having a cubic structure in which each carbon atom is tetrahedrally bonded to four other carbon atoms through single bonds using sp^3 hybrid orbitals. On the other hand, the graphite has a hexagonal layered structure in which each carbon atom is bonded to three other carbon atoms through single and double bonds using sp^2 hybrid orbitals. The distance between the hexagonal layers in graphite is 0.3354 nm, and the layers are held together by weak Van der Waal's forces. The formation of BC8, another stable phase of carbon, under high pressure is predicted and simulated (Oganov et al., 2013). This unusual tetrahedral BC8 structure is observed when the diamond subjected to dynamic compression above 1 TPa. Apart from these crystalline forms, coke and charcoal are relatively impure and amorphous forms of carbon

used mainly as fuel. In addition to these bulk materials, there are a few synthetically prepared carbon nanomaterials such as fullerenes, carbon nanotubes (CNT) and graphene that are considered as the new allotropes of carbon. The fullerene is discovered by Smalley and co-workers in 1985, during their studies on the evolution of carbon in the interstellar medium (Kroto et al., 1985). The fullerene has football-like cage structure containing pentagonal and hexagonal rings formed from sp^2 and sp^3 hybridized carbon atoms. Iijima (1991) discovered the CNT. The CNT has a tubular structure. The ends of the tube are capped with carbon hemispheres. The hemispherical caps contain pentagonal and hexagonal carbon rings whereas the walls of the CNTs are made up of only hexagonal carbon rings. The CNTs are available in single-walled (SWNT) and multi-walled forms (MWNT). The MWNT contain concentric tubes that are separated by a distance of 0.3354 nm. Graphene is a two-dimensional, single atomic layer of hexagonal carbon discovered by Novoselov et al. (2004). The chemistry and material aspects of the carbon nanomaterials are well-reported in the literature (Loh et al., 2010; Shearer et al., 2014; Tasis et al., 2006; Vilatela and Eder, 2012). The structure of various allotropic forms of carbon is shown in Figure 1.1.

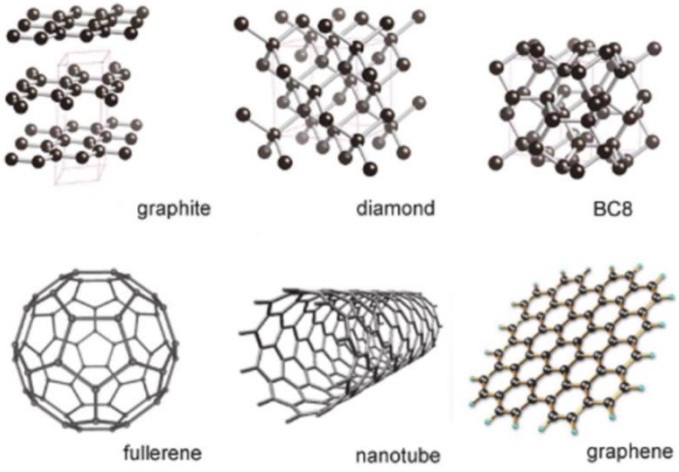

Figure 1.1: Allotropes of carbon (Oganov et al., 2013)

Carbon provides materials with excellent properties for a large spectrum of industrial applications. The properties of carbon materials depend on the type of bonding between the carbon atoms, crystal structure and microstructure

(Pierson, 1993). Carbon materials show extremely high thermal stability in the inert atmosphere, very low thermal expansion coefficient, tunable electrical and thermal conductivities and high strength and modulus (Savage, 1993). Unlike other engineering materials, carbon-based materials show an increase in their mechanical properties with temperature (Savage, 1993). Therefore, they are considered for high-temperature applications. From carbon we obtain the strongest fibers, one of the best solid lubricants (graphite), one of the best electrically conducting materials (graphite electrodes), the best structural material for high temperature tribological application (carbon–carbon composites), one of the best porous gas adsorbents (activated carbon), an essentially non-crystalline impermeable material (vitreous carbon), and the hardest material (diamond). In addition, the carbon nanomaterials are used in applications such as sensors (Cuong et al., 2010; Suehiro et al., 2005), electronic devices (Anantram and Léonard, 2006; Xu et al., 2007), medical field (Balasubramanian and Burghard, 2006; Sun et al., 2008), and reinforcements in polymer (Potts et al., 2011; Sahoo et al., 2010), ceramic (Thostenson et al., 2001; Walker et al., 2011), and metal (Wang et al., 2012b) matrix composites. The carbon-based materials are used in their dense and porous forms for the structural and functional applications. The dense carbon materials like carbon-carbon composites and graphite are used for the thermal protection (Savage, 1993), aircraft brake system (Blanco et al., 1997), heating element for high temperature furnaces, mould for hot pressing, nuclear applications, electrolysis, etc. On the other hand, the porous carbon materials are finding a lot of applications due to its lightweight combined with properties like tunable thermal conductivity, good electrical conductivity, high surface area and pore volume. A review of porous carbon materials is summarized in the following section.

1.2 Porous Carbon

Porous carbon materials are the class of porous solids which are having characteristic porosity in the carbon structure. The properties of the porous carbon mainly depend on the porosity, pore size, pore structure and the surface chemistry

of the carbon. Porous carbon has attracted a lot of applications in the separation, adsorption and storage of gases, water purification, catalytic support, etc., due to its high surface area, chemical and thermal inertness, low cost of manufacturing and tunable surface functionality (Marsh and Reinoso, 2006; Sircar et al., 1996). The porous carbon materials are classified into microporous, mesoporous and macroporous based on the pore size by International Union of Pure and Applied Chemistry (IUPAC) (Rouquerol et al., 2013; Sing, 1985). The microporous carbon contains pores of < 2 nm. The mesoporous carbon contains pores of size in the range of 2 to 50 nm, and macroporous carbon contains pores of size > 50 nm. The method of preparation of the above mentioned three classes of porous carbons is discussed below.

1.2.1 Microporous Carbon

An important microporous carbon material is activated carbon (AC) which is generally prepared by carbonization and activation of naturally available resources like wood, peat, nutshell, sawdust and some synthetic organic polymers (Marsh and Reinoso, 2006; Sircar et al., 1996). The precursors are carbonized in an inert atmosphere. The carbonized materials have a low surface area and porosity. In order to enhance the porosity, the activation step is carried out. The activation process can be done by two methods: (a) physical or thermal activation (Ahmadpour and Do, 1996) and (b) chemical activation (Caturla et al., 1991). The physical or thermal activation is carried out by reacting carbonized product with the reactive gases like CO_2, steam or a combination of the two at temperature in the range of 700 to 1000 ^{o}C (Marsh and Reinoso, 2006). These gases react with the surface carbon to form oxygenated carbon complexes. The decomposition of the oxygenated carbon complexes into gases like CO and H_2, which takes away the carbon by leaving pores according to the following equations (1.1 and 1.2).

$$C + CO_2 \rightarrow 2CO \quad (1.1)$$

$$C + H_2O \rightarrow CO + H_2 \quad (1.2)$$

The chemical activation is performed by mixing the carbon precursors with activating agents like KOH, NaOH, H_3PO_4 and $ZnCl_2$ followed by carbonization (Caturla et al., 1991; Kierzek et al., 2004; Teng et al., 1998; Tseng, 2007). Subsequently, the chemical activating reagent or their reaction products are removed by washing to get activated carbon. The temperature for chemical activation is lower than the physical activation. The majority of pores in the AC are less than 2 nm. The main drawbacks of the AC are the wide distribution of pore size and poor controllability of the porosity. This indeed affects their applications.

The special type of activated carbon is molecular sieving carbon (MSC), prepared by using controlled pyrolysis of carbon precursors like coal, synthetic organic resins and some naturally renewable organic molecules (Miura et al., 1991). The MSCs contain pores in the ultramicropore size range (< 1 nm) produced due to the misalignment of aromatic domains in the carbon material (Figure 1.2). The MSCs can also be prepared by the carbonization of ion-exchange resins containing different cations like H^+, K^+, Na^+, Ca^{2+}, Zn^{2+}, Cu^{2+}, Ni^{2+}, Fe^{2+}, etc. (Nakagawa et al., 1999). Here, the multivalent cations retain sharp pore size distribution in the carbonized material due to the effective cross-linking of the polymer chains. The MSC has the property of separating gases from their mixtures (e.g. N_2 from the air).

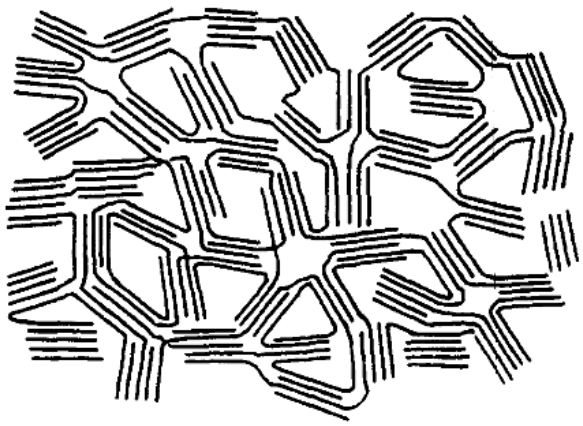

Figure 1.2: Schematic showing the misalignment of aromatic domains in MSCs cause ultramicropores (Franklin, 1951)

The ordered microporous carbon is synthesized by the zeolite template method (Kyotani et al., 1997). Zeolite is the aluminosilicate containing ordered uniform micropores and rigid porous architecture. Zeolites with a range of pore sizes are available. Here, the organic precursor resin is infiltrated into the zeolite, which is then carbonized in an inert atmosphere. The subsequent removal of the zeolite template by leaching with hydrofluoric acid (HF) solution produces ordered microporous carbon. The commonly used organic precursors are furfuryl alcohol, phenolic resin, sucrose solution and polyacrylonitrile (PAN) (Kyotani, 2000; Ma et al., 2001). Vapour phase infiltration of carbon by Chemical Vapour Deposition (CVD) is also used for the preparation of ordered microporous carbon from zeolite template (Kyotani et al., 1997; Ma et al., 2000). Figure 1.3 shows the schematic of ordered microporous carbon prepared from a zeolite as the template.

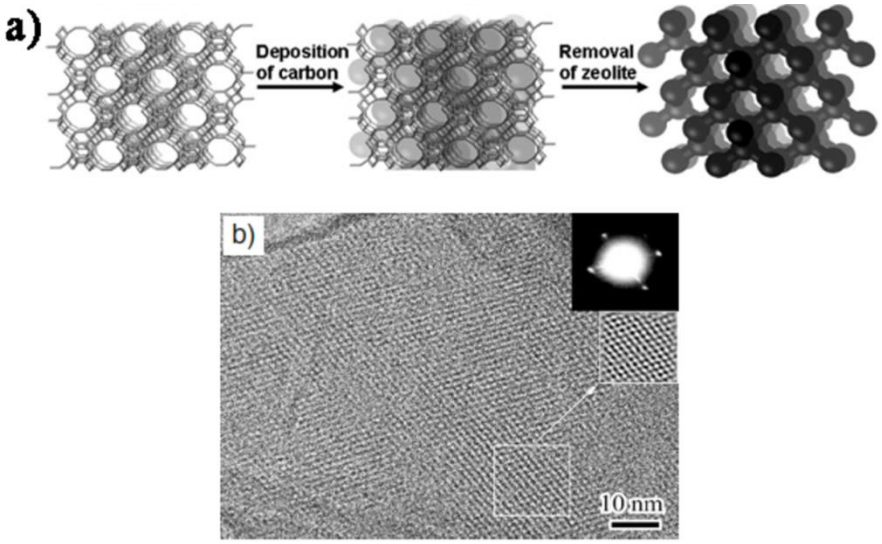

Figure 1.3: (a) Schematic of ordered microporous carbon prepared from zeolite as the template and (b) Transmission Electron Microscopy (TEM) micrograph of the ordered microporous carbon (Ma et al., 2000)

1.2.2 Mesoporous Carbon

Mesoporous carbons are porous carbons which contain the pore in the size range of 2-50 nm. The mesoporous carbons have applications such as adsorbent for dyes, electrodes, catalyst support, etc. (Hao et al., 2010; Lee et al., 1999b; Su et al., 2005b). Carbon aerogels fall into the category of mesoporous

carbon materials. The carbon aerogels are prepared by the carbonization of the organic aerogels (Figure 1.4) (Job et al., 2005; Pekala, 1989; Pekala and Alviso, 2011). The organic aerogels are generally prepared by the sol-gel polycondensation of the phenol or resorcinol and formaldehyde in a basic aqueous solution followed by supercritical drying. The CO_2 is commonly used for the supercritical drying of polymer gels to produce polymer aerogels. The supercritical drying avoids the surface tension forces and thus prevents the pore collapse. The carbon aerogels have very high porosity and surface area. The pore size of the organic aerogel, thus carbon aerogel, can be controlled by the monomer to water and monomer to catalyst weight ratios. Due to the high cost of supercritical drying, carbon cryogels are developed by drying the polymer gels in freeze dryers (Mathieu et al., 1997; Tamon et al., 1999, 2000).

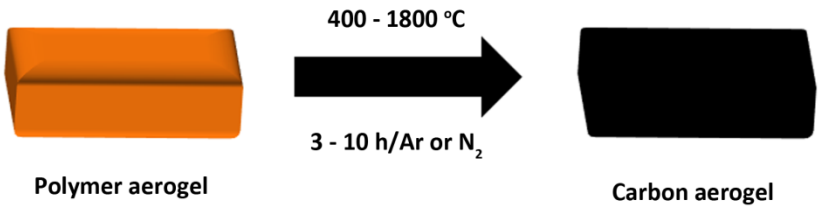

Figure 1.4: Schematic of preparation of carbon aerogel from polymer aerogel

Mesoporous carbon materials are also prepared by using suitable organic or inorganic pore templates (Ryoo et al., 2001). Silica is the inorganic template extensively used for the synthesis of mesoporous carbon as it can be easily removed by dissolving in HF or NaOH solution (Han and Hyeon, 1999). The silica template is used either in the form of sol or porous glass. In the silica sol based method, the carbon precursor resin is prepared by the *in situ* polymerization of the monomers in the sol medium (Han and Hyeon, 1999). The subsequent setting by cross-linking followed by carbonization and template removal results in mesoporous carbon. In the case of the porous glass template, mesoporous carbon is obtained by infiltration of the template with the precursor resin followed by carbonization and template removal. (Alumino)silica with ordered mesopores (e.g. MCM-48 and SBA-15) are used as a pore template for the preparation of

ordered mesoporous carbon (Figure 1.5) (Lee et al., 1999a). The phenolic resin, furfuryl alcohol, PAN, and sucrose are used as carbon precursors for the preparation of ordered mesoporous carbon (Jun et al., 2000; Kim et al., 2003; Ryoo et al., 2001). The ordered mesoporous carbon can also be prepared from the soft template approach. Surfactants like amphiphilic block copolymers are generally used as the soft pore templates (Che et al., 2003; Kleitz et al., 2003; Yang et al., 2002). These amphiphilic block copolymers self-assemble in the carbon precursor resin, which is cured by further polymerization. Removal of the self-assembled surfactant molecules during the subsequent carbonization creates ordered mesopores.

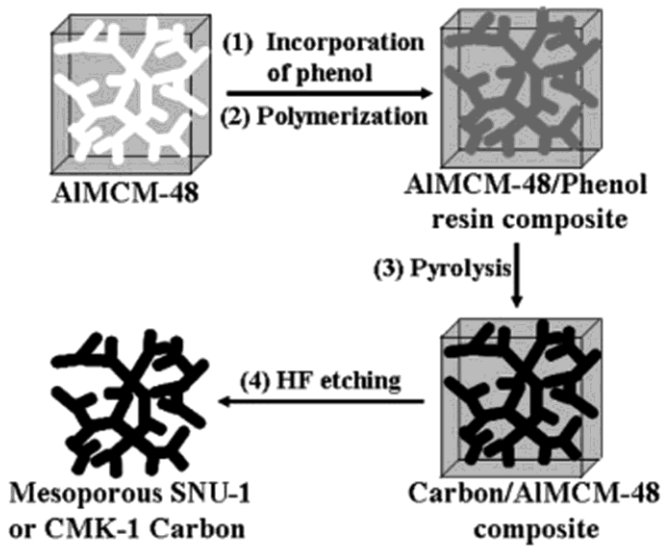

Figure 1.5: Schematic representation of the formation of an ordered mesoporous carbon (Lee et al., 1999a)

1.2.3 Macroporous Carbon

Macroporous carbon materials can be prepared by two techniques: (1) by using pores template and (2) by foaming. In the first method, the templates such as polymer beads, silica particles, sodium chloride crystals, etc., incorporated in the carbon precursor resin are removed after carbonization to produce the macropores. In the second method, organic foams obtained by foaming and setting of the precursor resin are carbonized to produce macroporous carbon

(carbon foams). The details of carbon foams are discussed in the subsequent sections.

Three-dimensionally ordered macroporous carbon is prepared using colloidal crystals (opal) as pore templates (Kang et al., 2002; Yu et al., 2002; Yu et al., 2001; Zakhidov, 1998). Spherical colloidal silica undergoes self-organization into the colloidal crystal. The carbon precursors infiltrated into the pores are subsequently polymerized and carbonized. Removal of the silica particles by dissolving in HF produces three-dimensionally ordered macroporous carbon structure. It is termed as "Inverse opal carbon". Figure 1.6 shows the schematic of the colloidal crystal template method for the preparation of three-dimensionally ordered macroporous carbon and Scanning Electron Microscopy (SEM) microstructure of the macroporous carbon (Yu et al., 2002). The important parameters for the preparation of macroporous carbon in this approach are the quality of the colloidal crystal and the complete impregnation of the carbon precursors (Yu et al., 2002; Yu et al., 2001). In order to achieve the complete replication, the liquid precursors like phenolic resin and sucrose solution are used (Kang et al., 2002; Yu et al., 2001). Deposition of pyrolytic carbon in the voids in the colloidal crystals by CVD using hydrocarbons such as methane and propylene are also used for the preparation of three-dimensionally ordered macroporous carbon (Zakhidov, 1998). The polystyrene beads are also used as a template for the preparation of three-dimensionally ordered macroporous carbon (Baumann and Satcher, 2003). The macroporous carbon prepared by this method generally has high surface area and pore volume. On the other hand, the nature of carbon (graphitic, glassy or diamond structure) can be decided by the proper selection of precursor materials.

1.3 Carbon Foam

Carbon foam is a macroporous cellular carbon material. They are porous carbon materials containing regularly shaped, predominantly concave,

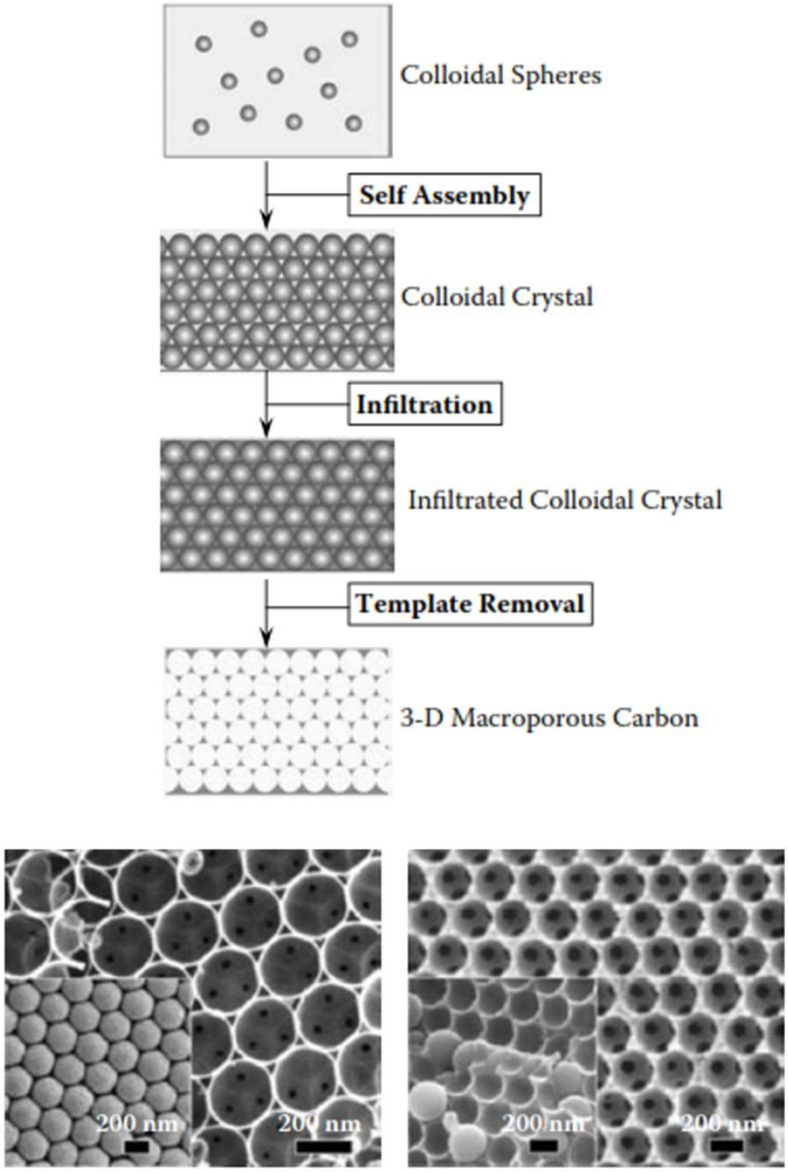

Figure 1.6: Schematic of the colloidal-crystal template method for the preparation of three dimensionally ordered macroporous carbon and SEM microstructure of the macroporous carbon (Yu et al., 2002)

homogeneously dispersed cells which interact to form a three-dimensional array throughout a continuum material of carbon (Scheffler and Colombo, 2006). They have interesting and characteristic properties like lightweight, tunable thermal and electrical conductivity, fire resistance, good mechanical properties and chemical inertness. In addition, they have the capability to absorb sound and electromagnetic radiations. The carbon foams are characterized by its density, compressive strength, cell size, cell interconnectivity and cell morphology. They

have either open or closed cellular structure. In open cell foams there are one or more interconnections (cell window) between the neighboring cells which allow the transport of materials. On the other hand, in closed cell foams the cells are rarely connected each other. There is a third type of carbon foam named as reticulated carbon foam which contains a network-like struts and ligaments. The carbon foams can also be classified into graphitic and non-graphitic based on the crystallinity of the carbon. The crystallinity of the carbon foams mainly depends on the carbon precursors, processing conditions, heat treatment temperature and use of the catalyst. Figure 1.7 shows the microstructure of open cell, closed cell and reticulated carbon foams.

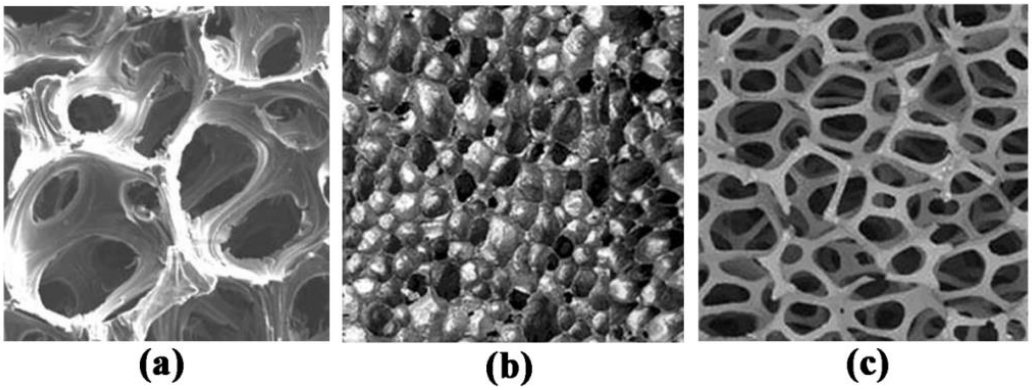

Figure 1.7: SEM micrographs of (a) open cell carbon foam (b) closed cell carbon foam and (c) reticulated carbon foam

The history of carbon foams begins with the report of the direct carbonization of foams of polymers such as phenol-formaldehyde, polyurethane, and polyester by Ford Walter (1964). Googin et al. (1967) reported the preparation of carbon foam by the carbonization of poly (furfuryl alcohol) modified polyurethane foam in 1967. RD Klett et al reported the preparation of carbon foam from the cork, an alternate carbon precursor, in 1975 (Klett, 1975). The first petroleum pitch based carbon foam is patented by Bonzom et al. (1981). James W Klett from Oak Ridge National Laboratories and Stiller and co-workers from West Virginia University, USA, independently developed viable technologies for the manufacture of carbon foams with a wide range of properties from petroleum-derived mesophase pitch and coal tar pitch, respectively (Chen et

al., 2006; Klett et al., 2000). Many studies on the preparation, properties and applications of Coal tar pitch and mesophase pitch derived carbon foams are reported in the late 1990s and early 2000s (Calvo et al., 2005; Chen et al., 2007; Fathollahi and Zimmer, 2007; Gaies and Faber, 2002; Li et al., 2005; Sanchez-Coronado and Chung, 2003; Wang et al., 2009a; Wang et al., 2008b). Over the last five decades, there is a large number of reports on the preparation of carbon foams from synthetic polymeric precursors such as phenol-formaldehyde, furfural resin, polyimide, poly (aryl acetylene), etc. (Inagaki et al., 2004; Lei et al., 2010; Liu et al., 2007a; Lorjai et al., 2009; Wu et al., 2011; Zhang et al., 2010). Prabhakaran et al. (2007) reported the preparation of carbon foam from sucrose. Preparation of carbon foam from tannin, another naturally renewable precursor, was first reported by Tondi et al. (2009).

1.3.1 General Approach for the Preparation of Carbon Foams

Carbon foams are prepared from organic precursor materials which leave large amounts of carbon residue during pyrolysis. There are two general methods for the preparation of carbon foams. One is the foaming of the precursor resin, and the other is using a polymer foam template. The foaming process uses a blowing agent, which produces gas molecules either by evaporation or by thermal decomposition and a foam stabilizing agent. Low boiling liquids such as hexane, pentane, diethyl ether, etc., or compounds such as sodium bicarbonate, azodicarbonamide, etc., are generally used as blowing agents. Surfactants and particles with suitable wetting characteristics are used as foam stabilizing agents. The conversion of the precursor materials to carbon foam by the foaming method involves different steps such as foaming, foam setting, carbonization, and in some cases graphitization. The foaming process of the polymer resin has three main steps: (1) bubble nucleation (2) bubble growth and (3) stabilization. The gas produced from the blowing agent in the resin causes the nucleation of the bubbles. The bubbles started to grow further by the diffusion of the excess gas in the resin into the nuclei or due to the Ostwald ripening process (Rosebrock et al., 2005; Shafi and Flumerfelt, 1997). While the bubbles grow, the following described

foam structures will be produced. During the growth process, the bubbles remain spherical until a close packed structure is reached. Further growth of bubbles and lowering of foam density then involves distortion of cells from spherical structure to polyhedral structures, sometimes idealized as pentagonal dodecahedrons. Viscosity and surface tension effects subsequently cause material to flow towards intersecting cell elements to form junctions of tricuspid cross-section. A final stage may involve rupture of cell walls to result in open cell foam. The foamed resin is subsequently set by further cross-linking reactions to form solid organic foam. The carbonization involves heating the solid organic foam in an inert atmosphere at a temperature up to 1200 ^{o}C. During the carbonization step, the heteroatoms such as hydrogen, oxygen and nitrogen present in the solid organic foam is removed leaving the foam structure in carbon. The carbon foam produced after carbonization is, in general, amorphous or turbostratic graphite. The planarity of the layer increases as well as defects in the plane decreases with an increase in temperature and amorphous carbon turns to graphite at a temperature in the range of 1800 to 3000 ^{o}C (Marsh and Reinoso, 2006). Figure 1.8 shows the schematic of the alignment of graphene layers with an increase of temperature leading to the graphite structure.

The polymer foam template methods are used for the preparation of reticulated carbon foams. Polyurethane foams of desired porosity and pore size are used as pore template. In this process, the polymer foam template is coated with the carbon precursor resin followed by curing; carbonization and graphitization resulted in carbon foam. In this, the porosity and pore size of the carbon foam are decided by the polymer foam template, nature of carbon precursor resin and number of impregnation. The various steps involved in carbon foam preparation are given in flow chart shown in Figure 1.9.

Recently, high internal phase emulsions (HIPE) based process is used for the preparation of carbon foams (Yang et al., 2013). An emulsion with the volume fraction of dispersed phase greater than 0.74 is called an HIPE. Here, an oil-in-

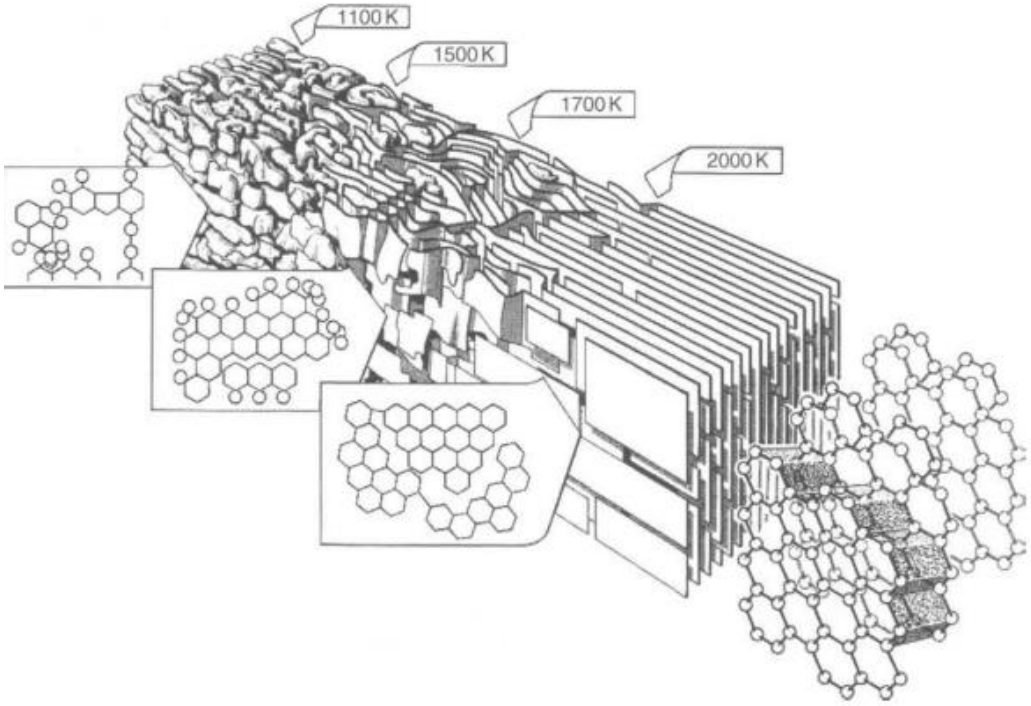

Figure 1.8: Development of the graphitic structure during the heat treatment temperature in the range of 1200 to 1800 ^{o}C (Marsh, 1991)

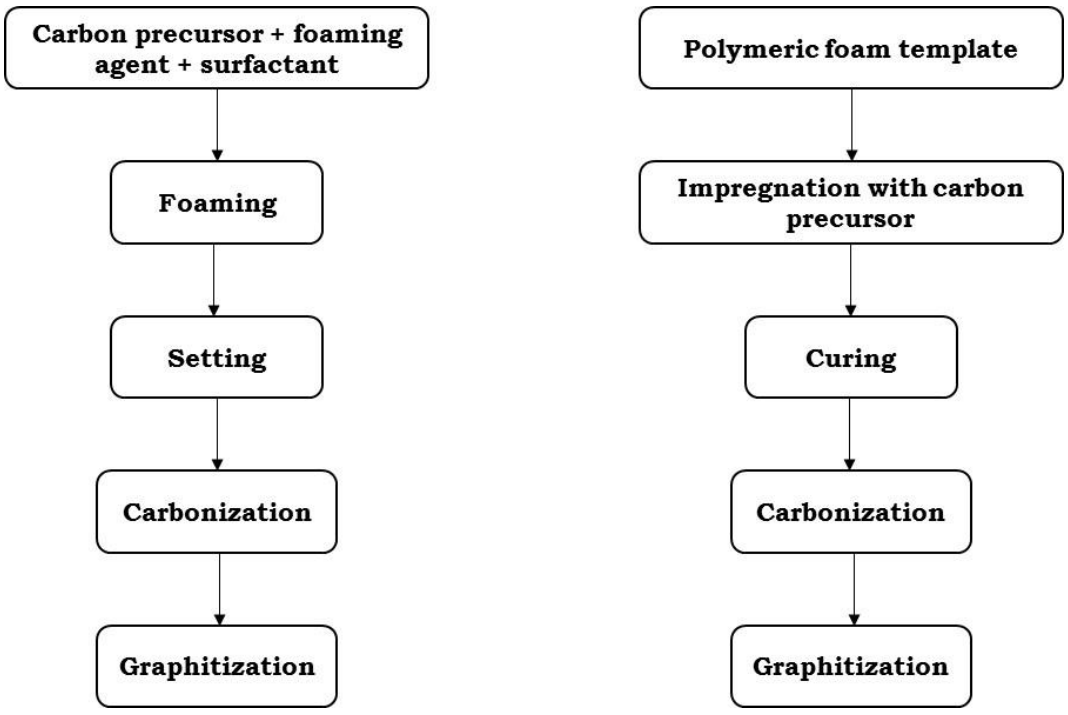

Figure 1.9: Flow charts for the preparation of carbon foams

water or water-in-oil HIPE containing carbon precursors in the continuous phase is prepared using a suitable emulsifying agent. The dispersed phase forms an interconnected structure and acts as the pore-forming template. The carbon precursors in the continuous phase are polymerized with the help of a suitable catalyst to form a solid structure. The dispersed phase is subsequently removed, and the polymerized carbon precursor is carbonized to produce the carbon foams.

1.3.2 Carbon Foam Precursors

The precursors of the carbon foams are categorized mainly based on the graphitizibility of the carbon derived from them. The precursor materials are broadly classified into thermoplastics and thermosetting resins. The thermoplastic precursors, such as coal-tar pitch, petroleum pitch, and synthetic mesophase pitch, are passing through a liquid plastic stage during carbonization. The carbon produced (soft carbon) develops long-range order (crystallinity) on further graphitization heat treatment. Due to the crystalline nature of the thermoplastic derived carbon foams, they show high mechanical strength and high thermal and electrical conductivities. Whereas thermosetting precursors do not form long-range ordered carbon during the carbonization due to their rigid cross-linked structure. The disordered carbon (hard carbon) produced does not form graphitic structure even at high graphitization temperature. Thermosetting precursors include the synthetic polymeric precursors and the natural renewable precursors.

1.3.2.1 Thermoplastic Precursors

Pitch is a tar-like material which is solid at room temperature and can be obtained from various sources like petroleum refining, destructive distillation of coal and pyrolysis of naphthalene and anthracene. It is a complex mixture of aromatic compounds of different sizes with the average molecular weight in the range of 300-400 depending on the source and the pre-treatment (Figure 1.10) (Kershaw and Black, 1993). In most of the cases, pitch is converted into a mesophase to achieve easy graphitization. Mesophase pitch is a nematic liquid-

crystal precursor containing domains of highly oriented molecules. Mesophase formation is achieved by heating pitch at about 350-450 ^{o}C in an inert atmosphere (Morgan, 2005). The advantage of the pitch for the production of carbon foam is its low cost when compared to the synthetic polymers.

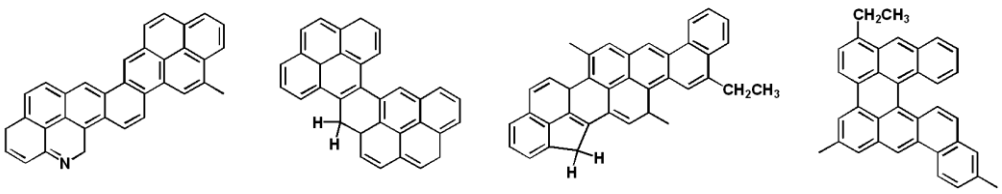

Figure 1.10: Molecular structures of coal-tar and petroleum pitch (Kershaw and Black, 1993)

Bonzom et al. (1981) reported the first process for the preparation of carbon foam from the petroleum derived pitch. In this process, a mixture of pitch and a blowing agent is subjected to high temperature and pressure in a mould. At this high pressure, the gases produced by the decomposition of the blowing agent dissolve in the molten pitch. Subsequently, the foaming and setting of the molten pitch are achieved by decreasing the pressure and temperature. The obtained foam is subjected to oxidative stabilization at 250 ^{o}C in air atmosphere and carbonization in the inert atmosphere to form the carbon foam. The interconnectivity of the cells in the cellular carbon foams can be controlled by the decompression pressure and temperature. The petroleum pitch is also used as the precursor for the preparation of reticulated carbon foam using polyurethane (PU) foam template (Chen et al., 2007). Here, the PU foam is impregnated with aqueous slurry of petroleum pitch containing an organic binder and a flow modifier. The impregnated foam is dried after removing the excess slurry by squeezing using rollers. Thus obtained pitch coated PU foam is subjected to an oxidative treatment in air at 350 ^{o}C followed by carbonization at 1000 ^{o}C and graphitization at 2800 ^{o}C in a high pure argon atmosphere to form partially graphitized reticulated carbon foam.

Chen et al. (2006); Stansberry et al. (2000) at West Virginia University developed carbon foams based on the coal-tar derived pitch which is comparatively cheaper than the petroleum based pitch. The coal tar pitch is heated (325-500 ^{o}C) in a mould under pressure (up to 100 MPa) and inert conditions. At this condition, the pitch undergoes pyrolysis, and the volatiles produced foams the pitch. The bubbles are stabilized by the viscosity increase due to the polymerization of the pitch. The foamed pitch is soaked for 8 h for coking and to render the foam infusible. The foamed pitch is carbonized up to 1200^{o}C in an inert atmosphere. The carbonized foam is graphitized at 2600 ^{o}C to increase the strength. Figure 1.11 shows the SEM microstructure of the coal tar pitch derived carbon foam.

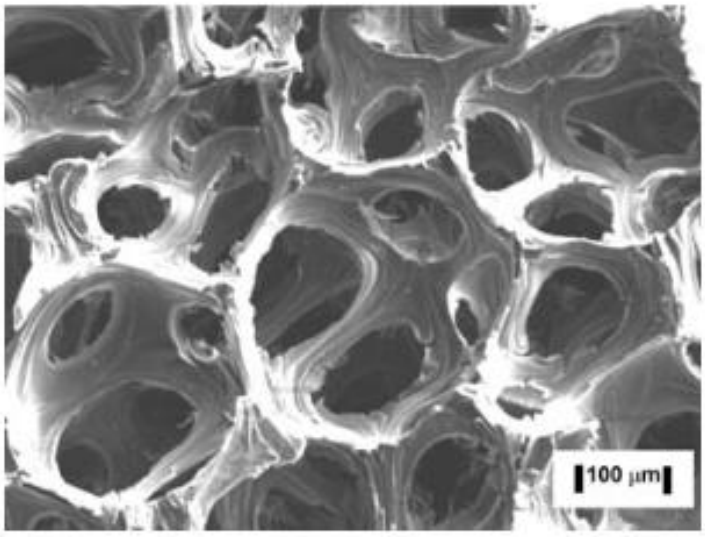

Figure 1.11: SEM microstructure of the carbon foam derived from the coal tar pitch (Scheffler and Colombo, 2006)

Kearns achieved foaming of mesophase pitch by heating in a mould at a temperature slightly higher than its melting point and under inert gas pressure followed by depressurization (Kearns, 1999). The solid organic foam thus obtained is subjected to oxidative stabilization, carbonization and graphitization to form the carbon foam. The carbon foam and graphitic carbon foam produced have very low density and very high specific compressive strength. The carbon foams produced have limited thermal and electrical conductivities due to two reasons.

First, the limited mobility of mesophase domain due to high viscosity of the pitch at the foaming temperature which is slightly higher than its melting point that hinder their orientation parallel to the cell walls. Second, the oxidative stabilization causes the surface layer infusible for further graphitization. Klett et al. (2000) from Oak Ridge National Laboratories, USA, developed a novel process for the preparation of graphite carbon foam with a high degree of crystallinity and thus the high thermal and electrical conductivities, from the mesophase pitches. In this, the mesophase pitch is heated in a mould under nitrogen gas pressure at a high temperature in the range of 500 to 800 ^{o}C. The volatiles produced by the pyrolysis of the mesophase pitch create bubbles which are stabilized by the viscosity increase by polymerization. The process ultimately leads to an infusible foam product which is removed from the mould after cooling and pressure release. The infusible foam obtained is subjected to carbonization and graphitization heat treatments to produce the graphite foam. This process overcomes the problems associated with the Hager-Kearns method as foaming is carried out at a temperature much higher than the melting point, and it is free from the oxidative stabilization step. Methods such as foaming at low pressure and foaming in a mould with restricted space at 1 atmosphere pressure are reported for the preparation of carbon foam from mesophase pitch (Wang et al., 2008b). Template based methods using salt particles and PU foams as foam template are also reported for the preparation of carbon foam from mesophase pitch (Prieto et al., 2012; Yadav et al., 2011).

1.3.2.2 Thermosetting Precursors

Thermosetting precursors are synthetic polymeric materials which leave a considerable amount of carbon during pyrolysis. The thermosetting precursors include phenol-formaldehyde, poly (furfuryl alcohol), polyimide, poly (aryl acetylene), cyanate esters and poly benzoxazine. These polymeric precursors are prepared in their low molecular weight forms called resins. There are generally three approaches for the preparation of carbon foams from these polymeric precursor resins. In the first approach, the precursor resins are foamed using a

suitable surfactant and blowing agent followed by curing, by further cross-linking reactions to form a polymer foam. The polymer foam is subsequently carbonized at high temperature in an inert atmosphere to form carbon foam. Preparation of carbon foam by this method has been reported from precursor resins such as phenolic, furfural, polyester, polyurethane, poly benzoxazine, cyanate ester resin, and polyarylacetylene (Figure 1.12) (Lei et al., 2010; Lin et al., 2014b; Liu et al., 2007a; Lorjai et al., 2009; Zhang et al., 2010).

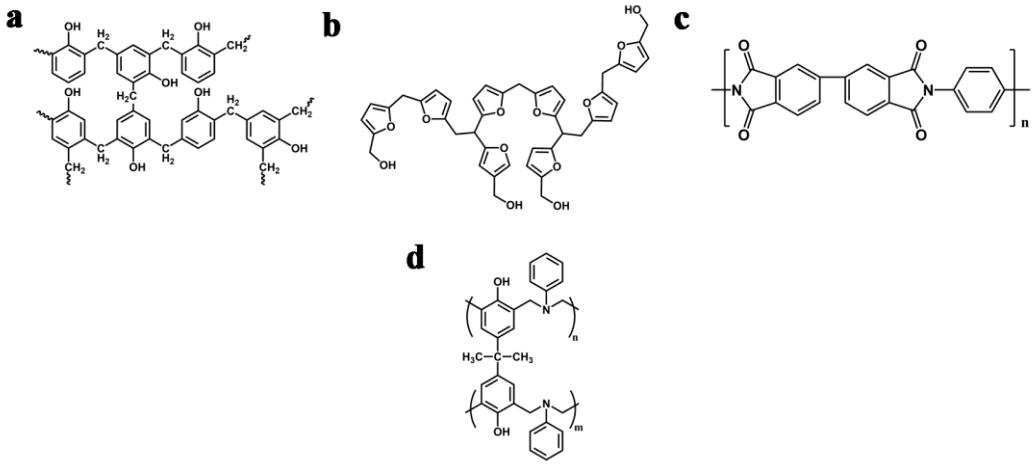

Figure 1.12: Molecular structures of polymer resin precursors (a) phenol-formaldehyde (b) polyfurfural (c) polybenzoxazine and (d) polyimide

The second approach for the preparation of carbon foams from the thermosetting resin is the impregnation of PU foam template with the carbon precursor resin followed by curing and carbonization. This method generally produces RVC foam. Knippenberg and Lersmacher (1976) modified the PU foam template by coating with polyvinyl alcohol to prevent their solubility in the alcohol which is used as the solvent for the carbon precursor resin. The multiple coating of carbon precursors such as phenolic and furfural resins is used to control the carbon foam properties (density, pore size, mechanical strength, etc.). The polyimide resin is also used as a precursor for the preparation of carbon foam by polyurethane foam template method (Inagaki et al., 2004). Here, ester type polyurethane foam is impregnated with the poly (amide acid) followed by the imidization at 200 ^{o}C to produce polyurethane/polyimide composite foam. During the pyrolysis at 800 ^{o}C, the polyurethane undergoes complete decomposition

without leaving any residue whereas the carbon produced from the polyimide retains the structure of the polyurethane foam template. Further heat treatment is carried out at 3000 ^{o}C for the graphitization.

Salt particles and liquid droplets are also used as the template for the preparation of carbon foam from thermosetting resin precursors. In the first case, the salt particle is uniformly dispersed in the carbon precursor resin followed by curing, carbonization and removal of salt by leaching with water to produce the carbon foam (Hopper and Pekala, 1989). Sodium chloride particles are generally used as pore templates and PAN, and phenolic resin are used as the carbon precursors. In the emulsion based method, an immiscible solvent is uniformly dispersed in a solution of the carbon precursor resin using an emulsifying agent. The emulsion is set by curing the carbon precursor resin by further polymerization and cross-linking. Subsequent removal of the immiscible liquid by solvent extraction and carbonization resulted in carbon foams. Liu et al. (2007b) used paraffin oil as the immiscible oil phase for making emulsions from aqueous resorcinol formaldehyde resin for the preparation of carbon foam. Phase inversion of polymer solutions followed by supercritical drying and carbonization is yet another method used for the preparation of carbon foams from thermosetting resin precursors. Gelation by phase inversion of PAN solution in solvents such as propylene carbonate and tetramethylene sulfone containing alkali metal halides using the triethanolamine is reported for the preparation of carbon foams by Brown and Simandl (1994).

1.3.2.3 Natural Renewable Precursors

Due to the fast depletion of the fossil fuels, the conventional carbon precursors like thermosetting synthetic polymers and thermoplastic pitch are to be replaced with the naturally renewable molecules. These bio-renewable molecules are the subclass of thermosetting precursors. But, the presence of large fraction heteroatoms in these carbon precursors, limited the carbon yield, which indeed limited the density and strength of the carbon foams. The preparation of carbon

foams from naturally renewable materials such as tannin, sucrose, olive stone, birch sawdust and lignin are reported in the literature (Jana and Ganesan, 2009; Li et al., 2012; Liu et al., 2013; Prabhakaran et al., 2007; Rios et al., 2006; Seo et al., 2014; Tondi et al., 2009; Wang et al., 2011).

Tannin is a commercially available material of vegetable origins. It is extracted from the bark of tannin tree (Tondi et al., 2009). Main composition of the tannin is 75 to 80 % polyflavonoids, and the rest is a mixture of carbohydrate monomers and oligomers. The structure of the main polyflavonoids present in tannin is shown in Figure 1.13 (a). The phenolic nuclei in the polyflavonoids can undergo reaction with formaldehyde as in phenol-formaldehyde reactions. Therefore, the method used for the preparation of foam from phenol-formaldehyde is adopted for the foaming of tannin by Tondi et al. (2009). Tannin-formaldehyde resin derived organic foam is very brittle. In order to improve the strength of organic foam, furfuryl alcohol is used as the additional strengthening agent. The microstructure, density, compressive strength and thermal conductivity of the carbon foam prepared from the tannin are tailored by modifying the resins with isocyanates (Li et al., 2012). Good fire resistance, acoustics absorption and EMI shielding properties are demonstrated for the tannin derived carbon foams (Amaral-Labat et al., 2013; Tondi et al., 2009). The SEM micrograph of carbon foam prepared from tannin is shown in Figure 1.13 (b).

Another important precursor of agricultural origin for the preparation of carbon foam is sucrose. It is considered as a hydrate of carbon and represented by the formula $C_{12}(H_2O)_{11}$ (Figure 1.14 (a)). The preparation of carbon foam from sucrose is first reported by Prabhakaran et al. (2007). Here, an aqueous sucrose solution is heated to produce a viscous resin. Herein, the sucrose undergoes hydrolysis in an aqueous acid medium to form glucose and fructose. The formed glucose and fructose undergo further oxidation due to the nitric acid to form a mixture of gluconic acid, saccharic acid, tartaric acid, etc. Further heating results in the viscous resin due to polymerization by intermolecular condensation through

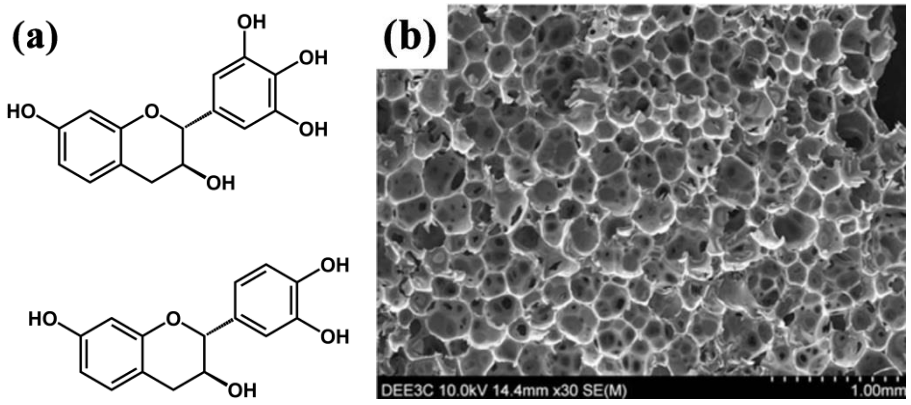

Figure 1.13: The structure of the main polyflavonoids present in tannin and SEM micrograph of carbon foam prepared from tannin (Tondi et al., 2009)

–OH and –COOH groups (Finar, 2007b). The foaming and setting of the sucrose resin are accomplished by heating in an open Teflon mould at 120 ^{o}C. The foaming is due to the blowing of the viscous resin due to the water vapour produced by the condensation reactions. The bubbles are captured in the position due to the increasing viscosity. The solid organic foam obtained is subsequently dehydrated and carbonized to produce the carbon foams. However, the carbon foams show low density (0.115 to 0.145 g/cm^3) and compressive strength (~0.9 MPa). The SEM microstructure of the carbon foam prepared from aqueous sucrose resin is shown in Figure 1.14 (b).

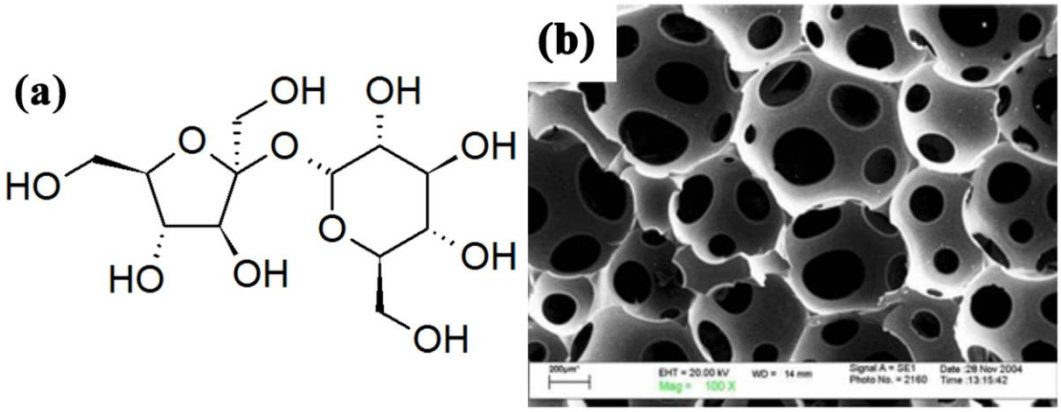

Figure 1.14: (a) Molecular structure of sucrose and (b) SEM microstructure of the carbon foam prepared from aqueous sucrose resin (Prabhakaran et al., 2007)

Jana and Ganesan (2009) studied the carbon foams prepared from sucrose for trapping of the radioactive nuclide, ^{137}Cs. They find that the trapping

efficiency and distribution coefficient of the ^{137}Cs between the carbon foam and molten sodium is comparable for both sucrose-derived carbon foam and commercially available reticulated vitreous carbon (RVC) foam. Jana and Ganesan (2011) also reported the preparation of the carbon-coated alumina foam by foaming a resin obtained by heating sucrose and aluminium nitrate. Herein, the NO_x gases produced from the aluminium nitrate produce bubbles which are stabilized by viscosity increase due to polymerization.

Olive stone, cork and birch sawdust are the other natural renewable carbon precursors for the preparation of carbon foam (Klett, 1975; Liu et al., 2013; Rios et al., 2006; Wang et al., 2011). Rios et al. (2006) reported the preparation of carbon foam by swelling and pyrolysis of olive stone particles in presence of a steam pressure of 1 MPa at 500 ^{o}C in a stainless steel reactor. Wang et al. (2011) reported the preparation of carbon foam from the birch sawdust. In this, the birch sawdust is liquefied by treating with a mixture containing phenol, sulfuric acid and phosphoric acid followed by a series of purification steps. The liquefied sawdust is subjected to resinification by reaction with formaldehyde in the presence of a base catalyst. Further, the resin is foamed using pentane as a blowing agent followed by carbonization in an inert atmosphere to produce the carbon foam. Seo et al. (2014); Yang et al. (2013) reported the preparation of carbon foam from lignin using poly (methyl methacrylate) beads as pore template.

1.3.3 Physical Properties of the Carbon Foams

The physical properties such as relative density, mechanical strength, thermal conductivity and electrical conductivity of carbon foams strongly depend on the crystallinity of the carbon, cell size, cell interconnectivity, morphology of the cells, and thickness of the struts and ligaments. The following sections discuss the physical properties of the carbon foam.

1.3.3.1 Relative Density

The most important structural property of the carbon foam is its relative density (ρ^*/ρ_s). The relative density of the foam is defined as the ratio of the density of the foam (ρ^*) to the density of the solid from which the foam is made up of (ρ_s). The porosity (1- ρ^*/ρ_s) is the fraction of pore space in the foam. According to Gibson and Ashby, the cellular foam materials have the relative densities less than 0.3 (Gibson and Ashby, 1997). On the other hand, the solids with relative density more than 0.3 are said to be porous solids. That is, the pores are isolated in the solid matrix. The important parameters that affect the relative densities are cell size, cell shape, cell interconnectivity, and thickness of struts and ligaments.

1.3.3.2 Thermal Conductivity

The thermal conductivity of the carbon foams strongly depends on the precursor materials as well as the heat treatment temperatures (Gibson and Ashby, 1997). The thermal conductivity of the carbon foams is due to conduction, convection, and radiation. However, the contribution due to convection in the small cells is negligible (Gibson and Ashby, 1997). The heat conduction through the foams is mainly attributed to the conduction through the solid and through the gas or the air filled in that (Gibson and Ashby, 1997). The conductivity in the cellular solids is usually described by equation (1.3).

$$\tilde{\lambda} = \frac{1}{3}\left(\left(\frac{\tilde{\rho}}{\rho_s}\right) + 2\left(\frac{\tilde{\rho}}{\rho_s}\right)^{3/2}\right)\lambda_s + \left(1 - \left(\frac{\tilde{\rho}}{\rho_s}\right)\right)\lambda_g \qquad (1.3)$$

Where λ_s and λ_g are conduction through the solid and gas, respectively. The thermal conduction of gas is very low (λ_g = 0.025 W/m/K). Thus, the conduction of the solid which mainly defines the thermal conductivity of the carbon foam. The carbon foam prepared from the thermosetting resins and

naturally renewable precursors usually have low thermal conductivity (0.035 to 0.5 W/m/K) due to the non-crystalline nature of the carbon (Li et al., 2012; Tondi et al., 2009; Wu et al., 2012). The carbon foams prepared from coal-tar and mesophase pitches show the thermal conductivity in the range of 23.5-110 W/m/K (Fawcett and Shetty, 2010; Li et al., 2007a; Li et al., 2007b; Li et al., 2010a, b, c, 2011c; Yadav et al., 2011; Zhu et al., 2007). Carbon foams with high thermal conductivity could be obtained by using mesophase pitch as the precursor and heat treatment up to 2800 ^{o}C. Thermal conductivity as high as 180 W/m/K is reported for mesophase pitch-derived carbon foam (Gallego and Klett, 2003; Klett et al., 2000).

1.3.3.3 Electrical Conductivity

The electrical conductivity of the cellular materials is related to its relative density (Gibson and Ashby, 1997). In general, electrical conductivity increases linearly with an increase in the relative density, according to the following equation (1.4).

$$R^* \propto \frac{R_s}{\left(\rho^*/\rho_s\right)} \tag{1.4}$$

Where R* is the resistivity of the foam, R_s is the resistivity of the solid, ρ^*/ρ_s is the relative density. The decrease in electrical conductivity with the decrease in relative density is due to the decrease in average cross-section available for conduction as well as increase in tortuosity of the current path (Gibson and Ashby, 1997). The carbon foams, in general, show good electrical conductivity due to the presence of free π electrons. However, the electrical conductivity depends on the carbon precursors and heat treatment temperature.

The non-crystalline carbon foams derived from synthetic polymers and natural renewable precursors show low electrical conductivity. The electrical

conductivity of the carbon foams derived from synthetic polymers reported in the range of 0.005 to 5 S/cm (Harikrishnan et al., 2007; Lorjai et al., 2009). The carbon foams from natural renewable precursors like tannin and sucrose show the electrical conductivity in the range of 0.2 to 1.4 S/cm (Prabhakaran et al., 2007; Tondi et al., 2009). On the other hand, graphitic foam obtained from mesophase pitch shows electrical conductivity in the range of 20 to 1250 S/cm (Stansberry et al., 2000).

1.3.3.4 Mechanical Strength

The mechanical strength of brittle foam materials like carbon foam is generally measured in terms of its compressive strength or crush strength. Figure 1.15 shows a typical compressive stress-strain graph of the elastic brittle solid foam. The stress-strain graph generally contains an initial elastic region followed by a plateau stress region and a region of densification. The initial elastic region depends on the cell size, relative density and nature of the solid. After the elastic region, the cells start collapsing, and the cell collapse continues throughout the plateau region. The debris formed by the cell collapse fill the cells in the remaining foam that resulted in an increase of foam density which is responsible for the increase of stress in the densification region. The stress observed in the plateau region is taken as the compressive strength and the slope of the initial elastic region in the stress-strain graph is taken as the Young's modulus. The increase in relative density of the foam increases Young's modulus, compressive strength and decreases the strain at which densification starts. The compressive strength of brittle foam materials like carbon foam is best described by the Gibson and Ashby model given in equation 1.5 where σ_f^* is the compressive strength of the foam, σ_f is the compressive strength of the solid carbon and ρ^*/ρ_s is the relative density (Gibson and Ashby, 1997).

$$\frac{\sigma_f^*}{\sigma_f} = 0.2\left(\frac{\rho^*}{\rho_s}\right)^{3/2} \tag{1.5}$$

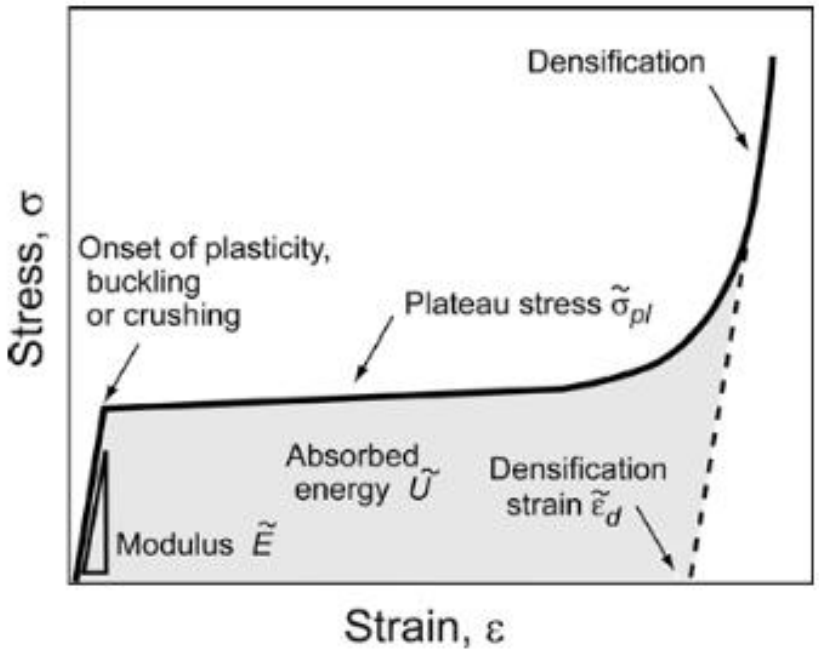

Figure 1.15: Typical stress-strain graph of brittle elastic foam (Scheffler and Colombo, 2006)

The compressive strength of carbon foams prepared from synthetic thermosetting resin precursors is reported in the range of 0.45–25.8 MPa (Lin et al., 2014b; Liu et al., 2007a; Luo et al., 2011a; Miller et al., 2013; Miller et al., 2010b; Wang et al., 2010; Wu et al., 2012; Wu et al., 2011), whereas the thermoplastic resin derived carbon foams show compressive strength in the range of 0.16 to 18.7 MPa (Chen et al., 2006; Fathollahi and Zimmer, 2007; Klett et al., 2000; Li et al., 2007a; Li et al., 2007b; Li et al., 2010a, 2011c; Prieto et al., 2012; Wang et al., 2008a, b; Wang et al., 2008c; Wang et al., 2006; Zhu et al., 2007). Naturally renewable precursors derived carbon foams show the compressive strength in the range of 0.52-8.4 MPa (Li et al., 2012; Prabhakaran et al., 2007; Tondi et al., 2009).

1.4 Reinforcements for Carbon Foams

The carbon foams show relatively high compressive strength. However, the proposed applications of carbon foam such as lightweight structural parts, core in composite panels, thermal protection material in the aerospace vehicles, etc.,

demand still higher mechanical performance. In order to improve the mechanical properties of the carbon foam and also to improve their other functional properties, suitable reinforcing agents are used. The mechanism of reinforcement is by stress transfer at the matrix-reinforcement interface. Reinforcements such as fibers, whiskers, dense and hollow particles, nanotubes, etc., are used (Fawcett and Shetty, 2010; Lafdi et al., 2008; Li et al., 2007b; Li et al., 2010a, 2011c; Wang et al., 2008a; Wang et al., 2010; Wang et al., 2009b; Wu et al., 2011; Wu et al., 2009; Zhu et al., 2007). The reinforcements are generally added to the precursor resin before foaming or impregnation on the polymer foam template. The following sections review the different reinforcements used in the carbon foams prepared from various precursors.

1.4.1 Reinforcements in Thermoplastic Resin Derived Carbon Foams

When compared to the thermosetting resin derived carbon foams, thermoplastic resin based carbon foams show good mechanical strength, thermal and electrical conductivity due to the graphitic structure of the carbon. Further improvement in the mechanical strength of the thermoplastic derived carbon foam is achieved by using suitable reinforcing agents. Wang et al. (2006) used Na-montmorillonite nanoclay as reinforcing additive in coal tar derived mesophase pitch-based carbon foams. They have observed ~ 83% improvement in the compressive strength of carbon foam with 10 wt.% nanoclay (Figure 1.16). The density of the carbon foams observed is in the range of 0.61 to 0.73 g/cm^3.

Natural graphite powder is used as reinforcing additives in carbon foams prepared from naphthalene based synthetic mesophase pitch and coal-tar pitch (Wang et al., 2008a; Zhu et al., 2007). The incorporation of natural graphite particles produces an improvement in compressive strength and thermal conductivity of the carbon foams. A maximum improvement in compressive strength of 110 and 237% is obtained for graphite particle reinforced carbon

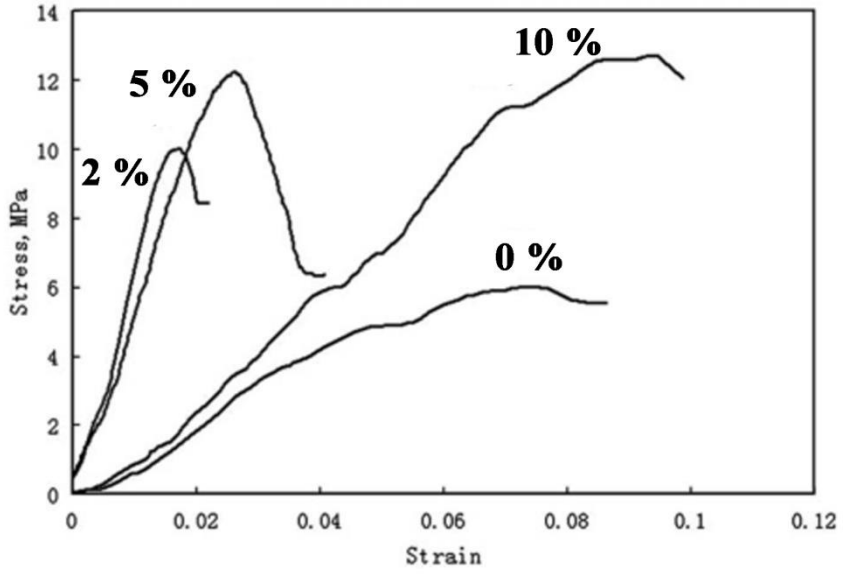

Figure 1.16: Compressive stress-strain graph shows the effect of the the addition of clay on the carbon foam (Wang et al., 2006)

foams derived from synthetic and coal tar mesophase pitches, respectively. The carbon nanofibers (CNF) are used as reinforcements in mesophase pitch derived carbon foams (Fawcett and Shetty, 2010). Fawcett and Shetty (2010) achieved an increase in strength, modulus and thermal conductivity in mesophase pitch carbon foams at low volume fraction (0 to 0.04) of CNF of 10 μm length. On the other hand, a decrease in compressive strength with an increase in the fiber fraction is observed at a CNF length of 100 μm due to non-uniform distribution of the longer CNF. The cell morphology is also affected by the fiber fraction as well as fiber length. Other reinforcements used for the thermoplastic precursor derived carbon foams are graphitized carbon black, short carbon fiber, zirconium and mesocarbon microbeads (Li et al., 2007b; Li et al., 2010a, 2011c).

1.4.2 Reinforcements in Thermosetting Resin Derived Carbon Foams

Thermosetting resin derived carbon foams show poor mechanical performance due to the presence of a large number of heteroatoms present in the precursor resin. During carbonization, the gases expelled create void and micro

cracks which are responsible for the poor mechanical performance. Thermosetting resin derived carbon foams are reinforced with carbon fiber, clay, whiskers, aluminosilicates, etc (Wang et al., 2010; Wang et al., 2009b; Wang et al., 2006; Wu et al., 2011). Miller et al. (2013) reported the carbon fiber reinforced carbon foam prepared from resorcinol formaldehyde resin. The carbon fiber bundles with the length between 2.5 and 25 mm are used. The RVC foam reinforced with clay is reported by Harikrishnan et al. (2007) by using PU foam as a template. The PU foam template is prepared by mixing a polyol containing dispersed Montmorillonite clay with a diisocyanate followed by foaming and curing. The PU foam is subsequently impregnated with a solution of p-toluene sulphonic acid (PTSA) catalyst and furfuryl alcohol. The impregnated furfuryl alcohol is polymerized and carbonized at 900 ^{o}C to obtain the clay reinforced RVC foam. The concentration of clay controls the cell size and thus the density of the RVC foam. The electrical conductivity of the RVC foam increases with the addition of the clay due to the increase in RVC foam density. Wang et al. (2009b) used a combination of carbon fiber reinforcement and densification by CVD and pitch impregnation to improve the density and mechanical strength of carbon foam. The carbon foams prepared from phenolic resin and 3 wt.% chopped carbon fiber of 3 mm length and 7.2 μm diameter show a maximum improvement in compressive strength (from 25 to 42 MPa) after two cycles of CVD and 3 cycles of pitch impregnation. Further, the addition of fiber decreases the brittleness of the composite foam as the carbon fiber deflects the micro-cracks or defects during propagation.

Ceramic microspheres are also used as reinforcing additives in carbon foams prepared from phenolic resin (Wang et al., 2010). Incorporation of 1 wt.% hollow ceramic microspheres results in an increase in compressive strength of carbon foam from 4.2 to 7.76 MPa and decrease in thermal conductivity from 0.25 to 0.15 W/m/K. Wu et al. (2011) used aluminosilicates, a waste product of mining and processing of coal, as a reinforcing agent for carbon foams prepared from phenol-formaldehyde resin. The maximum compressive strength and oxidation resistance are obtained at an aluminosilicate concentration of 11 wt.%. The

compressive strength increases from 3.8 to 6.4 MPa when the aluminosilicate content increases from 0 to 11 wt.%.

Considerable improvement in mechanical strength of carbon foams prepared from phenol-formaldehyde resin is achieved by incorporation of potassium titanate whiskers ($K_2Ti_6O_{13}$) as a reinforcing additive (Luo et al., 2011b). The potassium titanate whisker reinforced carbon foams show a maximum compressive strength of 7.5 MPa at a whisker concentration of 2 wt.%. On the other hand, the thermal conductivity decreases from 0.4 to 0.224 W/m/K when the whisker concentration increases from 0 to 4 wt.%. Lin et al. (2014b) used MWNT as reinforcement in the carbon foam prepared from cyanate ester resin. The compressive strength of carbon foam increases from 3 to 7.34 MPa when the MWNT concentration increases from 0 to 1 wt.%.

1.5 Applications of Carbon Foams

The carbon foam is the lightweight cellular macroporous carbon materials. Due to the combination of the properties such as chemical inertness, high thermal stability, relatively good mechanical property, lightweight, and tunable thermal and electrical conductivity, the carbon foam finds a lot of applications in various fields like aerospace, electronics, catalyst support, electromagnetic interference (EMI) shielding, electrode in battery, energy absorption materials, etc. Some of the important applications of the carbon foams are discussed in the following sections.

1.5.1 Thermal Insulating and Ablative Material

Ablative materials are traditionally used thermal protection system (TPS) in aerospace applications (Pulci et al., 2010). They work by the mechanism of some sacrificial surface mass loss to protect the internal structure from extreme thermal environment. Ablative insulation functions in three zones (a) virgin material zone: heat transfer through the conduction, (b) decomposition zone: heat

absorption due to fragmentation of the molecule and (c) char zone: heat absorption by ablation. Reactions can be endothermic (vaporization, sublimation) or exothermic (oxidation) and have a significant impact on net energy to the surface. Clearly, in comparison to reusable TPS, the interaction of ablative TPS materials with the surrounding environmental gases is much more complex as numerous mechanisms are active to accommodate the intense heating. Carbon foams are lightweight, fire resistant, thermally insulating and ablative materials which are studied for the thermal protection. As carbon foam is brittle and prone to debris formation, carbon foam-based sandwich structures are used in practical thermal protection applications (Brazel, 1990; Miller et al., 2010a; Rawal et al., 2003). For heat shield applications, Brazel (1990) reported the tri-element carbon based heat shield where an outer layer contains carbon-carbon composite, a middle layer includes pyrolytic graphite and an inner layer made up of carbon foam or felt. The outer layer is used for ablation and strength whereas inner layer, carbon foam or felt, is used for the thermal protection.

1.5.2 Thermal Management and Heat Sink Material

The high thermal conductive graphite foams offer the better solution for the thermal management devices for heat exchangers and heat sinks (Gallego and Klett, 2003; Klett and Conway, 2000; Lin et al., 2013; Wang et al., 2012c; Yu et al., 2006). Due to low density combined with the high thermal conductivity, the specific thermal conductivity of the graphite foams exceeds the corresponding values of copper and aluminium. ORNL's graphite foam developed by Klett et al has high thermal conductivity in the range of 50 – 150 W/m/K. The specific thermal conductivity of > 300 W/m/K/g/cm^3 observed is significantly higher than that of the existing conventional materials. The graphite foam is tested for heat sink applications by replacing a standard aluminum heat sink from a Pentium 133 microprocessor (Klett and Conway, 2000). The 8 g finned carbon foam performs better than the 44 g aluminium heat sink in the Pentium 133. Also, heat transfer ability of the graphite foam is tested for the heat exchanger applications. The

different configuration of graphite foam constructed for the heat exchanger studies is shown in Figure 1.17.

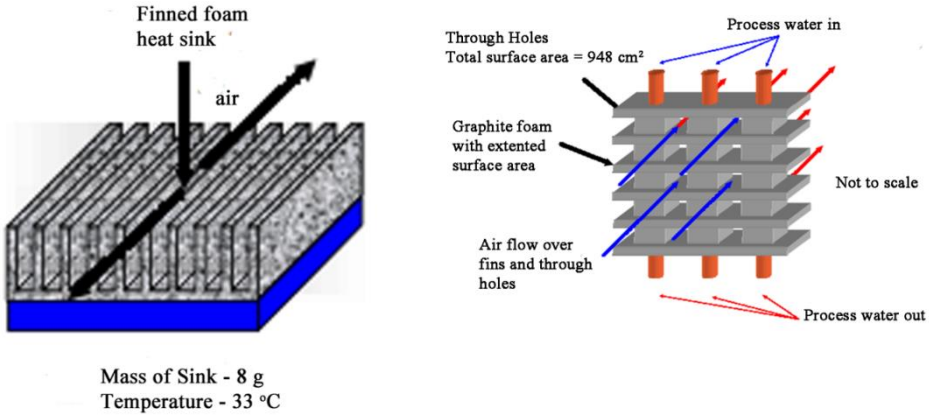

Figure 1.17: Different configurations of graphite foam constructed for heat exchanger studies (Klett and Conway, 2000)

1.5.3 Core Material for Sandwich Structure Material

A lightweight core material sandwiched between two stiff and strong skin materials is called a sandwich structure. Sandwich materials are widely used in the aerospace structures (Reyes and Rangaraj, 2011). Generally, fiber reinforced composite materials are used as skin materials. The core materials are either honeycomb or foam material. The skin and core are bonded by an adhesive layer. The sandwich materials have high strength and high stiffness to density ratio. Metallic foams are generally used as multifunctional core materials in the lightweight structures, which may require high strength and stiffness, thermal conductivity, wave scattering, mechanical energy absorption, etc. Despite the advantages of using the metallic foam core in composites, their use as a core in polymeric sandwich composites has been limited because of huge mismatch in their thermal expansion behaviors resulting in the delamination. Further, the bonding between the metallic foam core and the polymeric face sheets tend to be inherently weak. Carbon foam is recognized as having the greatest potential to replace the metallic foams in the laminated composite structures. (Kwon et al.,

1997; Sihn et al., 2012). Figure 1.18 shows the photograph of a carbon foam-sandwich composite structure.

Figure 1.18: Photograph of a carbon foam sandwich composite structure (Cfoam)

1.5.4 Electrode Material

Porous carbons are used as electrode material for various electrochemical applications such as sensors in electroanalytical studies, metal ion removal, synthesis of organic compounds, batteries and fuel cells, supercapacitors, etc. Usually porous carbon is mixed with a binder and solvent, drop casted over the conventional two-dimensional electrodes. Three-dimensional electrodes are having a lot of advantages over the two-dimensional electrodes due to their high space-time yield and high normalized space velocity (Friedrich et al., 2004).

RVC foam has high void volume, high external surface area, rigid structure, small pressure drop during fluid flow and high temperature and chemical resistances (Friedrich et al., 2004). Friedrich et al. (2004) reviewed the RVC foam for the electrode applications. The design of RVC electrode for electrochemical studies is necessary for uniform current and potential distribution, low ohmic internal resistance and high rates of mass transport of the electroactive species to the RVC surface. The surface of RVC electrodes is modified using various materials, including conducting polymers (Dalmolin et al., 2009, 2010). The RVC foam electrode surface is chemically modified using polyaniline for the

lithium-ion batteries. Dalmolin et al. (2009, 2010) modified the RVC foam surface using polyaniline and polypyrrole by electrodeposition and used as the cathode materials for lithium batteries, with improved charge-discharge cycles.

Coal-based carbon foam is used as the fuel cell electrode (Rogers and Plucinski, 2005). The electrochemical performance studied using cyclic voltammetry using ferricyanide system in KCl solution shows the improved Nernstian behavior when compared to glassy carbon, higher active surface area, and significant mass transfer effects. Kumar et al. (2013b) reported an enhancement in the capacitance of the carbon foams by the incorporation of ferrocene in the coal tar pitch used as the precursor. They have also showed that the incorporation of MWNT enhanced the electrochemical properties of carbon foams which are used as constructive electrode for lead acid batteries (Kumar, Kumari, Mathur, & Dhakate, 2014). The carbon foams prepared from graphite and poly (furfuryl alcohol) followed by catalytic graphitization show improved electrical conductivity and quasi-reversible behavior in the cyclic voltammogram (Amini et al., 2011). This is due to the improved specific electrochemical surface area and electron transfer rate due to the catalytic graphitization.

1.5.5 EMI Shielding

Electromagnetic interference is a new kind of pollution due to the development of electronics and instrumentation in civil and military sectors (Chung, 2000). EMI shielding in the microwave region (X and Ku band) is highly important to protect damages in defense and aerospace instruments. The mechanism of shielding is by reflection, absorption and multiple internal reflections of EM radiation. Conventionally used EMI shielding materials, like metals, are dense, difficult to process, have high cost and prone to corrosion. Also, the mechanism of EMI shielding in metals are through reflection which is not useful in military applications where stealth is necessary. The parameter used to measure the shielding performance is shielding effectiveness (SE). The SE of EMI shielding materials is determined by three losses: reflection loss (R), absorption

loss (A) and multiple reflection loss (M), and is defined by the following equation (Kumar et al., 2014a).

$$SE\ (dB) = SE_R + SE_A + SE_M \tag{1.6}$$

Carbon foam with a combination of properties such as lightweight, low thermal conductivity, good electrical conductivity, relatively high mechanical strength can be a good choice for EMI shielding material. Yang et al studied the carbon foam derived from mesophase pitch in the form of sandwich structures with glass fiber reinforced composite facings in the X and Ku band (Yang et al., 2004). They have achieved a maximum EMI shielding efficiency of 10 dB. Fang et al highlighted the importance of foam structure by comparing the dielectric loss and magnetic loss of carbon foam and powder obtained by pulverizing the same (Fang et al., 2007). The carbon foam shows large dielectric loss and extrinsically magnetic loss (artificial magnetic loss) compared to the pulverized carbon foam. They have also showed the carbon foam as a good radar absorbing material through theoretical simulation and validation studies. Moglie and co-workers studied the effect of thickness of carbon foam on the EMI shielding efficiency and achieved very good shielding efficiency at carbon foam thickness as low as 2 mm (Moglie et al., 2012). Rajeev kumar et al showed a tremendous improvement in EMI shielding efficiency of carbon foams prepared from mesophase pitch by the incorporation of nanoparticles like iron, nickel, Fe_3O_4 and ZnO (Kumar et al., 2014a; Kumar et al., 2014c). The incorporation of dielectric nanoparticles in the carbon foams greatly increases the absorption loss of the electromagnetic wave. This leads to their applications in stealth technology.

1.5.6 Host Structure for the Phase Change Material

Phase change materials (PCM) are the latent heat thermal energy storage materials where heat absorbed or released when the material undergoes a phase change (Pielichowska and Pielichowski, 2014; Shalaby et al., 2014). The phase change can be solid-solid, solid-liquid, solid-gas and liquid-gas or vice versa. Due

to the small change in volume and large latent heat during the phase change, solid–liquid PCMs are more attractive in thermal energy storage (Pielichowska and Pielichowski, 2014). The PCMs are widely used as a heat sink, thermal protection, computer cooling, etc. (Iten and Liu, 2014; Li et al., 2014; Zhou et al., 2013). Paraffin wax is a commonly used PCM. However, the application is very limited due to its poor thermal conductivity, which causes an increase in charge-discharge cycle time. The heat transfer in PCMs can be enhanced by using porous structures such as metallic foams, metallic fines, etc. having high thermal conductivity as hosts (Li et al., 2013; Xiao et al., 2014). Graphite foams having high thermal conductivity, high porosity, very good cell interconnectivity, good mechanical strength and chemical inertness are good candidates for host structures for PCM (Lafdi et al., 2008; Mesalhy et al., 2006).

Klett and Burchell (2004) reported the mesophase pitch-based carbon foam heat sink by filling the pores of the carbon foam with PCM. Because of the high thermal conductivity, fast heat transfer through the surface of the carbon foam to the PCM materials, allows rapid absorption or emission of the heat without a change in temperature. Efficient heat sink with improved structural integrality could be achieved by sandwiching the carbon foams filled with PCM between aluminium face sheets. Theoretical and experimental studies of different aspects of PCM/graphite foam composites for heat sink and energy storage applications are reported by various authors (Kim et al., 2014; Lafdi et al., 2008; Moeini Sedeh and Khodadadi, 2013; Xiao and Zhang, 2013; Zhao et al., 2014; Zhong et al., 2010).

1.5.7 Catalyst Support

Solid foams have attracted much attention as a catalyst support for heterogeneous catalytic reactions owing to their lower pressure drop and lower mass-transfer resistance compared to packed beds of particles (Inayat et al., 2011). Compared to other porous materials, carbon foams show good performance due to the relatively high thermal conductivity, high temperature tolerance, and good

mechanical properties. The open-cell foam with high surface area allows easy fluid flow and enables easy access to the catalyst coated on the surface (Bao et al., 2011; Wenmakers et al., 2008). Reactions such as reduction of NO and hydrogenation of cinnamaldehyde and 3-methyl-1-pentyne-1-ol has been reported using carbon foams as catalyst support (Wenmakers et al., 2010; Zhang et al., 2011).

1.6 Global and National Scenario on Carbon Foam Development and Applications

In the present scenario, the carbon foams are extensively used in the strategic applications such as thermal protection system, shock absorbers, EMI shielding, etc. The commercial applications of carbon foams are mainly in the electrodes for the batteries, catalytic supports, EMI shielding, host structure for the phase change materials, etc. The leading manufacturers of carbon foams are CFoam, Touchstone research laboratory, USA and POCO foam, ORNL, USA. Both the companies are mainly manufacturing the cellular carbon foams from coal-tar and petroleum pitch precursors. ERG Aerospace Corporation manufactures the reticulated vitreous carbon foam (RVC foam).

In India, the development of carbon foams is in the research and development stage. Few laboratories like National Physics Laboratory, Delhi and IGCAR, Kalpakkam are involved in the development of the carbon foams. The carbon foams are mainly studied in India for the strategic applications. The carbon foams are manufactured in India,for electrode applications in batteries, by Firefly Battery Private Limited, Gujarat whichis a subsidiary of Firefly Energy Limited, USA.

1.7 Objective and Scope of the Thesis

Carbon foams are generally prepared from petroleum or coal-derived pitches and synthetic polymers prepared from petroleum based monomers. Fast depletion of fossil fuels and the environmental concern drive the research community to find alternative naturally renewable carbon precursors for the carbon foam. Naturally renewable materials such as tannin, sucrose, olive stone and lignin are studied as precursors for the preparation of carbon foams. Among them, the sucrose is a widely available agricultural product. However, the carbon foams obtained by foaming of a resin prepared by heating an acidic sucrose solution have low density and mechanical strength. In addition, the foaming process is energy intensive. The main objective of this thesis is to study alternative methods for easy and energy efficient foaming of sucrose for the preparation of carbon foams. Another objective is to study the effect of reinforcing carbon additives in the preparation of carbon composite foams with higher mechanical strength from sucrose.

The specific objectives of this thesis are summarized below:

1. To study the foaming and setting of molten sucrose for the preparation of carbon foams.
2. To study the effect of chemical blowing agents such as aluminium nitrate and boric acid on the foaming characteristics of molten sucrose and the properties of the resultant carbon foams.
3. To study the effect of reinforcing additives such as AC particles and carbon short fibers on the foaming characteristics of molten sucrose and the properties of the resultant carbon composite foams.
4. To study the effect of nano reinforcing additives such as MWNT and graphene oxide on the foaming characteristics of molten sucrose and the properties of the resultant carbon composite foams.

5. To study the effect of reinforcing carbon additives in the foaming of aqueous sucrose resin for the preparation of carbon composite foams and properties of the resultant carbon composite foams.

1.8 Organization of the Thesis

This thesis describes the research on the processing of carbon foams from naturally renewable carbon precursor such as sucrose and various reinforcing carbon additives. The research focuses on the effect of additives on the foaming characteristics of the sucrose, structure-property relationship and different applications of the prepared carbon foam. The thesis is organized in nine chapters as below.

Chapter 1 provides a state-of-the-art literature survey on porous carbon and carbon foams along with their potential applications, research problem and objectives of the thesis.

In **Chapter 2**, the preparation of carbon foam from molten sucrose using an aluminium nitrate as a blowing agent is described. The effect of aluminium nitrate concentration on foaming and setting characteristics of molten sucrose, physical and mechanical properties and thermal conductivity of carbon foams is discussed. The formation of microporosity in the cell wall and strut of the carbon foam by an *in situ* activation and alumina pillaring is described. The application of this carbon foams in CO_2 capture is also discussed. The effect of alumina produced from the aluminium nitrate on the oxidation resistance of the carbon foam is also reported.

The preparation of boron-doped carbon foam from molten sucrose using a boric acid blowing agent is described in **Chapter 3.** The effect of boric acid concentration on the foaming and setting characteristics of molten sucrose and the properties of the resultant boron-doped carbon foams are reported. Also, the oxidation resistance of the boron-doped carbon foam is studied.

Chapter 4 describes the preparation of carbon composite foams by the thermo-foaming of AC powder dispersions in molten sucrose. The effect of AC powder concentration on foaming and setting characteristics of molten sucrose is reported. The role of AC particles on foam stabilization is established. The density, compressive strength, thermal conductivity, textural properties and CO_2 and oil adsorption characteristics of the resultant carbon composite foams are discussed as a function of AC particle concentration.

The carbon fiber reinforced carbon composite foam preparation from molten sucrose and milled carbon fiber is described in **Chapter 5**. The effect of fiber length and fiber concentration on the mechanical properties of the carbon composite foam is reported.

In **Chapter 6,** the effect of MWNT on the foaming and setting characteristics of molten sucrose is reported. The electrical conductivity, compressive strength and textural properties of the carbon composite foams are discussed as a function of MWNT concentration. EMI shielding performance of the carbon composite foam is also reported.

In **Chapter 7,** the effect of graphene oxide on the foaming and setting characteristics of molten sucrose is reported. The electrical conductivity, compressive strength and textural properties of the carbon composite foams are discussed as a function of graphene oxide concentration. EMI shielding performance of the carbon composite foam is also reported.

Chapter 8 reports the preparation of carbon composite foams by thermo-foaming of AC powder dispersions in an aqueous sucrose resin. The mechanisms of dispersion and foaming are disclosed. The effect of AC powder particle size on the foaming characteristics and properties of the carbon composite foam is described.

The results of the current work are summarized in **Chapter 9**. A mention of the scope for future research on this subject is also made.

CHAPTER 2

PROCESSING AND CHARACTERIZATION OF CARBON FOAMS FROM MOLTEN SUCROSE USING AN ALUMINIUM NITRATE BLOWING AGENT

2.1 Introduction

Low-density carbon foams with low thermal conductivity are suitable candidate for heat shielding material in aerospace applications (Chen et al., 2007; Inagaki et al., 2004; Klett, 1975; Stansberry et al., 2000). The commercially available low density carbon foams such as RVC foam are generally prepared from synthetic polymeric precursors (Chen et al., 2007; Harikrishnan et al., 2007; Inagaki et al., 2004). Preparation of low-density carbon foams from naturally renewable precursor is very important due to the fast depletion of fossil fuels, which are the sources of the synthetic polymers, and due to environmental concern (Bromley, 1986; Carhart Homer and Thompson Joseph, 1975; Danckwerts, 1979; Dubinin, 1966; G.D.Parfitt, 1981). Among tannin and sucrose, the widely studied natural renewable carbon precursors, sucrose is an abundant agricultural product (Jana and Ganesan, 2009; Prabhakaran et al., 2007; Tondi et al., 2009). Prabhakaran et al. (2007) reported the preparation of low-density carbon foams from sucrose through an aqueous resin route. In this, the carbon foam is prepared by the carbonization of a solid organic foam obtained by the thermo-foaming of a resin prepared by heating 50 wt.% aqueous sucrose solution using a nitric acid catalyst. The process is energy intensive as it involves a resin preparation and foaming steps. Moreover, the evaporation of water from the resin during the initial stages of foaming requires a large amount of energy. In addition to this, the process consumes long time as the foaming and setting of aqueous sucrose resin took nearly 48 h at 120 ^{o}C. Another disadvantage of the aqueous

sucrose based process is that a relatively thick surface hard layer is produced at the top of the solid organic foam. This hard layer is to be removed and discarded before carbonization. This reduces the yield of carbon foam. The foaming of molten sucrose is expected to overcome the above-mentioned difficulties. The present chapter reports the preparation of carbon foams by foaming of molten sucrose using an aluminium nitrate blowing agent. We have studied the effect of concentration of blowing agent on the foaming and setting characteristics of molten sucrose. Physical, thermal and CO_2 adsorption properties of the carbon foams as a function of the blowing agent concentration are discussed.

2.2 Experimental

2.2.1 Preparation of Carbon Foams

Analytical reagent grade sucrose ($C_{12}H_{22}O_{11}$) and aluminium nitrate ($Al(NO_3)_3.9H_2O$) were purchased from Merck India Ltd., Mumbai. The process flow chart for the preparation of carbon foam from molten sucrose is shown in Figure 2.1. 250 g sucrose and various concentrations of the aluminium nitrate were intimately mixed by ball milling in polyethylene containers on a roller mill using zirconia grinding media of 10 mm diameter for two hours. The sucrose to zirconia ball ratio used was 1:4 by weight. The aluminium nitrate concentrations used were in the range of 0.5 to 4 wt.% of the sucrose. The mixtures were heated in a 1 liter glass reaction kettle on a heating mantle at 160 ^oC for 15 min to form dark-brown homogeneous melts. The contents in the reaction kettle were mechanically stirred during the melting. The melts were transferred into 2.5 liter glass trays and heated in an air oven at 150 ^oC for foaming and setting into solid organic foams. The solid organic foams were cut into rectangular bodies of size 8 cm x 6 cm x 5 cm. The foam bodies were dehydrated in a muffle furnace at 250 ^oC in air atmosphere for 20 h. The heating rates used were 5 ^oC/min from room temperature to 150 ^oC and 1 ^oC/min from 150 to 250 ^oC. The foam bodies were then carbonized in an inert atmosphere furnace at 900 ^oC for 2 h. The heating rates used were 5 ^oC/min up to 250 ^oC and 2 ^oC/min from 250 to 900 ^oC. The furnace was cooled to room temperature by maintaining the inert atmosphere before

unloading the samples. Ultra-high pure argon gas was used for creating the inert atmosphere. The volume shrinkages of the foam bodies were calculated from their dimensions before and after the heat treatments. Densities of the foam bodies were calculated from their weights and dimensions.

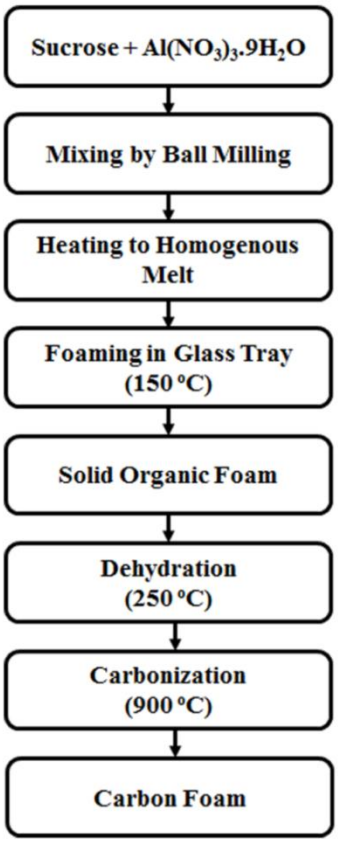

Figure 2.1: Flow chart of the preparation of carbon foam from molten sucrose

2.2.2 Characterization

2.2.2.1 Determination of Foam Rise

Mixtures containing 50 g sucrose and various concentrations of aluminium nitrate were melted in 1 liter borosilicate glass beakers to form homogenous melts. The melts were heated in an air oven at various temperatures in the range of 120 to 150 ^{o}C for 24 h. The ratio of the final height of the foam to the initial height of the resin was taken as the foam rise.

$$Foam\ rise = \frac{Final\ height\ of\ the\ foam\ (mm)}{Initial\ height\ of\ the\ resin\ (mm)} \quad (2.1)$$

2.2.2.2 Foaming and Setting Time Measurements

Mixtures containing 50 g sucrose and various concentrations of aluminium nitrate were melted in 1 liter borosilicate glass beakers. The melts were heated in an air oven at 150 ^{o}C. The heights of the foams were measured after every half an hour. The time after which there is no further increase in the foam height was measured as the foaming time. After the completion of foaming, the foams were physically inspected at an interval of 1 h. The time required for the soft foam to get transform into a hard one was determined as the foam setting time.

2.2.2.3 Viscosity Measurements

Nearly 13 ml of the molten sucrose prepared at various aluminium nitrate concentrations were taken in a small sample holder of a RVT model Brookfield viscometer (Brookfield Engineering Inc. USA). Viscosities of the molten sucrose at 150 ^{o}C were measured using a cylindrical spindle (SC 21 and 29) at shear rates in the range of 0.125 to 25 s^{-1}. All measurements were taken in the increasing order of the shear rate. The temperature of the molten sucrose was maintained at 150 ^{o}C during the viscosity measurements with the help of a Thermosel accessory.

2.2.2.4 Thermogravimetric Analysis

Thermogravimetric analysis (TGA) of the solid organic foam samples was carried out in both air and nitrogen atmospheres using a thermogravimetric analyzer (Q-50, TA instruments, USA) at a heating rate of 2 ^{o}C/min.

2.2.2.5 Isothermal Dehydration of Foam Body

A rectangular solid organic foam body of size 8 cm x 6 cm x 5 cm was heated in air atmosphere in a muffle furnace at 250 ^{o}C. Weight losses at various time intervals of the body were recorded using an electronic balance. The heating

rates used were 5 ^{o}C/min from room temperature to 150 ^{o}C and 1 ^{o}C/min from 150 to 250 ^{o}C.

2.2.2.6 Fourier Transform Infrared Spectroscopy

Fourier transform infrared (FTIR) spectra of the foam samples were recorded using a FTIR spectrophotometer (Spectrum-150, PerkinElmer, USA) in the spectral range of 4000 to 400 cm^{-1}. Samples for FTIR measurements were prepared by mixing the foams with KBr using a mortar and pestle and pressing into pellets by using a hydraulic press at 5 kN for 5 min.

2.2.2.7 X-Ray Diffraction

X-Ray diffraction (XRD) measurements of the carbon foam samples were carried out in an X-ray diffractometer (X'pert Pro, Philips, USA) using Cu Kα radiations (λ = 1.54056 Å). Powder samples for XRD analysis were prepared by crushing the carbon foams using a mortar and pestle**.** The diffraction patterns were recorded at 2θ values in the range of 5 to 75^{o} with a step size of 0.07^{o} using monochromatic X-rays.

2.2.2.8 Scanning Electron Microscopy and Energy-Dispersive X-Ray Spectroscopy

The microstructure of the foam samples was observed using a scanning electron microscope (SEM) (FEI Quanta FEG200, HRSEM). The samples for SEM analysis were prepared by cutting the foam bodies with a sharp knife. The cell size and cell window size of the foams were measured from the microstructures. The concentration of alumina on the as formed surface of a cell wall and on the fractured surface of a strut was analyzed using Energy-Dispersive X-ray spectroscope (EDAX) attached to the SEM.

2.2.2.9 Transmission Electron Microscopy

Transmission electron microscopy (TEM) images were obtained using a high resolution transmission electron microscope (JEOL JEM – 200) operating at 200 kV. The samples were crushed and dispersed in water by sonicating for 1 h using probe sonicator. The dispersions were then drop-casted on the carbon-coated copper grid and dried in room temperature for 2 days.

2.2.2.10 Compressive Strength Measurements

The compressive strength of the carbon foams was measured using a universal testing machine (Instron 5050, Instron USA) at a crosshead speed of 0.5 mm/min with 25 mm x 25 mm x 12 mm samples (ASTM standard C365/C365M-05). The maximum stress in the stress-strain graph was noted as the compressive strength. The reported compressive strength is the average of six measurements.

2.2.2.11 Thermal Conductivity Measurements

The thermal conductivity of the carbon foam samples was measured using modified transient plane source method (MTPS) at room temperature. The 20 mm x 20 mm x 6 mm samples were used for the thermal conductivity measurements. The reported thermal conductivity is the average of four measurements.

2.2.2.12 Textural Properties

The porous textural properties of the carbon foams were analyzed using the volumetric N_2 adsorption-desorption at -196 ^{o}C and CO_2 adsorption at 0 ^{o}C using a surface area analyzer (Micromeritics Tristar II, USA). The samples were degassed at 300 ^{o}C for 16 h prior to the analysis. The Brunauer-Emmett-Teller (BET) method was used for the calculation of the surface area. To get the reliable BET surface area, an appropriate p/p_o range was selected to ensure that a positive

line intersect of multi-point BET fitting (C > 0) would be obtained (Sing, 1998). The total pore volume was estimated from the amount of N_2 adsorbed at the relative pressure of 0.99. The micropore volume was obtained by using t-plot method in N_2 adsorption at -196 ^oC. The pore size distribution (PSD) was calculated using density functional theory (DFT) using N_2 adsorption isotherm by assuming slit-pore model (Lastoskie et al., 1993). The information about the ultramicropores was obtained from CO_2 adsorption isotherm at 0 ^oC (Dubinin, 1966).

2.2.2.13 CO_2 Adsorption Studies

The CO_2 adsorption of the carbon foam samples was evaluated at 0 and 25 ^oC by volumetric gas adsorption studies using a surface area analyzer (Micromeritics Tristar II, USA). Prior to the measurements, the samples were crushed using an agate and mortar and degassed overnight at 300 ^oC. The heat of adsorption was obtained by using a differential scanning calorimeter (DSC, TA Instruments Q20, USA).

2.2.2.14 Oxidation Studies

The oxidation studies of the carbon foams were carried out under non-isothermal condition using TGA and under isothermal condition using a muffle furnace. The amount of sample used for the non-isothermal oxidation study was 10 $\pm$ 1 mg. The heating rate of 10 ^oC/min and air flow rate of 60 ml/min was used. In the isothermal studies, approximately 0.5 g carbon foam samples were heated in the muffle furnace at temperatures in the range of 300 to 500 ^oC for 3 h in a static air atmosphere and noted their weight losses.

2.3 Results and Discussion

2.3.1 Melting and Polymerization of Sucrose

A range of melting points from 169 to 185 ^{o}C have been reported in the literature for sucrose (Finar, 2007a). It has been observed that the sucrose used in the present work melts into a clear liquid at the temperature of nearly 170 ^{o}C. The melt on further heating forms a dark brown viscous liquid called caramel containing a complex mixture of compounds. Caramelization of sucrose involves the formation of glucose and fructose anhydrides followed by their condensation to caramelan and caramelen with the molecular formula $C_{24}H_{36}O_{18}$ and $C_{36}H_{50}O_{25}$, respectively (deMan, 1999). Caramelan and caramelen are water soluble compounds with the melting point of 138 and 154 ^{o}C, respectively. Further condensation reactions of caramelan and caramelen with their precursor molecules continue at higher temperatures to form humin or caramelin, a water insoluble product of average molecular formula $C_{125}H_{188}O_{80}$ (Darder and Ruiz-Hitzky, 2005; deMan, 1999). The aluminium nitrate melts at 80 ^{o}C and decomposes at temperatures in the range of 90 to 170 ^{o}C to form O_2 and NO_x gases such as NO_2, NO and N_2O (Pacewska and Keshr, 2002). Addition of aluminium nitrate decreases the melting point of sucrose as a solution always has a lower melting point than the solvent (Atkins and DE Paula, 2007). It is observed that the sucrose containing 4 wt.% aluminium nitrate forms a paste-like consistency at a temperature of nearly 100 ^{o}C and then forms a pale yellow free flowing melt at a temperature of nearly 125 ^{o}C. The colour of the melt changes to dark brown when the temperature increases to ~ 160 ^{o}C. The melt expected to contain glucose and fructose anhydrides, their condensation products ($C_{24}H_{36}O_{18}$ and $C_{36}H_{50}O_{25}$), and dissolved NO_x gases produced by the partial decomposition of aluminium nitrate, sucrose and un-decomposed aluminium nitrate.

Figure 2.2 shows the effect of aluminium nitrate concentration on viscosity at various shear rates of molten sucrose. The molten sucrose in general shows shear thinning flow character. The molten sucrose without aluminium nitrate shows viscosities in the range of 2.5 to 4 Pa.s at shear rates in the range of

25 to 0.625 s^{-1}, respectively. The viscosity and shear thinning character of the molten sucrose increase with an increase in the aluminium nitrate concentration. The molten sucrose prepared at 0.5 wt.% aluminium nitrate shows viscosities in the range of 9.9 to 14 Pa.s at shear rates in the range of 25 to 0.625 s^{-1}, respectively. The increase in viscosity of the molten sucrose is remarkably high when the aluminium nitrate concentration increases from 0.5 to 2 wt.%. The viscosities of the molten sucrose at 2 wt.% aluminium nitrate are in the range of 39.5 to 52 Pa.s at shear rates in the range of 5 to 0.625 s^{-1}, respectively. Measurement of realistic values of viscosity of the molten sucrose prepared at aluminium nitrate concentrations of 3 and 4 wt.% is difficult with the present viscometer, due to rapid foaming during the measurement.

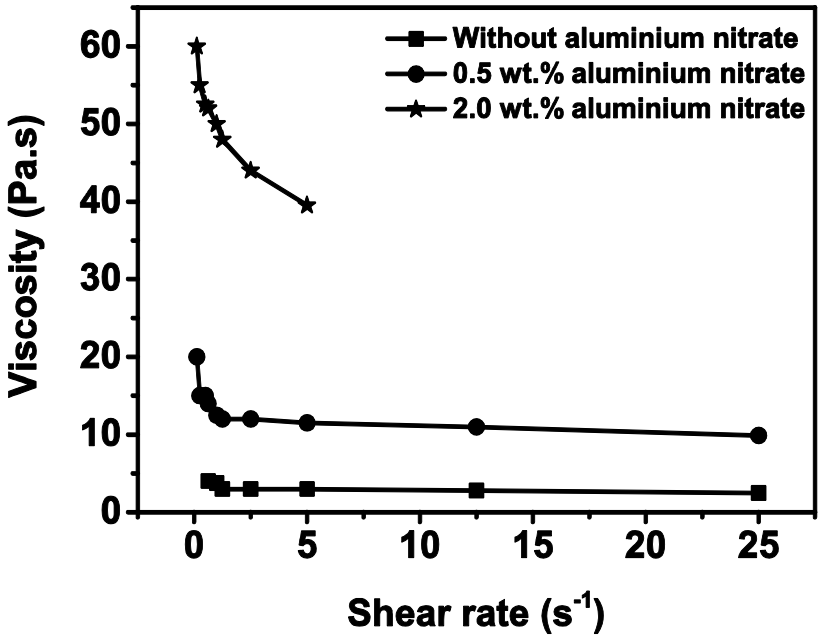

Figure 2.2: Effect of aluminium nitrate concentration on viscosity at various shear rates of molten sucrose

2.3.2 Foaming and Setting Characteristics of Molten Sucrose

The molten sucrose containing aluminium nitrate when heated in an air oven undergo slow foaming and subsequent setting into solid organic foams. During the foaming and setting, condensations of $C_{24}H_{36}O_{18}$ and $C_{36}H_{50}O_{25}$ with

their precursor molecules such as glucose and fructose anhydrides continue to form polymeric molecules like $C_{125}H_{188}O_{80}$ (deMan, 1999). The effect of temperature and aluminium nitrate concentration on the foam rise of molten sucrose is shown in Figure 2.3. The molten sucrose without the aluminium nitrate shows low foam rise values between 1 and 3 in the temperature range of 120 to 150 ^{o}C. At a particular foaming temperature, the foam rise of the molten sucrose increases with an increase in the aluminium nitrate concentration. The molten sucrose prepared at aluminium nitrate concentrations in the range of 0.5 to 4 wt.% shows foam rise values in the range of 4 to 9, respectively, at 150 ^{o}C. At temperatures above 150 ^{o}C, vigorous foaming of the molten sucrose to very high foam height is observed, even without aluminium nitrate. This vigorous foaming collapses the foams before setting. Therefore, 150 ^{o}C is chosen for all further foam preparations using an aluminium nitrate blowing agent. The effect of aluminium nitrate concentrations on approximate foaming and setting time of molten sucrose at 150 ^{o}C is shown in Figure 2.4. The foaming time decreases from 20 to 1 h, and the setting time decreases from 28 to 7 h when the aluminium nitrate concentration increases from 0 to 4 wt.%. The total time required for foaming and setting in the present process is much lower than that reported for the aqueous sucrose resin based process (Jana and Ganesan, 2009; Prabhakaran et al., 2007).

2.3.3 Mechanism of Foaming and Foam Setting

Successful preparation of foam requires the formation of gas bubbles in a liquid medium and stabilization of the bubbles against coalescence and rupture. The stabilization of bubbles in a liquid medium can be achieved either by reducing the gas-liquid interfacial tension using a suitable surfactant or by increasing the viscosity of the liquid to a sufficiently higher value (Rosebrock et al., 2005). The molten sucrose on heating in an air oven produces water vapour by condensation between the hydroxyl groups. This water vapour and NO_x gases produced by the decomposition of the aluminium nitrate generate bubbles

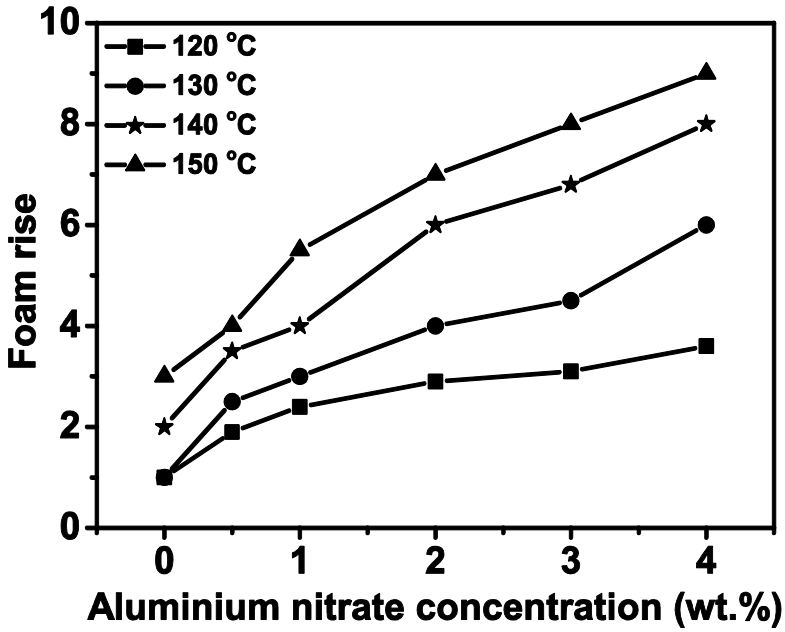

Figure 2.3: Effect of aluminium nitrate concentration and temperature on the foam rise of molten sucrose

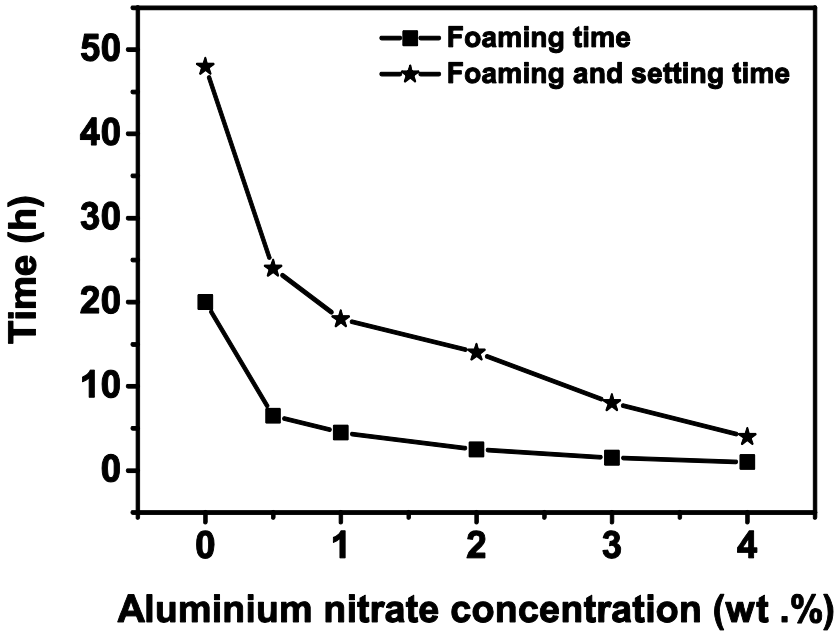

Figure 2.4: Effect of aluminium nitrate concentration on foaming and setting time of molten sucrose (foaming temperature – 150 ^{o}C)

resulting in the slow foaming. It has been observed that the foaming starts at the surface of the molten sucrose as the pressure imbalance required for the formation

of bubbles is created, first, at the upper surface. Subsequent bubbles are formed at the foam-melt interface results in the slow rise of the foam. Similar observation is made by Wang et al. (2009a), during foaming of pitch melt for preparation ofcarbon foams. The decrease in foaming time with an increase in aluminium nitrate concentration is due to the higher rate of production of the gaseous molecules. It is well-known that mineral acids act as the catalyst for the condensation between –OH groups to form -C-O-C- linkages (Finar, 2007b). The pH of molten sucrose measured using a pH paper shows values in the range of approximately 3 to 1 at aluminium nitrate concentrations in the range of 0.5 to 4 wt.%, respectively. The acidic pH is due to the H^+ generated by the hydrolysis of the Al^{3+} ions as represented below. The faster foaming and foam setting at higher aluminium nitrate concentrations is due to the higher rate of condensation between the –OH groups in the presence of the higher concentration of the acid catalyst.

$$Al^{3+} + 3NO_3^- + 3H_2O \leftrightharpoons Al(OH)_3 + 3NO_3^- + 3H^+ \qquad (2.2)$$

In the present case, the bubbles are stabilized against coalescence and rupture due to the higher viscosity of the molten sucrose in presence of aluminium nitrate. It is worthy to note that the foam produced from the molten sucrose without aluminium nitrate above 170 ^oC collapses by coalescence and rupture of the bubbles, due to its low viscosity. In the case of molten sucrose containing aluminium nitrate, the aluminium ions co-ordinate with the hydroxyl groups of the condensation products such as $C_{24}H_{36}O_{18}$ and $C_{36}H_{50}O_{25}$ results in cross-linking of these molecules through the aluminium ions (deMan, 1999; Koh et al., 2002). The increase in viscosity of molten sucrose with an increase in aluminium nitrate concentration is due to both the increase in rate of the condensation reaction and the increase in number of the aluminium cross-links.

The co-ordination of aluminium ions with the –OH groups is clearly evidenced in the FTIR spectra of the solid organic foams. Figure 2.5 shows the FTIR spectra of the solid organic foams prepared at various aluminium nitrate

concentrations. The solid organic foam prepared from molten sucrose without aluminium nitrate shows a broad peak at 3285 cm^{-1} corresponding to the stretching vibrations of –OH groups, which are involved in hydrogen bonding. FTIR peaks observed at 2905, 1720, 1668 and 1031 cm^{-1} are attributed to stretching vibrations of -C-H, -O-C=O, -C=C- and –C-O-C- groups, respectively (Jana and Ganesan, 2009). In the case of solid organic foams prepared from molten sucrose containing aluminium nitrate, a new peak observed in the FTIR spectra at 3565 cm^{-1} corresponding to the stretching vibrations of –OH groups, which are not involved in hydrogen bonding. It appears that in the solid organic foams without aluminium nitrate, polymeric molecules like $C_{125}H_{188}O_{80}$ formed by the condensation reactions self-assemble through inter-molecular hydrogen bonding. On the other hand, in the solid organic foams containing aluminium nitrate, the aluminium ions occupy positions in-between $C_{125}H_{188}O_{80}$ molecules and interact with a fraction of the hydroxyl groups present in the molecules through co-ordinate bonding (Darder and Ruiz-Hitzky, 2005; deMan, 1999). This increases the distance between the polymeric molecules that unable the remaining hydroxyl groups to interact through the hydrogen bonding. The additional FTIR peak observed at 3565 cm^{-1} in the solid organic foams containing aluminium nitrate is due to these hydroxyl groups. The structure of the solid organic foam with and without aluminium nitrate is schematically shown in Figure 2.6. It is clear from the above discussions that the aluminium nitrate helps in generation of gas bubbles in molten sucrose, stabilizes the bubbles, and enables faster setting of the foams.

Figure 2.7 shows the photograph of 250 g molten sucrose containing 4 wt.% aluminium nitrate foamed in a 2.5 liter glass tray at 150 ^{o}C and a solid organic foam body prepared by cutting using a sharp knife. Qualitative inspection shows uniform pore structure throughout the foam body. The unstructured thick fluffy top layer responsible for lower carbon foam yield of the aqueous sucrose resin based process is absent in the molten sucrose based process (Jana and Ganesan, 2009; Prabhakaran et al., 2007).

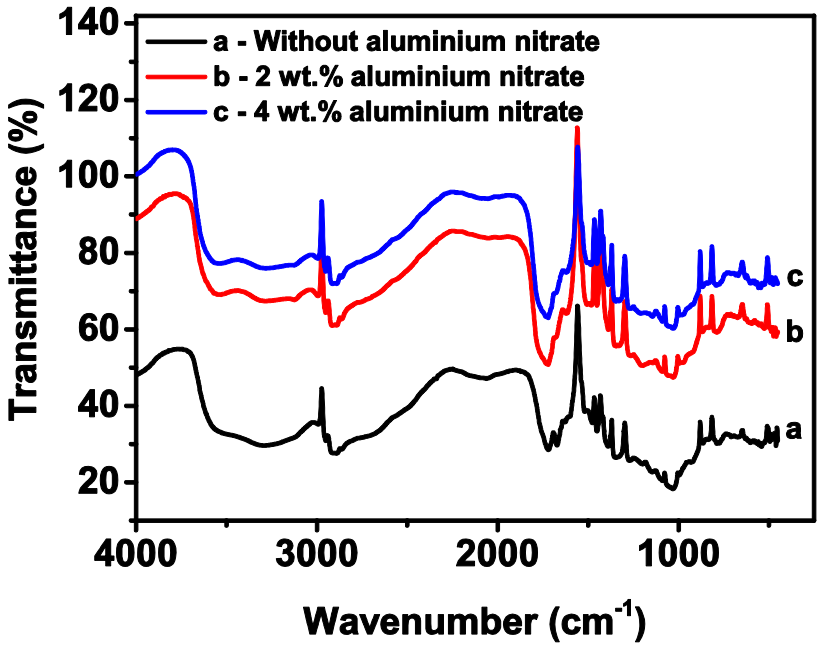

Figure 2.5: FTIR spectra of the solid organic foams prepared from molten sucrose at various aluminium nitrate concentrations

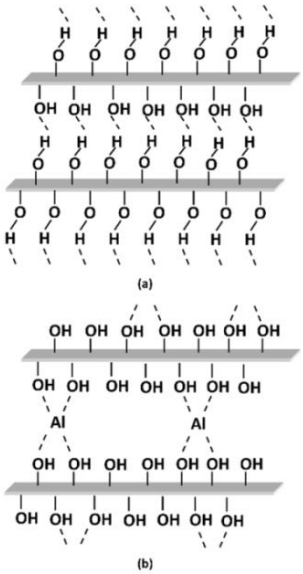

Figure 2.6: Schematic of the proposed structure of the solid organic foams (a) without and (b) with aluminium nitrate

Figure 2.7: Photograph of 250 g sucrose foamed in a 2.5 liter glass tray and a solid organic foam body (aluminium nitrate concentration - 4 wt.%)

The importance of caramelization in the foaming process is established as follows: The simultaneous melting and foaming of 50 g batch of sucrose-aluminium nitrate mixtures containing aluminium nitrate concentrations in the range of 0.5 to 4 wt.% in 1 liter borosilicate glass beakers in an air oven at 150 ^{o}C results in vigorous foaming to high foam volume followed by foam collapse before setting into solid organic foams. On the other hand, simultaneous melting and foaming of the sucrose-aluminium nitrate mixtures at temperatures of 130 and 140 ^{o}C results in solid organic foams with non-uniform pores. Many large voids of more than 10 mm size are observed especially in the solid organic foams produced at aluminium nitrate concentrations of 3 and 4 wt.%. The viscosities of the molten sucrose containing 0.5 and 2 wt.% aluminium nitrate measured immediately after melting are 4 and 8 Pa.s, respectively, at the shear rate of 0.625 s^{-1}. The rate of formation of NO_x gases and water vapour by the thermal decomposition of the aluminium nitrate and by the –OH condensations, respectively, is highest initially and decreases with time. The high rate of formation of the NO_x gases and water vapour in the melt having the low viscosity results in large bubble growth. Further, the bubbles in a low viscosity melt are more susceptible to growth by coalescence also. These large bubbles undergo rupture before setting leading to the foam collapse. Caramelization by heating at 160 ^{o}C under stirring for 15 min increases the viscosity (shear rate - 0.625 s^{-1}) of the molten sucrose containing 0.5 and 2 wt.% aluminium nitrate to 14 Pa.s and 52

Pa.s, respectively. Moreover, caramelized sucrose being a partially reacted system, the rate of formation of the NO_x gases and water vapour by further reaction during foaming at 150 ^oC will be low. The low rate of formation of the gaseous molecules in the caramelized sucrose melt having high viscosity results in slow foaming to form solid organic foams with the uniform pore structure.

2.3.4 Dehydration and Carbonization of Solid Organic Foams

Figure 2.8 shows the TGA plots of the solid organic foam prepared from molten sucrose at 4 wt.% aluminium nitrate. The solid organic foam shows the more or less similar thermal decomposition pattern in both air and nitrogen atmosphere in the temperature range of 40 to 350 ^oC. This indicates that the weight losses in this temperature range are mainly due to dehydration. Weight losses observed in this temperature range are 36.79 and 39.12 % in nitrogen and air atmospheres, respectively. The dehydration continues along with the oxidation of carbon at the temperatures above 350 ^oC in air atmosphere and leaves only 1.22 wt.% char residue at 600 ^oC. On the other hand, nearly 35 wt.% char residue is retained at 600 ^oC in nitrogen atmosphere. The carbon yield obtained in the nitrogen atmosphere is much lower than the theoretical carbon content of sucrose. This suggests that at the temperatures between 350 to 600 ^oC, loss of carbon as CO and CO_2 takes place due to the cleavage of -C-O-C- and -O-C=O groups along with the dehydration in the nitrogen atmosphere.

Though the TGA shows weight loss corresponding to dehydration up to 350 ^oC, a majority of the dehydration can be possible by heating the solid organic foams at 250 ^oC in air atmosphere for a longer time. The weight loss at various time intervals of a solid organic foam body of size 8 cm x 6 cm x 5 cm under the isothermal condition at 250 ^oC is shown in Figure 2.9. The foam body shows a weight loss of nearly 25 % in the first two hours. The rate of weight loss decreases with time and reaches a near plateau in 20 h at which the body recorded a total weight loss of 47 %.

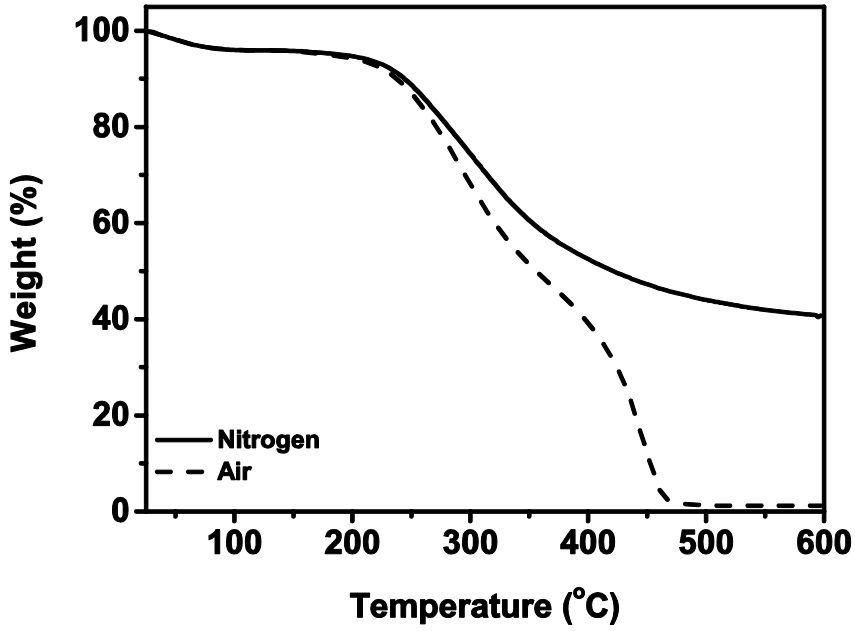

Figure 2.8: TGA plots of the solid organic foams (aluminium nitrate concentration - 4 wt.%)

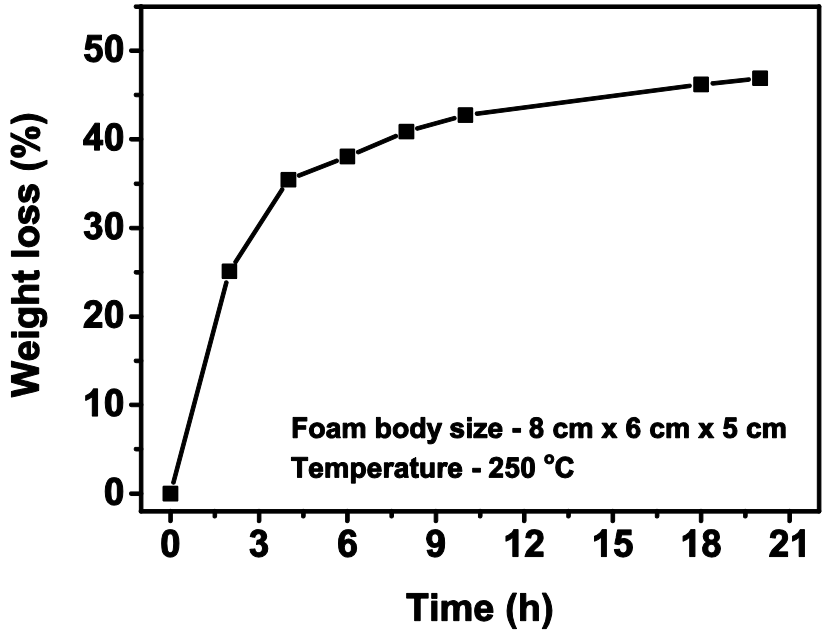

Figure 2.9: Isothermal dehydration kinetics of a large solid organic foam body

The solid organic foams undergo large shrinkages during the isothermal dehydration. The volume shrinkage during dehydration increases from 28 to 31.3

% when the aluminium nitrate concentration increases from 0.5 to 2 wt.%. Thereafter, the dehydration shrinkage rapidly increases to 43.5 and 46.3 vol.% at aluminium nitrate concentrations of 3 and 4 wt.%, respectively. The effect of aluminium nitrate concentrations on the shrinkages during dehydration and carbonization of the foam bodies is shown in Figure 2.10. It is well-known that the rapid shrinkage of large foam bodies during carbonization heat treatment results in formation of cracks. The isothermal dehydration allows the foam bodies to shrink at a slow rate, which prevents the formation of cracks. The shrinkages during the carbonization are larger than that observed during the dehydration. The dehydration shrinkage, carbonization shrinkage and total shrinkage observed are in a ranges of 30 to 43 vol.%, 44 to 46 vol.% and 61 to 76 vol.%, respectively, at the aluminium nitrate concentrations in the range of 0.5 to 4 wt.%. The foams undergo near-isotropic shrinkage during dehydration and carbonization as the linear shrinkage observed in the foam rise direction and in the lateral directions are more or less same. No crack or deformation is observed in the foams during the carbonization. The carbon foams prepared at 900 ^{o}C do not show peaks corresponding to the –OH, -C-H, -O-C=O and –C-O-C- groups in the FTIR spectra. This indicates that most of the residual hydrogen and oxygen atoms present in the dehydrated solid organic foams are removed during the carbonization. Figure 2.11 shows the photograph of a carbon foam body prepared at 900 ^{o}C.

The carbon foams prepared at 900 ^{o}C show electrical conductivity. It has been reported that the pyrolysis of organic polymers like polyvinyl chloride, cellulose, phenolic resin, and organic foam derived from aqueous sucrose resin, etc. produce tangled narrow graphite ribbons, which are responsible for the electrical conductivity of the resulting carbon (Jana and Ganesan, 2009, 2011; Prabhakaran et al., 2007). The XRD spectra of the carbon foams prepared from the molten sucrose show two peaks, corresponding to the crystalline reflections from (002) and (101) planes, irrespective of the aluminium nitrate concentrations

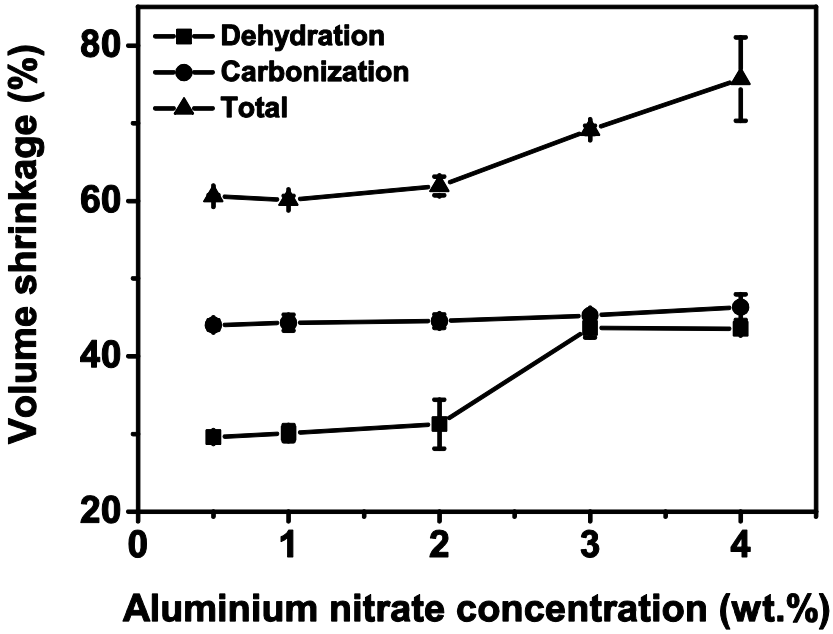

Figure 2.10: Effect of aluminium nitrate concentration on the shrinkages during dehydration and carbonization of foam bodies

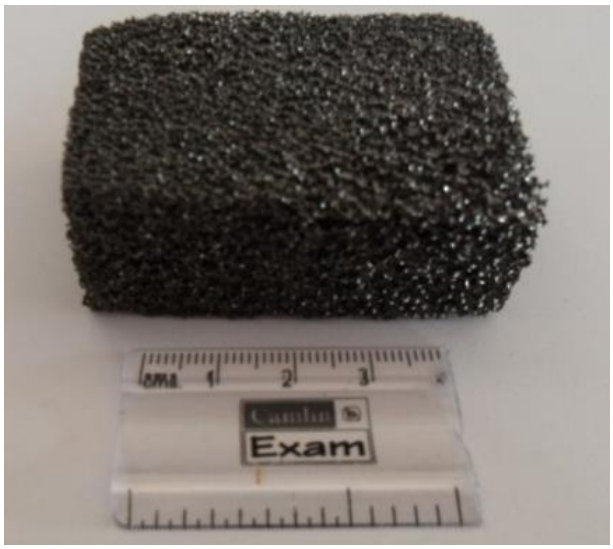

Figure 2.11: Photograph of a carbon foam body prepared at 900 ^{o}C

(Fang et al., 2007). The 2θ values at which the intensity maximum observed for the (002)/(101) planes are 25.10/43.68, 24.84/43.76, 24.71/44.63 and 24.23/43.69 for the carbon foams prepared at aluminium nitrate concentrations of 0, 0.5, 2 and 4 wt.%, respectively. However, previous work reports the corresponding intensity maximums at 2θ values in the range of 23/44 to 22.15/43.39 for the carbon foams

prepared from aqueous sucrose resin (Jana and Ganesan, 2009; Prabhakaran et al., 2007). The interplanar distances (d-spacing) calculated from Bragg's equation for the carbon foams prepared from molten sucrose at aluminium nitrate concentrations of 0, 0.5, 2 and 4 wt.% are 3.61, 3.58 , 3.6 and 3.67 Å, respectively. However, the corresponding d-spacing reported for the carbon foams prepared from aqueous sucrose resin are in the range of 4.09 to 3.8 Å (Jana and Ganesan, 2009; Prabhakaran et al., 2007). It is clear that the carbon foams prepared from the molten sucrose have turbostratic graphite structure. Also, the carbon prepared from the molten sucrose has better alignment of the graphite ribbons compared to that prepared from aqueous sucrose resin. Slight increase in the d-spacing with an increase in aluminium nitrate concentration indicates that the alumina produced from the aluminium nitrate hinder the packing of the graphite ribbons. The XRD spectra of carbon foams prepared from molten sucrose containing various aluminium nitrate concentrations is shown in Figure 2.12. The small peaks observed at 2θ values of 49.24 and 51.18^{o} at 4 wt.% aluminium nitrate are attributed to the alumina formed from aluminium nitrate.

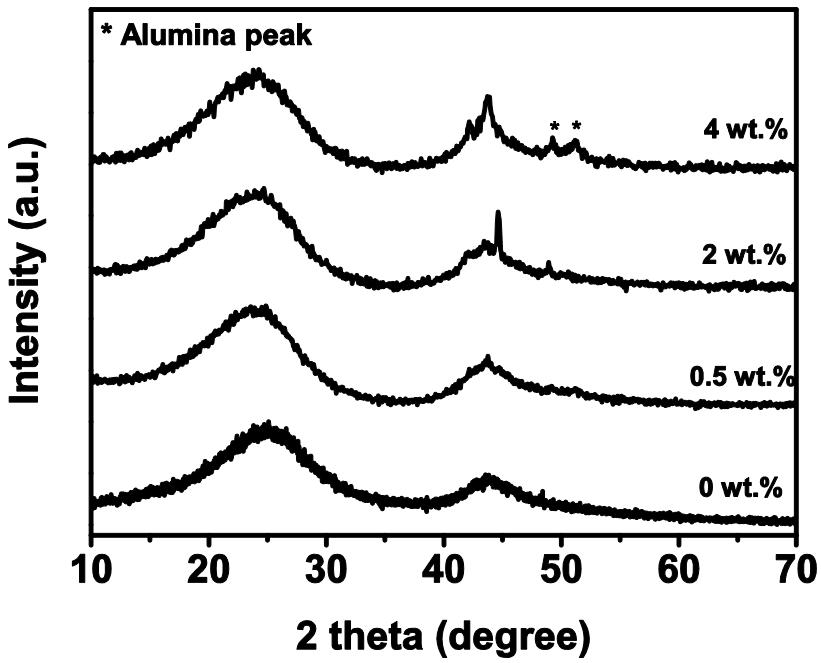

Figure 2.12: XRD spectra of the carbon foams prepared from molten sucrose at various aluminium nitrate concentrations

2.3.5 Density and Microstructure of the Carbon Foams

Figure 2.13 shows the density and average cell size of the carbon foams prepared at various aluminium nitrate concentrations. The density decreases from 0.15 to 0.053 g/cm^3 when the aluminium nitrate concentration increases from 0 to 4 wt.%. The corresponding porosities calculated from the theoretical density (2.26 g/cm^3) of graphite and bulk density of the carbon foams are in the range of 93.81 to 97.65 vol.%, respectively (Jana and Ganesan, 2009). The lower density of the carbon foams obtained at higher aluminium nitrate concentrations is due to the higher foam rise caused by large volume of the gases generated. The average cell size of the carbon foam decreases from 1.62 to 0.83 mm when the aluminium nitrate concentration increases from 0 to 4 wt.%. The cell size gradually decreases from 1.62 to 1.45 mm when an aluminium nitrate concentration increases from 0 of 2 wt.%. Thereafter, the average cell size drastically decreases to 0.83 mm when the aluminium nitrate concentration increases to 3 wt.%. Further increase in the aluminium nitrate concentration to 4 wt.% does not make any change in the average cell size. At the higher aluminium nitrate concentrations, large number of gas molecules (water vapour and NO_x) are homogenously generated in a small time interval in the molten sucrose at 150 ^oC. These gas molecules nucleate a large number of bubbles. The growth of these bubbles beyond a certain size either by incorporations of additional gas molecules or by coalescence is restricted by higher melt viscosity at the higher aluminium nitrate concentrations (Rosebrock et al., 2005). This restricted bubble growth due to the higher melt viscosity is the reason for the smaller cell size at higher aluminium nitrate concentrations.

Figure 2.14 shows SEM micrographs of the solid organic foam and the carbon foams prepared at various aluminium nitrate concentrations. The micrograph of the solid organic foam itself clearly shows interconnected cellular structure. The cells in the carbon foams have near-spherical morphology. The thickness of the struts and ligaments decreases with the increase in aluminium nitrate concentrations. Every cell contains few circular or oval shaped cell

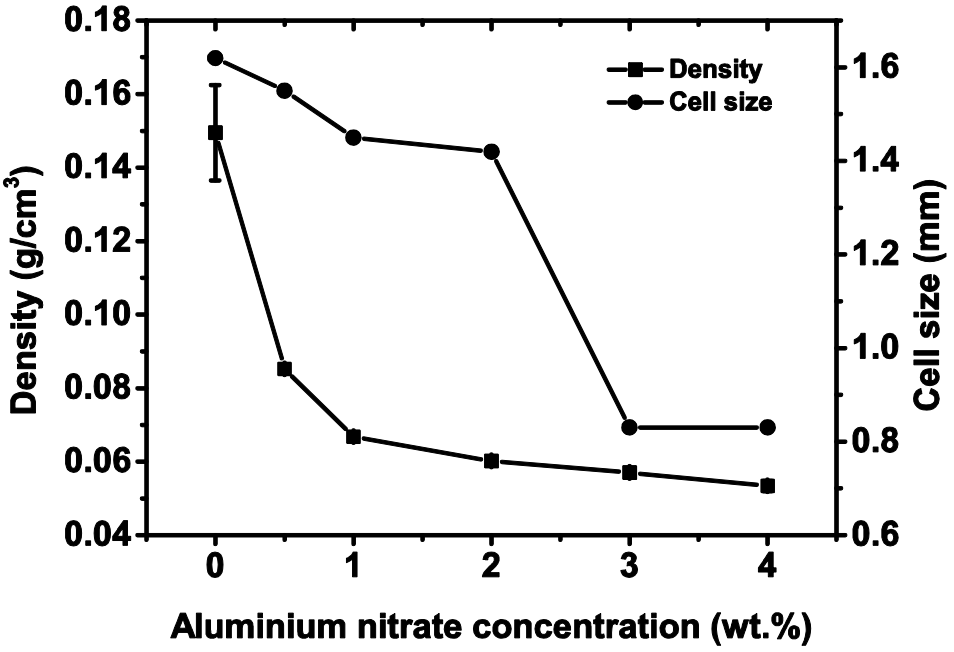

Figure 2.13: Effect of aluminium nitrate concentration on density and average cell size of the carbon foams

windows, which make connections between the cells. The hemispherical portion of each cell contains 4 to 5 such cell windows. The water vapour and NO_x gases continue to produce inside the bubbles even towards the setting of the foams. This increases the pressure inside the bubbles that results in a large difference between pressure inside and outside the bubbles. The cell windows which connect the cells are created by the rupture of cell walls when the pressure difference exceeds the strength of cell walls (Li et al., 2011a). The size of the cell windows which connects the cells decreases with an increase in aluminium nitrate concentrations. The sizes of these cell windows observed are in the range of approximately 50 to 500 μm. It is interesting to note that in the carbon foams prepared at aluminium nitrate concentrations of 3 and 4 wt.%, the small closed cells of sizes in the range of approximately 20 to 150 μm are observed in the ligaments and struts. These smaller cells are due to gas bubbles nucleated in the ligaments and struts after the formation of the cells at which the viscosity of the melt would be sufficiently high to prevent their further growth and rupture (Rosebrock et al., 2005). The abnormal increase in the shrinkage observed (Figure 2.10) during the dehydration of the

solid organic foams when the aluminium nitrate concentration increases from 2 to 3 wt.% is due to the shrinkage of these bubbles.

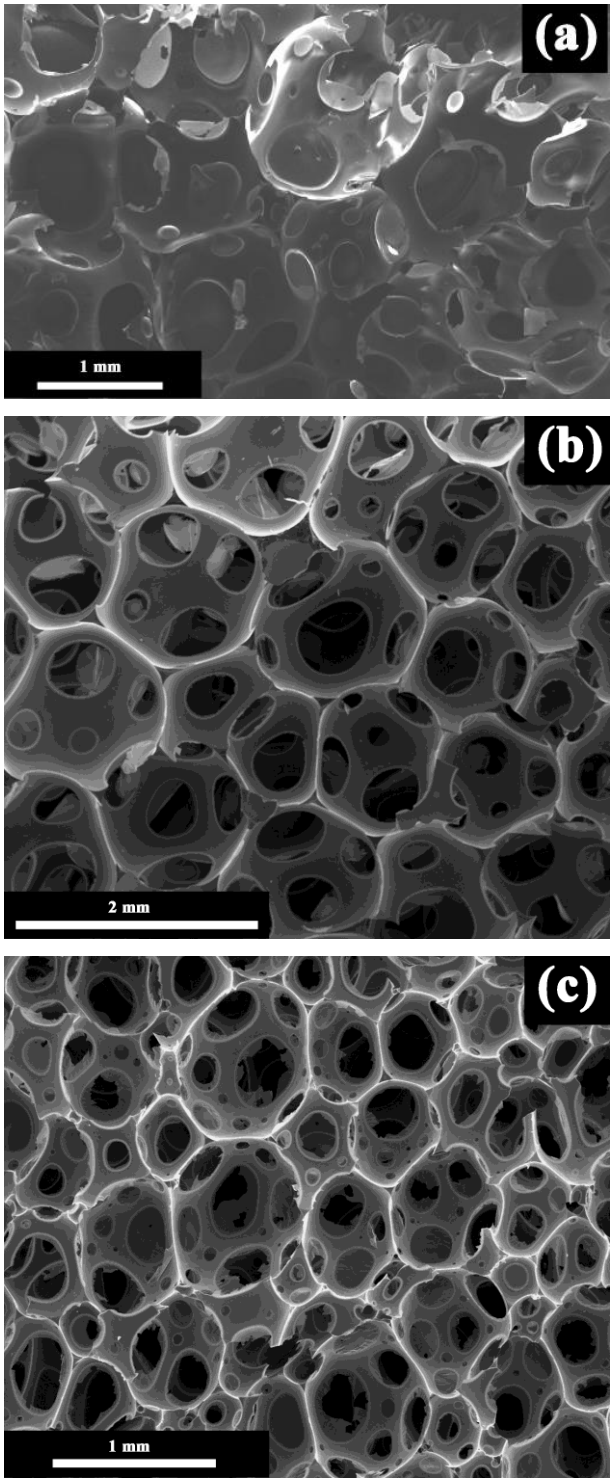

Figure 2.14: SEM photographs of (a) the solid organic foam and (b and c) the carbon foams prepared at various aluminium nitrate concentrations (aluminium nitrate concentration: a - 4 wt.%, b - 0.5 wt.%, c - 4 wt.%)

The amount of alumina produced from 0.5 to 4 g aluminium nitrate added to 100 g sucrose is in the range of 0.068 to 0.544 g, respectively. Calculations based on the carbon content in sucrose (42.1 %) show an alumina content of 0.16 to 1.3 wt.% in the carbon foams. On the other hand, calculations based on the carbon residue obtained at 600 ^{o}C in the TGA in nitrogen atmosphere result in alumina content in the range of 0.2 to 1.58 wt.%. Figure 2.15 shows EDAX spectra using SEM-EDAX recorded on the as formed surface of a cell wall and on the fractured surface of a strut of the carbon foam prepared at 4 wt.% aluminium nitrate. The atomic percentages of carbon, oxygen and aluminium on the as formed cell wall surface are 93.85, 3.37 and 2.78, respectively. On the other hand, the corresponding atomic percentages on the fractured surface of the strut are 95.94, 3.32 and 0.74, respectively. This indicates that the alumina produced from aluminium nitrate concentrate more on the surface of cell walls, ligaments and struts. Jana and Ganesan (2011) reported coating of carbon over alumina in carbon-alumina foam containing 19 wt.% carbon prepared from aqueous solution containing sucrose and aluminium nitrate. It appears that at the higher alumina concentration (81 wt.%), the alumina crystallites join each other by sintering to form a foam framework. During the carbonization heat treatment, the carbon present is expelled to surface of the alumina resulting in the coating of carbon over the alumina (Jana and Ganesan, 2011). On the other hand, in the present case, the carbon crystallizes (alignment of graphite ribbons) by expelling the low concentrations (0.2 to 1.58 wt.%) of the alumina to the surface. This results in the higher concentration of alumina on the surface of cell wall, ligament and strut. The atomic ratio of aluminium to oxygen on the as formed cell wall surface is close to that in Al_2O_3, indicating the absence of oxygen attached to the carbon. As 0.74 atoms of aluminium require only 1.11 atoms of oxygen to form alumina, the remaining 2.21 atomic percentage of oxygen on the fractured surface of the strut is attached to the carbon. This observation suggests that the complete removal of heteroatoms like oxygen from the interior portion of the relatively thick struts requires temperatures higher than 900 ^{o}C.

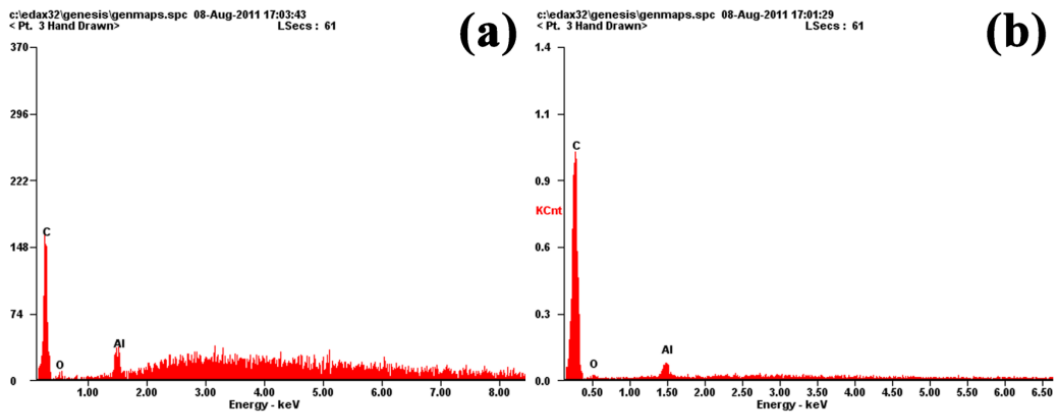

Figure 2.15: EDAX spectra of carbon foam recorded (a) on the as formed surface of a cell wall and (b) on the fractured surface of a strut

2.3.6 Compressive Strength and Thermal Conductivity

The compressive strength of the carbon foams mainly depends on the density, cell size, cell morphology and the addition of reinforcements (Gibson and Ashby, 1997; Li et al., 2012). In general, compressive strength of the carbon foam increases with an increase in the density and decrease in the cell size. The compressive strength and Young's modulus of the carbon foams prepared from molten sucrose with various aluminium nitrate concentrations are shown in Figure 2.16 (a). The compressive strength of the carbon foam decreases from 0.64 to 0.06 MPa when the aluminium nitrate concentration increases from 0 to 1 wt.%. This rapid decrease is due to the observed increase in cell size and decrease in foam density. On further increase of aluminium nitrate concentration shows an increase in compressive strength up to 2 wt.% followed by a decrease. The increase in compressive strength observed from 1 to 2 wt.% aluminium nitrate concentration is attributed to the thick cell wall and struts. On the other hand, the decrease in compressive strength observed for aluminium nitrate concentrations beyond 2 wt.% is due to the decrease of density and presence of additional pores in the cell walls and struts. Similarly, there is a decrease in the Young's modulus from 22 to 2.9 MPa when the aluminum nitrate concentration increases from 0 to 0.5 wt.%. Further increase in aluminium nitrate concentration does not have much effect on the Young's modulus of the carbon foams. The specific compressive strength of

the carbon foams with various aluminium nitrate concentrations is shown in Figure 2.16 (b). The maximum specific compressive strength of 4.8 MPa/g/cm^3 is attained for the carbon foam prepared at an aluminium nitrate concentration of 2 wt.%.

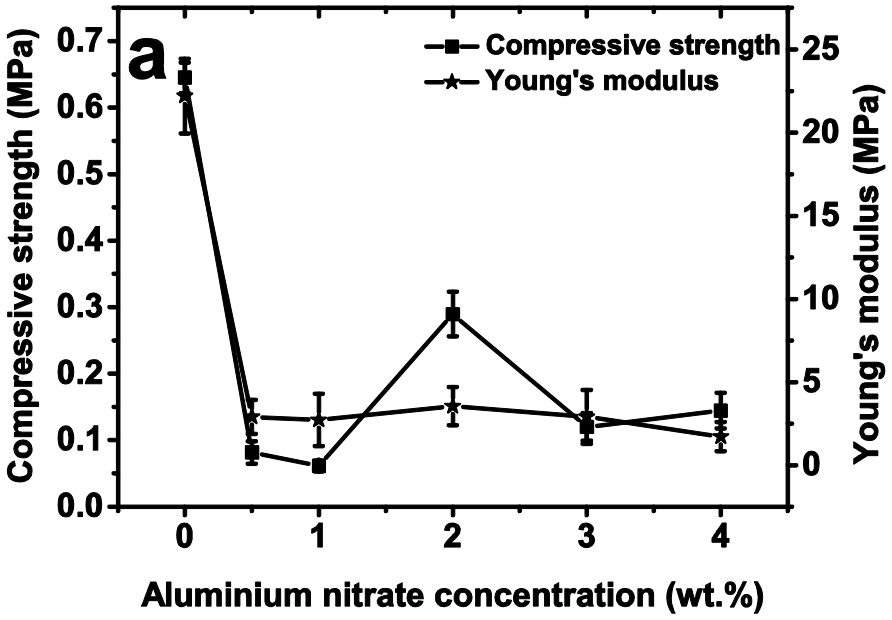

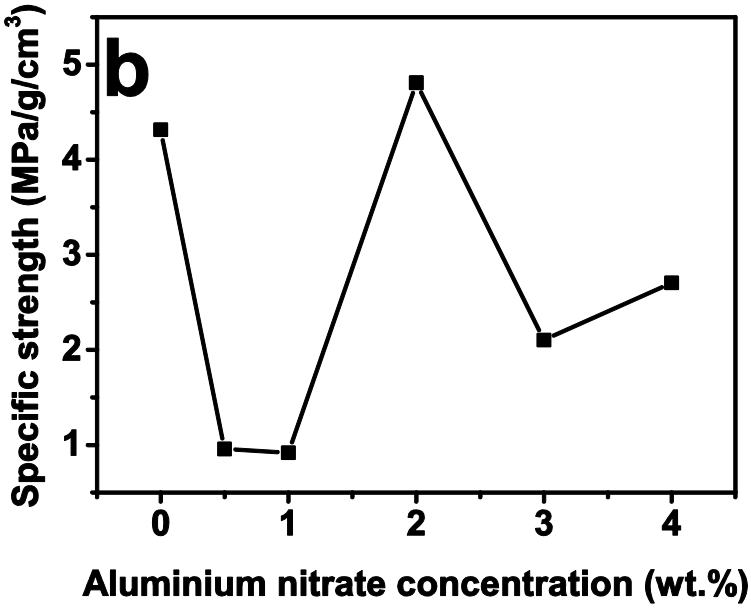

Figure 2.16: (a) Compressive strength and Young's modulus and (b) specific strength of the carbon foams prepared from molten sucrose at various aluminium nitrate concentrations

The thermal conductivity of the carbon foams with various aluminium nitrate concentrations is shown in Figure 2.17. The thermal conductivity of the carbon foams prepared from sucrose without aluminium nitrate shows 0.07 W/m/K. The carbon foam prepared at an aluminium nitrate concentration of 0.5 wt.% shows a lower thermal conductivity of 0.04 W/m/K. On the other hand, further increase in aluminium nitrate concentration results in an increase in thermal conductivity. The carbon foams prepared at aluminium nitrate concentration in the range of 0.5 to 4 wt.% show thermal conductivities in the range of 0.04 to 0.053 W/m/K. Initial decrease in thermal conductivity is due to the observed decrease in the foam density. On the other hand, the increase in thermal conductivity with an increase in aluminium nitrate concentration is attributed to both the increase in crystallinity of the carbon and the increase in concentration of alumina (alumina is having higher thermal conductivity than turbostratic graphite).

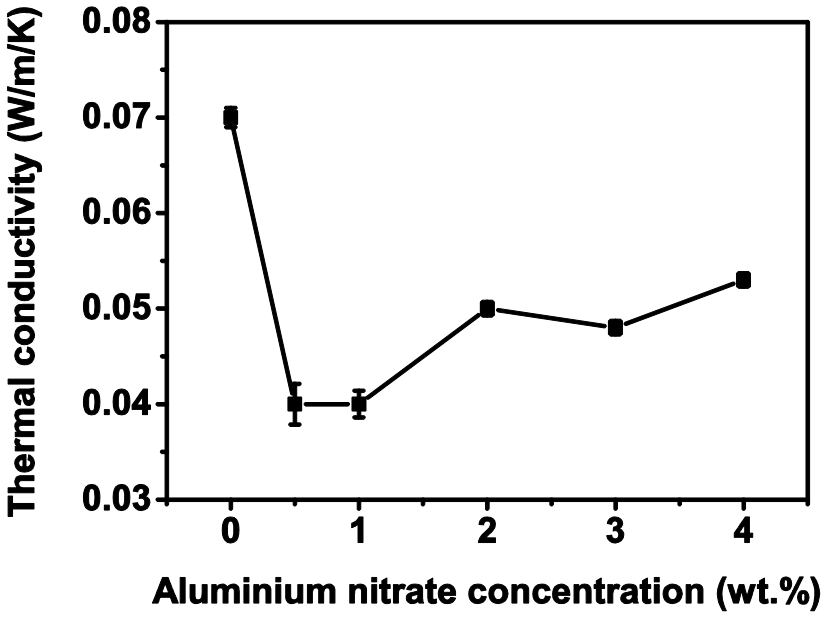

Figure 2.17: Thermal conductivity of the carbon foams prepared from molten sucrose at various aluminium nitrate concentrations

2.3.7 Textural Properties

The carbon foams show Type I N_2 adsorption-desorption isotherm indicating their microporous characteristics. The homogeneous distribution of micropores in the cell walls and struts is evidenced from the TEM analysis. There are no detectable mesopores observed in the TEM analysis. A TEM image and N_2 adsorption-desorption isotherms are given in Figure 2.18 (a) and (b), respectively.

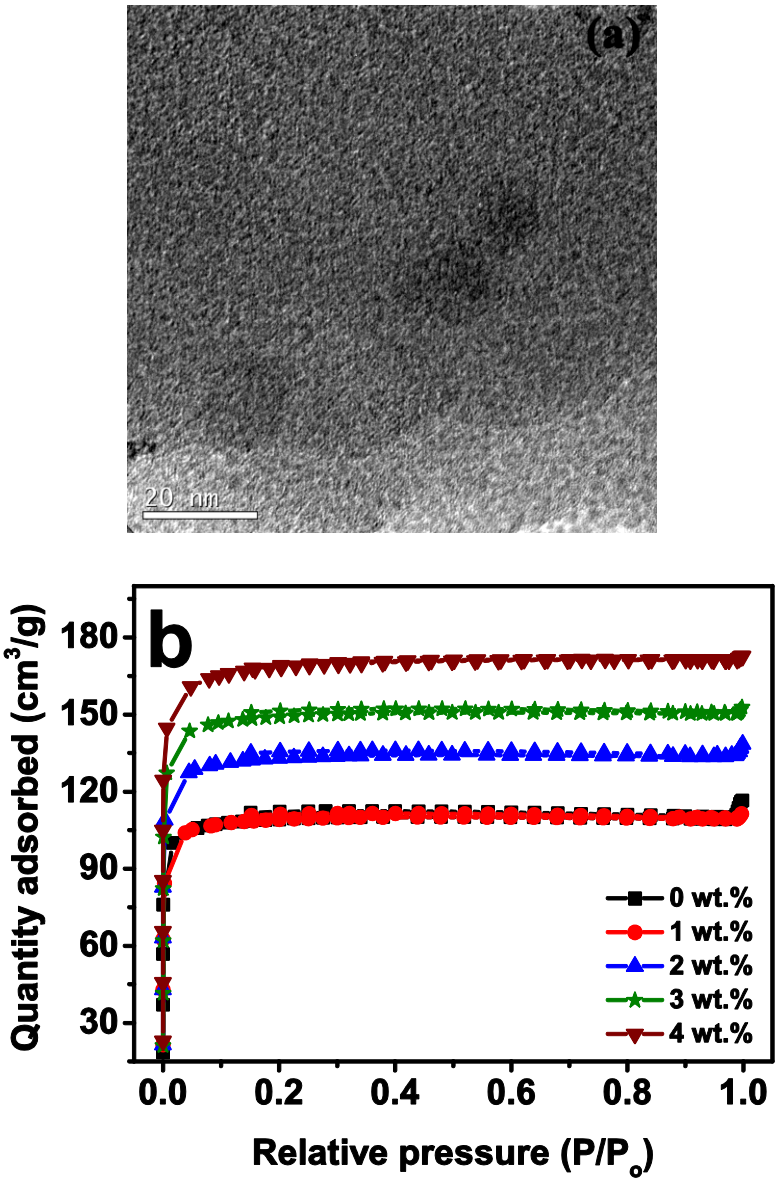

Figure 2.18: (a) TEM micrograph of the carbon foam prepared without aluminium nitrate blowing agent and (b) N_2 adsorption-desorption isotherm of carbon foams prepared from molten sucrose at various aluminium nitrate concentrations

The formation of micropores in the cell walls and struts of carbon foam is explained as follows: The solid organic foam obtained from molten sucrose contains C-O-C groups due to the -OH to -OH condensations and carbonyl groups formed by oxidation (Jana and Ganesan, 2009). This is evidenced by the peaks at 1060 and 1700 cm^{-1} corresponding to the ether and carbonyl groups, respectively, in the FTIR spectrum of the foam sample carbonized at 400 ^{o}C (Figure 2.19). Further, the elemental analysis shows the presence of 19.7 wt.% oxygen in the foam sample carbonized at 400 ^{o}C. The foam sample carbonized at 400 ^{o}C shows a surface area of 0.89 m^2/g and a negligible micropore volume. The surface area increases from 0.89 to 367 m^2/g and micropore volume increases from 0 to 0.18 cm^3/g when the carbonization temperature is increased from 400 to 900 ^{o}C. The rapid increase in surface area and pore volume and rapid decrease in oxygen content are observed from 500 to 600 ^{o}C. The effect of carbonization temperature on surface area, pore volume and oxygen content of the carbon foam prepared without aluminium nitrate blowing agent is shown in Figure 2.20. The increase in surface area and micropore volume with an increase in carbonization temperature can be explained by *in situ* activation. The *in situ* activation is due to the formation of CO from the C-O-C and carbonyl groups during carbonization in the temperature range from 500 to 900 ^{o}C.

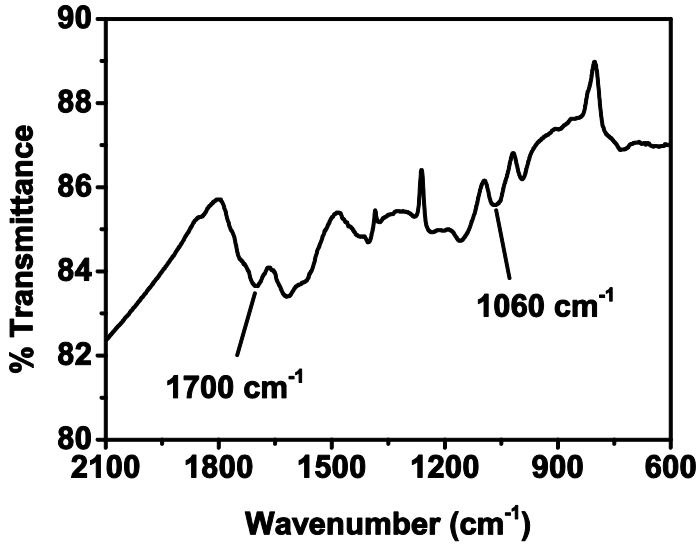

Figure 2.19: FTIR spectrum of the solid organic foam sample carbonized at 400 ^{o}C

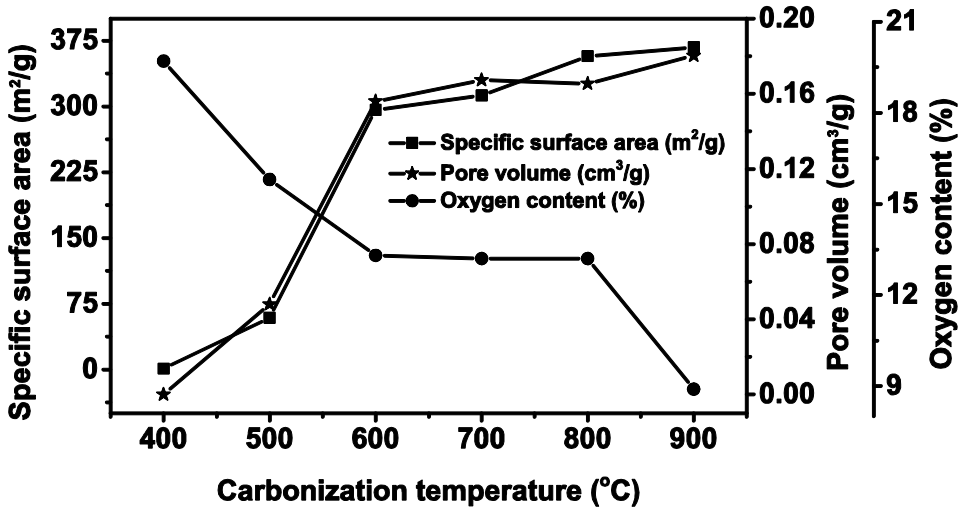

Figure 2.20: Surface area, pore volume and oxygen content of carbon foam prepared without aluminium nitrate at various carbonization temperatures

The aluminium nitrate used as blowing agent not only aid the faster foaming and setting of molten sucrose but also contribute to the formation of microporosity in the carbon foams. The effect of aluminium nitrate concentration on surface area and pore volume of the carbon foams is shown in Figure 2.21. The surface area of the foams carbonized at 900 ^{o}C increases from 367 to 540 m^2/g when the aluminium nitrate concentration increases from 0 to 4 wt.%. The corresponding increase in micropore volume obtained is from 0.18 to 0.27 cm^3/g. It appears that the alumina nanoparticles produced from the aluminium nitrate blowing agent during carbonization acts as pillars in-between the graphite ribbons. This alumina pillaring produces additional slit-like micropores. The formation of slit-like micropores by alumina pillaring is schematically shown in Figure 2.22.

The proposed mechanism of alumina pillaring is supported by the fact that the alumina obtained by burning-off the carbon from the carbon foam at 600 ^{o}C for 5 h shows particles in the size range of 1 to 2 nm when analyzed using the TEM. The selected area electron diffraction (SAED) pattern of the sample shows amorphous nature of the alumina. However, very broad reflections corresponding to the γ-alumina phase is observed in the XRD. The TEM photomicrograph,

SAED pattern and XRD spectrum of the alumina obtained by burning-off the carbon from the carbon foams is shown in Figure 2.23.

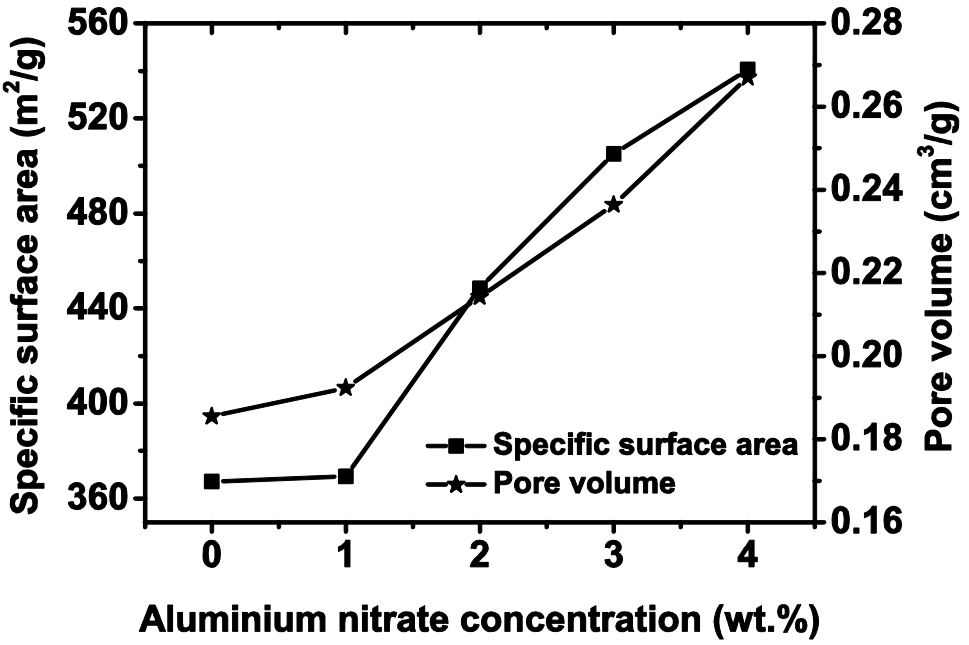

Figure 2.21: Surface area and pore volume of carbon foams prepared from molten sucrose at various aluminium nitrate concentrations

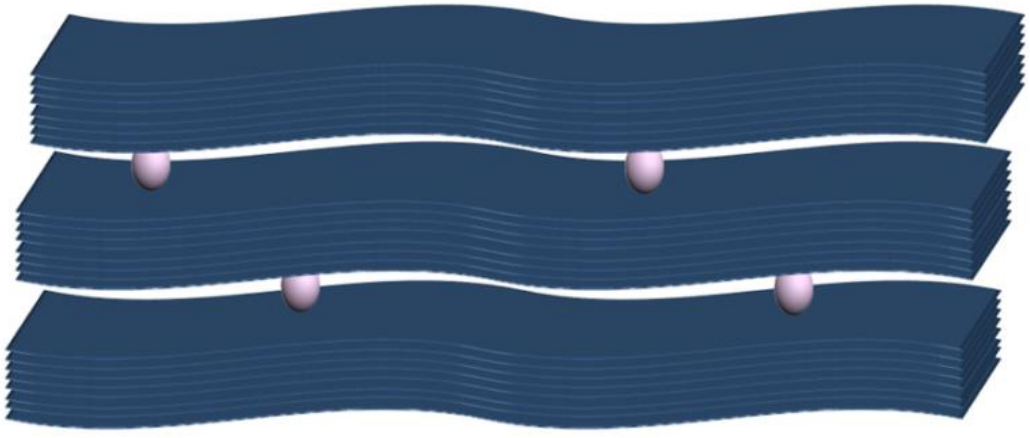

Figure 2.22: Schematic showing the formation of micropores by the alumina pillaring

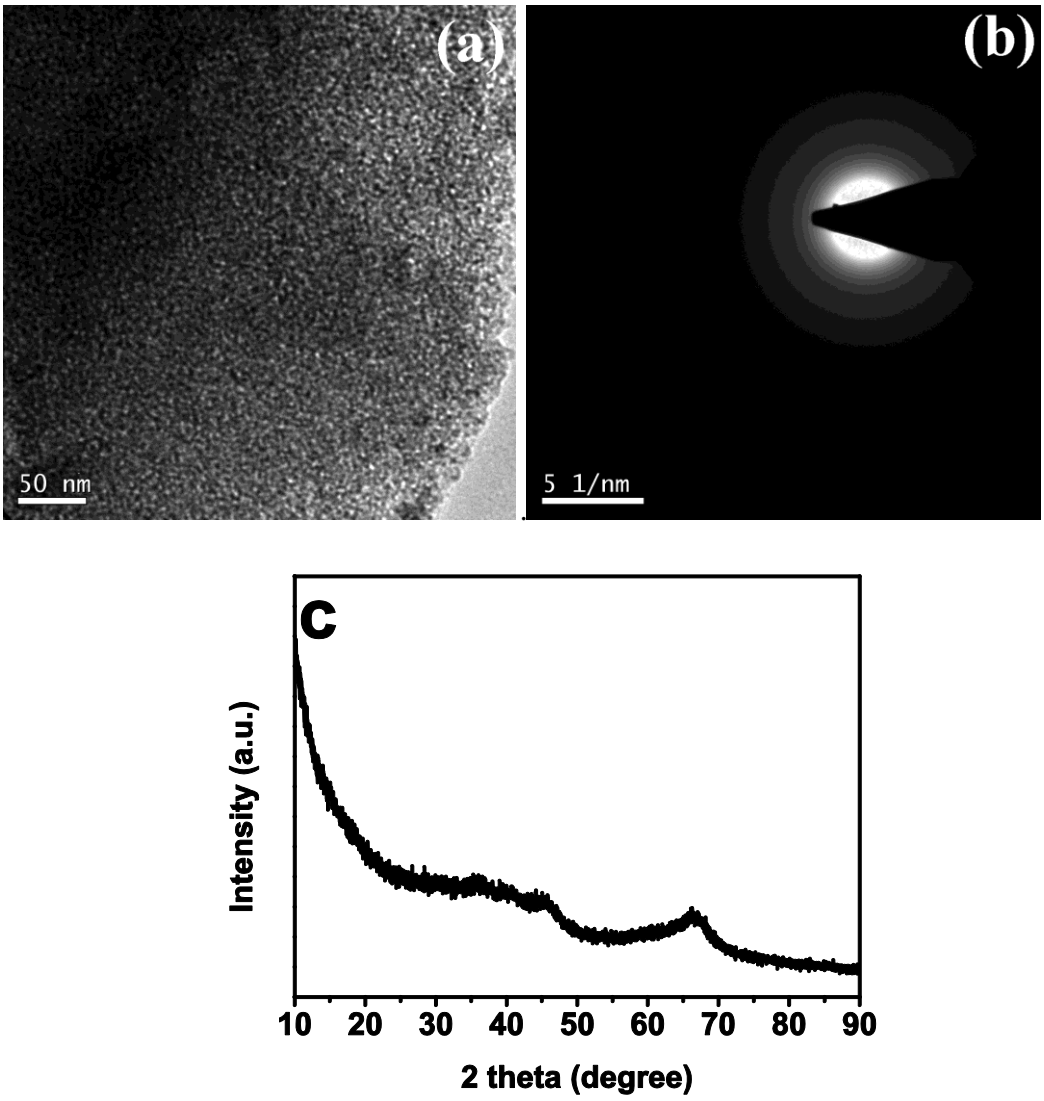

Figure 2.23: (a) TEM photomicrograph (b) SAED pattern and (c) XRD spectrum of the alumina obtained by burning-off the carbon from the carbon foams at 600 ^{o}C for 5 h

The PSD of the carbon foams calculated from the N_2 adsorption using DFT by assuming the slit-like pore model shows pore size less than 2 nm. In order to understand the level of microporosity in the ultramicropores range (pore size less than 0.7 nm), the DFT calculations on CO_2 adsorption at 0 ^{o}C is used, as the problems at low temperatures (Dubinin, 1966). The PSD obtained from DFT calculations on N_2 and CO_2 adsorption of carbon foam samples prepared at various aluminium nitrate concentrations is given in Figure 2.24. The majority of pores are in the size range of 0.5 to 1.2 nm. The micropore size range observed in

the carbon foams is ideal for CO_2 adsorption (Sevilla and Fuertes, 2011; Silvestre-Albero et al., 2011).

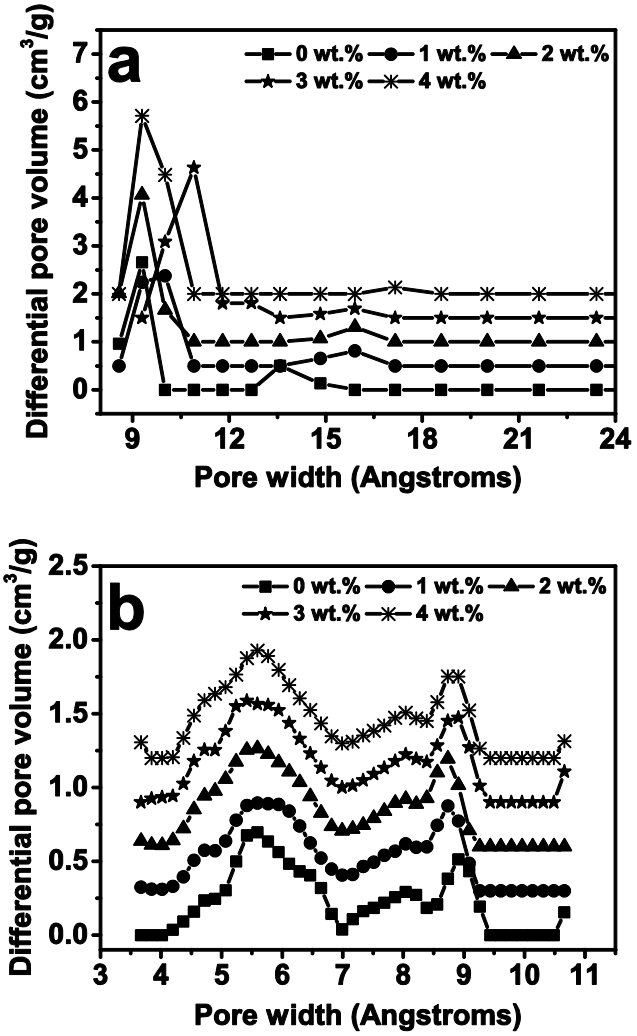

Figure 2.24: PSD of the carbon foams prepared from molten sucrose at various aluminium nitrate concentrations (a) N_2 adsorption and (b) CO_2 adsorption

2.3.8 CO_2 Adsorption

The microporous carbons are widely used for the CO_2 adsorption. The textural properties of the carbon foam prepared at various aluminium nitrate concentrations show the presence of micropores in the cell walls and struts. The CO_2 adsorption capacity at 25 ^oC of the carbon foams prepared without aluminium nitrate blowing agent increases from 1.08 to 2.24 mmol/g when the

carbonization temperature increases from 400 to 900 ^{o}C. The CO_2 adsorption capacity of the carbon foams depends on the aluminium nitrate concentration and adsorption temperature. The CO_2 adsorption capacity increases considerably with aluminium nitrate concentration up to 2 wt.%. Further increase in aluminium nitrate concentration up to 4 wt.% produces only a marginal increase in CO_2 adsorption capacity. The CO_2 adsorption capacity at 25 ^{o}C increases from 2.24 to 2.5 mmol/g when the aluminium nitrate concentration increases from 0 to 4 wt.%. On the other hand, at 0 ^{o}C the CO_2 adsorption capacity observed is in the range of 2.87 to 3.37 mmol/g. Figure 2.25 (a) and (b) shows the CO_2 adsorption isotherms measured at 25 ^{o}C and 0 ^{o}C, respectively, of the carbon foams prepared at various aluminium nitrate concentrations. The increase in CO_2 adsorption capacity with an increase in carbonization temperature is due to the increase in micropore volume. On the other hand, the increase in CO_2 adsorption capacity with an increase in aluminium nitrate concentration can be due to two reasons. One is the observed increase in pore volume with an increase in aluminium nitrate concentration. The second is the modification of the surface of the micropores with more polar alumina as the CO_2 with a large quadrupole moment interacts strongly with $Al^{+}O^{2-}Al^{+}$ surface sites (Zukal et al., 2010).

The selectivity of CO_2 over N_2 is very important for CO_2 capture from post-combustion flue gases that typically contain 70 % N_2 and 15 % CO_2. Figure 2.26 (a) shows CO_2 and N_2 adsorption isotherms at 25 ^{o}C. Under identical conditions, the CO_2 adsorption in mmol/g is nearly 7 to 8 times the N_2 adsorption in the same units. The alumina modification on the micropore surface is expected to enhance the selectivity of CO_2 adsorption with an increase in the aluminium nitrate concentration. However, the selectivity of CO_2 over N_2 adsorption, calculated from the slope of the linear portion of the isotherms, as reported by Hao et al. (2011), shows a decrease from 22 to 14 when the aluminium nitrate concentration increases from 0 to 4 wt.%. The decrease in selectivity observed is due to the increase in pore size with an increase in the aluminium nitrate concentration. The selectivity of carbon foams obtained is comparable to the values reported for microporous carbon monoliths (Hao et al., 2011).

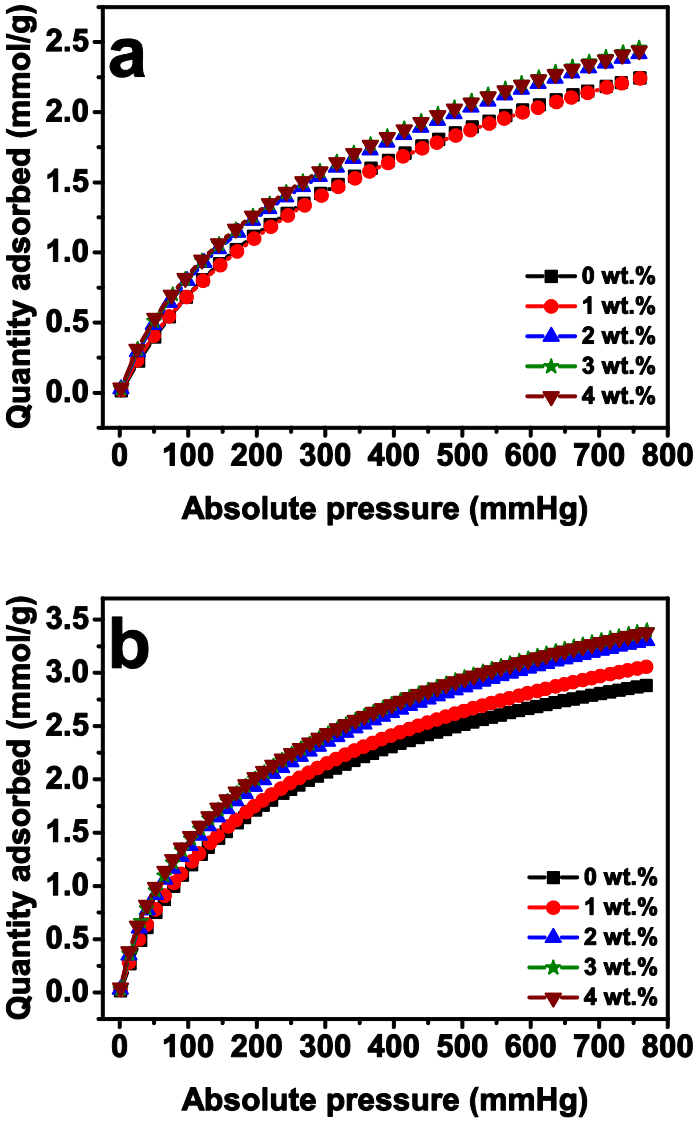

Figure 2.25: CO_2 adsorption isotherms at (a) 25 ^oC and (b) 0 ^oC of the carbon foams prepared from molten sucrose at various aluminium nitrate concentrations

Easy and energy efficient regeneration are the important criteria for an adsorbent material considered for CO_2 capture. A typical DSC curve of the CO_2 adsorption and desorption in a carbon foam sample is shown in Figure 2.26 (b). The desorption of the CO_2 from the carbon foams takes place at a low temperature of 50 ^oC showing the energy efficient regeneration of the adsorbent. The heat of adsorption calculated from the DSC analysis indicates physical adsorption and the values increased from 42 to 58 kJ/mol when the aluminium nitrate concentration

increases from 0 to 4 wt.%. The increase in heat of adsorption is due to the increase in interaction between the quadrupole of CO_2 and the electric field created on the micropore surface by alumina modification. The reversibility of CO_2 adsorption on carbon foams has been tested at room temperature over five cycles. The CO_2 adsorption capacity of the carbon foam samples remains unaltered in the repeated adsorption-desorption cycles as seen in Figure 2.26 (c). This indicates that the carbon foams have very good recyclability.

2.3.9 Oxidation Studies

Figure 2.27 (a) shows the non-isothermal TGA of carbon foam prepared at the aluminium nitrate concentrations in the range of 0 to 4 wt.%. The alumina produced from aluminium nitrate influences the oxidation behavior of the carbon foam. The TGA shows that the alumina present stabilizes the carbon foams against oxidation up to an aluminium nitrate concentration of 1 wt.%. Further increase in concentration of aluminium nitrate up to 4 wt.%, accelerates the oxidation of the carbon foams. There is a decrease of 40 and 125 ^{o}C in oxidation onset and oxidation completion temperature, respectively, when the aluminium nitrate concentration increases from 0 to 4 wt.%. Fig. 2.27 (b) shows the isothermal oxidation weight loss of carbon foams prepared at aluminium nitrate concentrations in the range of 0 to 4 wt.% at various temperatures. The carbon foams starts oxidation at 350 ^{o}C under isothermal conditions. The carbon foams prepared at aluminum nitrate concentrations in the range of 1 to 4 wt.% show 11 to 15 % weight loss in 3 h at 400 ^{o}C. The oxidation of the carbon foams prepared using aluminium nitrate blowing agent is almost completed at 500 ^{o}C in 3 h. The carbon foams prepared at the aluminum nitrate concentrations in the range of 0 to 4 wt.% leave 8 to 3 wt.% residue at 500 ^{o}C after 3 h. It appears that the alumina formed from the aluminium nitrate acts as a catalyst for carbon oxidation due to its electron accepting character (Lewis acid) (Yamaguchi et al., 1996). The formed alumina accepts electrons from the π bonds in the turbostratic graphitic carbon and weakens the C-C bond. This facilitates the oxidation of the carbon foam.

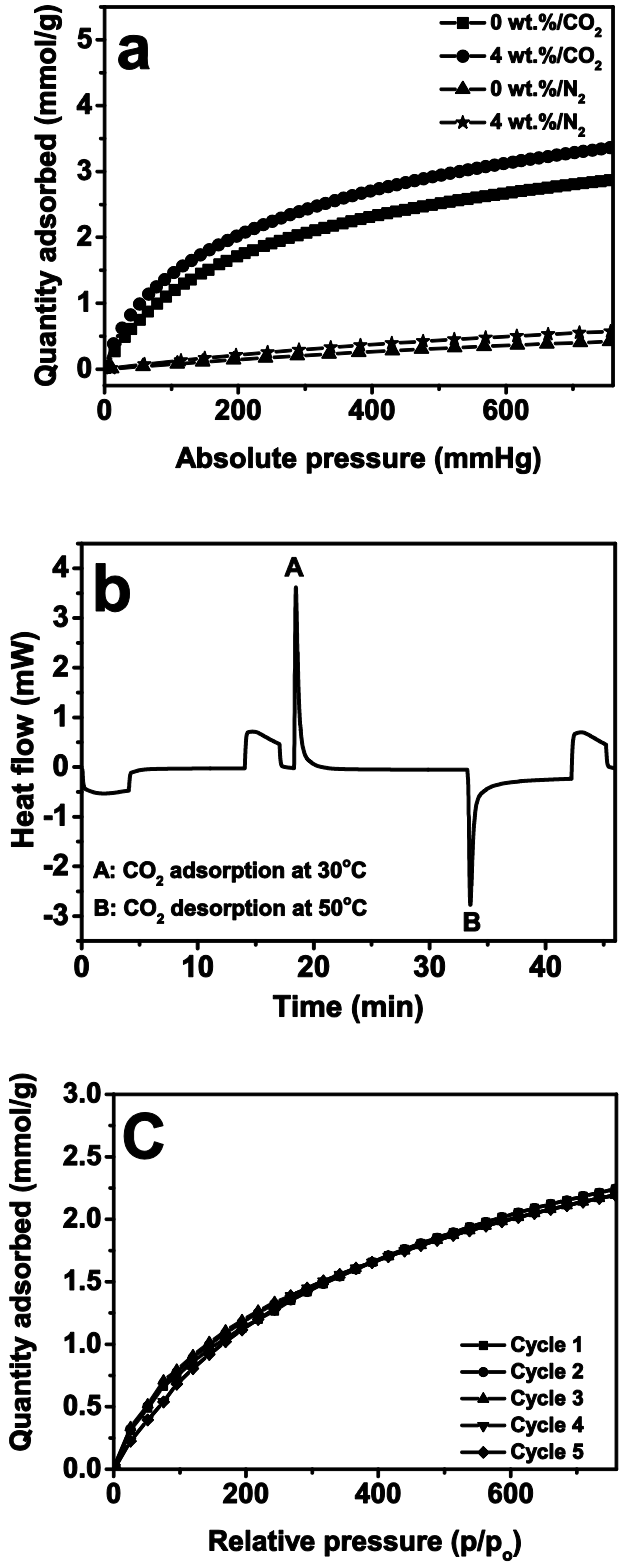

Figure 2.26: (a) CO_2 and N_2 adsorption isotherms at 0 ^oC showing selectivity of the carbon foams (b) typical DSC plot of CO_2 adsorption and desorption and (c) CO_2 adsorption isotherm at 25 ^oC showing recyclability of the carbon foam prepared from molten sucrose at 4 wt.% aluminium nitrate concentration

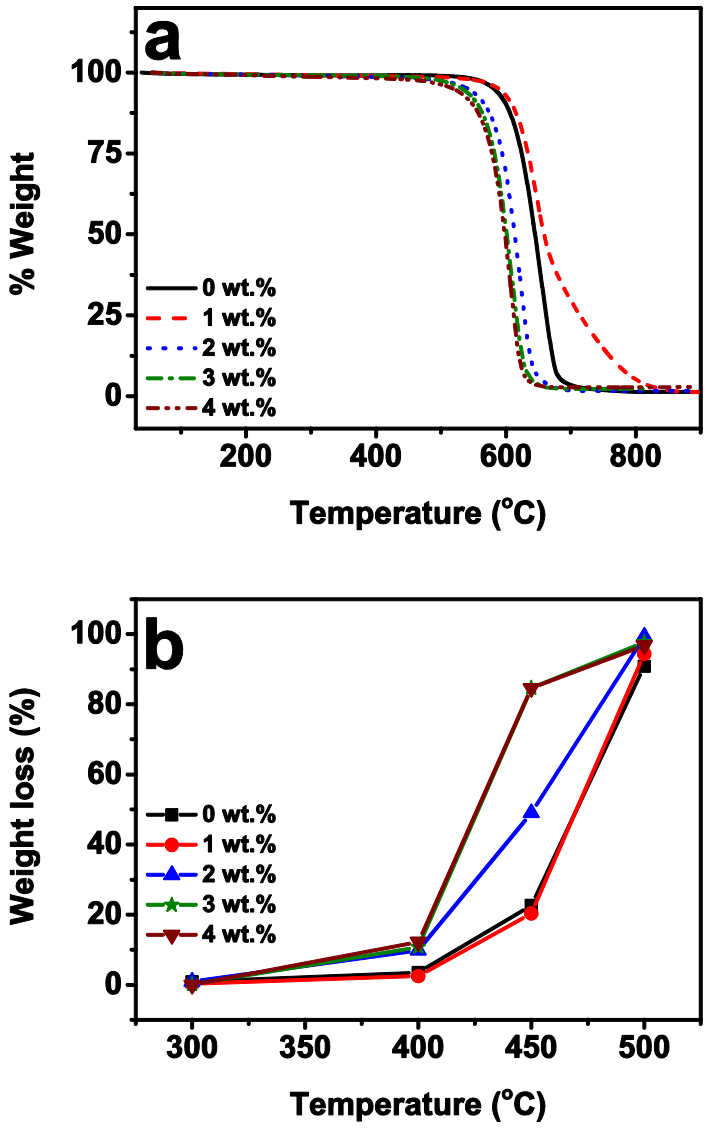

Figure 2.27: (a) Non-isothermal TG and (b) isothermal oxidation weight loss of the carbon foams prepared at an aluminium nitrate concentration in the range of 0 to 4 wt.%

2.4 Conclusions

Carbon foams with densities in the range of 0.053 to 0.085 g/cm^3 are prepared by foaming of molten sucrose using aluminium nitrate (0.5 to 4 wt.% of sucrose) blowing agent to solid organic foams followed by dehydration and carbonization. The aluminium nitrate helps in generation and stabilization of gas bubbles in molten sucrose which enable its faster foaming and setting. The solid organic foams undergo near isotropic shrinkage during dehydration and

carbonization. The carbon foams have near spherical cellular structure and the cells are interconnected through circular or oval-shaped windows. The density, the cell size and the cell window size decrease with an increase in aluminium nitrate concentration. The carbon produced during pyrolysis of the solid organic foams has a turbostratic graphite structure. The alumina (~ 0.2 to 1.58 wt.%) produced from the aluminium nitrate, concentrates more on the surfaces of cell walls, ligaments and struts. The compressive strength (0.06 to 0.64 MPa), Young's modulus (2.9 to 22 MPa) and thermal conductivity (0.04 to 0.07 W/m/K) of the carbon foams depend on the aluminium nitrate concentration. The surface area and pore volume of the carbon foams increase with an increase in aluminum nitrate concentration. The mechanism of formation of micropore due to *in situ* activation and alumina pillaring is established. The CO_2 adsorption capacity (2.87 to 3.37 mmol/g at 0 ^oC and 760 mmHg) of the carbon foams increases with an increase in aluminium nitrate concentration. The CO_2 adsorption in carbon foams shows very good selectivity over N_2 adsorption and adsorbent could be easily regenerated by heating at 50 ^oC. The alumina formed from the aluminum nitrate blowing agent catalyzes the carbon oxidation due to its Lewis acid character.

CHAPTER 3

PROCESSING AND CHARACTERIZATION OF CARBON FOAMS FROM MOLTEN SUCROSE USING A BORIC ACID BLOWING AGENT

3.1 Introduction

A serious drawback of the carbon-based materials is their poor oxidation resistance. It is well-known that the oxidation of carbon materials starts at a temperature as low as 350 ^{o}C (Sheehan, 1989). The mechanism of oxidation in carbon materials involves: (1) adsorption of oxygen on the active sites like edges, defects and vacancies; (2) the reaction between carbon and oxygen and (3) desorption of oxides of carbon. The amorphous carbon materials are more prone to oxidation than the crystalline carbon materials due to the presence of more number of active sites for carbon-oxygen gasification reactions (Walker Jr et al., 1991). That is, the amorphous carbon foams prepared from the renewable molecules like sucrose are more susceptible to oxidation compared to the graphitic carbon foams prepared from coal-tar pitch and petroleum pitch (McEnaney and Rand, 1985). Moreover, the carbon foams prepared from sucrose (chapter 2) show poor oxidation resistance because alumina produced from aluminium nitrate catalyzes the carbon oxidation due to its Lewis acid character.

Generally two approaches are used to increase the oxidation resistance of carbon-based materials. One is active site poisoning and the other is coating the surface of carbon-based material with an oxidation resistant barrier material (McKee, 1991). The coating suffers drawbacks such as delamination due to interfacial crack developed because of thermal mismatch between carbon and coated materials which expose the carbon materials to the oxidative atmosphere (Sheehan, 1989). Incorporation of heteroatoms like halogens, boron and

phosphorous into the carbon is a better option for the improvement of oxidation resistance of carbon foams. These heteroatoms strongly adsorb on the active sites such as dangling bonds, steps, vacancies and dislocation where carbon-oxygen reaction initiates (McKee, 1991). The strong adsorption of these heteroatoms on the active sites retards the carbon-oxygen reaction and improves the oxidation resistance. Boron is widely used to increase the oxidation resistance of the carbon materials (Hu and Chung, 1996; Kowbel et al., 1993; Zhong et al., 2000). The boron oxide film formed on the carbon surface at higher temperature protects the carbon from oxidation. Another mechanism of oxidation inhibition by boron is by decreasing the electron density at the graphene edges as proposed by Jones and Thrower (Jones and Thrower, 1987). In addition, boron acts as a catalyst for the graphitization of carbon (Jones and Thrower, 1987; Marinković et al., 1969; Zaldivar et al., 1991). In the present work, boric acid is used as a blowing agent as well as a boron precursor for the preparation of boron-doped carbon foams. The boron-doped carbon foams are assessed for the isothermal and non-isothermal oxidation behavior.

3.2 Experimental

3.2.1 Preparation of Boron-doped Carbon Foams

Analytical reagent grade sucrose and orthoboric acid (H_3BO_3) used for the preparation of boron-doped carbon foams were procured from Merck India Ltd, Mumbai. The process flow chart for the preparation of boron-doped carbon foam from molten sucrose is shown in Figure 3.1. 200 g sucrose was heated at 180 ^oC in a borosilicate glass reaction kettle for 15 min to form a homogeneous melt. Various concentrations of the boric acid were added slowly to the molten sucrose with continuous stirring. The heating and stirring were continued for 2 min after the complete addition of the boric acid. The melt was then transferred to a 1.5 litre borosilicate glass tray and heated in an air oven at 120 ^oC for 48 h for foaming and setting. The foam rise, the ratio of the final height of the foam to the initial height of the resin, was measured according to the procedure in Chapter 2. The organic foams were cut into rectangular pieces and dehydrated in a muffle

furnace at 250 ^{o}C for 16 h. The dehydrated foams were carbonized in an ultra-high pure argon atmosphere in a tubular furnace at 900 ^{o}C for 2 h. The heating rate used for dehydration and carbonization was 2 ^{o}C/min. The same inert atmosphere was maintained during the cooling of the furnace. The density of the boron-doped carbon foam samples was calculated from their weight and dimensions.

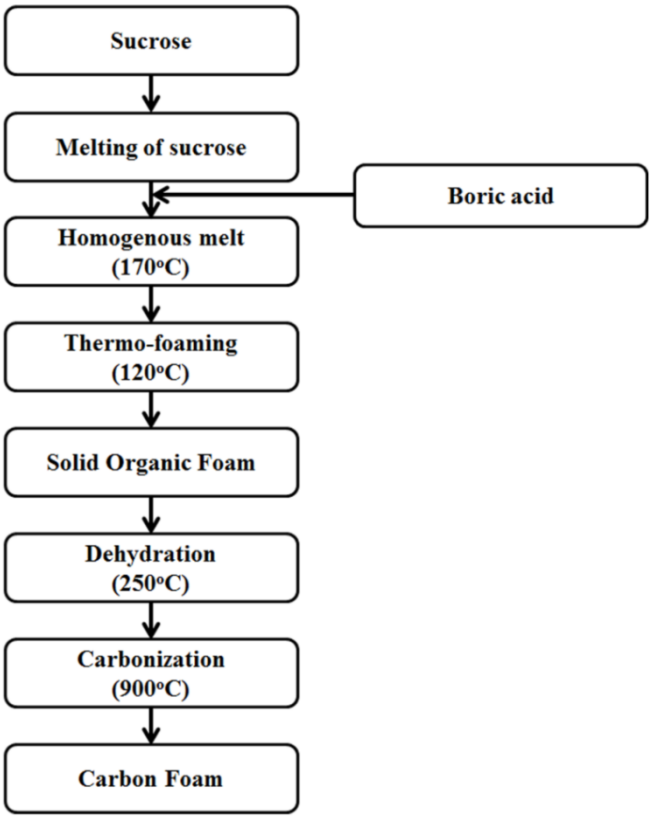

Figure 3.1: Flow chart for the preparation of boron-doped carbon foams from molten sucrose

3.2.2 Characterization

TGA of the solid organic foam samples was carried out in a high-pure argon atmosphere up to 900^{o}C using a thermo gravimetric analyzer (Q-50, TA Instruments, USA). The functional group characterization of the solid organic foams was carried out using FTIR spectrophotometer in the wavenumber ranges from 4000 to 650 cm^{-1} with the resolution of 4 cm^{-1}. The microstructure of the

carbon foams was analyzed using scanning electron microscope (SEM, FEI Quanta FEG200) and energy dispersive spectroscopy (EDAX). The average cell size of the carbon foams was measured from the SEM images. The compressive strength of the carbon foams was measured using a universal testing machine (Instron 5050, Instron USA) at a crosshead speed of 0.5 mm/min with 25 mm x 25 mm x 12 mm samples (ASTM standard C365/C365M-05). The thermal conductivity of the carbon foam samples was measured using modified transient plane source method (MTPS) at room temperature. The 20 mm x 20 mm x 6 mm samples were used for the thermal conductivity measurements. The reported thermal conductivity is the average of four measurements. The porous textural properties of the carbon foams were analyzed using the volumetric N_2 adsorption-desorption at -196 ^{o}C using a surface area analyzer (Micromeritics Tristar II, USA).

The boron concentration in the carbon foams was estimated by inductively coupled plasma (ICP) optical emission spectroscopy (Perkin-Elmer Optima 5300 DV). 100 mg of the powdered carbon foam samples taken in a platinum crucible was thoroughly mixed with 1 g of sodium carbonate and heated at 850 ^{o}C for 4 h in a muffle furnace. The melt present in the platinum crucible was dissolved in 2 vol.% hydrochloric acid solution and quantitatively transferred to a 100 ml standard flask. The solution was made up to 100 ml and analyzed for boron, based on the emission intensity at a wave length of 249.773 nm.

The oxidation studies of the carbon foams were carried out under non-isothermal condition using TGA and under isothermal condition using a muffle furnace. The amount of sample used for the non-isothermal oxidation study was 10 ± 1 mg. The heating rate of 10 ^{o}C/min and air flow rate of 60 ml/min was used. In the isothermal studies, approximately 0.5 g carbon foam samples were heated in the muffle furnace at temperatures in the range of 300 to 500 ^{o}C for 3 h in a static air atmosphere and noted their weight losses.

3.3 Results and Discussion

3.3.1 Effect of Boric Acid Concentration on Foaming

It is well-known that molten sucrose undergoes caramelization on heating. Caramelization of sucrose involves the formation of glucose and fructose anhydrides and their further condensation to polymeric products such as caramelan ($C_{24}H_{36}O_{18}$), caramelen ($C_{36}H_{50}O_{25}$) and caramelin ($C_{125}H_{188}O_{80}$) (Darder and Ruiz-Hitzky, 2005; deMan, 1999). It is also known that the formation of the polymer products by the –OH to –OH condensation is catalyzed by H^+. The boric acid acts as a strong acid in molten sucrose due to the formation of a sucrose-boric acid complex. The schematic of the formation of H^+ by the reaction between boric acid and sucrose is shown in Figure 3.2.

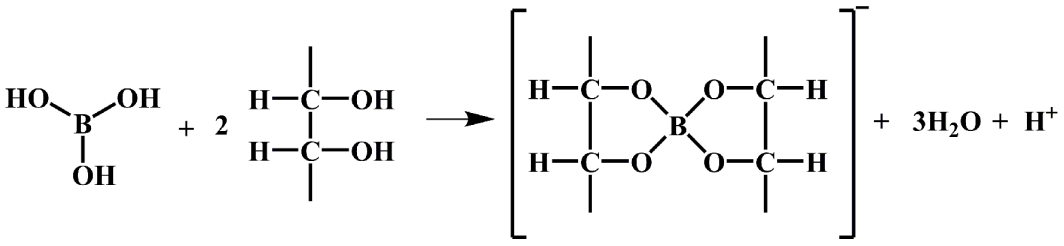

Figure 3.2: Schematic of the formation of H^+ by the sucrose-boric acid reaction

The H^+ formed from the boric acid due to the above reaction catalyzes the condensation of glucose and fructose anhydrides to the polymeric structures (Prabhakaran et al., 2007). The sucrose-boric acid melt prepared at the boric acid concentrations in the range of 2 to 8 wt.% undergoes slow foaming and subsequent setting to form solid organic foams when heated in an air oven at 120 ^oC. On the other hand, no foaming is observed at 120 ^oC in molten sucrose without boric acid even after 120 h. The foaming of the molten sucrose is by the water vapour generated due to the –OH to –OH condensation catalyzed by the H^+. The foaming time and foam setting time decrease with an increase in boric acid concentration. Faster foaming and setting observed at higher boric acid concentration is the result of higher rate of –OH to –OH condensation due to the higher concentration of H^+ generated. Figure 3.3 shows the effect of boric acid

concentration on the foaming time and foam setting time of molten sucrose. It is worthy to note that the sucrose-boric acid melt undergoes foaming at lower temperature compared to the sucrose-aluminium nitrate melt reported in Chapter 2. The foaming of sucrose-boric acid melt is rapid at temperatures higher than 120 ^{o}C and the foams produced have large bubbles. The foams produced at 130 and 140 ^{o}C at boric acid concentrations of 6 and 8 wt.% collapse before setting due to the excessive bubble growth.

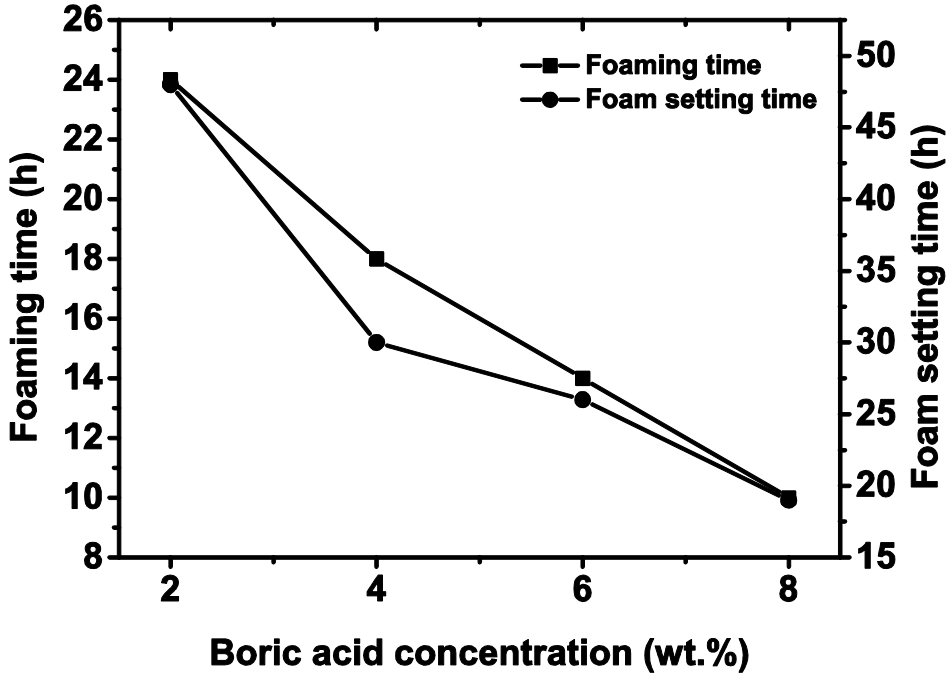

Figure 3.3: The effect of boric acid concentration on the foaming time and foam setting time at 120 ^{o}C

The foam rise, a measure of foam volume, increases with an increase in boric acid concentrations. The foam rise observed is in the range of 7 to 11.5 at boric acid concentrations in the range of 2 to 8 wt.% of sucrose. Figure 3.4 shows the effect of boric acid concentration on the foam rise of molten sucrose. The foam rise observed using boric acid blowing agent at 120 ^{o}C is higher than that observed using aluminium nitrate blowing agent at 150 ^{o}C.

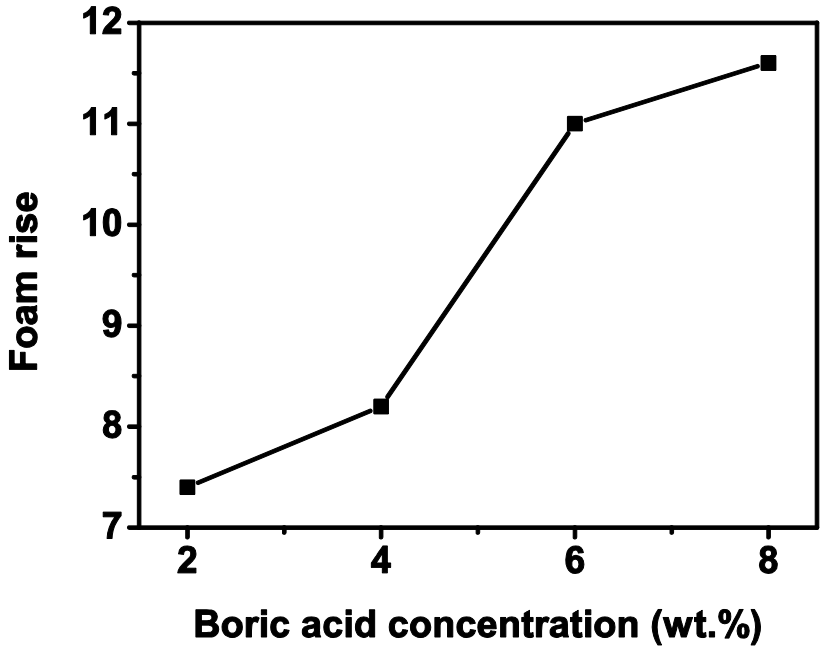

Figure 3.4: The effect of boric acid concentration on the foam rise

3.3.2 Effect of Boric Acid Concentration on Char Yield

Figure 3.5 shows the TG and DTG in an argon atmosphere of solid organic foams prepared at various concentrations of boric acid. In general, the thermal stability of the solid organic foams increases with an increase in boric acid concentration. The sucrose polymer prepared by heating molten sucrose without boric acid at 150 ^{o}C shows only one peak at 278 ^{o}C in the DTG and leave only 24 wt.% char residue at 900 ^{o}C. The solid organic foams prepared using boric acid blowing agent show an additional peak at 350 ^{o}C in the DTG. The intensity of the second peak increases with boric acid concentration. The char residue at 900 ^{o}C increases from 24 to 39 wt.% when the boric acid concentration increases from 0 to 8 wt.%. The char yield of the solid organic foams prepared at various boric acid concentrations is given in Table 3.1. It is well-known that the carbon yield from precursor materials increases with the degree of cross-linking (Savage, 1993). The boric acid cross-links the polymeric condensation products through B-OH to C-OH condensation. The increase in char yield with an increase in boric acid concentration is due to the increase in the number of the -B-O-C-

cross-links. Thermal decomposition of the cross-linked polymeric products at a temperature below 300 ^{o}C produces thermally stable structures that decompose in the second stage at higher temperatures.

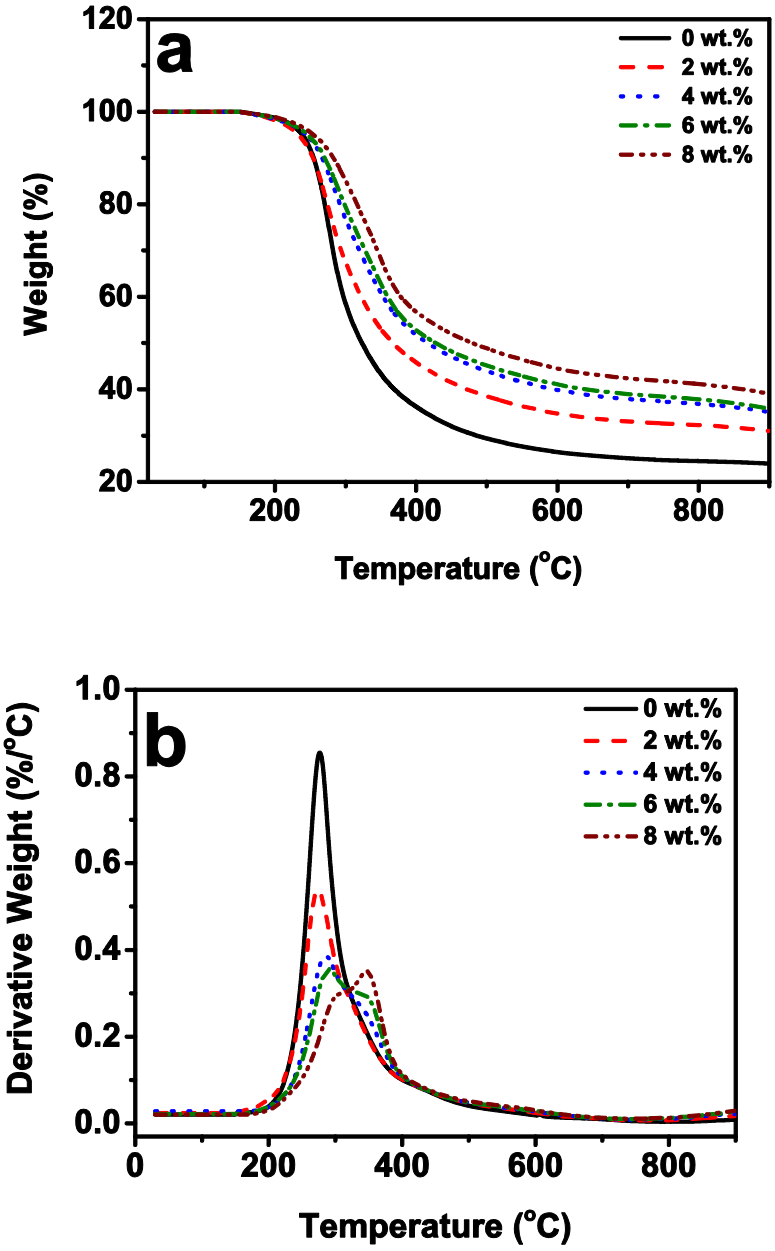

Figure 3.5: (a) TG and (b) DTG curves of the solid organic foams prepared at various boric acid concentrations

Table 3.1: The effect of boric acid concentration on the char yield

Boric acid concentration (wt.%)	Char yield (wt.%)
0	24.00
2	32.03
4	32.03
6	34.47
8	37.41

The cross-linking of the sucrose polymer by boric acid is further evidenced from the FTIR analysis. Figure 3.6 shows the FTIR spectra of the solid organic foam samples. The peaks observed in FTIR spectra at 2905, 1720, 1668 and 1031 cm^{-1} are corresponding to the stretching vibrations of -C-H, -O-C=O, -C=C- and –C-O-C- groups, respectively (Jana and Ganesan, 2009). The peak corresponding to the vibrations of -B-O-C- is not resolved in the FTIR spectra as the –B-O-C- and –C-O-C- vibration frequencies are very close to each other. A decrease in intensity of –C=C- peak at 1668 cm^{-1} with an increase in boric acid concentration is observed in the FTIR spectra. This is due to the less availability of –C-OH groups for the elimination reaction to form -C=C- as number of C-OH groups involve in B-OH to C-OH condensation to form B-O-C cross-links at higher boric acid concentrations.

3.3.3 Effect of Boric Acid Concentration on Carbonization Shrinkage and Density

The carbonization shrinkage of the solid organic foams and density and cell size of the carbon foams depend on the boric acid concentration. The carbonization shrinkage and density decrease from 63.7 to 58.2 vol.% and 0.16 to 0.103 g/cm^3, respectively, when the boric acid concentration increases from 2 to 8 wt.%. The shrinkage during carbonization is higher than that of the solid organic foams prepared using aluminium nitrate blowing agent. On the other hand, the density is

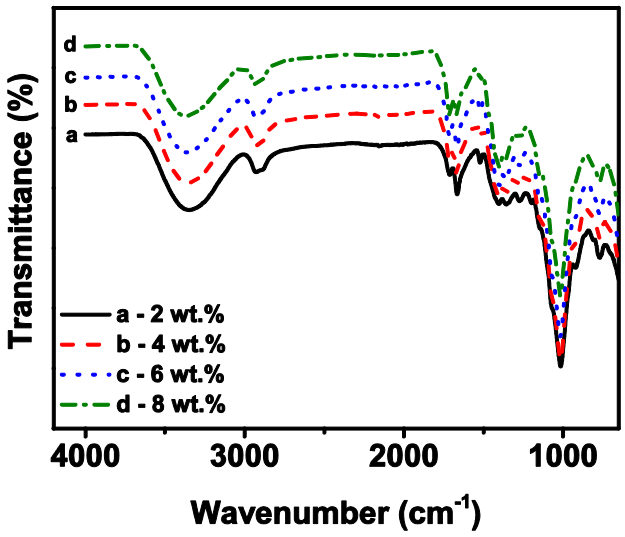

Figure 3.6: FTIR spectra of the solid organic foams prepared at various boric acid concentrations

higher than that of the carbon foams obtained using aluminium nitrate blowing agent. The higher foam density obtained using boric acid blowing agent in spite of higher foam volume is due to the thick cell walls and struts. The effect of boric acid concentration on carbonization shrinkage and carbon foam density is shown in Figure 3.7.

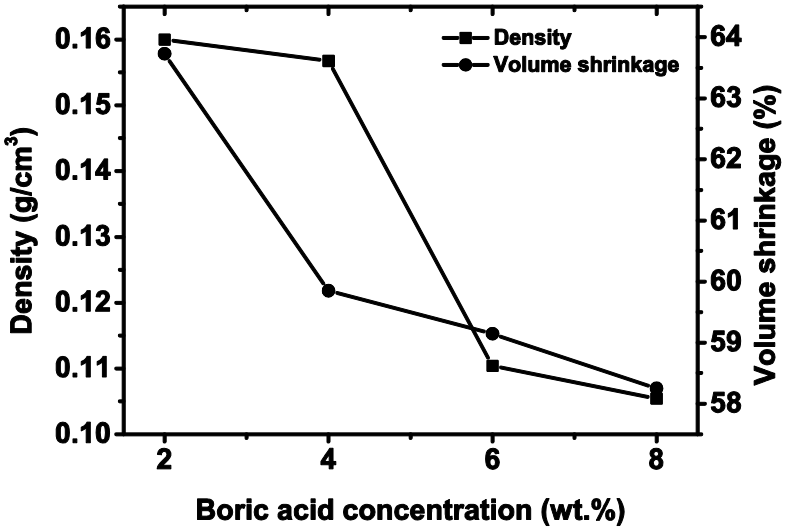

Figure 3.7: The effect of boric acid concentration on carbonization shrinkage and carbon foam density

3.3.4 Effect of Boric Acid Concentration on Microstructure

The carbon foams have cellular structure. The near spherical cells are connected through circular and oval shaped cell windows. The average cell size increases from 0.67 to 1.17 mm when the boric acid concentration increases from 2 to 8 wt.%. Figure 3.8 shows the SEM micrographs of the carbon foams prepared at various boric acid concentrations. The thickness of struts and cell walls decreases with an increase in boric acid concentration. The strut thickness observed is in the range of 116 to 80 μm at boric acid concentrations in the range of 2 to 8 wt.% (Table 3.2). The strut thickness obtained is much higher than that obtained (20 to 45 μm) for the carbon foams prepared using aluminium nitrate blowing agent. The higher thickness of the struts and cell walls is the reason for the higher carbon foam density in spite of the higher foam volume**.** Microcracks are observed in the cell walls of carbon foams prepared at a boric acid concentration of 4 wt.% and above. The microcracks, just initiated from the edges of the cell windows at 4 wt.% boric acid, advance through the cell walls at higher boric acid concentrations.

Table 3.2: The strut thickness of the boron-doped carbon foams prepared from molten sucrose

Boric acid concentration (wt.%)	**Strut thickness (μm)**
2	116
4	119
6	89
8	80

The ICP analysis shows the presence of 0.44 to 3.40 wt.% boron in the carbon foams prepared at a boric acid concentration in the range of 2 to 8 wt.%. The EDAX analysis shows oxygen concentration in the range of 0.7 to 4.7 wt.% in the carbon foams prepared at a boric acid concentration in the range of 2 to 8 wt.%. The amount of oxygen required to form all B-O-C bonds with the entire

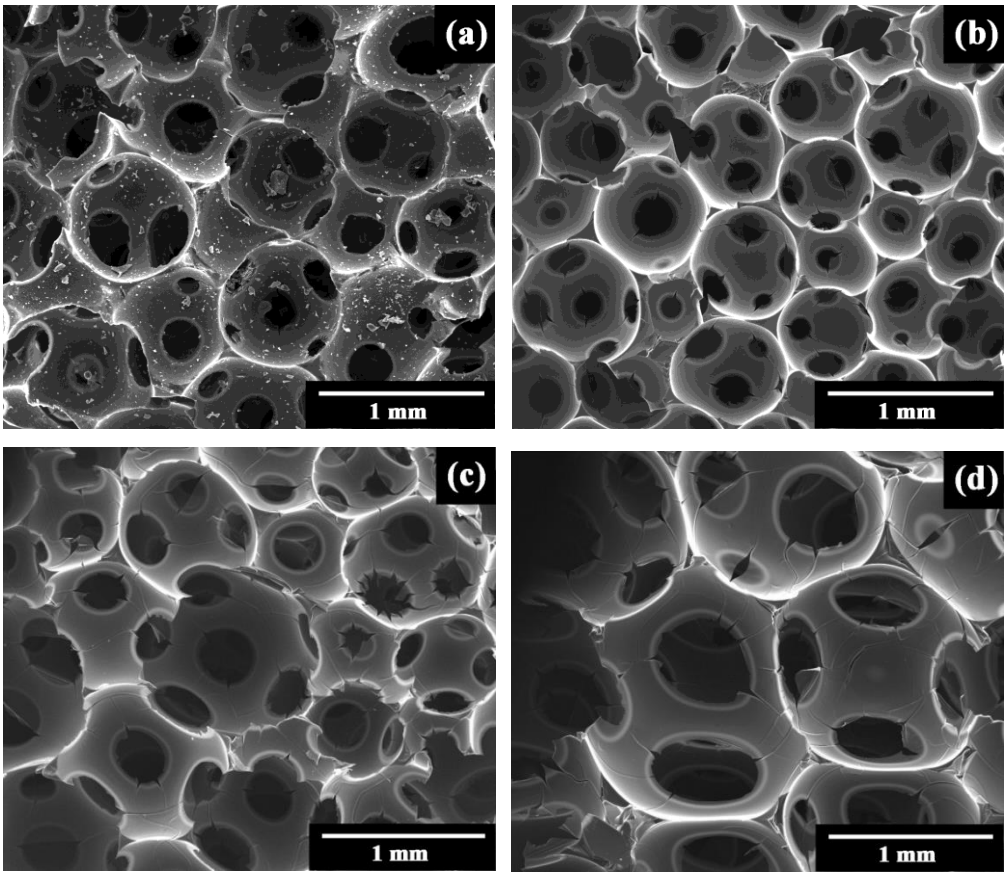

Figure 3.8: SEM images of the boron-doped carbon foam (a – 2 wt.% boric acid; b – 4 wt.% boric acid; c – 6 wt.% boric acid and d – 8 wt.% boric acid)

boron present in carbon foams is in the range of 2.11 to 16.32 wt.%. This indicates that the boron is attached to the carbon through both the B-C and the B-O-C linkages. The formation of B-C bonds at temperature lower than 900 ^{o}C has already been reported by Mondal and Banthia (2005). The average cell size, the average cell window size, the boron concentration and the oxygen concentration of the carbon foams prepared at various boric acid concentrations are given in Table 3.3.

3.3.5 Compressive Strength

Figure 3.9 shows the compressive stress-strain graph of the boron-doped carbon foams prepared at various boric acid concentrations. An elastic region

Table 3.3: Effect of boric acid concentration on the characteristics of carbon foams

Boric acid concentration (wt.%)	Cell Size (mm)	Cell window size (mm)	Boron concentration (wt.%)	Oxygen content*(wt.%)
0	-	-	0.00	-
2	0.67 ± 0.08	0.25 ± 0.03	0.44	0.7
4	0.68 ± 0.07	0.21 ± 0.04	1.05	1.8
6	0.94 ± 0.09	0.39 ± 0.04	2.98	2.8
8	1.17 ± 0.05	0.59 ± 0.05	3.40	4.7

*Obtained from EDAX

followed by a yield point, a plateau region and a region of densification, typical for a rigid cellular material is observed in the stress-strain curves (Gibson and Ashby, 1997; Tondi et al., 2009). It is well-known that the strength of cellular materials increases with an increase in the bulk density, thickness of the strut and thickness of ligaments and decreases with an increase in cell size (Chen et al., 2006; Deqing and Ziyuan, 2003; Gallego and Klett, 2003; Gibson and Ashby, 1997). The effect of boric acid concentration on the compressive strength and Young's modulus of carbon foams is shown in Figure 3.10. The carbon foams prepared at 2 wt.% boric acid show the highest compressive strength of 1.1 MPa. The compressive strength drastically decreases to 0.2 when the boric acid concentration increases to 4 wt.% and then remains constant up to a boric acid concentration of 6 wt.%. Further increase in boric acid concentration results in a considerable decrease in the compressive strength. Similarly, there is a decrease in the Young's modulus from 19.2 to 6.7 MPa when the boric acid concentration increases from 2 to 8 wt.%. The remarkable decrease in the compressive strength is observed for a marginal decrease in the carbon foam density when the boric acid concentration increases from 2 to 4 wt.%. This is due to the microcracks observed on the edges of the cell windows in carbon foam obtained at boric acid concentration of 4 wt.%. It appears that the microcracks present on the edges of

the pores propagate under the compressive load and leads to the failure of the carbon foams at lower stress values. The poor mechanical strength of the carbon foam at the boric acid concentration of 8 wt.% is due to the microcracks present in the cell walls and struts.

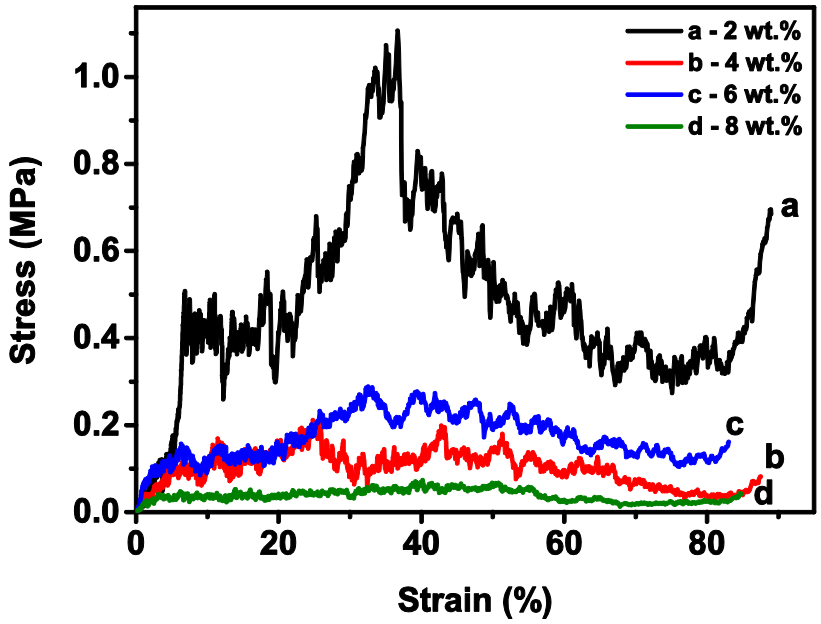

Figure 3.9 Stress-strain graph of boron-doped carbon foams prepared at various boric acid concentrations

3.3.6 Thermal Conductivity

The glassy carbon foams have low thermal conductivity compared to the graphite foams (Gallego and Klett, 2003). The thermal conductivity of boron-doped carbon foams prepared at various boric acid concentrations is given in Table 3.4. The thermal conductivity of boron-doped carbon foams decreases from 0.057 to 0.043 W/m/K when the boric acid concentration increases from 2 to 8 wt.%. Thermal conductivity of the boron-doped carbon foams are slightly lower than that reported for the RVC foams (0.085 W/m/K for 0.042 g/cm^3) (Gallego and Klett, 2003). On the other hand, the thermal conductivity obtained for the

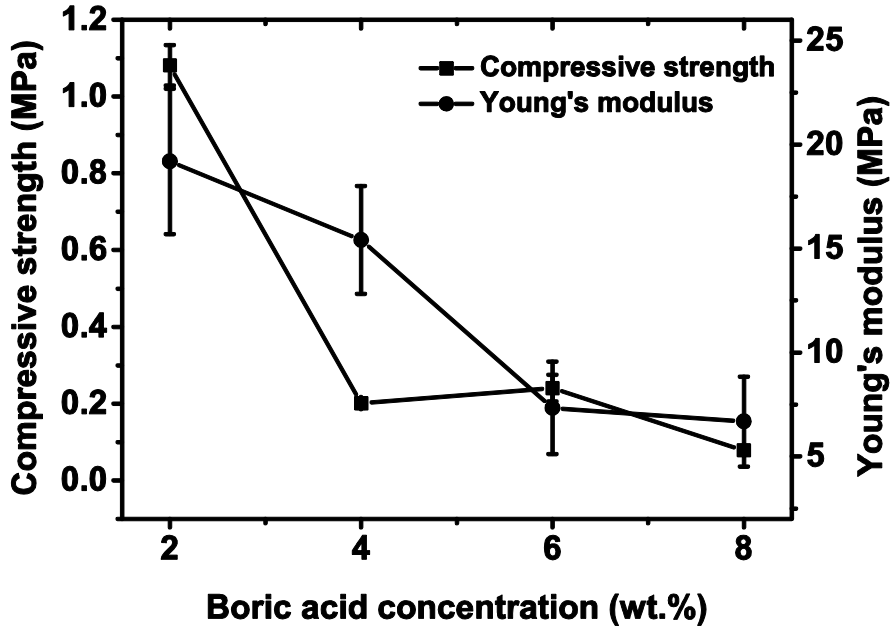

Figure 3.10: Compressive strength and young's modulus of the boron-doped carbon foams prepared at various boric acid concentrations

boron-doped carbon foams are very close to that of cellular vitreous carbon foams of similar densities prepared from tannin by Li et al (0.065 to 0.09 W/m/K for 0.07 to 0.18 g/cm^3) (Li et al., 2012).

Table 3.4: Thermal conductivity of the boron-doped carbon foams

Boric acid concentration (wt.%)	**Thermal conductivity (W/m/K)**
2	0.057 $\pm$ 0.0007
4	0.048 + 0.0014
6	0.045 $\pm$ 0.0014
8	0.043 $\pm$ 0.0006

The thermal conductivity of glassy carbon foams depends on the bulk density, cell size, and strut and cell wall thickness. Highly porous materials having constant pore structure but different total porosity shows a linear increase in thermal conductivity with density in a small range of porosities (Li et al., 2012). The thermal conductivity at room temperature plotted as a function of density of the carbon foams prepared at various boric acid concentrations is

shown in Figure 3.11. In the present case, the graph largely deviates from linearity. This is attributed to the variation of composition of the foams with boric acid concentration and the presence of microcracks in the cell walls at boric acid concentration above 2 wt.%.

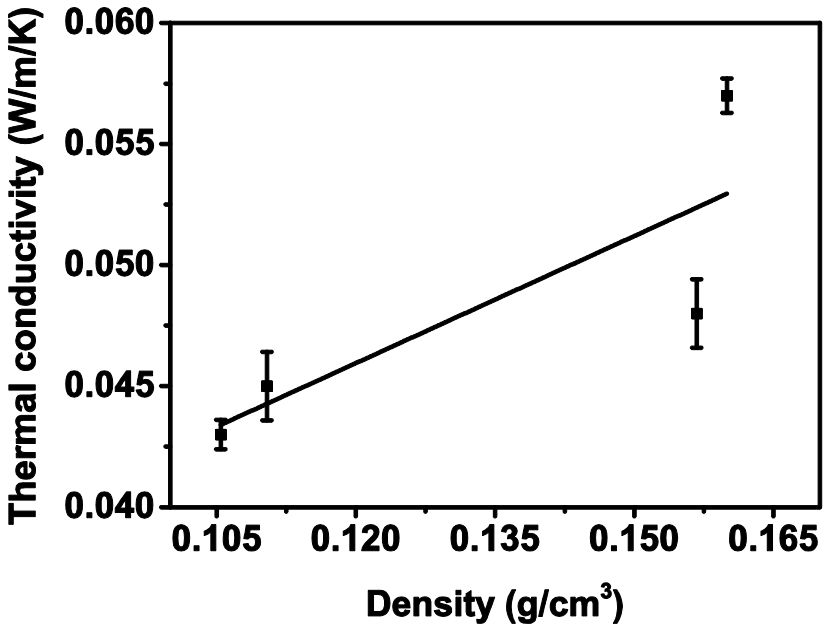

Figure 3.11: Density versus thermal conductivity plot of the boron-doped carbon foams prepared at various boric acid concentrations

3.3.7 Textural Properties

Figure 3.12 (a) shows the N_2 adsorption-desorption isotherms of the carbon foams prepared at various boric acid concentrations. The carbon foams shows a typical type I isotherm curves, according to IUPAC classification, which shows the presence of characteristic micropores in the carbon foams. Figure 3.13 shows the BET specific surface area, pore volume and microporosity of the carbon foams prepared at various boric acid concentrations. The surface area and total pore volume of the carbon foam prepared without the addition of boric acid are 367 m^2/g and 0.1854 cm^3/g, respectively. The surface area and total pore volume of the carbon foams increase with an increase in the boric acid concentrations up to 6 wt.% and then decreases with further increase in boric acid

concentration. The maximum surface area and pore volume obtained are 570 m^2/g and 0.2656 cm^3/g, respectively. On the other hand, the microporosity of the carbon foams decreases from 76 to 42 % when the boric acid concentration increases from 0 to 8 wt.%. Figure 3.12 (b) shows the DFT-PSD of the carbon foams prepared at various boric acid concentrations. The carbon foam prepared without boric acid showed peaks at 9.3 and 13.6 Å. However, the peaks shifted to higher pore sizes with an increase in the concentration of boric acid. The mechanism of the micropore formation in the cell walls and struts is same as the *in situ* activation reported in Chapter 2.

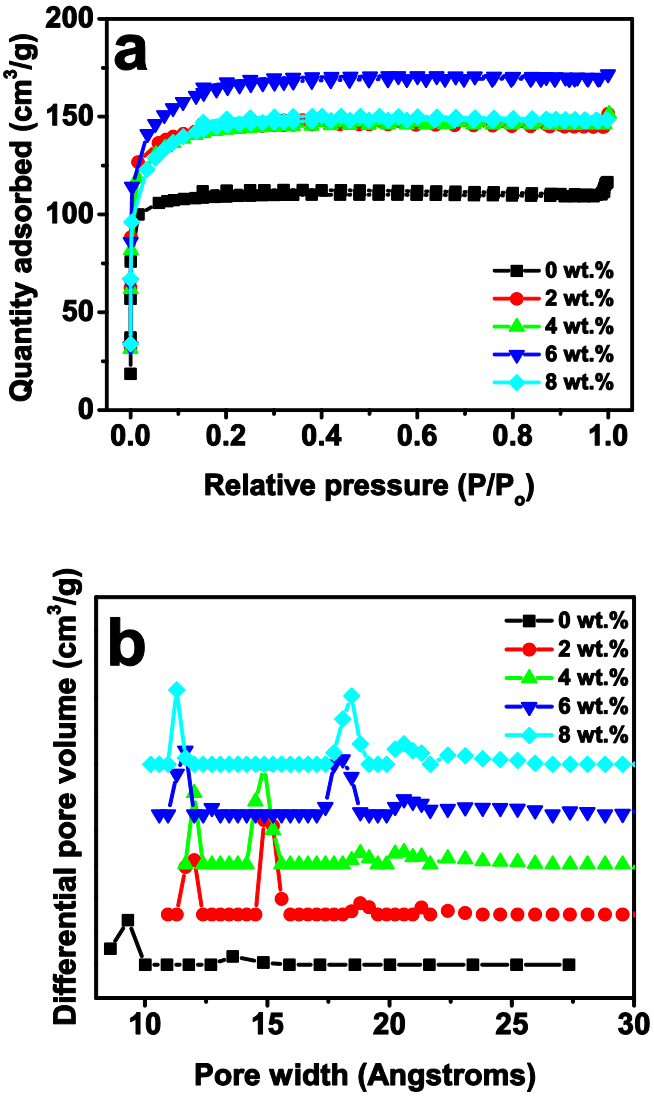

Figure 3.12: (a) N_2 adsorption-desorption isotherm and (b) DFT-PSD of the un-doped and the boron-doped carbon foams prepared at various boric acid concentrations

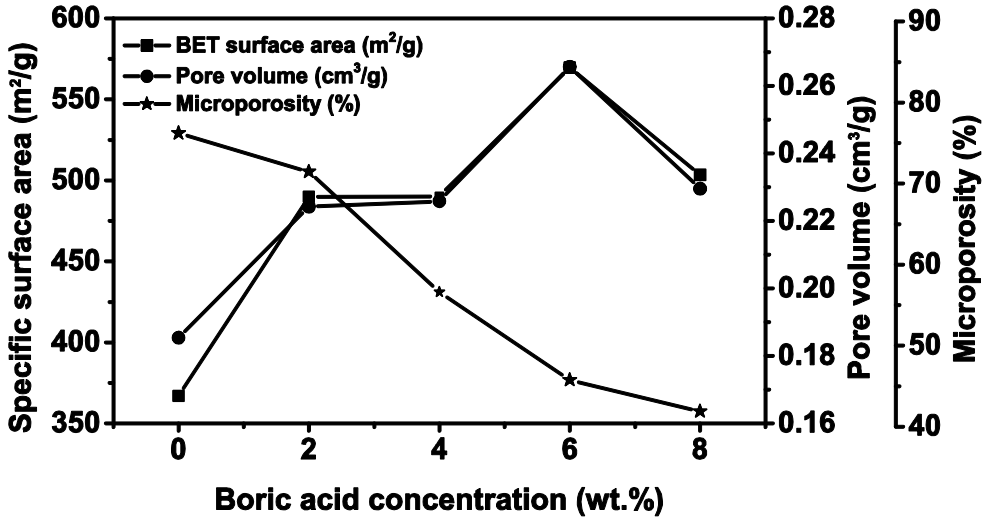

Figure 3.13: Surface area, pore volume and microporosity of the un-doped and the boron-doped carbon foams prepared at various boric acid concentrations

3.3.8 Effect of Boric Acid Concentration on Oxidation Resistance

Figure 3.14 shows the non-isothermal (a) TG and (b) DTG curves in air atmosphere of the un-doped carbon and boron-doped carbon foams prepared at various boric acid concentrations. The oxidation of un-doped carbon derived from molten sucrose starts at 450 ^{o}C and completes in a single stage at temperature less than 650 ^{o}C. On the other hand, DTG of the boron-doped carbon foams shows two stage decomposition with peaks centered at ~ 600 and 800 ^{o}C. The percentage weight loss observed in both first and second stage decomposition decreases with an increase in the boric acid concentration. The T_{10}, the temperature for 10 % weight loss, increases from 574 to 610 ^{o}C when the boric acid concentration increases from 0 to 8 wt.%. The char residue retained at 900 ^{o}C in TG increases from 0 to 36.6 wt.% when the boric acid concentration increases from 0 to 8 wt.%.

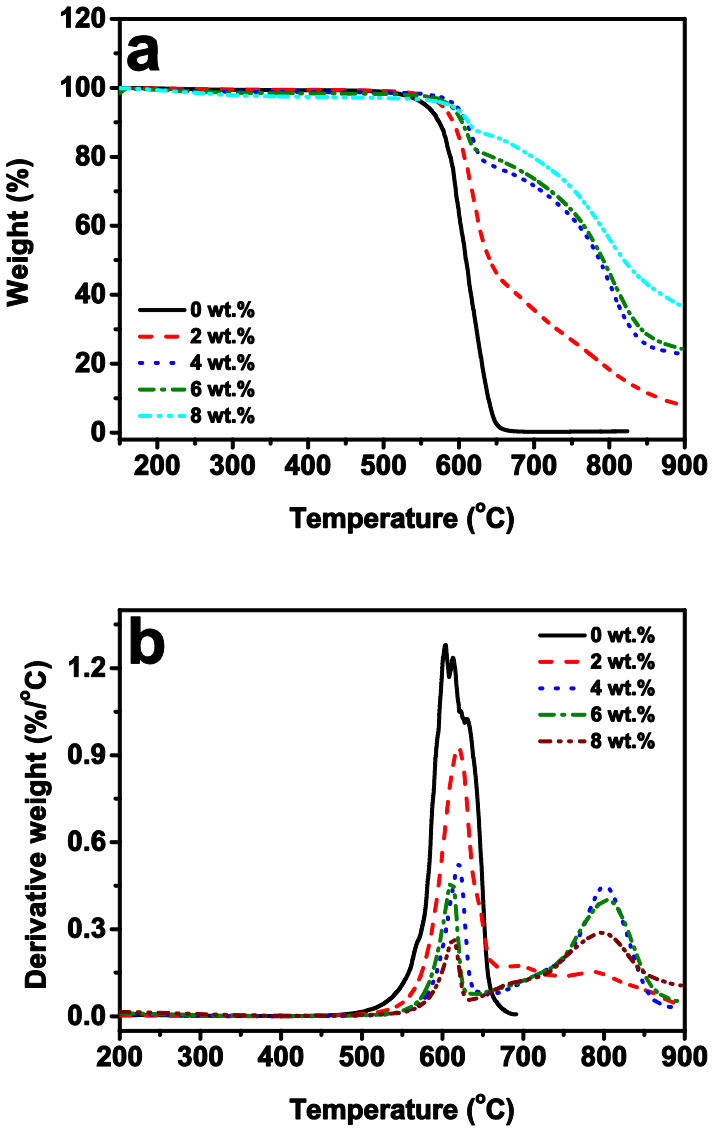

Figure 3.14: Non-isothermal (a) TG and (b) DTG plots of the un-doped carbon and the boron-doped carbon foams prepared at various boric acid concentrations

The weight loss due to isothermal oxidation at various temperatures from 300 °C to 500 °C for 3 h in a static air atmosphere of the un-doped and boron-doped carbon foams is shown in Figure 3.15. The un-doped and boron-doped carbon foam samples found stable in air atmosphere up to 400 °C. The weight loss observed at 400 °C is in the range of 0.65 to 0.7 % at boric acid concentrations in the range of 0 to 8 wt.%. The percentage weight loss in the temperature range of 400 to 500 °C decreases from 92 to 46 when the boric acid concentration increases from 0 to 8 wt.%. The foam structure is well-retained in the case of carbon foams

prepared at 6 and 8 wt.% of boric acid even after oxidation at 500 ^{o}C for 3 h. It appears that the boron oxide formed during the oxidation of the boron doped-carbon foams in the temperature range of 400 to 500 ^{o}C, blocks the surface active sites and retards further oxidation (McKee, 1991). In addition to the active site poisoning, oxidation resistance by the formation of molten boron oxide layer on the carbon foam surface is likely at higher temperatures (McKee, 1991). It is clear that the carbon foams prepared using boric acid blowing agent have better oxidation resistance than that prepared using aluminium nitrate blowing agent reported in chapter 2.

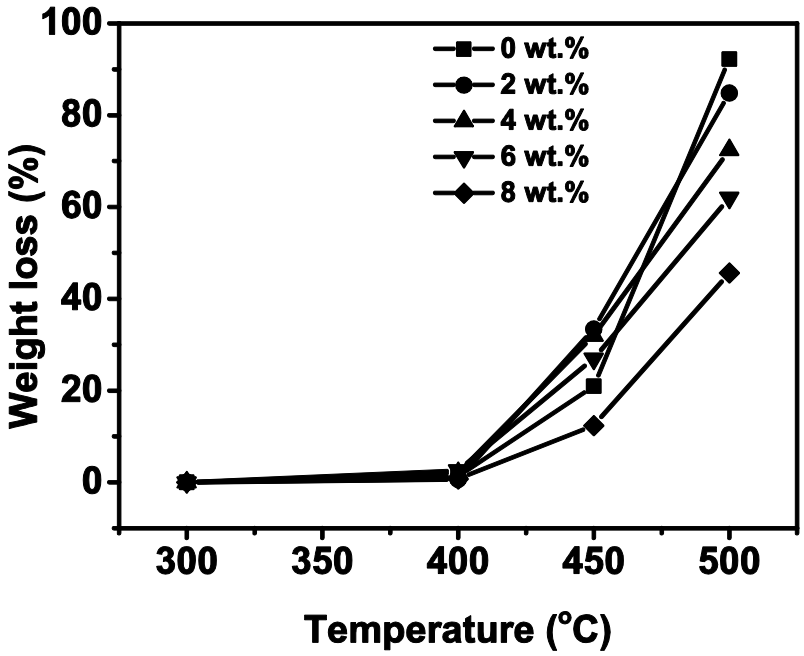

Figure 3.15: Isothermal oxidation behaviour of the un-doped and boron-doped carbon foams prepared at various boric acid concentrations

3.4 Conclusions

Boric acid is used as a blowing agent as well as a boron precursor for the preparation of boron-doped carbon foams from molten sucrose. The H^{+} generated from boric acid due to the formation of sucrose-boric acid complex catalyzes the -OH to -OH condensation reactions leading to the foaming and setting of the molten sucrose. The char yield of the solid organic foams increases from 24 to 39

wt.% when the boric acid concentration increases from 0 to 8 wt.% due to the formation of the B-O-C cross-links between sucrose polymer by B-OH to C-OH condensation. The density and compressive strength decrease and cell size increases with an increase in boric acid concentration. The room temperature thermal conductivity of the boron-doped carbon foams (0.057 to 0.043 W/m/K) is very close to the value reported for the cellular vitreous carbon foams of similar density range. The surface area and pore volume increase with an increase in the boric acid concentration up to 6 wt.% and then decrease. The boron present (0.44 to 3.4 wt.%) retards the oxidation of carbon foams as evidenced from the increase in the oxidation onset temperature and char residue at 900 ^{o}C with an increase in boric acid concentration. The oxidation resistance of carbon foams prepared using boric acid blowing agent is much higher than that of carbon foams prepared using aluminium nitrate blowing agent.

CHAPTER 4

PROCESSING AND CHARACTERIZATION OF CARBON COMPOSITE FOAMS FROM MOLTEN SUCROSE AND ACTIVATED CARBON POWDER

4.1 Introduction

The carbon foams prepared from molten sucrose using blowing agents such as aluminium nitrate and boric acid have relatively low density and compressive strength. Moreover, the blowing agent like aluminium nitrate produces hazardous nitrous fumes during melting and foaming. Recently, preparation of foams and emulsions by stabilizing the gas-liquid and liquid–liquid interfaces using particles is getting increased attention (Binks and Horozov, 2005; Binks and Lumsdon, 2000; Bromley, 1986; Dickinson et al., 2004; Gonzenbach et al., 2006a, b; Nakamae et al., 1999; Subramaniam et al., 2006). In this, the particles with suitable wetting characteristics irreversibly adsorb on the air-liquid and liquid-liquid interfaces. The possibility to control the wetting characteristics of the particles by modifying their surface using amphiphilic molecules further widen the scope of particle stabilized foams. The particle stabilized foams and emulsions are more stable than the surfactant stabilized counterparts. The particle stabilized foams are resistant to foam drainage and bubble coalescence by Ostwald ripening (Dickinson et al., 2004). The stabilization of bubbles by particles is used for the foaming of powder suspensions for the preparation of ceramic and polymer foams (Gonzenbach et al., 2006c; Thareja et al., 2008; Wong et al., 2010). The foaming of polymer melts by bubble stabilization using polymer particles of suitable wetting characteristics is also reported (Thareja et al., 2008). In the present chapter, activated carbon (AC) particles are used to induce the foaming of molten sucrose by stabilizing the bubbles. The AC particles not only stabilize the bubbles by adsorbing on the molten sucrose-gas interface but

also increase the carbon yield. In addition, the acidic surface functional groups present in the AC particles catalyse the –OH to –OH condensation leading to faster foaming and setting of the molten sucrose. The carbon composite foams produced show good CO_2 adsorption and oil absorption from an oil-in-water emulsion.

4.2 Experimental

4.2.1 Materials

The analytical reagent grade sucrose, acetone and AC powder used were procured from Merck India Ltd., Mumbai. The wood derived AC powder used was amorphous and contained particles in the size range of few micrometers to few hundred micrometers. The AC powder received from the supplier was planetary ball milled in acetone medium for 1 h using zirconia jar and zirconia grinding balls. The AC powder to the ball weight ratio used was 1:10. The average particle size (measured using a particle size analyzer) and surface area (measured using a surface area analyzer) of the ball milled AC powder was 7 μm and 883 m^2/g, respectively. The SEM photomicrographs of the as received and planetary ball milled AC powder are shown in Figure 4.1 (a) and (b), respectively. The particle size distribution of the planetary ball milled AC powder is shown in Figure 4.1 (c).

4.2.2 Preparation of Carbon Composite Foams

The flow chart for the preparation of carbon composite foams is shown in Figure 4.2. The sucrose (300 g) and various amounts of the AC powder were intimately mixed in a mixer-grinder for 10 min. The sucrose-AC powder mixtures were heated in glass trays at 170 ^oC to melt the sucrose and then stirred well with a glass rod to achieve uniform dispersion of the AC particles in the molten sucrose. The molten sucrose containing dispersed AC powder was heated in an air

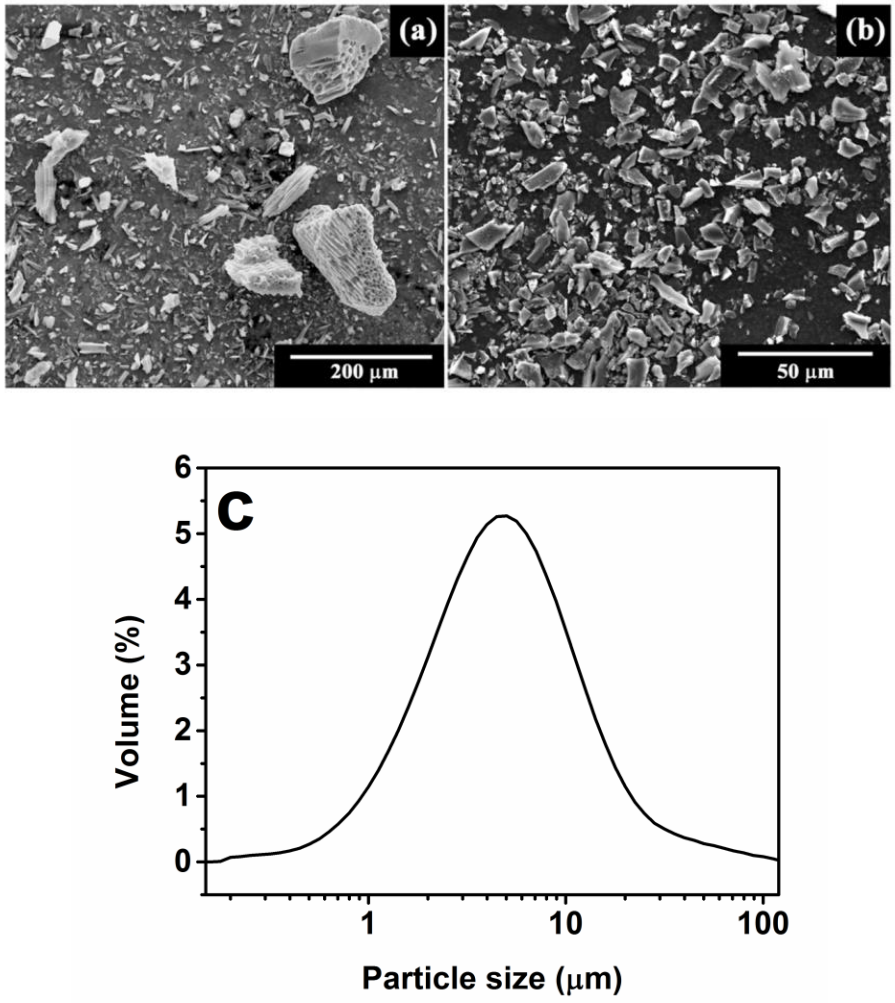

Figure 4.1: SEM photomicrographs of the (a) as received, (b) planetary ball milled AC powder, and (c) particle size distribution of the planetary ball milled AC powder

oven at 130 ^{o}C for 36 h for foaming and setting. The organic foams thus obtained were dehydrated at 200 ^{o}C in an air oven for 3 h. The heating rate used was 2 ^{o}C/h. The dehydrated foams were carbonized by heating in the high-pure argon atmosphere at 900 ^{o}C for 2 h. The heating rate used was 2 ^{o}C/min. The samples were unloaded after cooling the furnace to room temperature. The inert atmosphere was maintained throughout the cooling.

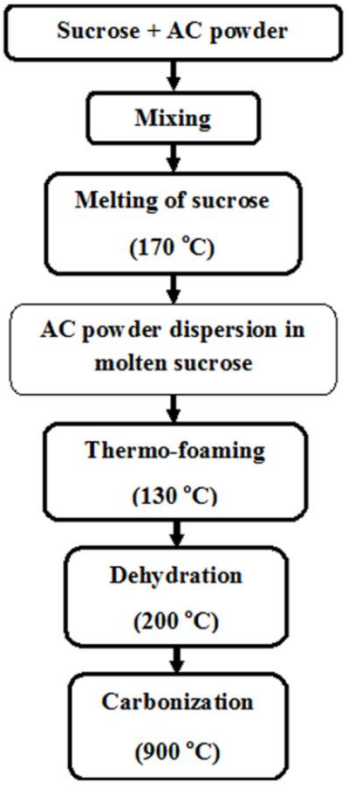

Figure 4.2: The flow chart for the preparation of carbon composite foams

4.2.3 Characterization

The viscosity measurement of the AC powder dispersions in molten sucrose was carried out at various shear rates in the range of 1 to 1000 s^{-1} at 130 ^{o}C using a Rheometer (MCR 102 Modular Compact Rheometer, Anton Paar, USA) with a cone and plate measurement system. The foam rise (a measure of foam volume) was calculated as the ratio of the initial height of the AC powder dispersion and the final height of the foam. The samples were physically inspected during foaming and foam setting at an interval of one hour to determine the approximate foaming and foam setting time. The char yield is taken as the weight retained after dehydration and carbonization of the large (8 cm x 5 cm x 2 cm) solid organic foams. The densities were calculated from the weight and dimension of rectangular carbon composite foam bodies. The microstructure of the carbon composite foams was observed using a Scanning Electron Microscope (SEM, FEI Quanta FEG200). The cell size of the carbon composite foams was

measured using ImageJ software from the SEM microstructure. The compressive strength of the carbon composite foams was measured using a universal testing machine (Instron 5050, Instron USA) at a crosshead speed of 0.5 mm/min with 25 mm x 25 mm x 12 mm samples (ASTM standard C365/C365M-05). The maximum stress in the stress-strain graph was noted as the compressive strength. The thermal conductivity of the carbon composite foam samples was measured using modified transient plane source method (MTPS) at room temperature. The 20 mm x 20 mm x 6 mm samples were used for the thermal conductivity measurements. The reported thermal conductivity is the average of four measurements.

The textural properties of the carbon composite foams were analyzed using the volumetric N_2 adsorption-desorption at -196 ^oC and CO_2 adsorption at 0 ^oC using a surface area analyzer (Micromeritics Tristar II, USA). The samples were degassed at 300 ^oC for 16 h prior to the analysis. The BET (Brunauer-Emmett-Teller) method was used for the calculation of the surface area. The total pore volume was estimated from the amount of N_2 adsorbed at a relative pressure of 0.99. The micropore volume was obtained by using t-plot method from N_2 adsorption at -196 ^oC. The pore size distribution (PSD) was calculated using density functional theory (DFT) using N_2 adsorption isotherm by assuming the slit pore model.

4.2.3.1 Estimation of Surface Functional Groups on AC Powder

Boehm titration was used to estimate the acidic oxygen surface functional groups on the AC powder (Boehm, 1994; Goertzen et al., 2010). The AC powder samples of mass 1.5$\pm$0.001 g each was added to 50 ml of 0.05 M solution of NaOH, $NaHCO_3$ and Na_2CO_3 taken in different iodine flasks. The solutions were closed tightly and shaken using wrist shaker for 24 h. After 24 h, the contents in the iodine flasks were filtered through Whatman filter papers to collect the solutions. 10 ml of aliquot taken from each solution was acidified with 50 ml of 0.05M HCl and then back titrated with 0.05 M standardized NaOH

solution using phenolphthalein indicator. The concentration of carboxylic, lactonic and phenolic functional groups present on the AC powder surface was calculated from the titer values according to equation 4.1:

$$n_{CSF} = \frac{n_{HCl}}{n_B}[B]V_B - ([HCl]V_{HCl} - [NaOH]V_{NaOH})\frac{V_B}{V_a} \quad (4.1)$$

where n_{csf} is the number of moles of carbon surface functionality, [B] and V_B are the concentration and volume of the base mixed with the carbon, V_a is the volume of aliquot taken from the V_B, [HCl] and V_{HCl} are the concentration and volume of the acid added to the aliquot taken from the original solution, [NaOH] and V_{NaOH} are the concentration and volume of titrant NaOH in the back titration (Goertzen et al., 2010).

4.2.3.2 Contact Angle Measurement

The contact angle of molten sucrose on a monolithic carbon surface was measured using a Goniometer (OCA 20, Dataphysics, Germany). The monolithic carbon was prepared by carbonizing a piece of wood at 900 ^{o}C in an inert atmosphere. The monolithic carbon surface was thoroughly cleaned with acetone and dried prior to the measurement. The static contact angle was measured by placing the molten sucrose on the monolithic carbon surface.

4.2.3.3 CO_2 Adsorption

The CO_2 adsorption of the carbon composite foam samples was evaluated at 0 and 25 ^{o}C by volumetric gas adsorption studies using the surface area analyzer. Prior to the measurements, the samples were crushed using an agate and mortar and degassed overnight at 300 ^{o}C.

4.2.3.4 Oil Absorption

Accurately weighed carbon composite foam bodies of size 2.5 cm x 2.5 cm x 2.5 cm were immersed in various organic solvents for 5 min. The foam sample removed from the solvent after 5 min was immediately weighed. The oil absorption ability was calculated from the increase in weight of the foam sample. The oil absorption of the carbon composite foams from water-oil mixtures and oil-in-water emulsion were also tested. The oil-in-water emulsion was prepared by mixing 90 ml water, 10 ml toluene and 0.1 g cetyltrimethyl ammonium bromide surfactant using an ultrasonicator.

4.3 Results and Discussion

4.3.1 Effect of the AC Powder Concentration on the Rheological and Foaming Characteristics of the Molten Sucrose

The sucrose in the sucrose-AC particle mixture melts when heated at 170 ^{o}C in an air oven. The AC particles uniformly disperse in the molten sucrose when the melt is stirred with a glass rod. The dispersion of a powder in a fluid medium is assessed by the rheological studies. The viscosity at various shear rates of molten sucrose containing dispersed AC powder measured at 130 ^{o}C is shown in Figure 4.3. The molten sucrose shows viscosities in the range of 17 to 10.9 Pa.s at shear rates in the range of 1 to 1000 s^{-1}. The AC powder dispersions with the AC powder to sucrose weight ratio up to 0.1 show viscosities lower than that of the molten sucrose at all shear rates. Beyond this ratio, the dispersions show viscosity higher than that of the molten sucrose at lower shear rates. However, at higher shear rates, the dispersion viscosity falls below that of the molten sucrose. The shear rate at which the viscosity of the AC powder dispersion falls below that of molten sucrose increases with an increase in the AC powder to sucrose weight ratio. The viscosity of a fluid depends on the intermolecular forces. The relatively high viscosity of molten sucrose is due to the intermolecular hydrogen bonding through the hydroxyl groups. It is well-known that the particles in a powder dispersion experience an interparticle attractive interaction due to the Van der

Waals forces (G.D.Parfitt, 1981). This Van der Waals interaction increases with an increase in the powder loading. Generally, the powder dispersions show higher viscosity than that of the dispersion medium due to the Van der Waals interaction between the particles (G.D.Parfitt, 1981). Contrary to this, the AC powder dispersions at an AC powder to sucrose weight ratio less than 0.1 show lower viscosities than that of molten sucrose. This can be possible if the AC particles interrupt the intermolecular hydrogen bonding exist in molten sucrose. It appears that a fraction of the sucrose –OH groups interact with the functional groups present on the AC particle surface instead of intermolecular hydrogen bonding. This sucrose-AC particle interaction results in the dispersion of the AC particles in molten sucrose. At higher AC powder loadings, the increase in viscosity due to the increased Van der Waals attraction between the AC particles outweighs the viscosity decrease due to the interruption of intermolecular hydrogen bonding by the AC particles. The weak particle agglomerates formed at higher powder loading due to the Van der Waals attraction break at higher shear rates. This results in a decrease in viscosity below that of molten sucrose.

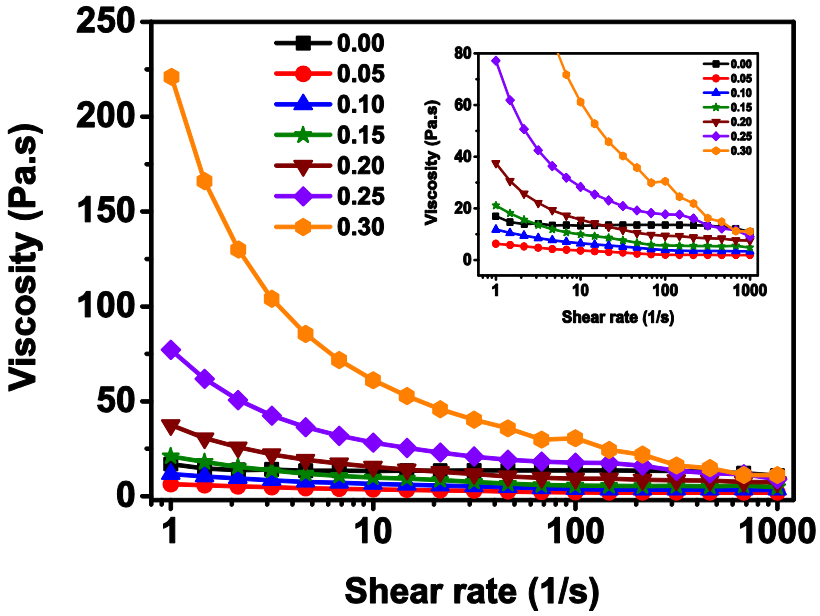

Figure 4.3: Viscosity versus shear rate of the AC powder dispersions at various AC powder to sucrose weight ratios measured at 130 ^{o}C (shear rate showed in logarithmic scale)

The AC powder dispersions in molten sucrose undergo slow foaming and setting when heated at 130 ^{o}C in an air oven. Figure 4.4 is a photograph showing the effect of AC powder to sucrose weight ratio on the foam volume. A constant foaming time of 24 h is given for all the compositions. The foaming of molten sucrose without AC powder is not initiated whereas the foaming of the AC powder dispersions is completed in 24 h. The foam volume increases with an increase in the AC powder to sucrose weight ratio. Inspection of cross-section of the foams using a magnifying glass reveals the uniform cell structure at AC powder to sucrose weight ratios in the range of 0.05 to 0.25. On the other hand, at an AC powder to sucrose weight ratio of 0.3, large and non-uniform cells are observed. The foaming time and foam setting time decrease with an increase in the AC powder to sucrose weight ratio. The foaming of molten sucrose without AC powder is initiated after 24 h and completes in nearly 72 h. The foamed molten sucrose without AC powder takes nearly 120 h for complete setting. On the other hand, the AC powder dispersions in molten sucrose at the AC powder to sucrose weight ratios in the range of 0.05 to 0.3 take 16 to 1 h for foaming and 32 to 8 h for foam setting. Figure 4.5 shows the foam rise, foaming time and foam setting time at various AC powder to sucrose weight ratios.

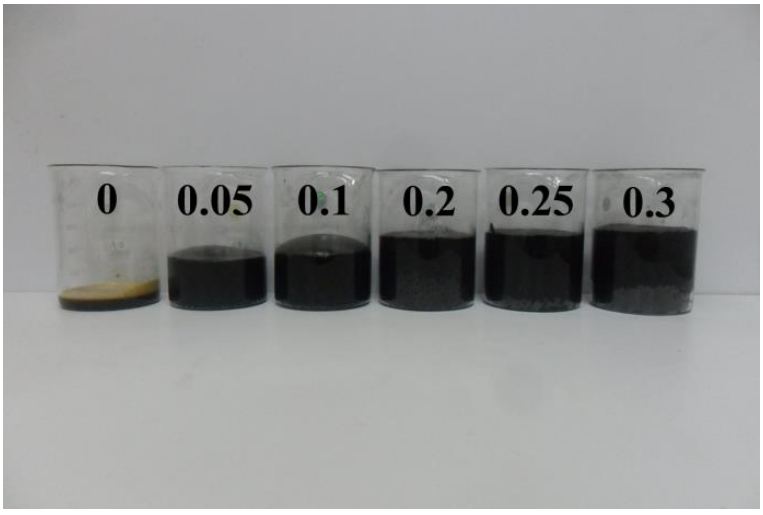

Figure 4.4: Digital photograph showing the foaming characteristics of the dispersions prepared at various AC powder to sucrose weight ratios (foaming temperature 130 ^{o}C and foaming time 24 h)

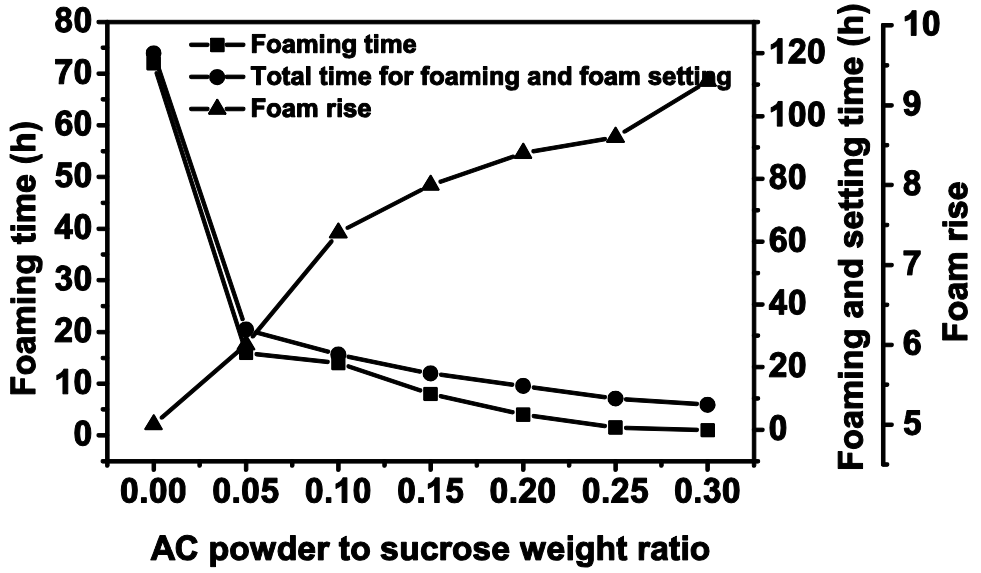

Figure 4.5: Foaming time, foam setting time and foam rise of the AC powder dispersions in molten sucrose with different AC powder to sucrose weight ratios foamed at 130 ^{o}C

The mechanism of foaming of molten sucrose is reported in Chapter 2. Accordingly, the water vapour generated due to the intermolecular –OH condensation between glucose and fructose anhydrides formed from sucrose produce bubbles in molten sucrose, which are stabilized by the increase in viscosity due to the condensation reaction (Finar, 2007b). It appears that the molten sucrose without AC powder takes nearly 24 h at 130 ^{o}C to reach the viscosity required for bubble stabilization that results in its delayed foaming. The early foaming of AC powder dispersions is due to the stabilization of bubbles in the low viscous molten sucrose by the AC particles. The AC particles adsorb on the molten sucrose-gas interface and stabilize the bubbles. It has been reported that a contact angle in the range of 60 to 80^{o} is suitable for foam stabilization using particles (Binks and Horozov, 2005; Binks and Lumsdon, 2000). The photograph showing the contact angle of molten sucrose on a carbonized wood surface is shown in Figure 4.6. The contact angle of 68^{o} observed between molten sucrose and the wood-derived carbon surface indicates that the AC particle can stabilize the gas bubbles generated in molten sucrose. The increase in foam volume with an increase in the AC powder loading is due to the increase in bubble stability by the enhanced AC particle coverage on bubble surface. At an AC

powder to sucrose weight ratio above 0.25, the viscosity of the dispersion is too high for a homogenous foaming that results in a non-uniform cell structure.

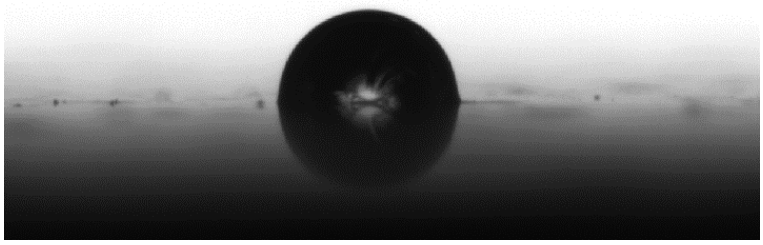

Figure 4.6: The contact angle between the molten sucrose and wood derived carbon monolith

Figure 4.7 shows the viscosity variation with time of the AC powder dispersions in molten sucrose measured at 130 ^{o}C at a constant shear rate of 10 s^{-1}. The viscosity of the molten sucrose without the AC powder gradually increases with time over a period of more than 10 h. On the other hand, the viscosity of the AC powder dispersions initially shows a gradual increase and then a rapid increase with time. The time at which the rapid increase in viscosity observed decreases with an increase in the AC powder loading. This indicates that the AC particles catalyse the –OH condensation responsible for the viscosity increase. Acids are well-known catalysts for the –OH condensation. The FTIR spectrum of the AC powder shows peaks at 1737, 3443 and 1031 cm^{-1} corresponding to the presence of carboxyl, hydroxyl and lactonic groups, respectively (Figure 4.8). The carboxyl, phenolic and lactonic functional groups on the AC powder surface quantitatively estimated by Bohemn titration are given in Table 4.1. The lactonic groups present on the surface of the AC powder dispersed in molten sucrose expected to form carboxyl groups by the reaction with water vapour. The H^{+} ions produced from the carboxyl groups on the AC particle surface catalyzes the –OH condensation leading to an early viscosity increase of the dispersions at the higher AC powder loadings. The decrease in foaming time and foam setting time with an

increase in the AC powder loading is due to the increase in the rate of –OH condensation.

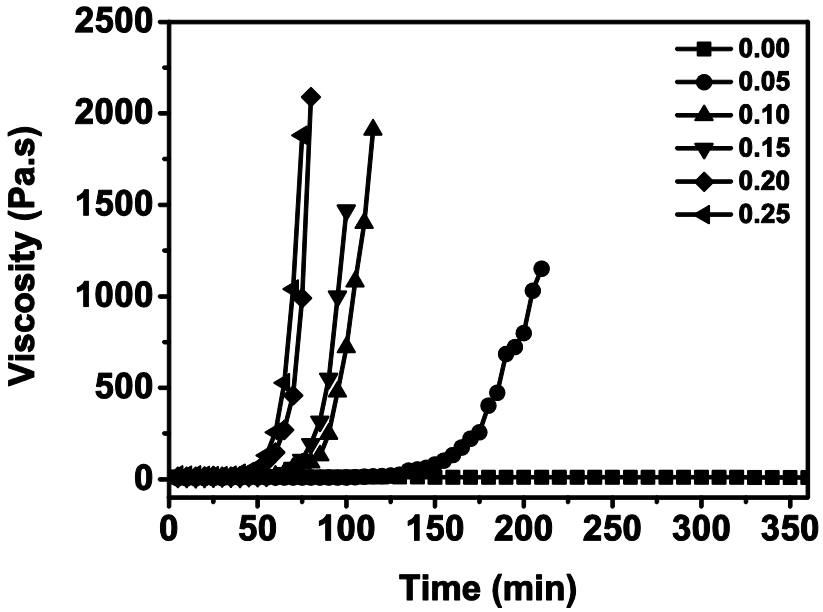

Figure 4.7: Viscosity versus time of the molten sucrose with various AC powder to sucrose weight ratios measured at a shear rate of 10 s^{-1} and at 130 ^{o}C

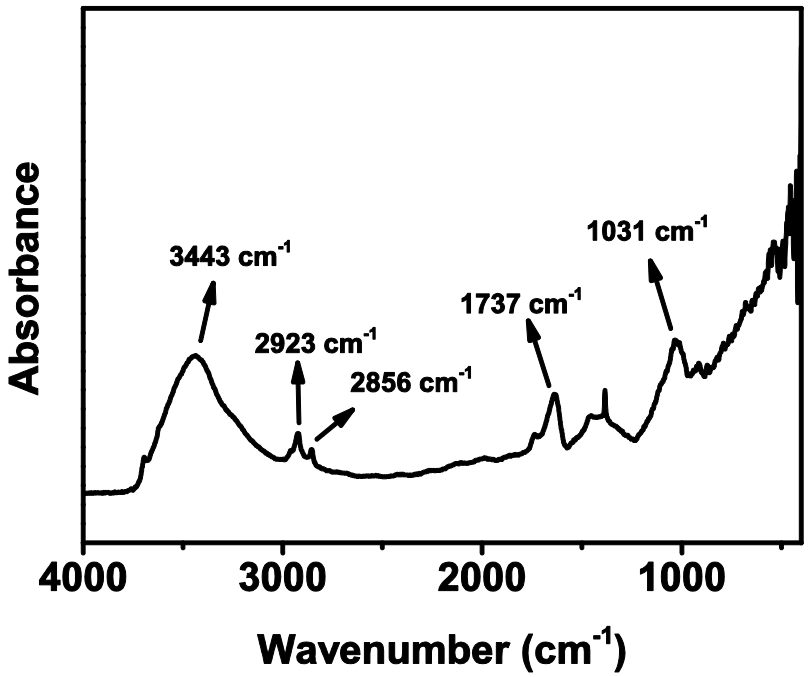

Figure 4.8: FTIR spectrum of the AC powder

Table 4.1: Carbon surface functionalities estimated using Boehm titration of AC powder

Functional groups	n_{csf}^{*} (μmol/g)
Phenolic	202
Lactonic	282
Carboxylic	162

*Carbon surface functionality

4.3.2. Carbonization of Solid Organic Foams

Figure 4.9 shows the TGA in inert atmosphere of the solid organic foams prepared from molten sucrose at AC powder to sucrose weight ratios of 0 and 0.1. The decomposition of the solid organic foams starts at 150 ^{o}C. It is worthy to note that the solid organic foam prepared at AC powder to sucrose weight ratio of 0.1 shows higher weight loss at temperatures in the range of 150 to 250 ^{o}C compared to that prepared from molten sucrose without AC powder. This is due to the catalytic activity of AC powder towards –OH to –OH condensation, which is responsible for the weight loss at this temperature range. The DTG shows peaks at 280 and 260 ^{o}C for the solid organic foams at AC powder to sucrose weight ratios of 0 and 0.1, respectively. The thermal decomposition of the solid organic foam prepared without AC powder is almost complete at 600 ^{o}C. The solid organic foams without AC powder leave 24.2 wt.% char. On the other hand, the solid organic foam at AC powder to sucrose weight ratio of 0.1 shows weight loss up to 900 ^{o}C. The char yield observed at 900 ^{o}C is 30.5 wt.%. This indicates that the initial weight loss in solid organic foam prepared with AC powder is mainly due to –OH to –OH condensation which leaves large number of ether linkages that decompose at higher temperatures. Whereas the initial weight loss in solid organic foams prepared without AC powder is due to the removal of water by α-elimination. The volume shrinkage during carbonization and char yield of the solid organic foam bodies prepared at various AC powder to sucrose weight ratios are shown in Table 4.2. The char yield increases from 33.2 to 47.2 wt.% when the AC powder to sucrose weight ratio increases from 0.0 to 0.25. However, the volume shrinkage decreases from 68 to 46.1 % when the AC powder to sucrose

weight ratio increases from 0.0 to 0.25. The char yield obtained from slow dehydration and carbonization of solid organic foam bodies is higher than that obtained from TGA. This indicates that the slow heating in air atmosphere during dehydration (130 to 200 ^{o}C) produces more cross-links which resulted in higher char yield (Savage, 1993).

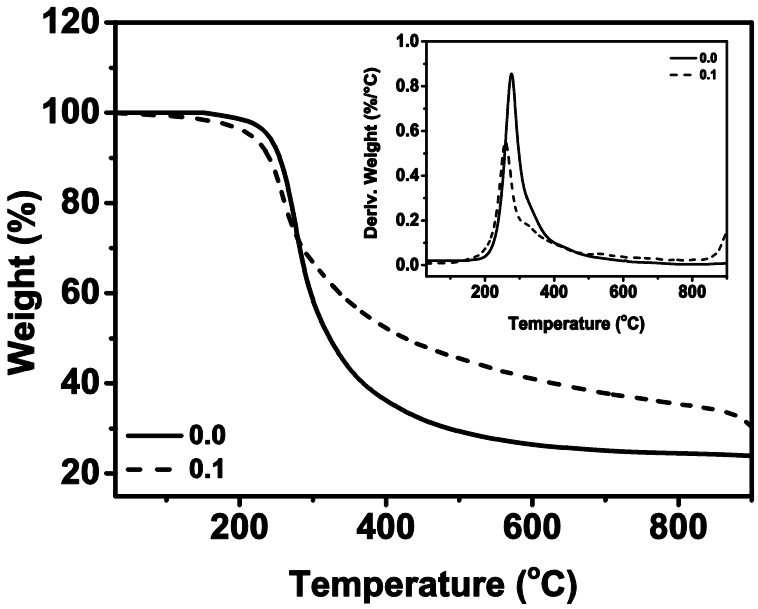

Figure 4.9: TGA of the solid organic foams prepared from 0.0 and 0.1 AC powder to sucrose weight ratios (Inset: DTG of the solid organic foams)

The density of the carbon foams prepared without the AC powder is 0.22 g/cm^3. The density of the carbon composite foams decreases to 0.164 g/cm^3 when the AC powder to sucrose weight ratio increases to 0.05. The density of the carbon composite foams then increases to 0.169 and 0.177 g/cm^3 when the AC powder to sucrose weight ratio increased to 0.1 and 0.15, respectively. Thereafter, the density of the carbon composite foam decreases to 0.16 when the AC powder to sucrose weight ratio increases to 0.25. The density of the carbon composite foams prepared at various AC powder to sucrose weight ratios is given in Table 4.2.

Table 4.2: Volume shrinkage and char yield of the solid organic foams and the density of the carbon composite foams prepared at various AC powder to sucrose weight ratios

Sample	Volume shrinkage (%)	Char yield* (%)	Density (g/cm^3)
0.00	67.97	33.16	0.2205
0.05	63.32	34.73	0.1645
0.10	59.00	38.59	0.1691
0.15	56.04	41.42	0.1771
0.20	51.28	44.58	0.1699
0.25	46.06	47.25	0.1603

*Char yield obtained from large solid organic foam bodies

The preparation of large carbon composite foam body is essential for the practical applications. Thermo-foaming in large batch (up to 1 kg sucrose) did not produce any inhomogeneity in the foam microstructure. The large organic foam bodies can be dehydrated and carbonized without any deformation. The photograph of a large carbon composite foam body of size 15 cm x 15 cm x 4 cm prepared at AC powder to sucrose weight ratio of 0.1 is shown in Figure 4.10.

Figure 4.10 Large carbon composite foam body prepared at an AC powder to sucrose weight ratio of 0.1

4.3.3 Microstructure, Compressive Strength and Thermal Conductivity of the Carbon Composite Foams

The carbon composite foams obtained by carbonization of the solid organic foams have interconnected cellular morphology. Figure 4.11 shows the SEM photomicrographs of the carbon composite foams prepared at the AC powder to sucrose weight ratios of 0.05, 0.15 and 0.25. Higher magnification images show the increased concentration of AC particles on the cell wall surfaces with an increase in the AC powder to sucrose weight ratio. This confirms the foaming due to bubble stabilization by the AC particles. The cell size of the carbon composite foams prepared at various AC powder to sucrose weight ratios is summarized in Table 4.3. The cell size of the carbon composite foams decreases from 0.895 to 0.647 mm when the AC powder to sucrose weight ratio increases from 0 to 0.05. Further addition of AC powder results in the increase in cell size due to the enhanced bubble stabilization by the increased adsorption of AC particles on the cell wall surfaces, which leads to a decrease in the carbon composite foam density. The rapid increase in viscosity at higher AC particle concentration also provides additional bubble stability that result in higher cell size and lower foam density. The lower density of carbon composite foam at AC powder to sucrose weight ratio of 0.05 in spite of its lower cell size indicates that the incorporation of AC powder modifies the foaming behaviour leading to a lower thickness of the cell walls and struts.

The carbon composite foams show the typical compressive stress-strain behaviour of elastic-brittle foams (Figure 4.12). The compressive strength of brittle foam materials increases with an increase in density, and decrease in cell size (Gibson and Ashby, 1997). Figure 4.13 shows the compressive strength and thermal conductivity of the carbon composite foams at various AC powder to sucrose weight ratios. The carbon composite foams prepared at the AC powder to sucrose weight ratios in the range of 0 to 0.25 show compressive strength in the range of 1.36 to 0.31 MPa with a maximum at an AC powder to sucrose weight

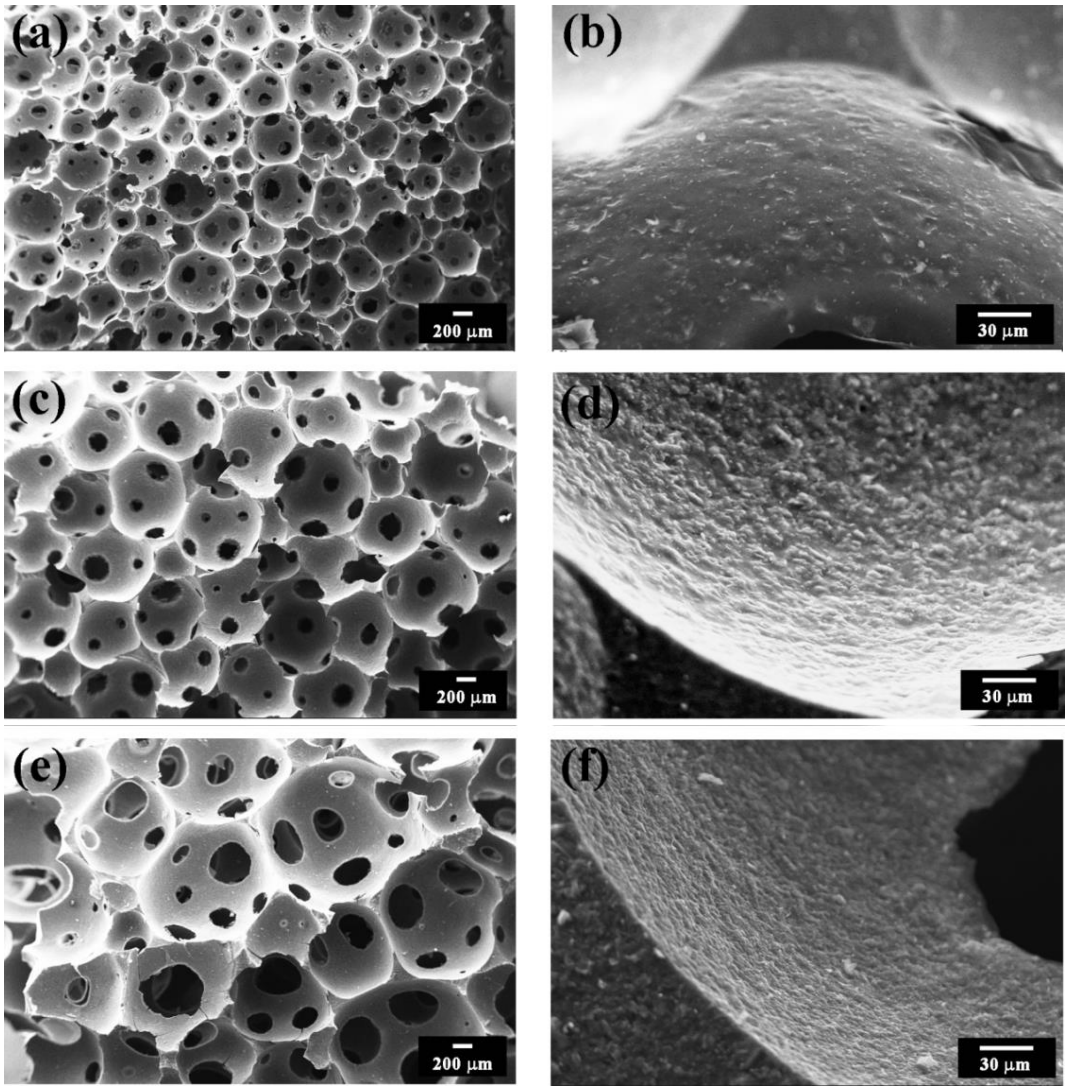

Figure 4.11: SEM photomicrographs of the carbon composite foams prepared at the AC powder to sucrose weight ratios of 0.05 (a and b), 0.15 (c and d) and 0.25 (e and f)

Table 4.3: Cell size of the carbon composite foams

Sample	Cell size[a] (mm)
0.00	0.895 ± 0.092
0.05	0.647 ± 0.088
0.10	0.983 ± 0.098
0.15	1.121 ± 0.096
0.20	1.606 ± 0.206
0.25	1.765 ± 0.257

[a]Cell size measured using ImageJ software from SEM micrographs

ratio of 0.05. Similarly, the carbon composite foams prepared at the AC powder to sucrose weight ratios in the range of 0 to 0.25 show Young's modulus in the range of 17.6 to 49.5 MPa with a maximum at an AC powder to sucrose weight ratio of 0.05. The variation in compressive strength with the AC powder to sucrose weight ratio is in tune with the variation of cell size and foam density. The specific compressive strength of the carbon composite foam increases from 5.03 to 8.3 MPa/g/cm^3 when the AC powder to sucrose weight ratio increases from 0 to 0.05. Further increase in AC powder to sucrose weight ratio from 0.05 to 0.25 decreases the specific compressive strength from 8.3 to 1.9 MPa/g/cm^3. The thermal conductivity of the carbon composite foams decreases marginally from 0.07 to 0.067 W/m/K when the AC powder to sucrose weight ratio increases from 0 to 0.1. Further increase in AC powder to sucrose weight ratio up to 0.25 did not make any change in the thermal conductivity.

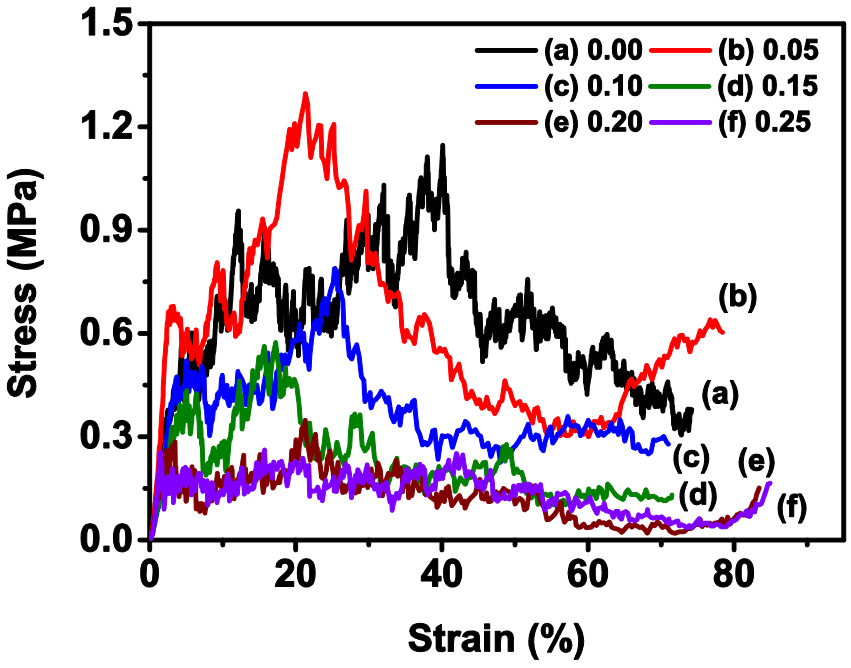

Figure 4.12: Stress-strain graph of the carbon composite foams prepared at various AC powder to sucrose weight ratios

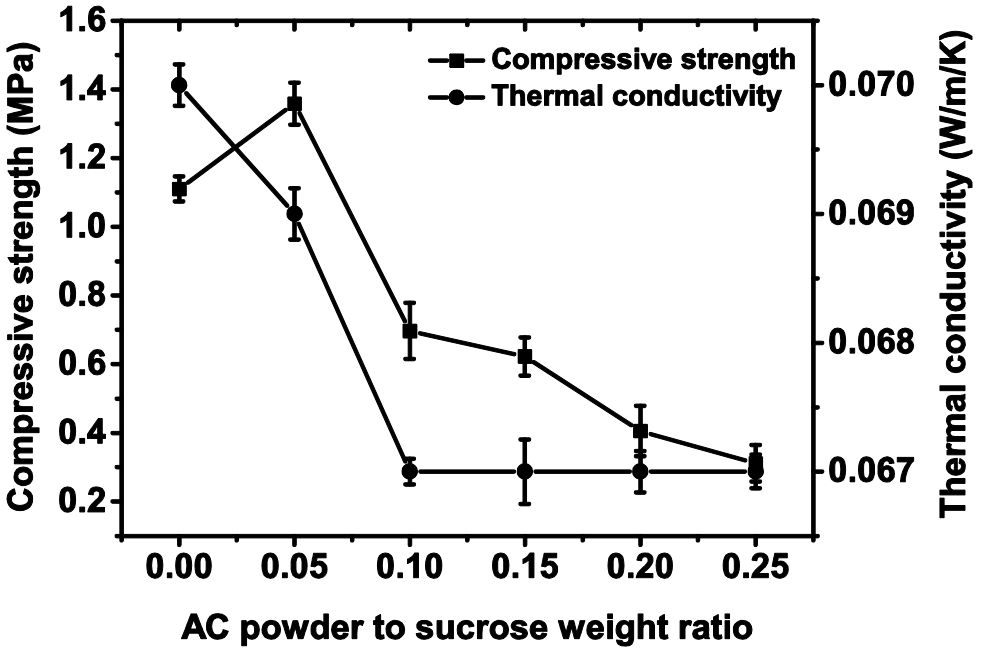

Figure 4.13: Compressive strength and thermal conductivity of the carbon composite foams prepared at various AC powder to sucrose weight ratios

4.3.4 Textural Properties and CO_2 Adsorption

Figure 4.14 (a) shows the N_2 adsorption-desorption isotherms of the AC powder and the carbon composite foams prepared at various AC powder to sucrose weight ratios. The AC powder shows considerable hysteresis in the sorption isotherm corresponding to a combination of Type I and Type IV isotherms whereas the carbon composite foams show Type-I isotherm (according to the IUPAC classification). The PSD calculated by using DFT assuming slit pore model is shown in Figure 4.14 (b). The AC powder shows a combination of micro and mesopores. The micropores in the AC powder have size between 10 and 20 Å. However, the carbon composite foams show only micropores that have size below 10 Å. This indicates that the molten sucrose seep into the mesopores and large micropores present in the AC powder, which are subsequently reduced to the micropores having size less than 10 Å during carbonization. The ultramicropore size measured from CO_2 adsorption shows a tri-model distribution with peaks nearly at 5.6, 7.9 and 8.7 Å as shown in Figure 4.15. The textural

properties of the AC powder and carbon composite foams are summarized in Table 4.4. The carbon foam prepared from molten sucrose alone shows surface area, total pore volume, micropore volume, and microporosity of 367 m^2/g, 0.18 cm^3/g, 0.12 cm^3/g, and 71 %, respectively. The carbon composite foams prepared from the AC powder dispersions show higher surface area, total pore volume and micropore volume and lower microporosity than that prepared from molten sucrose alone. However, the carbon composite foam prepared at an AC powder to sucrose weight ratio of 0.05 shows the highest surface area and pore volume and the finest micropores.

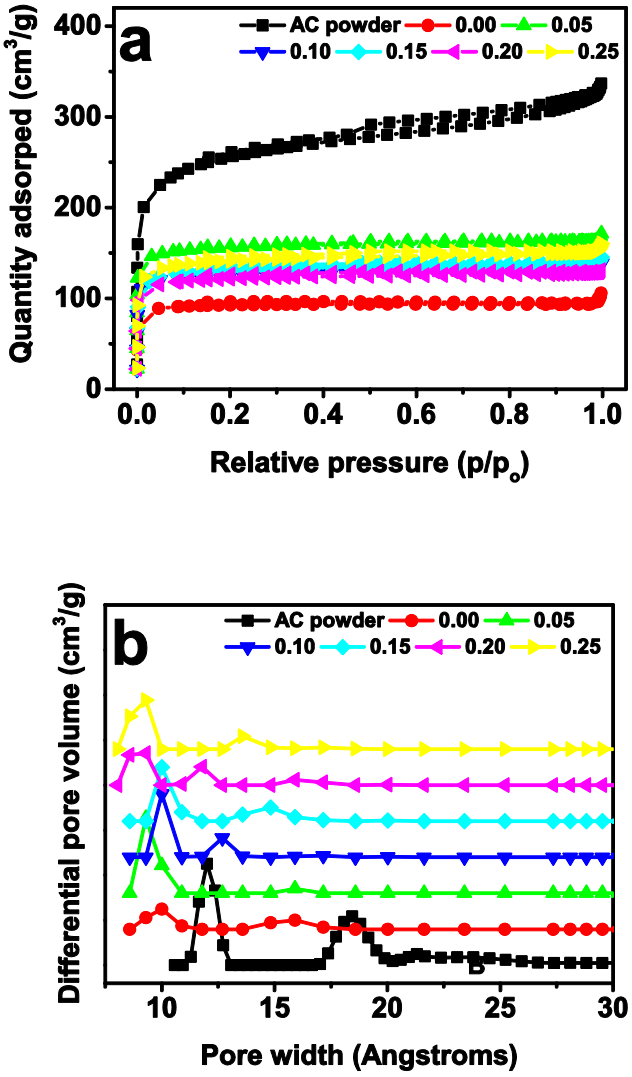

Figure 4.14: (a) N_2 adsorption-desorption isotherms and (b) DFT PSD of the carbon composite foams prepared at various AC powder to sucrose weight ratios

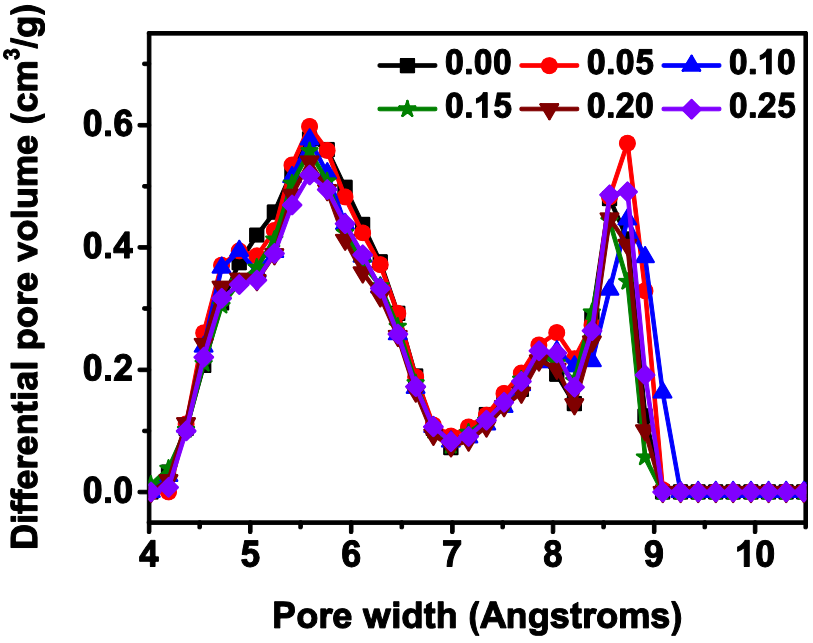

Figure 4.15: PSD plots of the carbon composite foams prepared at various AC powder to sucrose weight ratios using CO_2 adsorption at 0 °C

Table 4.4: Textural properties of the carbon composite foams

AC powder to sucrose weight ratio	BET (m^2/g)	V_{total}[a] (cm^3/g)	V_{micro}[b] (cm^3/g)	Microporosity (V_{micro}/V_{total})
0.00	367	0.1803	0.1171	71.53
0.05	527	0.2648	0.1949	73.62
0.10	429	0.2151	0.1533	71.26
0.15	446	0.2248	0.1524	67.76
0.20	455	0.2154	0.1532	71.12
0.25	480	0.2418	0.1606	66.43
AC powder	883	0.5155	0.1897	36.80

[a]Total pore volume from $p/p_o = 0.995$; [b]Micropore volume from t-plot

The mechanism of the micropore formation is same as the *in situ* activation explained in Chapter 2. Accordingly, the oxygen retained in the carbon structure, due to the –OH to –OH condensation, reacts with the carbon at higher temperatures to form CO molecules and produces the micropores. The surface

area values calculated from the char yield of sucrose (33 wt.%) and surface area of AC powder (883 m^2/g) and carbon foam without AC powder (367 m^2/g) are in the range of 390 to 560 m^2/g at the AC powder to sucrose weight ratios in the range of 0.05 to 0.25. The measured surface area values are lower than the calculated ones except at an AC powder to sucrose weight ratio of 0.05. This is due to the filling of large micropores and mesopores in the AC powder by the molten sucrose.

Figure 4.16 (a) and (b) show the CO_2 adsorption isotherms obtained at 25 and 0 ^oC, respectively, measured by volumetric method. The carbon composite foams prepared at the AC powder to sucrose weight ratios in the range of 0 to 0.25 show the CO_2 adsorption capacities in the range of 1.86 to 2.15 mmol/g at 25 ^oC. The adsorption capacity increases with a decrease in temperature and becomes in the range of 2.59 to 3.04 mmol/g at 0 ^oC. The exceptionally high CO_2 adsorption capacity of the carbon composite foam prepared at an AC powder to sucrose weight ratio of 0.05 at 0 ^oC is due to its fine micropore size. The pore filling, the prominent mechanism of CO_2 adsorption in microporous carbon at low temperatures, is more favoured in an adsorbent with the finest pore size. On the other hand, at 0 ^oC, the carbon composite foams adsorb 0.42 mmol/g of N_2 showing their selectivity of CO_2 adsorption over the N_2. The selectivity of CO_2 over N_2 adsorption, calculated from the linear portion of the isotherm shows a value of 14.6 (Figure 4.17 (a) and (b)).

The regeneration of the carbon composite foam sorbents is easy and energy efficient as desorption of CO_2 from the carbon composite foams takes place at a temperature of 50 ^oC as evidenced from the DSC studies. Figure 4.18 is a DSC graph showing the heat change during CO_2 adsorption and desorption as a function of temperature. The enthalpy of adsorption calculated from the DSC gives values close to 40 kJ/mol which is corresponding to the physical adsorption. The carbon composite foams do not show any decrease in CO_2 adsorption capacity after several adsorption-desorption cycles (Figure 4.19). The relatively

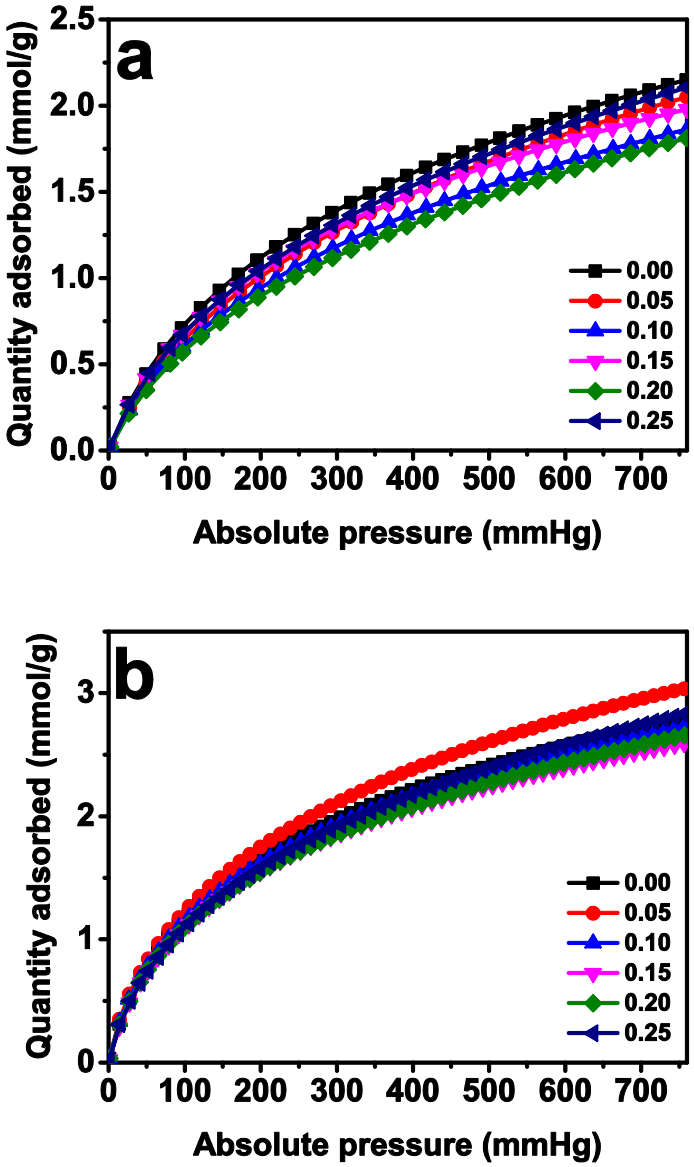

Figure 4.16: CO_2 adsorption isotherms at (a) 25 ^oC and (b) 0 ^oC of the carbon composite foams prepared at various AC powder to sucrose weight ratios

high adsorption capacity and very good selectivity and recyclability coupled with the demonstrated capability to prepare large carbon composite foam bodies (Figure 4.10) from molten sucrose and AC powder can pave the way for the development of carbon foam based CO_2 scrubber systems.

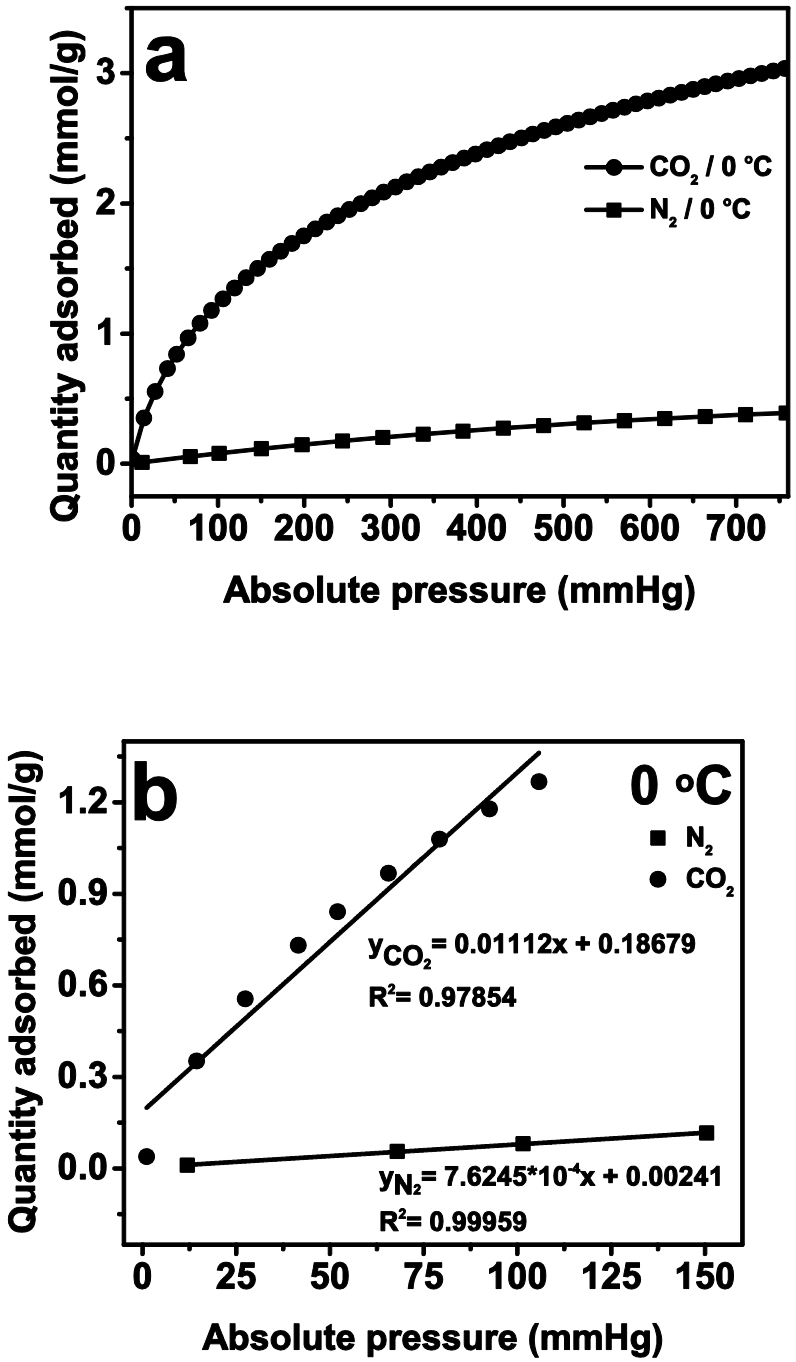

Figure 4.17: (a) CO_2 and N_2 isotherms at 0 ^oC showing the selectivity of the carbon composite foam (AC powder to sucrose weight ratio - 0.05) and (b) Initial slope calculation for CO_2 and N_2 isotherms at 0 ^oC of the carbon composite foam prepared at an AC powder to sucrose weight ratio of 0.05

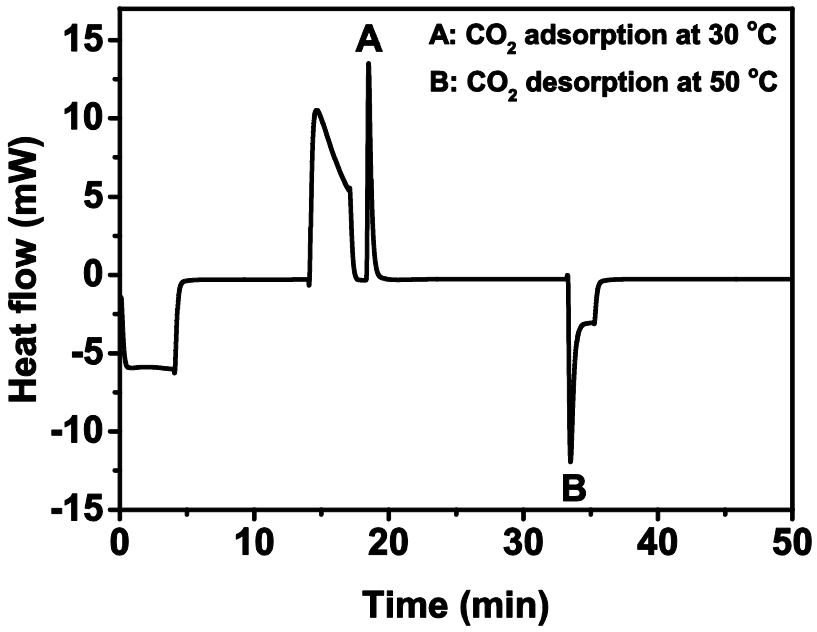

Figure 4.18: Typical DSC graph of CO_2 adsorption and desorption using carbon composite foam (AC powder to sucrose weight ratio – 0.05)

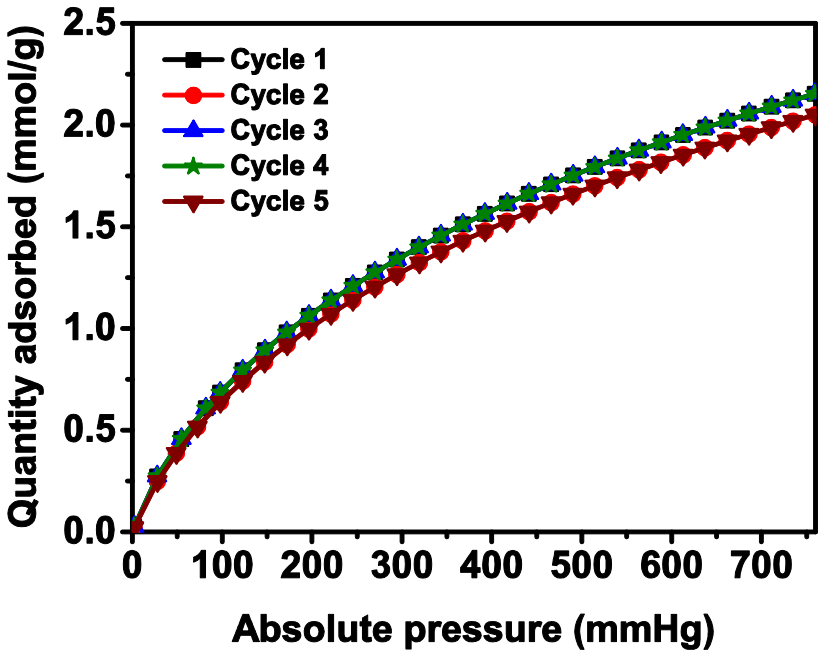

Figure 4.19: CO_2 adsorption at 25 ^oC showing the recyclability of the carbon composite foam (AC powder to sucrose weight ratio - 0.05)

4.3.5 Oil Absorption

The carbon composite foams prepared from the AC powder dispersions absorb oil phase from water-oil mixtures indicating their hydrophobic nature. The oil absorption capacity of the carbon composite foams, studied using toluene, increases with an increase in the AC powder to sucrose weight ratio (Figure 4.20 (a)). The carbon composite foams prepared at the AC powder to sucrose weight ratios in the range of 0 to 0.25 absorb 290 to 430 wt.% of toluene. The carbon composite foams hold the oil phase inside the cells. The cells with rough walls have the capacity to retain more oil phase compared to the one with smooth walls. The increase in oil absorption capacity is due to the increase in surface roughness due to the increase in concentration of AC particles on the cell wall surfaces as evidenced in higher magnification images as shown in Figure 4.21. The absorption capacity of carbon composite foam prepared at an AC powder to sucrose weight ratio of 0.25 towards various organic solvents is shown in Figure 4.22 (b). The oil absorption capacity increases with an increase in density and viscosity of the organic solvents as reported by (Wang et al., 2013).

Separation of oil phase from wastewater containing emulsified oil, generated in petrochemical, food, textile, leather, steel, and metal finishing industries, before disposal is very important because they are harmful to the environment (Chen et al., 2009; Gui et al., 2013; Shi et al., 2013; Yang et al., 2013; Zeng et al., 2014; Zhang et al., 2013). Separation of oil phase from surfactant stabilized emulsions got the recent attention because the traditional techniques such as oil skimmers, centrifuges, coalescers, settling tanks, magnetic separations, and flotation technologies are useful for the separation of immiscible oil/water mixtures, but are not effective for emulsified oil-water mixtures. The carbon composite foams prepared from the AC powder dispersions in molten sucrose absorb oil phase from the surfactant stabilized oil-in-water emulsions. Figure 4.22 is a photograph showing the surfactant stabilized 10/90 toluene-in-

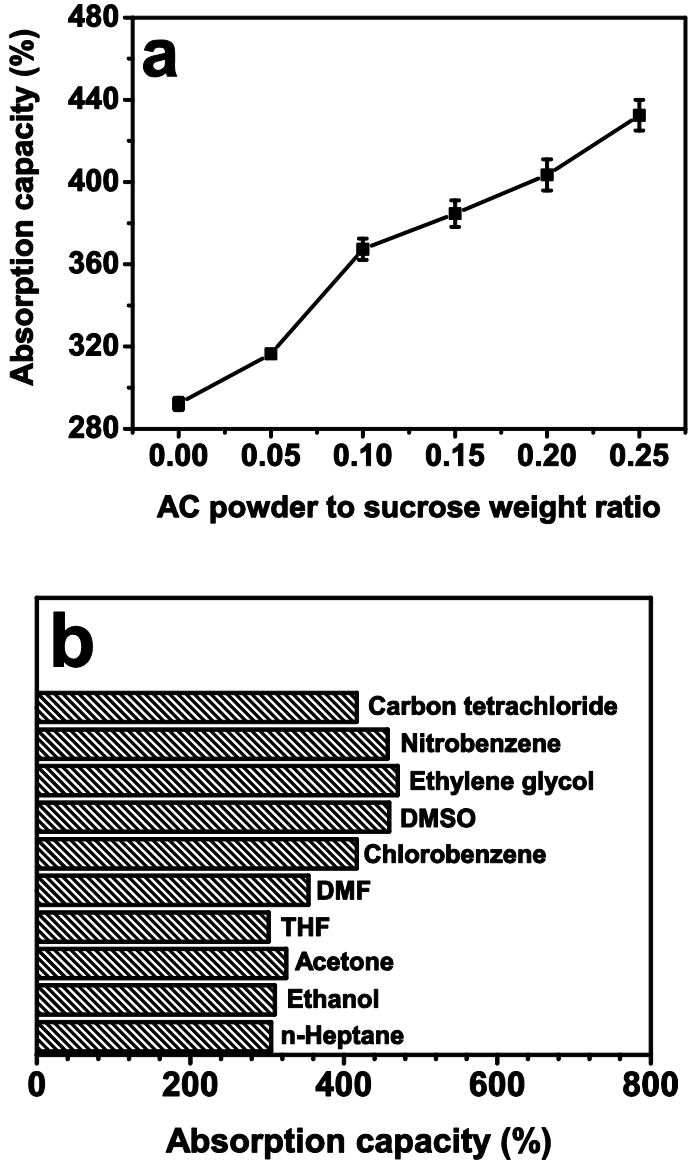

Figure 4.20: (a) Toluene absorption capacity of carbon composite foams prepared at various AC powder to sucrose weight ratios and (b) absorption of various organic solvents on the carbon composite foam prepared at an AC powder to sucrose weight ratio of 0.25

water emulsion with and without a carbon composite foam after two hours. The complete separation of toluene from the 100 ml of 10/90 toluene-in-water emulsion takes nearly 2 h upon the addition of 5 g of carbon composite foams prepared at an AC powder to sucrose weight ratio of 0.25. The carbon composite foams used for oil absorption from oil-in-water emulsion can be easily regenerated by heating at 400 ^{o}C in a N_2 atmosphere. The oil absorption capacity

of the foam remains unchanged even after several absorption-regeneration cycles (Figure 4.23)

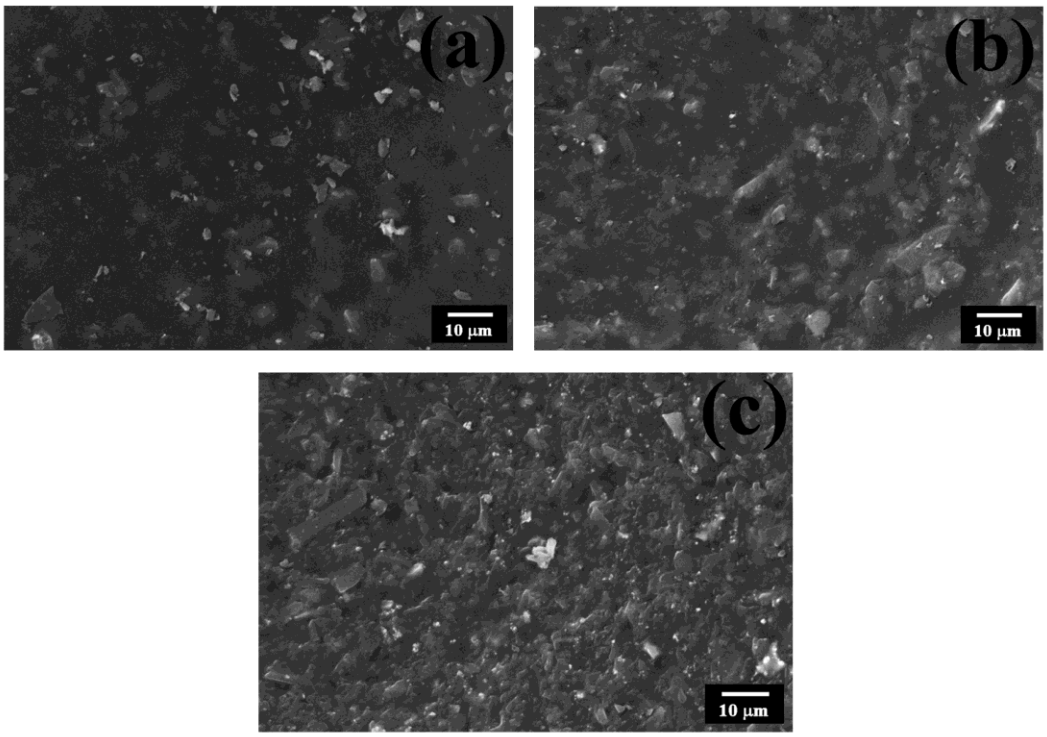

Figure 4.21: SEM photomicrographs of the carbon composite foam cell wall surfaces prepared at the AC powder to sucrose weight ratios of (a) 0.05, (b) 0.15 and (c) 0.25

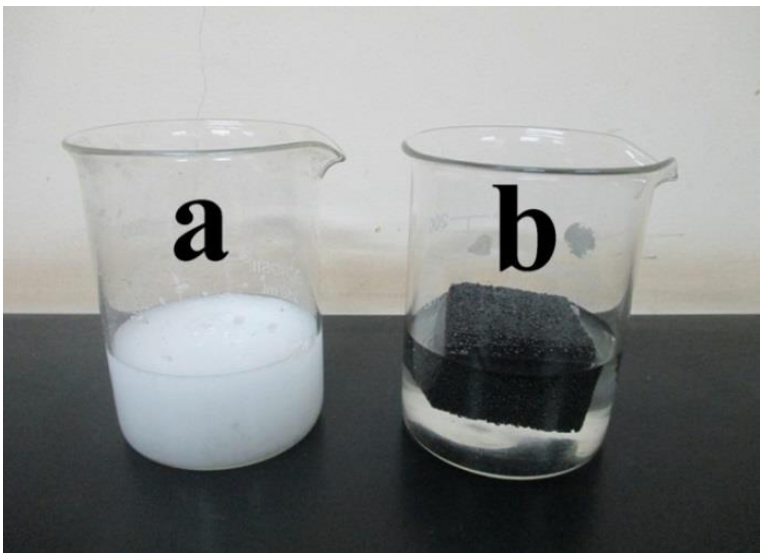

Figure 4.22: Photograph of the surfactant stabilized emulsion (a) without and (b) with the carbon composite foam after 2 h

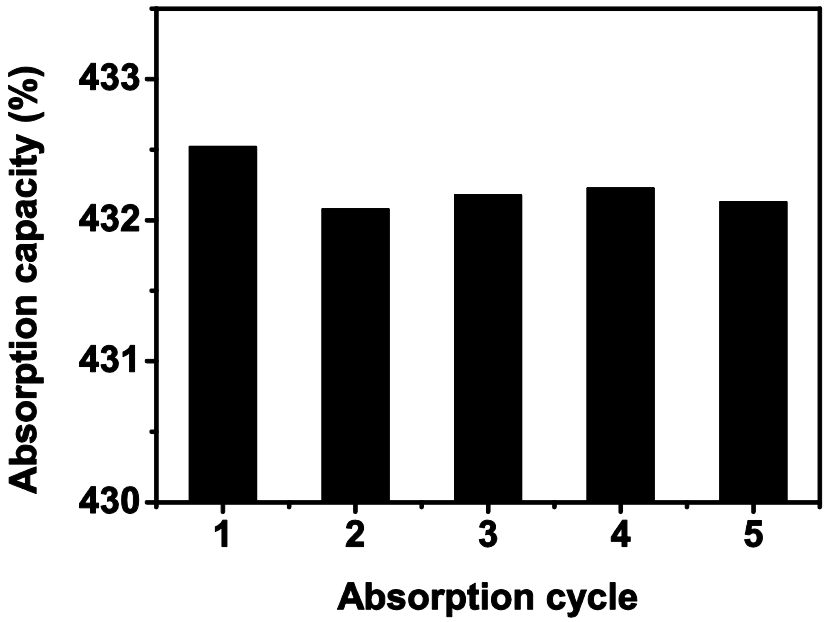

Figure 4.23: Toluene absorption – regeneration cycles of the carbon composite foam prepared at an AC powder to sucrose weight ratio of 0.25

4.4 Conclusions

The carbon composite foams are prepared by the thermo-foaming of AC powder dispersions in molten sucrose followed by dehydration and carbonization. The interaction between sucrose molecules and the dispersed AC particles interrupt the intermolecular hydrogen bonding in molten sucrose as evidenced from the viscosity decrease of molten sucrose upon the addition of AC powder. The dispersed AC powder has multiple roles as it induces the foaming by stabilizing the bubbles by adsorbing on the molten sucrose-gas interface, accelerates the foaming and foam setting by catalyzing the –OH to –OH condensation and increases the char yield. The density, cell size, compressive strength, and thermal conductivity of the carbon composite foams depend on the AC powder to sucrose weight ratio. The carbon composite foams have a hierarchical pore structure with interconnected macro cells made up of carbon containing micropores. The carbon composite foams show relatively high (2.59 to 3.04 mmol/g) CO_2 adsorption capacity with very good CO_2/N_2 selectivity and excellent recyclability. The carbon composite foams selectively absorb oil phase

from oil-water mixtures and surfactant stabilized oil-in-water emulsion. The oil absorption capacity increases with an increase in AC powder to sucrose weight ratio.

CHAPTER 5

PROCESSING AND CHARACTERIZATION OF CARBON COMPOSITE FOAMS FROM MOLTEN SUCROSE AND CARBON FIBER

5.1 Introduction

Various reinforcements like natural graphite particles, clay particles, carbon black, carbon nanofibers, CNT, graphene, carbon fibers, etc. are used to improve the mechanical properties of the carbon foams (Fawcett and Shetty, 2010; Harikrishnan et al., 2007; Li et al., 2007b; Li et al., 2010a, c, 2011c; Luo et al., 2011a; Wang et al., 2008a; Wang et al., 2010; Wang et al., 2009b; Wu et al., 2011; Wu et al., 2009; Zhu et al., 2007). The reinforcements are added to the precursor resins prior to their foaming or impregnation on the polymer foam template. The mechanical properties of the carbon foams prepared from molten sucrose using aluminium nitrate, and boric acid blowing agent are relatively low. Incorporation of AC powder in molten sucrose produced carbon composite foams with improved mechanical strength. The maximum compressive strength achieved is only 1.36 MPa. However, carbon foams with high compressive strength are desirable for many applications.

Carbon fibers are widely used as reinforcing agents in polymer, ceramic, metal and carbon matrix composites due to their high strength and modulus, low thermal expansion, low cost and high electrical conductivity (Morgan, 2005). The composite properties depend on the size, orientation and loading of the carbon fiber (Morgan, 2005). There are few reports on the carbon fiber reinforced carbon foams prepared from the carbon precursors like phenolic resin and pitches (Fawcett and Shetty, 2010; Li et al., 2010c; Miller et al., 2010b; Wang et al., 2009b; Wu et al., 2009). The present chapter reports the preparation of carbon

fiber reinforced carbon composite foams from sucrose and milled carbon fiber. The effect of average fiber length and fiber loading on the mechanical strength of carbon composite foams is studied.

5.2 Experimental

5.2.1 Preparation of the Carbon Fiber Reinforced Carbon Composite Foams

Sucrose and acetone used were analytical reagent grade and procured from Merck (India), Mumbai. Polyacrylonitrile (PAN) based milled carbon fiber used was purchased from Zoltex (Germany). The average length and diameter of the carbon fiber were 300 and 7.2 μm, respectively. The SEM photomicrograph of the as received carbon fiber is shown in Figure 5.1.

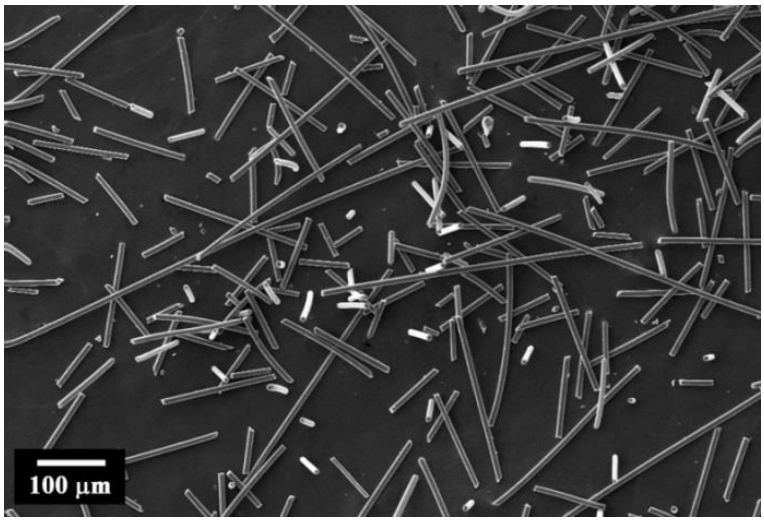

Figure 5.1: SEM photomicrograph of the as received carbon fibers

Figure 5.2 shows the flow chart of the preparation of carbon composite foams. Sucrose was mixed with various weight percentages of carbon fiber and ball milled in acetone medium in a planetary ball mill for various time periods in the range of 0.5 to 3 h to reduce the carbon fiber length and to achieve proper mixing. The sucrose to acetone and sucrose to zirconia balls weight ratios used were 1:3 and 1:10, respectively. The ball milling speed used was 200 RPM. The

slurries obtained after ball milling was dried in an air oven at 80 ^{o}C. For the preparation of carbon composite foams with 300 μm carbon fiber, the sucrose was ball milled for 1 h at the above mentioned conditions and the resulting slurry was mixed with the as received carbon fiber using a mechanical stirrer. The sucrose-carbon fiber mixtures were heated at 170 ^{o}C in a glass tray to melt the sucrose. The sucrose melt was stirred well with a glass rod to achieve uniform dispersion of the carbon fiber. The molten sucrose containing dispersed carbon fiber was heated in an air oven at 140 ^{o}C for foaming and foam setting. The solid organic foams thus obtained were dehydrated at 200 ^{o}C for 3 h at a heating rate of 2 ^{o}C/h. The dehydrated foams were carbonized at 900 ^{o}C for 2 h in a high-pure argon atmosphere. The heating rate used was 2 ^{o}C/min. The density of the carbon composite foams was calculated from their weights and dimensions.

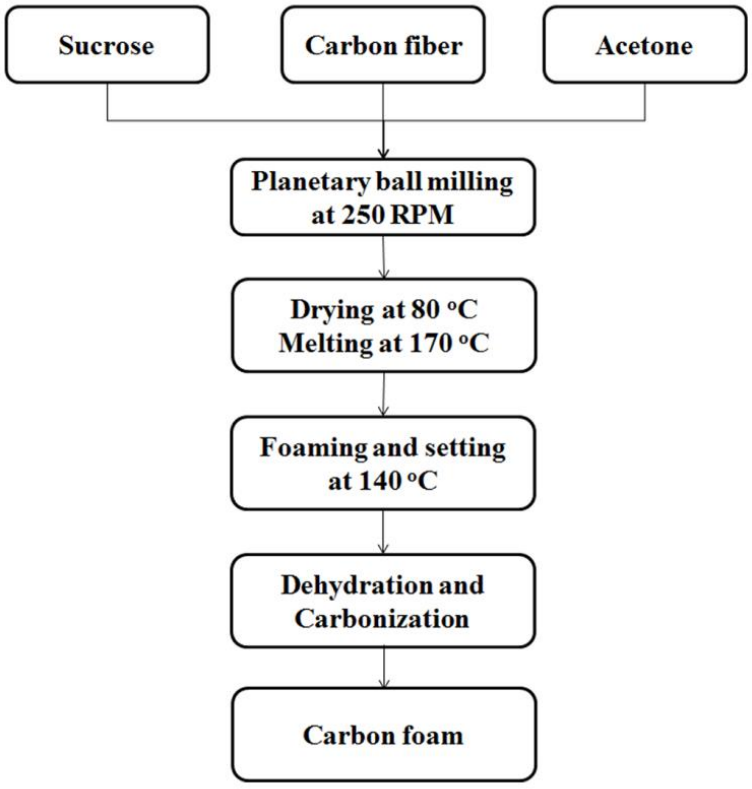

Figure 5.2: Flow chart for the preparation of carbon fiber reinforced carbon composite foams

5.2.2 Fiber Length Measurements

The sucrose-carbon fiber mixture samples obtained after ball milling were stirred with water to dissolve the sucrose and to disperse the carbon fiber. The carbon fiber suspensions in water were drop-casted on glass slides and observed under an optical microscope (Leica DM2700, Germany). The average fiber length was measured from the optical images using the ImageJ software.

5.2.3 Characterization

The viscosity measurement of the carbon fiber dispersions in molten sucrose was carried out at various shear rates in the range of 1 to 100 s^{-1} at 140 ^{o}C using a Rheometer (MCR 102 Modular Compact Rheometer, Anton Paar, USA) with a cone and plate measurement system. The microstructure of the carbon composite foams was observed using a Scanning Electron Microscope (SEM, FEI Quanta FEG200). The cell size was measured using ImageJ software from the SEM microstructure. The compressive strength of the carbon composite foams was measured using a universal testing machine (Instron 5050, Instron USA) at a crosshead speed of 0.5 mm/min with 25 mm x 25 mm x 12 mm samples (ASTM standard C365/C365M-05). The maximum stress in the stress-strain graph was taken as the compressive strength. The thermal conductivity of the carbon composite foam samples was measured using modified transient plane source method (MTPS) at room temperature. The 20 mm x 20 mm x 6 mm samples were used for the thermal conductivity measurements. The reported thermal conductivity is the average of four measurements.

5.3 Results and Discussion

The viscosity at various shear rates of the carbon fiber dispersed molten sucrose measured at 140 ^{o}C is shown in Figure 5.3. The average length of fibers used in this measurement is 300 μm. The molten sucrose without carbon fiber

shows the viscosities in the range of 2.8 to 2.34 Pa.s at shear rates in the range of 1 to 100 s^{-1}. The viscosity and shear thinning nature of the carbon fiber dispersed molten sucrose increase with an increase in the fiber concentration. The viscosity measured at a shear rate of 10 s^{-1} increases from 2.44 to 3.51 Pa.s when the fiber concentration increases from 0 to 6 wt.%. This is due to the increase in agglomeration of carbon fiber by fiber bridging with an increase in fiber concentration. The foaming of carbon fiber dispersed molten sucrose is completed at ~ 48 h and foam setting is completed at ~ 96 h, irrespective of the carbon fiber concentrations. That is, the carbon fiber does not influence the foaming and setting of molten sucrose. This is attributed to the relatively small number of surface functional groups due to the low surface area (30 m^2/g) of carbon fiber.

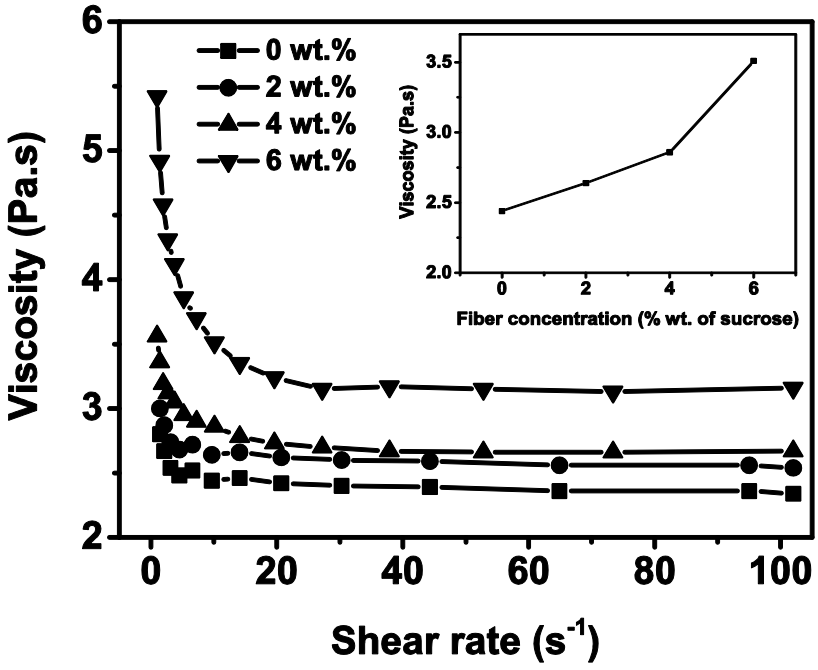

Figure 5.3: Effect of fiber concentration on the shear rate vs viscosity of the carbon fiber dispersions in molten sucrose at 140 °C (average carbon fiber length of 300 μm). Inset shows the effect of fiber concentration on the viscosity at the shear rate of 10 s^{-1}

Figure 5.4 shows the TGA of the solid organic foams prepared at carbon fiber concentrations of 0 and 4 wt.%. The decomposition onset temperatures of the solid organic foams containing 0 and 4 wt.% carbon fiber are 155 and 141 °C, respectively. The solid organic foams prepared without carbon fiber and with 4

wt.% carbon fiber show the peaks at 277 and 262 °C, respectively, in the DTG. This indicates that the incorporation of carbon fiber has negligible effect on the thermal decomposition of the solid organic foams. However, the solid organic foams prepared without carbon fiber and with 4 wt.% carbon fiber produce 24 and 26.3 wt.% char residue, respectively, at 900 °C. The increase in char residue is due to the contribution from the carbon fiber.

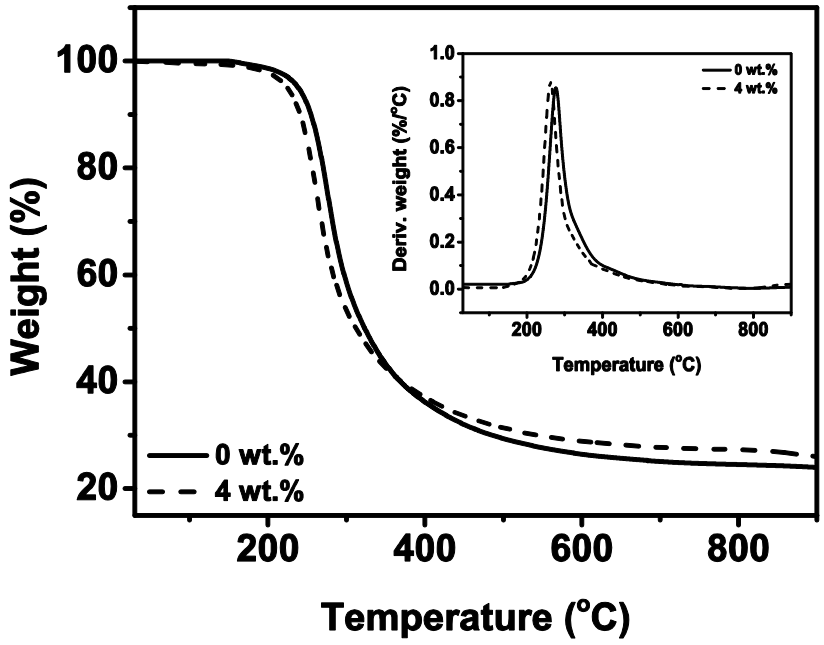

Figure 5.4: TGA and DTG of the solid organic foams prepared at carbon fiber concentrations of 0 and 4 wt.%

The solid organic foams of 8 cm x 6 cm x 3 cm size prepared at various carbon fibers loading did not show any crack or deformation during dehydration and carbonization. The solid organic foam prepared without carbon fiber shows a total shrinkage of 67 vol.% during dehydration and carbonization. The total volume shrinkage decreases from 67.1 to 53.5 % when the fiber concentration increases from 0 to 6 wt.% of sucrose (Table 5.1). This indicates that the carbon fiber network resists the shrinkage of solid organic foams during carbonization. On the other hand, the local shrinkage of sucrose polymer within the fiber network is expected. This leaves a large amount of porosity in the struts and cell walls.

Table 5.1: Total volume shrinkage of solid organic foams prepared at various carbon fiber concentrations (average carbon fiber length: 300 μm)

Carbon fiber concentration (wt.% of sucrose)	0	2	4	6
Volume shrinkage (%)	67.1	65.4	56.9	53.5

The carbon composite foam prepared from molten sucrose without the carbon fiber has a density of 0.19 g/cm^3. The density of the carbon composite foams prepared using the as received carbon fiber of average length 300 μm decreases from 0.19 to 0.16 g/cm^3, when the carbon fiber concentration increases from 0 to 6 wt.% of the sucrose. The compressive strength and specific compressive strength of the carbon composite foams also decrease with an increase in fiber concentration. This indicates that there is no reinforcement effect at the average carbon fiber length of 300 μm. The density, compressive strength and specific compressive strength of carbon composite foams as a function of carbon fiber concentration are shown in Figure 5.5. The decrease in density and strength with an increase carbon fiber concentration is the result of fiber agglomeration by the bridging of longer fibers (Wang et al., 2009b). The carbon foam without the carbon fiber shows the spherical cellular structure whereas there is a large distortion from the spherical cell morphology in the carbon composite foams as evidenced from the SEM microstructures shown in Figure 5.6. The carbon foam without the carbon fiber shows the well-defined struts with an average thickness of 121 μm. Generally, the cell wall thickness will be much lower than the strut thickness. This indicates that the strut and cell walls of the carbon composite foam cannot accommodate the 300 μm long carbon fiber in the thickness direction. The carbon fibers are either embedded on the cell wall surfaces or protruded out from the cell wall surfaces. Moreover, the struts are not well formed in the composite foams due to the fiber agglomeration. The agglomeration of carbon fibers in the strut region of the carbon composite foam is evidenced from the SEM image at high magnification (Figure 5.6 (d)). It is well-known that the strength of brittle foams depends on the strut region (Gibson and Ashby, 1997). A thick and dense strut region is always desirable to achieve high

mechanical strength. However, the fiber agglomeration produces additional pores in the strut region as evidenced from the high magnification image of the composite foams. The extent of fiber agglomeration increases with an increase in fiber concentration that result in an increased porosity in struts which is mainly responsible for the decrease in density and compressive strength of the carbon composite foams prepared at an average fiber length of 300 μm.

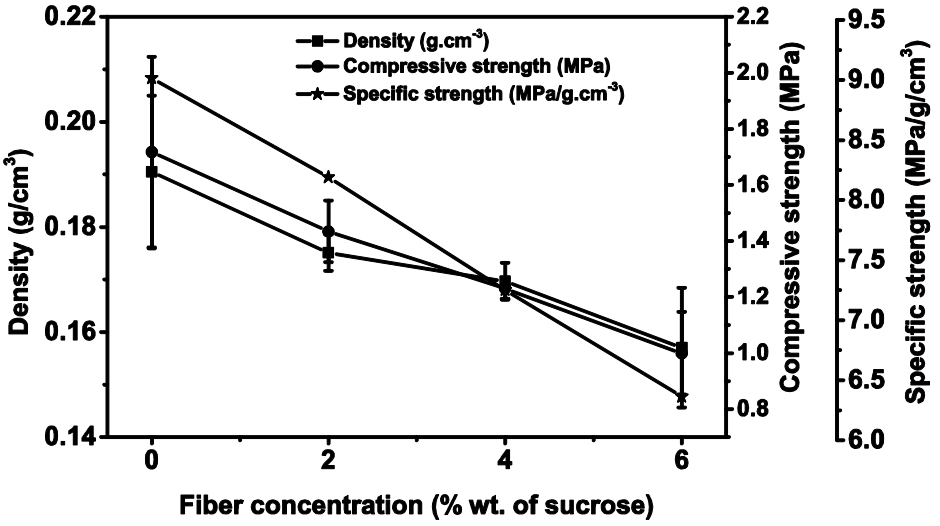

Figure 5.5: Effect of fiber concentration on density, compressive strength and specific strength of the carbon composite foams at average carbon fiber length of 300 μm

5.3.1 Effect of Fiber Length on the Properties of Carbon Composite Foams

As the incorporation of carbon fiber with an average length of 300 μm results in decrease of density and compressive strength of carbon composite foams due to extensive fiber agglomeration, the fiber length is decreased by planetary ball milling of sucrose-carbon fiber mixtures. Figure 5.7 is the optical micrographs of carbon fiber showing the decrease in fiber length with ball milling time. The average fiber length decreases from 300 to 15 μm when the ball milling time increases from 0 to 3 h. The effect of milling time on average fiber length of carbon fiber is shown in Figure 5.8.

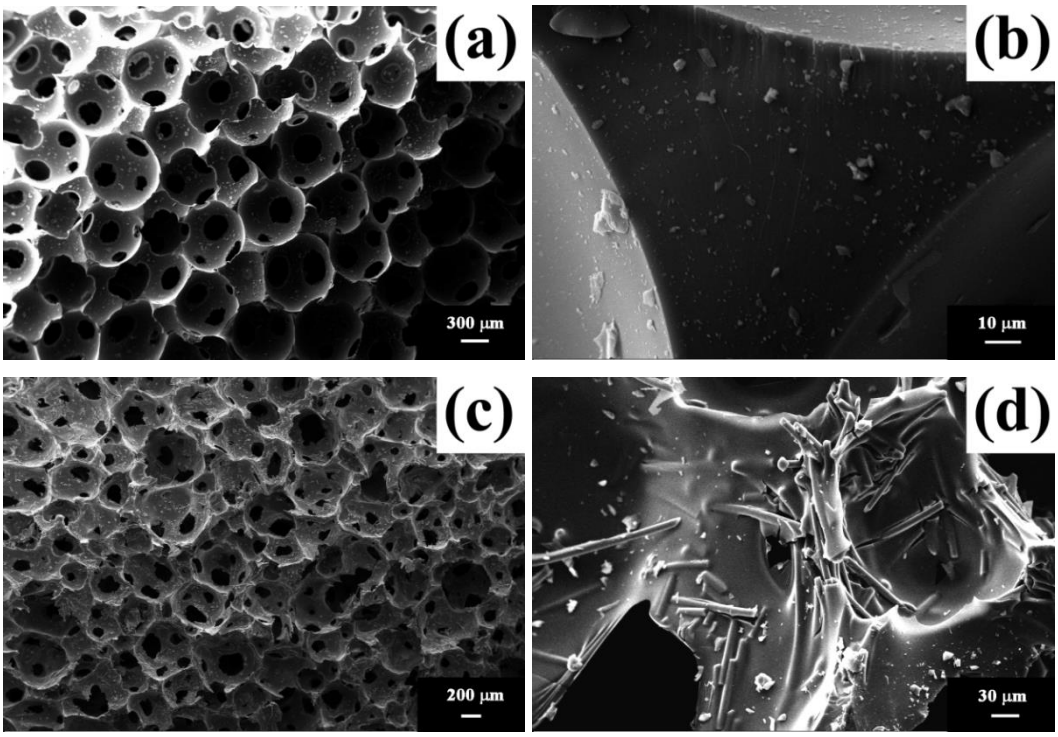

Figure 5.6: SEM microstructure of the carbon foams: (a) and (b) without carbon fiber showing the spherical cells and well defined nonporous strut, (c) and (d) with 4 wt.% carbon fiber of length 300 μm showing distorted cells and porous struts due to fiber agglomeration

Figure 5.9 shows the effect of fiber length on viscosity of carbon fiber dispersions in molten sucrose at a fiber concentration of 4 wt.% of sucrose. There is a drastic decrease in viscosity when the average fiber length decreases from 300 to 70 μm. Further decrease in the fiber length produces only a marginal decrease in the viscosity. This indicates that the extent of agglomeration by fiber bridging decreases with a decrease in average fiber length. This is further evidenced from the increase in total volume shrinkage of solid organic foams with a decrease in average fiber length (Table 5.2). The total volume shrinkage of solid organic foams prepared at a fiber concentration 4 wt.% of sucrose increases from 56.9 to 67.5 % when the average fiber length decreases from 300 to 15 μm.

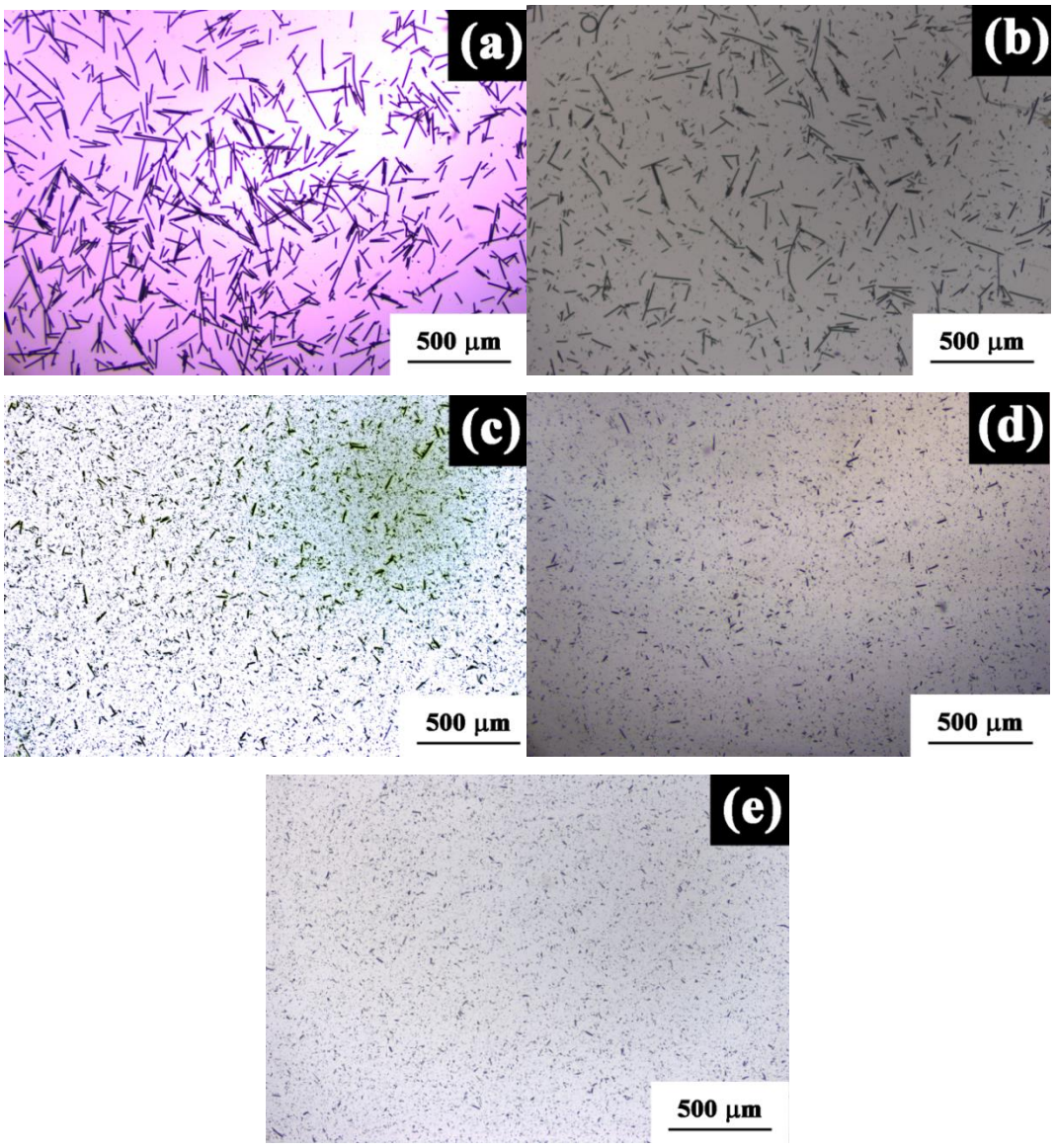

Figure 5.7: Optical micrographs of carbon fibers showing the decrease in fiber length with ball milling time (a – 0 h; b – 0.5 h; c – 1.5 h; d – 2.5 and e – 3 h)

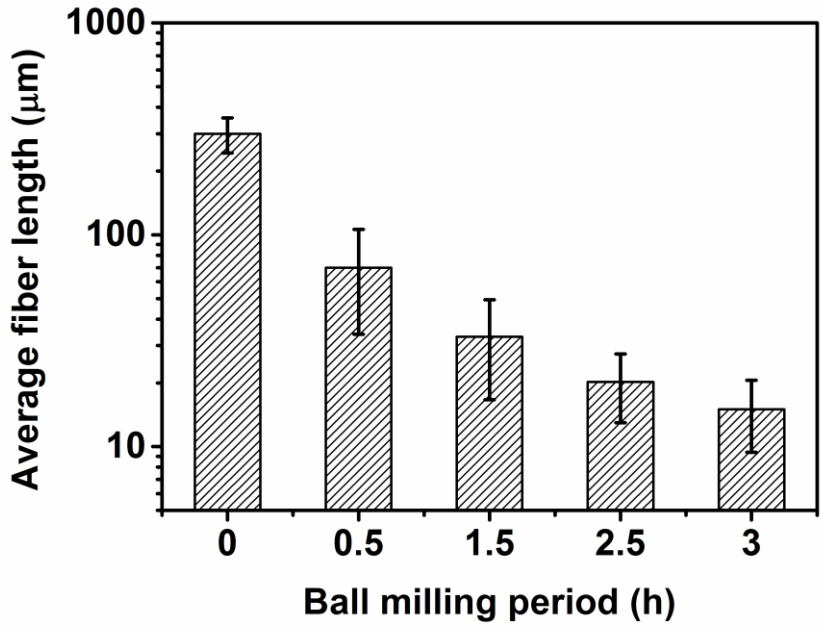

Figure 5.8: Effect of milling time on the average length of carbon fiber

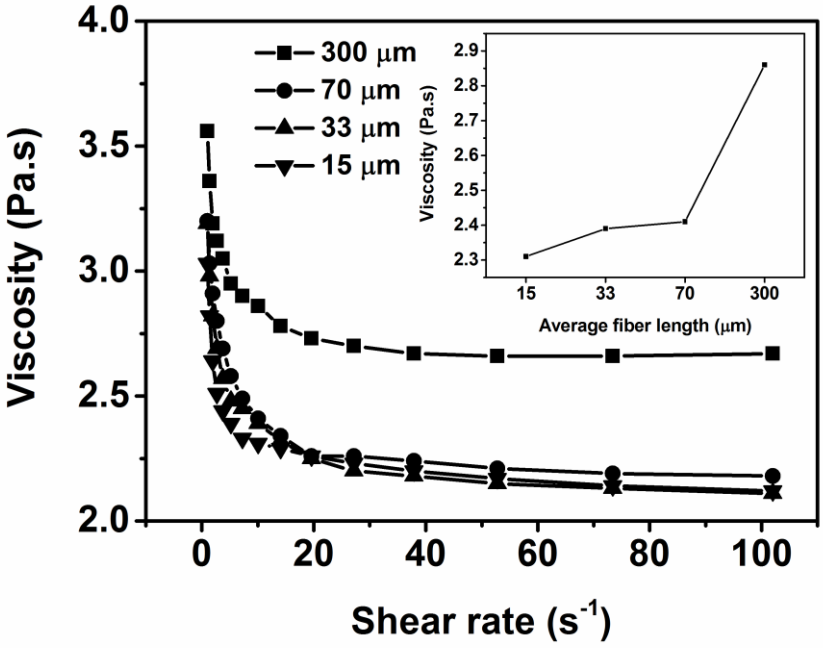

Figure 5.9: Effect of fiber length on the shear rate vs. viscosity of the carbon fiber dispersed molten sucrose measured at 140 ^{o}C. Inset shows the average fiber length vs. viscosity (carbon fiber concentration – 4 wt.% of sucrose)

Table 5.2: Total volume shrinkage of solid organic foams prepared at various average carbon fiber length (fiber concentration: 4 wt.% of sucrose)

Average fiber length (μm)	300	70	33	20	15
Volume shrinkage (%)	56.9	62.5	66	66.4	67.5

The density of carbon composite foam prepared at 4 wt.% carbon fiber concentration using carbon fiber of various average fiber length is given in Table 5.3. The density of the carbon composite foams increases from 0.17 to 0.23 g/cm^3 when the average fiber length decreases from 300 to 15 μm. This is due to decrease in the fiber agglomeration with a decrease in fiber length. The carbon composite foams prepared at carbon fiber lengths in the range of 70 to 15 μm show near spherical cells. The composite foams at these fiber lengths have well-formed and dense struts indicating the absence of fiber agglomeration due to fiber bridging. Moreover, the carbon fibers are not protruded out from the cell wall surfaces at lower fiber lengths. Figure 5.10 shows the microstructure of carbon composite foam prepared at carbon fiber of average length 33 μm showing the near-spherical cells and high magnification image showing the well-defined non-porous strut and cell wall surface. The cell size of the carbon foam composite also depends on the average carbon fiber length. The cell size decreases from 0.69 to 0.38 mm when the average carbon fiber length decreases from 300 to 33 μm and then increases marginally with further decrease in carbon fiber length (Table 5.3). This is attributed to the decrease in bubble stability due to the decrease in viscosity of the carbon fiber dispersions in molten sucrose.

Figure 5.11 (a) shows the stress-strain curves of carbon foams with different fiber length at fiber concentration 4 wt.% of sucrose. The stress-strain curves show a typical behavior of the elastic, rigid, solid foam with an initial linear elastic region followed by a stress maximum and finally a densification region. The compressive strength of the composite foams increases from 1.23 to

.

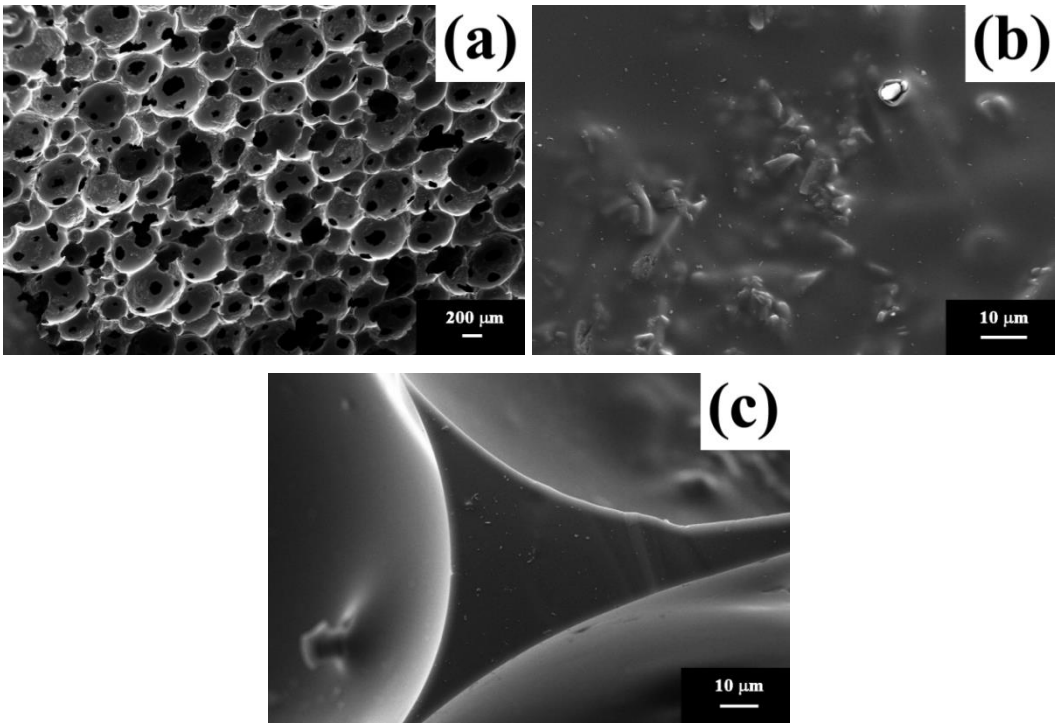

Figure 5.10: SEM microstructures of carbon composite foam containing 4 wt.% 33 μm carbon fiber (a) cell structure (b) cell wall and (c) well-defined non-porous strut

Table 5.3: Effect of fiber length on the carbon composite foam properties

Carbon fiber length (μm)	300	70	33	20	15
Density (g/cm^3)	0.169	0.196	0.219	0.223	0.232
Cell size (mm)	0.67 ± 0.11	0.52 ± 0.08	0.38 ± 0.05	0.45± 0.04	0.43± 0.06

3.11 MPa when the average fiber length decreases from 300 to 33 μm. A further decrease in the fiber length decreases the compressive strength of the composite foams. The composite foams prepared at fiber length of 20 and 15 μm show the compressive strength of 2.67 and 2.60 MPa, respectively. The study suggests that maximum reinforcement is achieved at a fiber length of 33 μm, which is obtained by ball milling sucrose-carbon fiber mixture for 1.5 h, due to effective matrix to fiber stress transfer. The effect of fiber length on compressive strength of the carbon composite foams prepared at carbon fiber concentration 4 wt.% of sucrose

is shown in Figure 5.11 (b). It is worthy to note that the maximum compressive strength is obtained at carbon fiber length much lower than the strut thickness. The fiber length lower than the strut and cell wall thickness enables the carbon fiber to disperse uniformly and orient in all possible directions without fiber bridging and protruding out from the cell wall surface. However, at an average fiber length lower than 33 μm, the carbon fiber acts more like particles because the aspect ratio is only in the range of 2 to 3 that decreases the effectiveness of stress transfer resulted in a decrease in compressive strength of the composite foams.

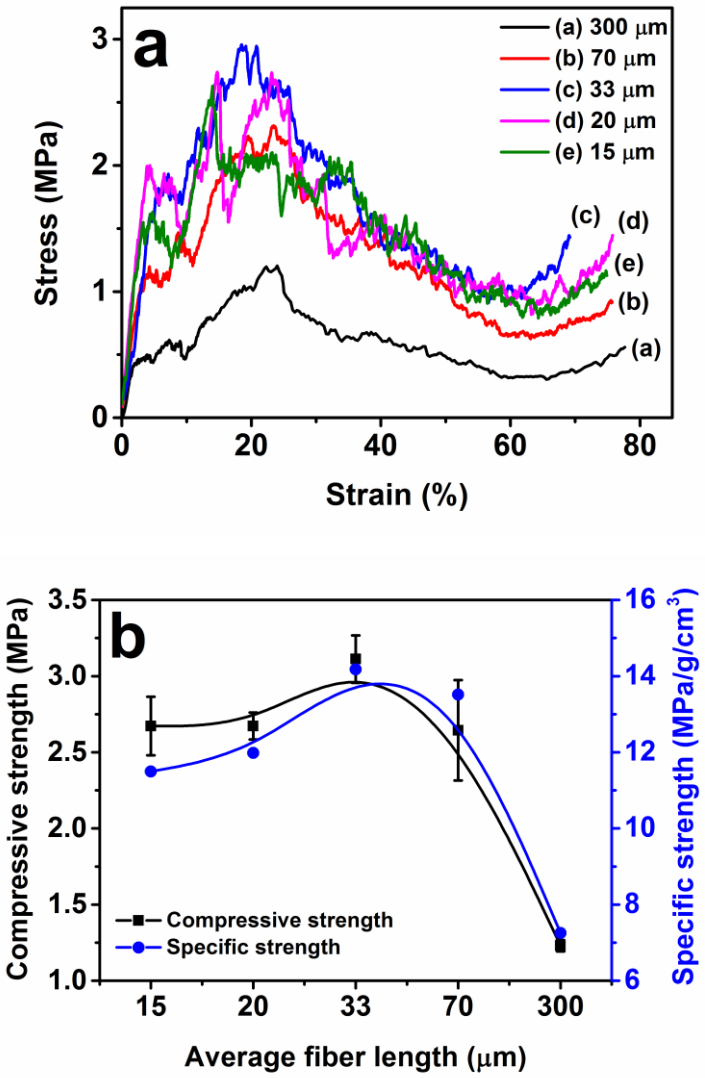

Figure 5.11: (a) Stress-strain graph and (b) compressive strength and specific strength of the carbon composite foams prepared at various average carbon fiber lengths

5.3.2. Effect of the Fiber Loading on the Properties of the Carbon Composite Foams

The effect of fiber loading on properties of carbon composite foams is studied at the optimum average fiber length of 33 μm (milling time - 1.5 h). The density of the carbon composite foams increases from 0.19 to 0.22 g/cm^3, when the fiber concentration increases from 0 to 2 wt.% of sucrose. A further increase in fiber concentration does not produce much variation in the foam density. On the other hand, the cell size decreases from 0.89 to 0.38 when the carbon fiber concentration increases from 0 to 2 wt.%. A further increase in carbon fiber concentration does not make much change in the cell size. The effect of carbon fiber concentration on the density and cell size of the composite foam is shown in Figure 5.12.

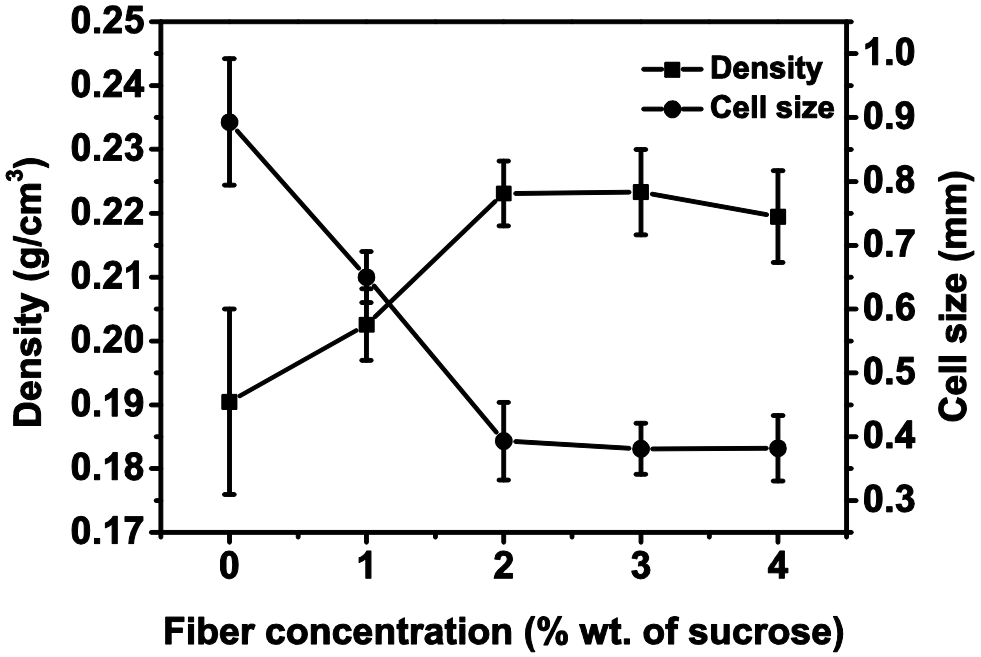

Figure 5.12: Effect of carbon fiber concentration on density and cell size of carbon foam composites at carbon fiber length of 33 μm

The effect of carbon fiber concentration on the compressive strength and specific strength of the carbon composite foams prepared at the fiber length of 33

μm is shown in Figure 5.13. The compressive strength of the carbon composite foams increases with an increase in the carbon fiber concentration up to 2 wt.% of sucrose. A further increase in the carbon fiber concentration decreases the compressive strength of the carbon composite foams. The maximum compressive strength obtained is 3.86 MPa. This corresponds to an increase of 125% from carbon foam without carbon fiber reinforcement. It is well-known that the solid organic foam prepared from molten sucrose retain nearly 25 wt.% carbon during pyrolysis. This indicates that the sucrose-carbon fiber mixture with a carbon fiber concentration in the range of 1 to 4 wt.% of sucrose produces carbon composite foams with a carbon fiber concentration in the range of 4 to 16 wt.% of the carbon matrix. That is, the maximum compressive strength of the carbon composite foam is achieved at a fiber concentration ~ 8 wt.% of the carbon matrix.

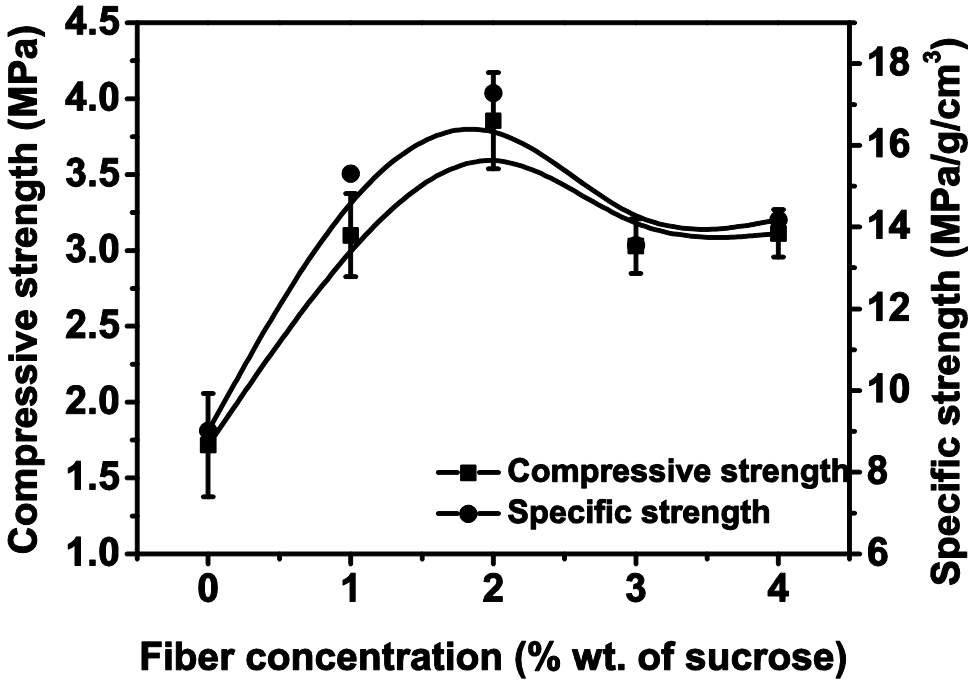

Figure 5.13: Effect of carbon fiber concentration on compressive strength and specific strength of the carbon composite foams at a carbon fiber length of 33 μm

It is well-known that the compressive strength of a brittle foam material increases with an increase in foam density and a decrease in cell size (Gibson and Ashby, 1997). Therefore, the increase in compressive strength observed with a

decrease of carbon fiber length and increase in concentration of carbon fiber (33 μm) can be due to a combination of the effect of cell size decrease, density increase and reinforcement by the carbon fiber. The decrease in compressive strength of carbon composite foams at carbon fiber length below 33 μm in spite of an increase in density reveals the maximum reinforcement at the carbon fiber length of 33 μm. The maximum reinforcement at carbon fiber concentration 2 wt.% of sucrose is further evidenced from the fact that the compressive strength of the composite foams decreases beyond the carbon fiber concentration 2 wt.% of sucrose, even though, the density and cell size remain more or less constant. The thermal conductivity of the carbon composite foams increases marginally from 0.069 to 0.071 W/m/K when the carbon fiber concentration increases from 0 to 4 wt.%.

5.4 Conclusions

The carbon composite foams are prepared by the thermo-foaming of sucrose-milled carbon fiber mixtures followed by dehydration and carbonization. The effect of fiber concentration and fiber length on the properties of the carbon composite foams is studied. The carbon composite foams prepared using carbon fiber of average length 300 μm show a decrease in density and specific strength with fiber concentration due to the agglomeration by bridging of longer fibers. The fiber length is reduced by the planetary ball milling of sucrose - carbon fiber mixtures in the acetone medium. The average fiber length is decreased from 300 to 15 μm when the ball milling time increased from 0 to 3 h. The density and specific strength of carbon composite foams increase with a decrease in fiber length and reaches a maximum at a fiber length of 33 μm. The density and specific compressive strength of the carbon composite foam show a maximum at a fiber concentration 2 wt.% of sucrose (~ 8 wt.% of the matrix carbon). The maximum improvement in compressive strength and specific compressive strength obtained as a result of reinforcement with the carbon fiber is 125 % and 92 %, respectively.

CHAPTER 6

PROCESSING AND CHARACTERIZATION OF CARBON COMPOSITE FOAMS FROM MOLTEN SUCROSE AND MULTI-WALLED CARBON NANOTUBES

6.1 Introduction

The reinforcing additives like AC powder and carbon fiber improve the mechanical strength of the carbon foams prepared from molten sucrose. It is well-known that the nano-sized reinforcements are better compared to the micron sized reinforcements such as AC particles and carbon fiber (Coleman et al., 2006; Thostenson et al., 2001). They produce better improvement in mechanical properties at low concentrations due to their high surface area to volume ratio (Coleman et al., 2006). Carbon nanomaterials such as single-walled carbon nanotubes (SWNT) and multi-walled carbon nanotubes (MWNT) are widely used as reinforcements in polymer, ceramic and metallic matrix composites (Agarwal et al., 2010; Chen et al., 2003b; Sahoo et al., 2010; Thostenson et al., 2001; Xia et al., 2004; Zhan et al., 2003). In addition to the mechanical property improvement, the incorporation of carbon nanotubes increases the functional properties such as electrical conductivity, thermal conductivity and EMI shielding properties of composite materials (Anantram and Léonard, 2006; Balasubramanian and Burghard, 2006; Gui et al., 2013; Suehiro et al., 2005). In many cases, the MWNTs are preferred to SWNTs due to its low cost and easy synthesis and purification (Coleman et al., 2006; Thostenson et al., 2001). Preparation of MWNT reinforced carbon foams from precursors such as mesophase pitch, coal tar pitch and cyanate ester resin is reported in the literature (Kumar et al., 2013a; Kumar et al., 2014b; Li et al., 2011b; Lin et al., 2014b). The incorporation of

MWNT improves not only the compressive strength but also the electrochemical properties and EMI shielding effectiveness of the carbon foams (Kumar et al., 2013a; Kumar et al., 2014b). The present chapter reports the preparation of MWNT reinforced carbon composite foams from molten sucrose by thermo-foaming technique. The effect of MWNT concentration on foaming characteristics of molten sucrose and the properties of carbon composite foams is investigated. The EMI shielding effectiveness of the carbon composite foams is also investigated.

6.2 Experimental

6.2.1 Preparation of MWNT Reinforced Carbon Composite Foams

The MWNT procured from Sigma Aldrich, India has the diameter and length in the ranges of 10–25 nm and 5–10 μm, respectively. Analytical reagent grade sucrose and acetone used were procured from Merck, India, Mumbai. MWNTs and sucrose were mixed in acetone medium using planetary ball mill for 2 h at 200 RPM. The MWNT concentrations used were in the range of 0 to 2.5 wt.% of sucrose. The sucrose to zirconia ball weight ratio and sucrose to acetone weight ratio used were 1:6 and 1:3, respectively. After ball milling, the slurries were transferred into 1.5 liter glass tray and dried at 70 ^{o}C. The dried sucrose-MWNT mixtures were heated at 170 ^{o}C to melt the sucrose. The melt was stirred well to achieve uniform dispersion of MWNTs. The MWNT dispersions in molten sucrose were cooled to room temperature and then kept in an oven at 140 ^{o}C for 72 h for foaming and setting. The solid organic foams were cut into rectangular pieces of 8 cm x 6 cm x 4 cm and then dehydrated at 200 ^{o}C for 3 h using a heating rate of 2 ^{o}C/h. The dehydrated foam was subsequently carbonized in an ultra-high pure argon atmosphere at 900 ^{o}C for 2 h. The heating rate used was 0.5 ^{o}C/min. The density of the carbonized samples was calculated from the weights and dimensions.

6.2.2 Characterization

The viscosity measurement of the MWNT dispersions in molten sucrose was carried out at various shear rates in the range of 0.1 to 2000 s^{-1} at 140 ^{o}C using a rheometer (MCR 102 Modular Compact Rheometer, Anton Paar, USA) with a cone and plate measurement system. The samples were physically inspected during foaming and foam setting at an interval of one hour to determine the approximate foaming and foam setting time. Thermogravimetric analysis (TGA) of the solid organic foam samples was carried out in nitrogen atmosphere using a thermogravimetric analyzer (Q-50, TA instruments, USA) at a heating rate of 2 ^{o} C/min. The densities were calculated from the weight and dimension of rectangular carbon composite foam bodies. The microstructure of the MWNT and carbon composite foams was observed using a Scanning Electron Microscope (SEM, FEI Quanta FEG200). The cell size of the carbon composite foams was measured using ImageJ software from the SEM microstructure. The compressive strength of the carbon composite foams was measured using a universal testing machine (Instron 5050, Instron USA) at a crosshead speed of 0.5 mm/min with 25 mm x 25 mm x 12 mm samples (ASTM standard C365/C365M-05). The maximum stress in the stress-strain graph was noted as the compressive strength. X-Ray diffraction (XRD) measurements of the carbon composite foam samples were carried out in an X-ray diffractometer (X'pert Pro, Philips, USA) using Cu Kα radiations (λ = 1.54056 Å). Powder samples for XRD analysis were prepared by crushing the carbon foams using a mortar and pestle**.** The diffraction patterns were recorded at 2θ values in the range of 10 to 80^{o} with a step size of 0.07^{o} using monochromatic X-rays.

The textural properties of the carbon composite foams were analyzed using the volumetric N_2 adsorption-desorption at -196 ^{o}C using a surface area analyzer (Micromeritics Tristar II, USA). The samples were degassed at 300 ^{o}C for 16 h prior to the analysis. The BET (Brunauer-Emmett-Teller) method was used for the calculation of the surface area. The total pore volume was estimated from the amount of N_2 adsorbed at a relative pressure of 0.99. The micropore

volume was obtained by using t-plot method from N_2 adsorption at -196 ^oC. The pore size distribution (PSD) was calculated using density functional theory (DFT) using N_2 adsorption isotherm by assuming the slit pore model. The CO_2 adsorption of the carbon composite foams was evaluated at 0 ^oC by volumetric gas adsorption studies using the surface area analyzer. Prior to the measurements, the samples were crushed using an agate and mortar and degassed overnight at 300 ^oC.

6.2.2.1 Electrical Conductivity

The electrical conductivity of the MWNT-carbon composite foams was measured using a four probe technique. A constant current (*I*) was supplied from a programmable source (Keithley 6221) and the voltage drop (*V*) was measured between two pins separated by a distance of 2 mm using a digital nano-voltmeter. The current and voltage data were used for calculation of bulk electrical resistivity of the carbon composite foams using the equation (6.1), where ρ is electrical resistivity and s is the distance between the pins.

$$\rho = 2\pi s(\frac{V}{I}) \tag{6.1}$$

6.2.2.2 EMI shielding

The EMI shielding properties of the carbon composite foam were measured using a vector network analyzer (E5071C) by fixing the carbon composite foam in the cavity of a wave guide. The rectangular carbon foam samples of dimensions 22.7 mm X 10.2 mm X 5.0 mm were used for the measurement. The EMI shielding was measured for the X band (8.2 – 12.4 GHz) in the microwave region using the corresponding waveguides. The X-band frequency region has been divided in 201 frequency steps. The schematic of the experimental set up is given in Figure 6.1. In order to avoid the measurement errors, a full two-port VNA calibration was performed at the beginning of each test. The shielding effectiveness was used as the measure of shielding efficiency.

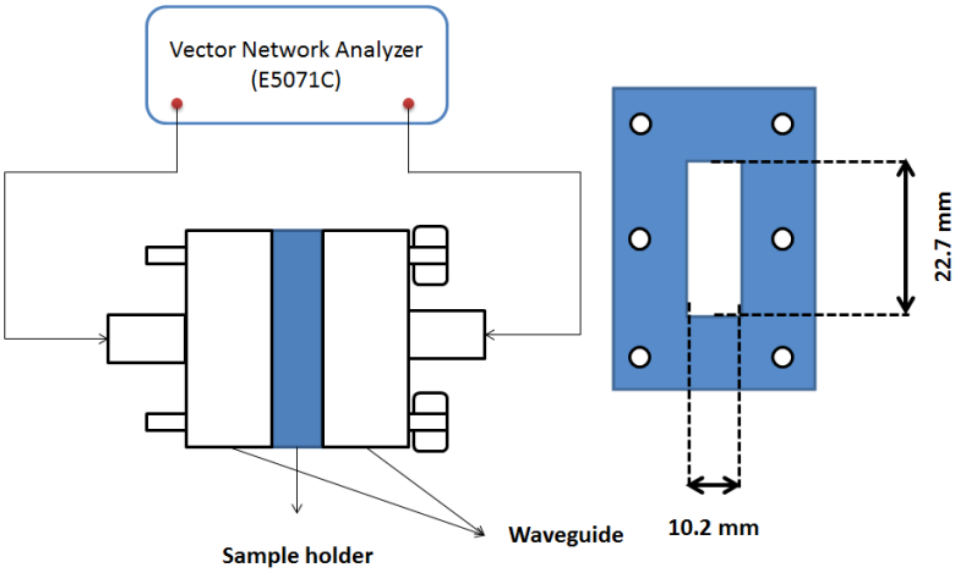

Figure 6.1: Schematic of the EMI shielding instrument set up

6.3 Results and Discussion

6.3.1 Dispersion of MWNT in the Molten Sucrose

The MWNT is highly entangled as evidenced from the high magnification SEM image (Figure 6.2). The proper dispersion of the entangled MWNT in the carbon matrix is necessary in order to improve the mechanical strength and other functional properties of the carbon foam (Coleman et al., 2006; Thostenson et al., 2001). The planetary ball milling ensures the uniform mixing of sucrose and MWNT. The sucrose in the mixture melt at 170 ^{o}C and MWNT is expected to disperse in the molten sucrose when vigorously stirred with a glass rod. The rheological studies were carried out to understand the dispersion state of the MWNT in the molten sucrose. Figure 6.3 shows the shear rate versus viscosity of the MWNT dispersions in molten sucrose at various MWNT concentrations measured at 140 ^{o}C. The effect of MWNT concentration on viscosity at a shear rate of 10 s^{-1} is shown as an insert in Figure 6.3. The dispersions showed the shear thinning character. The viscosity of the molten sucrose without MWNT is in the range of 2.90 to 2.36 Pa.s at the shear rate in the range of 1 to 2000 s^{-1}. The viscosity and shear thinning nature of the dispersions increases with an increase in the MWNT concentration. The viscosity of molten sucrose at a shear rate of 10 s^{-1}

increases gradually from 2.44 to 6.7 Pa.s when the MWNT concentration increases from 0 to 1.5. Further increase in MWNT concentration from 1.5 to 2.5 wt.% rapidly increases the viscosity from 6.7 to 54.7 Pa.s. The rheological studies indicate that the MWNT disperses well in molten sucrose up to a concentration of 1.5 wt.%. Further increase in MWNT concentration results in the agglomeration of MWNT due to the Van der Waal's interactions because of its high surface area. The high shear thinning nature at 2 and 2.5 wt.% MWNT concentrations is due to the breaking of these agglomerates at higher shear rates.

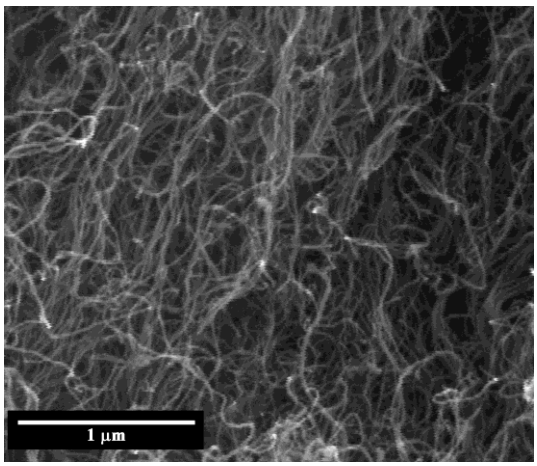

Figure 6.2: SEM micrograph of the entangled MWNT

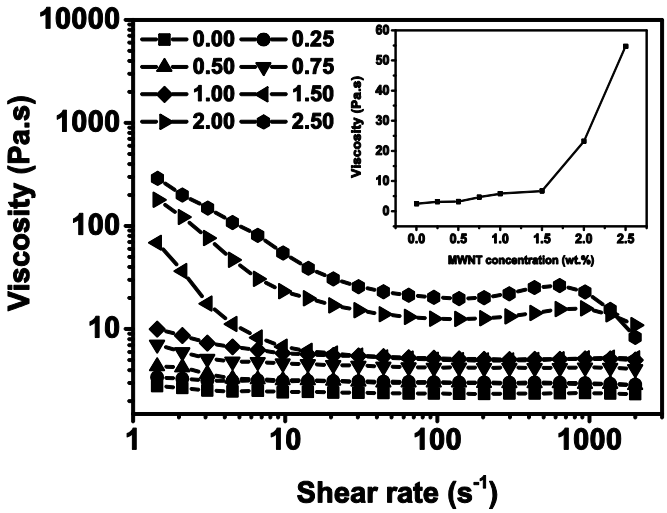

Figure 6.3: Shear rate vs. viscosity of the MWNT-molten sucrose dispersions at MWNT various concentrations in the range of 0 to 2.5 wt.% (Inset shows the MWNT concentration vs. viscosity)

6.3.2 Foaming and Setting Characteristics

Figure 6.4 shows the foaming time and foam setting time of the molten sucrose containing various MWNT concentrations. The foaming time and foam setting time of the dispersions decrease with an increase in the MWNT concentration. The foaming time of the dispersions decreases from 48 to 8 h when the MWNT concentration increases from 0 to 2.5 wt.%. Similarly, the foam setting time decreases from 96 to 52 h when the MWNT concentration increases from 0 to 2.5 wt.%. The mechanism of foaming of molten sucrose is reported in Chapter 2. The decrease in foaming and foam setting time with an increase in MWNT concentration indicates that the MWNT catalyzes the –OH to –OH condensation reactions responsible for the foaming and setting of molten sucrose. The catalytic activity of MWNT towards the oxidative dehydrogenation of methyl benzene, etc. is already reported in the literature by various authors (Pereira et al., 2004; Su et al., 2005a).

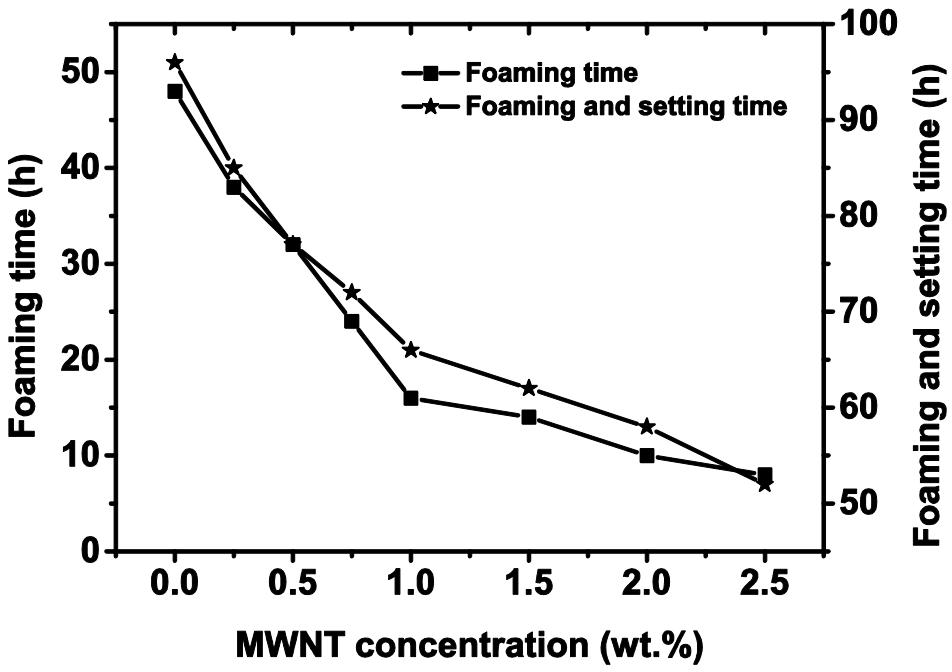

Figure 6.4: Foaming time and foam setting time of the MWNT dispersions in molten sucrose at various MWNT concentrations

Figure 6.5 shows the TGA of the solid organic foams at various MWNT concentrations. The decomposition onset temperature of the solid organic foams is 175 ^{o}C irrespective of MWNT concentrations. The DTG shows the peak at 275 ^{o}C for the solid organic foams irrespective of the MWNT concentrations. The thermal decomposition of the solid organic foam prepared without MWNT is almost complete at 600 ^{o}C. On the other hand, the solid organic foam with MWNT showed considerable weight loss at temperature in the range of 600 to 900^{o}C. The weight losses observed up to 400 ^{o}C is mainly due to the formation of water molecules. Further weight losses up to 900 ^{o}C is mainly due to the formation of CO. The decomposition of solid organic foam to form water molecules below 400 ^{o}C can take place either through –OH to –OH condensation or through elimination reaction involving –OH group and α-hydrogen. The TGA of the solid organic foam with MWNT shows higher percentage of residue at 400 ^{o}C compared to that without MWNT. The residue at 400 ^{o}C increases from 36.4 to 46.3 wt.% when the MWNT concentration increases from 0 to 2.5 wt.%. This indicates that in solid organic foam without MWNT the formation of water molecule is mainly due to the α-elimination. On the other hand, in presence of MWNT, –OH to –OH condensation is the favourable mechanism which leaves more residues due to the retention of oxygen atoms as C-O-C linkages. These oxygen atoms are removed at higher temperatures as CO. The char residue at 900 ^{o}C increases from 24 to 33.2 wt.% when the MWNT concentration increases from 0 to 2.5 wt.%. The increase in char residue is due to the contribution of MWNT.

6.3.3 Density and Microstructure

The bulk density and cell size of the carbon composite foams depend on the MWNT concentration. Figure 6.6 shows the bulk density and average cell size of the carbon composite foams prepared at various MWNT concentrations. The bulk density of the carbon foam without MWNT is 0.14 g/cm^3. By the addition of 0.25 wt.% MWNT, the bulk density of the carbon composite foam increases to 0.23 g/cm^3. Further increase in the MWNT concentration from 0.25 to 2 wt.% results in a marginal increase in density from 0.23 to 0.26 g/cm^3. The bulk density

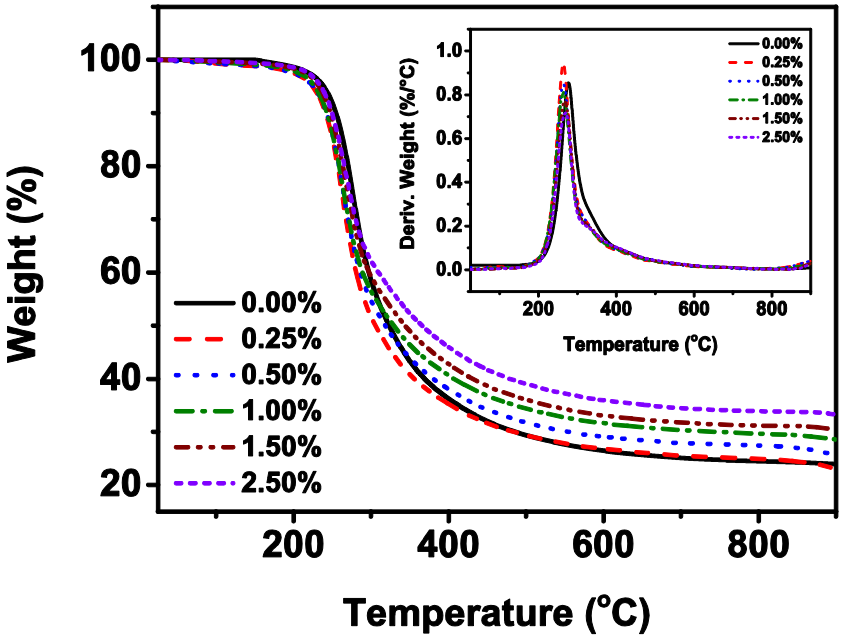

Figure 6.5: TGA in nitrogen atmosphere of the solid organic foams prepared at various MWNT concentrations (Heating rate - 2 °C/min). Inset showing the corresponding DTG

of the carbon composite foam shows a decreasing trend beyond 2 wt.% of MWNT. The average cell size of the carbon composite foams decreases from 0.89 to 0.5 mm when the MWNT concentration increases from 0 to 0.25 wt.%. Further increase in MWNT concentrations from 0.25 to 2.5 wt.% results in an increase in cell size from 0.5 to 1.4 mm. The initial decrease in cell size observed when the MWNT concentration increases from 0 to 0.25 is due to the difference in the bubble nucleation mechanism. The nucleation of bubbles in molten sucrose without MWNT is by homogeneous mechanism. On the other hand, in the case of MWNT dispersions, the MWNT acts as heterogeneous sites for the nucleation of large number of bubbles even at low concentration of water vapour. This results in increase in cell density and decrease in cell size as observed by Zeng et al. (2010). These heterogeneously nucleated bubbles grow at higher MWNT concentrations by the faster production of water vapour due to the catalytic activity of MWNT. Further, the increase in viscosity with an increase in MWNT concentrations stabilizes the larger bubbles. Figure 6.7 shows the SEM micrographs of the carbon composite foams prepared at various MWNT concentrations. The cells are having

near spherical morphology up to a MWNT concentration of 1.5 wt.%. Thereafter, the cells show distorted morphology.

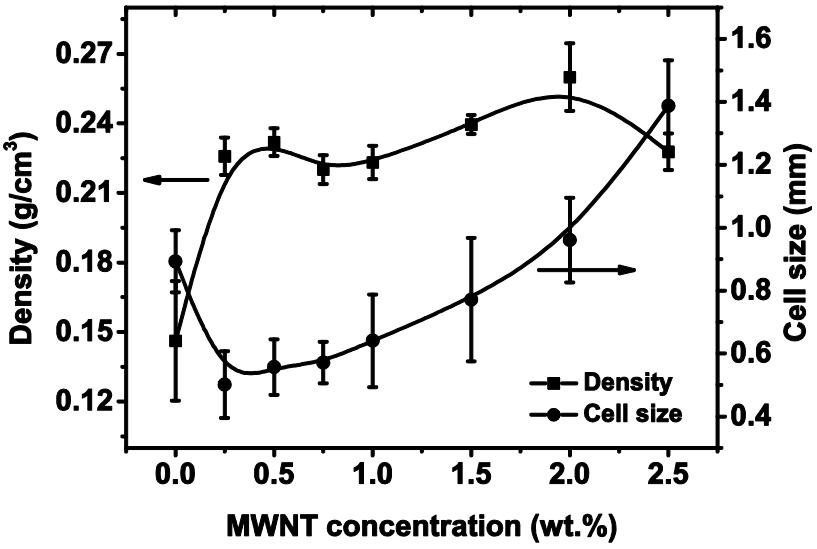

Figure 6.6: Average bulk density and average cell size of the MWNT reinforced carbon composite foams prepared in the range of 0 to 2.5 wt.% MWNT

6.3.4 Textural Properties

Figure 6.8 shows the nitrogen adsorption-desorption isotherms of the carbon composite foams prepared at various MWNT concentrations. The carbon foam without MWNT shows a narrow adsorption at $p/p_o < 0.02$ which corresponds to type I isotherm, according to IUPAC, due to the intrinsic micropores in the cell wall and struts of the carbon foam. In addition to the narrow adsorption at p/p_o <0.02, the carbon composite foams prepared at various MWNT concentration show the hysteresis loops at p/p_o are in the range of 0.80 to 0.99. This is the characteristics of the combination of type I and type IV isotherms. The magnitude of hysteresis loop is increasing with an increase in the MWNT concentrations. Figure 6.9 (a and b) shows the DFT and BJH PSD of the carbon foams prepared at

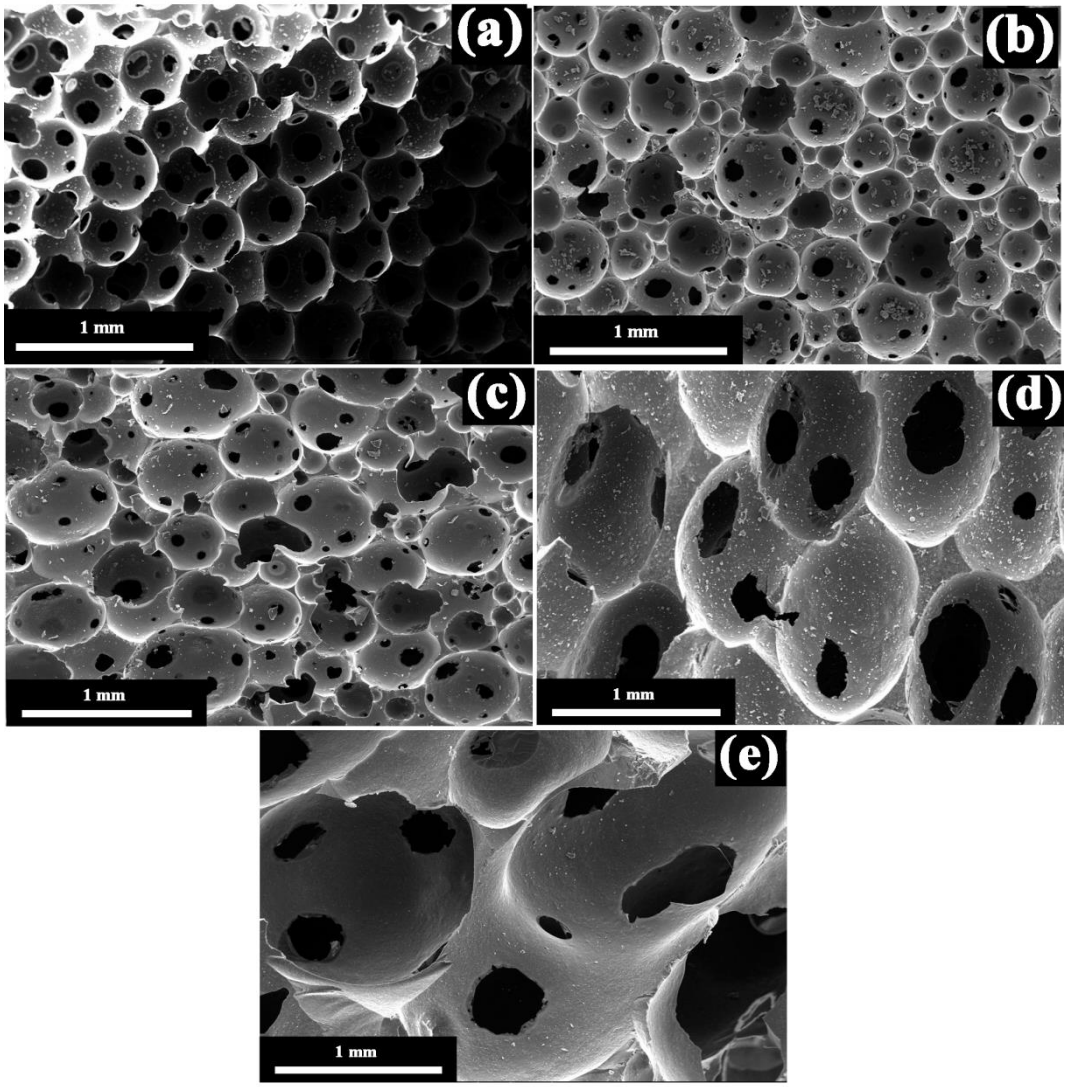

Figure 6.7: SEM micrographs of the MWNT reinforced carbon composite foams (a – 0 wt.%, b – 0.25 wt.%, c – 0.50 wt.%, d – 1.50 wt.% and e – 2.50 wt.%)

various MWNT concentrations. The DFT PSD plots show that the micropores present in the carbon foams is in the size range of 11 to 15 Å. On the other hand, the BJH plots show the presence of large pores in the size range of 500 – 1100 Å in the cell walls and struts of the carbon composite foams containing MWNT concentrations in the range of 0.25 to 2.5 wt.%. Whereas, the carbon foam without MWNT shows no peak in the BJH plot clearly showing the absence of mesopores. Figure 6.10 shows the specific surface area and total pore volume of the carbon composite foams prepared at various MWNT concentrations. The surface area and pore volume increases with an increase in the MWNT concentrations. The surface area of the carbon composite foams increases from

367 to 506 m^2/g when the MWNT concentration increases from 0 to 2.5 wt.%. Similarly, the pore volume of the carbon composite foams increases from 0.18 to 0.35 cm^3/g when the MWNT concentration increases from 0 to 2.5 wt.%. The mechanism of micropore formation in the carbon foam cell walls and struts due to the *in situ* activation has been discussed in the Chapter 2. That is, the micropores are produced by the reaction of oxygen, retained as a result of –OH to –OH condensation, with the carbon at higher temperatures to form CO. On the other hand, the mesoporosity is created by the local shrinkage of the sucrose polymer present within the MWNT agglomerates or bundles. The formation of mesopores at higher MWNT concentrations is schematically shown in Figure 6.11. The carbon composite foams prepared at MWNT concentrations in the range of 0 to 2.5 wt.% show the CO_2 adsorption capacity in the range of 2.4 to 2.83 mmol/g.

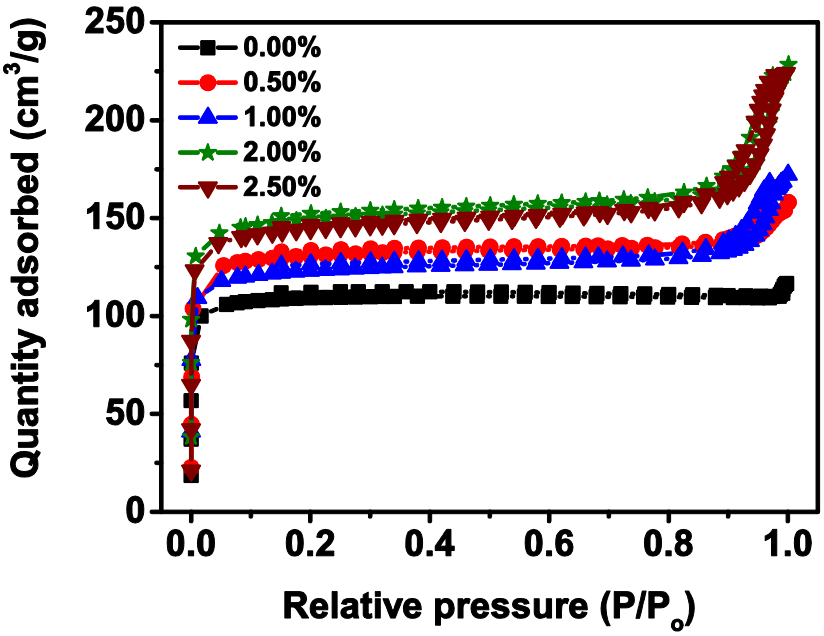

Figure 6.8: Nitrogen adsorption-desorption isotherms of the carbon composite foams prepared at various MWNT concentrations

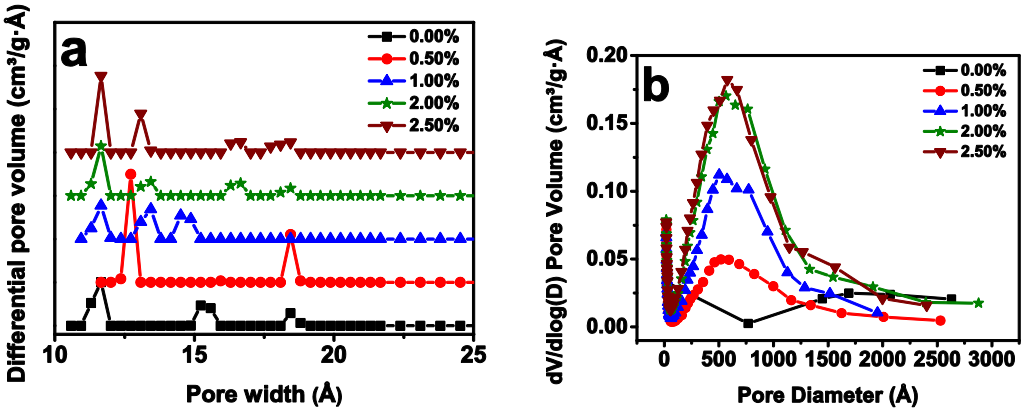

Figure 6.9: (a) DFT and (b) BJH plot of the carbon composite foams prepared at various MWNT concentrations

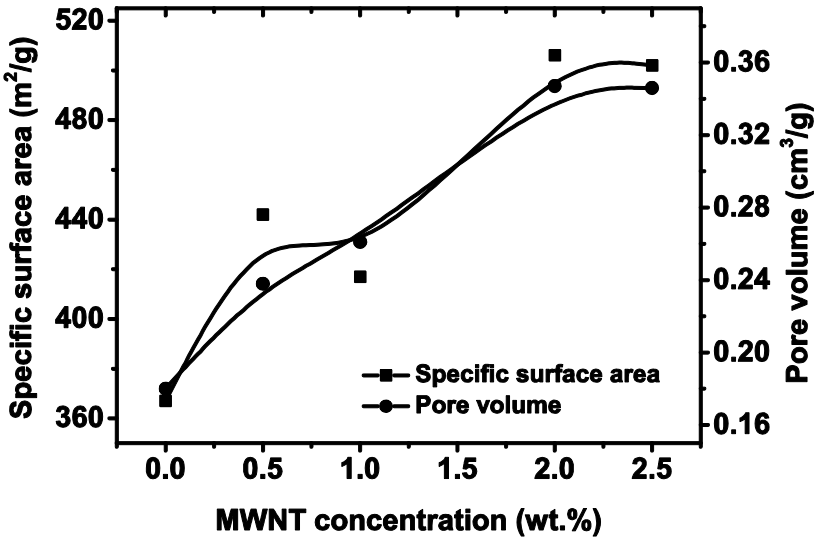

Figure 6.10: Specific surface area and pore volume of the carbon composite foams prepared at various MWNT concentrations

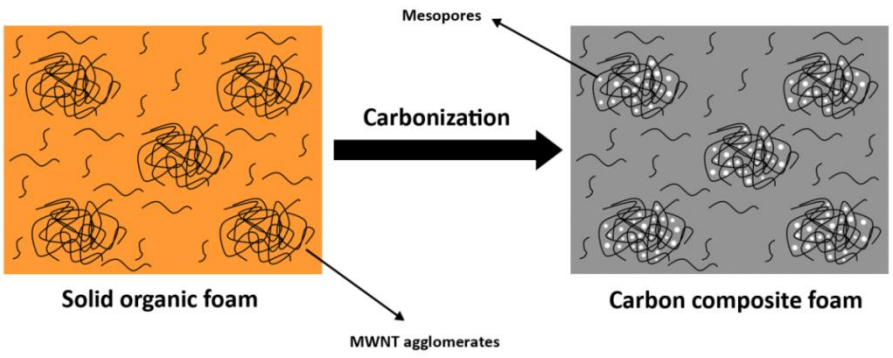

Figure 6.11: Schematic of the formation of mesopores at higher MWNT concentrations

6.3.5 Compressive Strength

The compressive strength of the carbon foams mainly depends on the density, cell size and types of reinforcement used (Gibson and Ashby, 1997). Generally, the compressive strength of the carbon foams increases with an increase in the density and decrease in cell size (Gibson and Ashby, 1997). Figure 6.12 shows the compressive strength and Young's modulus of the carbon composite foams at various MWNT concentrations. The compressive strength and Young's modulus of the carbon composite foam increases with an increase in the MWNT concentration and reach the maximum at an MWNT concentration of 0.50 wt.%. The compressive strength and Young's modulus of the carbon composite foam containing 0.50 wt.% MWNT are 4.90 and 65 MPa, respectively. Thereafter, it starts to decrease with an increase in the MWNT concentration. The improvement in the compressive strength with the incorporation of MWNT is due to the reinforcement effect of the MWNT. The compressive strength maximum at 0.5 wt.% of MWNT indicates uniform dispersion of MWNT in the molten sucrose which leads to the uniform distribution of MWNT in the carbon matrix. This creates maximum MWNT-carbon matrix interface which facilitates effective matrix to reinforcement stress transfer (Schadler et al., 1998). The decrease in compressive strength at MWNT concentration above 0.5 wt.% indicates that MWNT begins to agglomerates at MWNT concentration above 0.5 wt.%. However, the rheological measurements show a rapid increase in viscosity only after 1.5 wt.% of MWNT. This indicates that the rheological measurements are not much sensitive to the small levels of agglomerates formed in the MWNT concentrations in the range of 0.75 to 1.5 wt.%. However, these small levels of agglomerates produce a considerable decrease in compressive strength. The agglomeration of MWNT at concentrations above 0.5 wt.% is clearly evidenced from the high magnification SEM of the strut region of the carbon composite foams. Figure 6.13 shows the SEM micrographs of the fractured strut region of the MWNT reinforced carbon composite foams. The uniform distribution of MWNT in the strut region of carbon composite foams is observed up to a MWNT concentration of 0.5 wt.%. On the other hand, MWNT agglomerates are clearly

visible in high magnification images of the struts of carbon composite foams at MWNT concentrations above 0.5 wt.%. The extent of agglomeration increases with an increase in MWNT concentration.

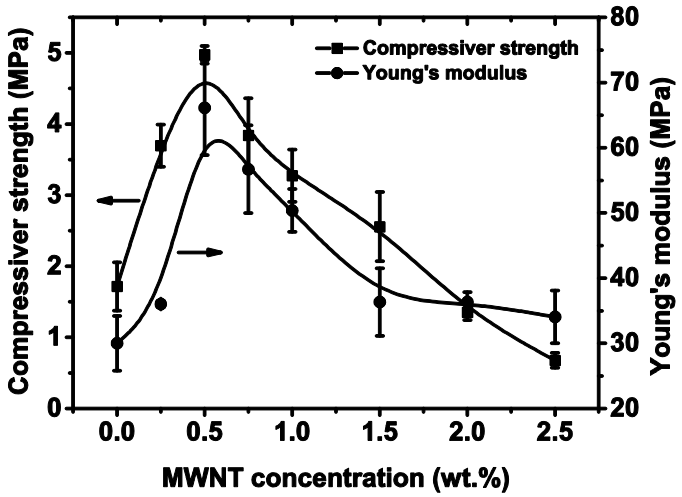

Figure 6.12: The effect of MWNT concentration on compressive strength and Young's modulus of the MWNT reinforced carbon composite foams

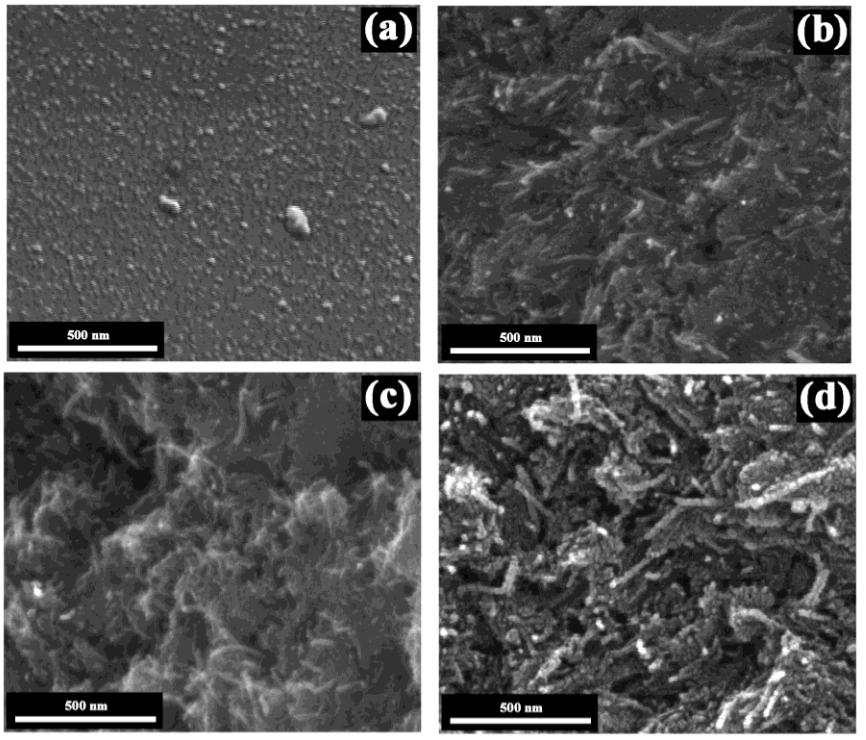

Figure 6.13: Fractured strut region of the carbon composite foams prepared at various MWNT concentrations (a – 0.50 wt.%; b – 0.75 wt.%; c – 1.00 wt.%; d – 2.5 wt.%)

The high specific properties of the materials are always desirable for the crucial applications like thermal protective systems and fire resistance structures in aerospace. Figure 6.14 shows the specific compressive strength of the carbon composite foams prepared at various MWNT concentrations. The MWNT reinforced carbon composite foam shows a maximum specific compressive strength of 21 MPa/g/cm^3 at 0.5 wt.% MWNT. This corresponds to a MWNT concentration nearly 2 wt.% of the carbon matrix as the solid organic foam without MWNT leave a char residue of 24 wt.%. The maximum improvement in the specific compressive strength is achieved by reinforcement with MWNT is 133 %. The maximum specific compressive strength obtained for MWNT reinforced carbon foam is higher than that (17 MPa/g/cm^3) obtained for the carbon fiber reinforced carbon composite foam reported in Chapter 5.

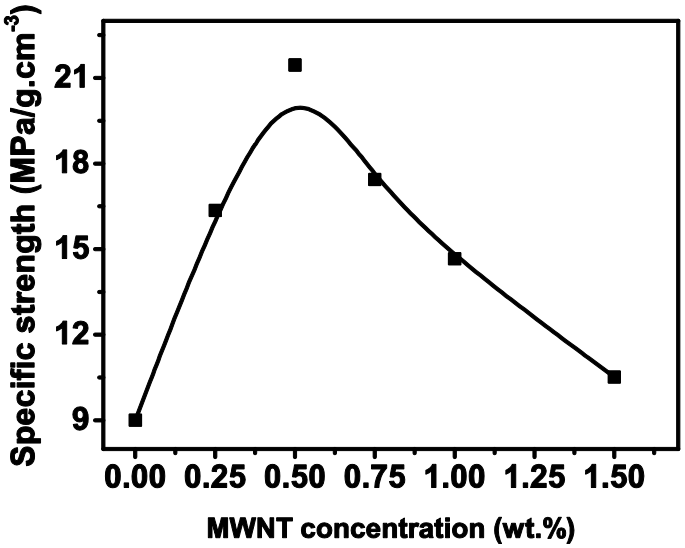

Figure 6.14: Specific compressive strength of the MWNT reinforced carbon composite foams in the range of 0 to 2.5 wt.% MWNT

6.3.6 X-Ray Diffraction

Figure 6.15 shows the XRD patterns of the carbon composite foams prepared at MWNT concentrations of 0, 0.5, 1.5 and 2.5 wt.%. The XRD pattern shows the amorphous nature of the carbon. The two broad peaks are observed at ~

25 and ~ 44° corresponding to (002) and (100) planes, respectively. The 2θ values of the d_{002} peak are 24.6, 25.1, 25.5 and 25.7° for the carbon composite foams at MWNT concentrations 0, 0.5, 1 and 2.5 wt.%, respectively. The d-spacing of the (002) peak of carbon foam without MWNT calculated by using Bragg's equation ($n\lambda = 2d\sin\theta$) is 0.361 nm. The d_{002} values decreases with an increase in the MWNT concentration. The d-spacing values obtained for the carbon composite foams prepared at 0.5, 1.5 and 2.5 wt.% MWNT are 0.354, 0.349 and 0.347 nm, respectively. The decrease in d-spacing value with an increase in the MWNT concentration may be due to the development of crystal structure along the axis parallel to the length of MWNT. Similar effect was observed by Kumar et al. (2013a); Lin et al. (2014b) in preparation of MWNT reinforced carbon foams from cyanate ester and coal tar pitch, respectively.

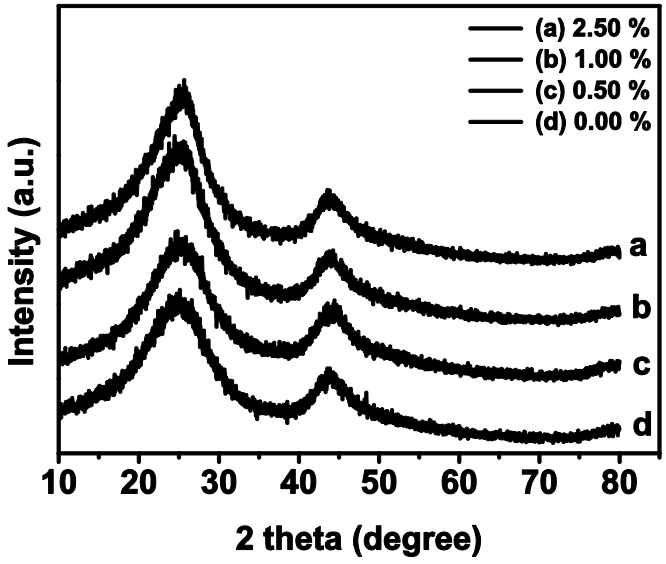

Figure 6.15: XRD patterns of the carbon composite foams prepared at various MWNT concentrations

6.3.7 Electrical Conductivity and EMI Shielding Properties

Figure 6.16 shows the electrical conductivity of the carbon composite foams. The electrical conductivity increases with an increase in the MWNT concentration. The electrical conductivity of carbon foam without MWNT is 3.5

$S.cm^{-1}$. The electrical conductivity increases from 3.5 to 4.9 $S.cm^{-1}$ when the concentration of MWNT increases from 0 to 1 wt.%. Further increase in MWNT concentration results in a marginal decrease in the electrical conductivity. This indicates that percolation takes place at MWNT concentration of 1 wt.%. The decrease in electrical conductivity at MWNT concentration higher than 1 wt.% is due to the heavy agglomeration of the MWNT. The decline of electrical conductivity at higher MWNT concentrations in polymer matrix due to agglomeration of MWNT is reported by various authors (Socher et al., 2011). The similar effect is observed in carbon composite foams prepared from cyanate ester and coal-tar pitch Kumar et al. (2014b); Lin et al. (2014b), respectively.

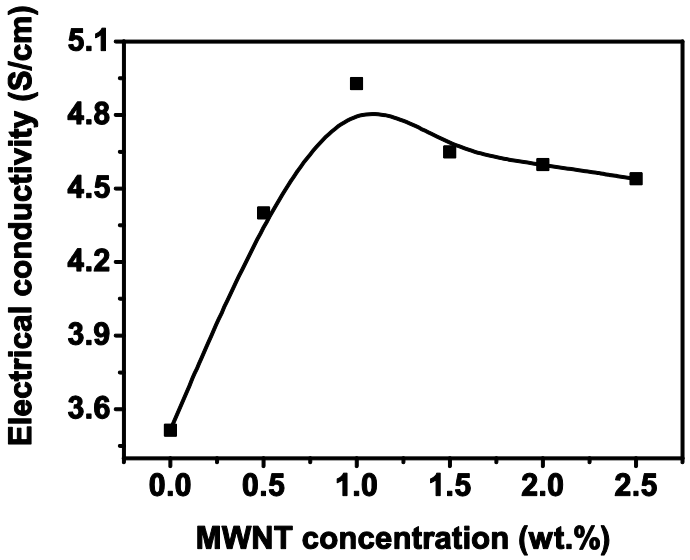

Figure 6.16: Electrical conductivity of the carbon composite foams prepared at various MWNT concentrations

The EMI SE is the ability of the shielding material to attenuate the electromagnetic radiation. It is measured as the ratio between the power of the incident radiation to the power of the transmitted radiation (Chung, 2000, 2001). It is expressed in the unit of dB. The mechanism of attenuation of EM radiation is mainly by reflection at the surface of the shielding material, absorption while the radiation passes through and multiple reflections of the radiations at various interfaces. Thus the SE, the sum of these three losses, is expressed as given in equation (6.2), where SE is the total SE of the material, SE_R is the reflection loss,

SE_A is the absorption loss, SE_{MR} is the loss due to multiple reflections. If SE is more than 10 dB, which is the case in most of the practical applications, the loss attributed due to the multiple reflections can be ignored. Thus, the SE can be given as in the equation (6.3):

$$SE = SE_R + SE_A + SE_{MR} \quad (6.2)$$

$$SE = SE_R + SE_A \quad (6.3)$$

Figure 6.17 (a) is a typical graph showing the shielding effectiveness of MWNT-carbon composite foam in X-band region (8.2 – 12.4 GHz). The SE is almost constant in the entire X-band region for the carbon composite foams at a particular MWNT concentration. The total SE has contributions from absorption, reflection and multiple reflections. The loss associated with the multiple reflections is ignored because all our MWNT-carbon composite foams showed SE greater than 10 dB. At all MWNT concentrations the absorption loss (SE_R) is dominating the reflection loss (SE_A). Figure 6.17 (b) shows the effect of MWNT concentration on the total, absorption and reflection SE of carbon composite foams. The reflection contribution increases from 6.3 to 9.5 dB when the MWNT concentration increases from 0 to 0.25 wt.%. The reflection contribution remains more or less same for the carbon foams at MWNT concentrations in the range of 0.25 to 2.5 wt.%. On the other hand, the absorption contribution increases from 13.8 to 17 dB when the MWNT concentration increases from 0 to 0.25 wt.% and then remains more or less same up to the MWNT concentration of 1.5 wt.%. Further increase in MWNT concentration produces a rapid increase in the EM absorption. The trend in total SE follows the trend in the absorption contribution. That is, the total SE increases from 20 to 26 dB when the MWNT concentration increases from 0 to 0.25 wt.% and then remain more or less constant up to the MWNT concentration of 1.5 wt.%. Further increase in MWNT concentration from 1.5 to 2.5 wt.% results in a rapid increase of total SE from 26 to 38 dB. The increase in SE of the carbon composite foams with MWNT concentrations can be due to the increase in the electrical conductivity as well as the improvement in the crystallinity of the carbon foam. The rapid increase in SE at MWNT

concentrations above 1.5 wt.% indicate that the MWNT agglomerates present in the carbon matrix contribute to the SE. The contribution of MWNT agglomerates towards EMI SE can be explained as follows: the MWNT agglomerates produce pores due to the local shrinkage of the sucrose polymer within the MWNT agglomerates during carbonization. These pores within the MWNT agglomerates create large area of new interfaces at which the EM radiation undergoes internal reflection. These reflected EM radiations are absorbed back in the material resulted in the rapid increase in the absorption contribution (Ji et al., 2014).

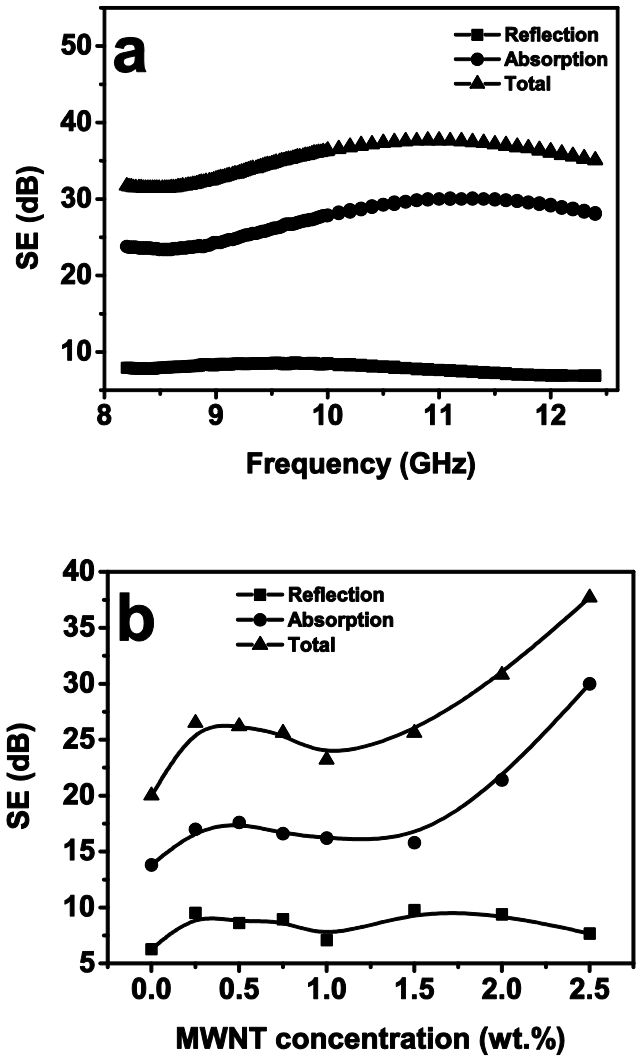

Figure 6.17: (a) SE of carbon composite foam at 2.5 wt.% MWNT in X-band region and (b) total, reflection and absorption SE of the carbon composite foams at various MWNT concentrations at 11 GHz

The specific shielding effectiveness (SSE), the attenuation of EM per unit density, is an important parameter especially for EMI shielding materials used in aerospace applications. Figure 6.18 shows the SSE of carbon composite foams at various MWNT concentrations. The carbon foam without MWNT shows a SSE of 136 dB/g/cm^3. The SSE decreases to 116 dB/g/cm^3 with the addition of 0.25 wt.% MWNT. The SSE remains more or less same with further increase in MWNT concentration up to 2 wt.% and then increases. The decrease in SSE is due to the observed increase in density of the carbon composite foams. The carbon composite foam at 2.5 wt.% MWNT concentration shows the highest SSE of 166 dB/g/cm^{-3}. This is much higher than the SSE (10 dB/g/cm^{-3}) of copper (Saini et al., 2012). The highest SSE (130 dB/g/cm^{-3}) value in carbon foam is reported by Kumar et al. (2013b); Kumar et al. (2014a); Kumar et al. (2014b) by incorporating iron nanoparticles in mesophase pitch derived carbon foam. The SSE of MWNT-carbon composite foam at 2.5 wt.% MWNT is higher than that of the iron nanopoarticle incorporated carbon foams.

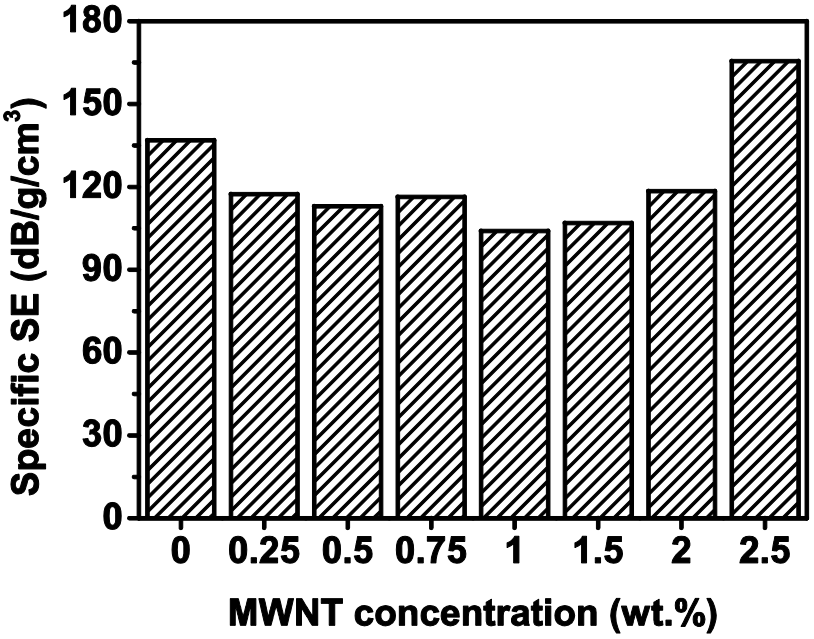

Figure 6.18: SSE of carbon composite foams at various MWNT concentrations

6.4 Conclusions

MWNT reinforced carbon composite foams are prepared by the thermo-foaming of MWNT dispersions in molten sucrose followed by dehydration and carbonization. The foaming time and foam setting time decrease with an increase in MWNT concentration due to the catalytic effect of MWNT towards –OH to –OH condensation which is responsible for the foaming and setting of molten sucrose. The cell size decreases from 0.71 to 0.35 mm when the MWNT concentration increases from 0 to 0.25 wt.% and then gradually increases to 1.39 mm when the MWNT concentration increases to 2.5 wt.%. The density of the MWNT reinforced carbon composite foam increases from 0.14 to 0.23 g/cm^3 when the MWNT concentration increases from 0 to 0.25 wt.% and then remain more or less constant with further increase in MWNT concentration. The compressive strength and specific compressive strength increase with an increase in the MWNT concentration up to 0.5 wt.% and then decrease with further increase in MWNT concentration. The decrease in compressive strength observed at MWNT concentration beyond 0.5 wt.% is due to the agglomeration of MWNT as evidenced from SEM micrographs. The XRD studies show a decrease in the d-spacing of (002) plane from 3.614 to 3.472 Å with an increase in MWNT concentration from 0 to 2.5 wt.% due to the development of crystal structure parallel to MWNT axis. The electrical conductivity increases with an increase in the MWNT concentration up to 1 wt.% and then marginally decreases due to MWNT agglomeration. The EMI SE of the carbon composite foams in the X-band region increases gradually with an increase in the MWNT concentration up to 1.5 wt.% and then rapidly. The pores created by the local shrinkage within the MWNT agglomerates contribute to the SE by acting as new interfaces for internal reflections which are responsible for rapid increase in SE at higher MWNT concentrations. The highest SE achieved is 39 dB at a MWNT concentration of 2.5 wt.%. The highest SSE of the MWNT reinforced carbon composite foam obtained is 166 dB/g/cm^3.

CHAPTER 7

PROCESSING AND CHARACTERIZATION OF CARBON COMPOSITE FOAMS FROM MOLTEN SUCROSE AND GRAPHENE OXIDE

7.1 Introduction

Graphene is a two-dimensional carbon nanostructure that finds a lot of potential applications due to its superior mechanical, thermal, electrical and electronics properties (Novoselov et al., 2004). One of the important applications of graphene is as the reinforcing agent in the polymer, metal, and ceramic matrix composites (Potts et al., 2011; Walker et al., 2011; Wang et al., 2012b). In addition, the incorporation of low volume fraction of graphene produces tremendous improvement in other functional properties of composites that enable their use in catalysis, energy storage and conversion, sensor, etc. (Cuong et al., 2010; Li et al., 2014; Lin et al., 2014a; Ning et al., 2011; Sun et al., 2008; Zhong et al., 2013; Zhu et al., 2010). However, the pristine graphene has a poor dispersibility due to its high surface area and very high cohesive Van der Waals interactions between the graphene sheets (Park et al., 2009). Graphene oxide (GO) is a highly oxygenated graphene that is having good solubility in polar solvents (Dreyer et al., 2010). Therefore, GO is used instead of graphene in majority of the composite processing. In many cases, the GO undergoes *in situ* reduction leading to the graphene reinforced composites (Becerril et al., 2008; Glover et al., 2011; Liu et al., 2011; Park et al., 2012). Jana et al. (2014) has used the exfoliated graphite as the reinforcement in the tannin based carbon foam. The incorporation of graphene as a reinforcement in carbon foam is not explored so far. The reason for the same may be the poor dispersion of GO in the carbon precursors as the commonly used precursors are highly non-polar in nature. However, GO is expected to disperse in sucrose as the sucrose is a highly polar compound. The

GO incorporated in the sucrose expected to undergo reduction during the carbonization process. The present chapter explores the preparation of the graphene reinforced carbon composite foams from molten sucrose. The effect of GO concentration on foaming characteristics of molten sucrose and properties of carbon composite foams is investigated. The EMI shielding effectiveness of the graphene reinforced carbon composite foams is also studied.

7.2 Experimental

7.2.1 Materials

Analytical reagent grade sucrose and acetone used were procured from Merck, India, Mumbai. The graphite powder (20 μm) was purchased from Sigma Aldrich, USA. The concentrated sulfuric acid (98%), concentrated hydrochloric acid (36%), potassium permanganate (99.5%), sodium hydroxide (96%), and hydrogen peroxide (30%) used were analytical reagent grade and purchased from Merck India, Mumbai. All reagents were used without further purification.

7.2.2 Preparation of Graphene Oxide

Graphene oxide (GO) was prepared from graphite powder using the procedure reported by Aboutalebi et al. (2011a); Aboutalebi et al. (2011b); (Jana and Ganesan, 2011). Graphite powder (5 g) and concentrated sulfuric acid (98%, 1 liter) were mechanically stirred using Teflon paddle for 2 h in a three-neck round bottom flask fitted with a water condenser. The temperature of the bath was maintained at 25 ^{o}C during the stirring. 50 g $KMnO_4$ was added lot wise to the mixture in 1 h so as to maintain the temperature of the reaction mixture below 50 ^{o}C. The temperature of the reaction mixture was then increased to 50 ^{o}C and maintained for 24 h with continuous vigorous stirring. One liter of distilled water was added after cooling the reaction mixture to a temperature of < 5 ^{o}C in an ice bath and then stirred for 1 h. 25 ml of 30 vol.% H_2O_2 was added to the reaction mixture to obtain a brown colloidal solution. The brown colloidal solution was

further stirred for 1 h and then centrifugally washed three times with 1M HCl solution. Further, the colloidal solution was centrifugally washed several times with distilled water until the pH reaches between 6 and 7. Finally, the water present in the GO solution was exchanged with acetone by repeated centrifugation and decanting. The GO concentration in the acetone solution was gravimetrically estimated as 4 $mg.ml^{-1}$.

7.2.3 Preparation of Graphene Reinforced Carbon Composite Foams

The sucrose was intimately mixed with GO in the acetone medium using a planetary ball mill for 2 h at 200 RPM. The GO concentration used was in the range of 0 to 1.25 wt.% of sucrose. The sucrose to zirconia ball weight ratio and sucrose to acetone weight ratio used were 1:6 and 1:3, respectively. After ball milling, the slurries were transferred to 1.5 L glass tray and dried at 70 ^{o}C. The dried sucrose-GO mixtures were heated in an air oven to melt the sucrose and stirred well using a glass rod to obtain GO dispersions in molten sucrose. The GO dispersions were then kept for foaming and setting in an oven at 120 ^{o}C. The foam rise, a measure of foam volume, was obtained from the ratio of the initial height of the resin to the final height of the foam. The solid organic foams were cut into rectangular pieces and dehydrated at 200 ^{o}C for 3 h using the heating rate of 2 ^{o}C/h. The dehydrated foams were subsequently carbonized in an ultra-high pure argon atmosphere at 900 ^{o}C for 2 h. The heating rate used was 0.5 ^{o}C/min. The density of the carbonized samples was calculated from their weights and dimensions.

7.2.4 Characterization

A Fourier transform infrared (FTIR) spectrum of the GO was recorded using a FTIR spectrophotometer (Spectrum-150, PerkinElmer, USA) in the spectral range of 4000 to 400 cm^{-1}. Thermogravimetric analysis (TGA) of the GO and solid organic foam samples was carried out in nitrogen atmosphere using a

thermogravimetric analyzer (Q-50, TA instruments, USA) at a heating rate of 2 ^{o} C/min. X-Ray diffraction (XRD) measurements of the GO and graphite were carried out in an X-ray diffractometer (X'pert Pro, Philips, USA) using Cu Kα radiations (λ = 1.54056 Å). The diffraction patterns were recorded at 2θ values in the range of 10 to 80^{o} with a step size of 0.07^{o} using monochromatic X-rays. Raman spectra were taken on a RAMAMLOG 6 (Spex, USA) using a 50 x objective lens with a 514.5 nm laser excitation. The atomic force microscope (AFM, Agilent, USA) was used to observe the topography of the GO. 50 μg of GO solution was drop casted on a freshly cleaved mica sheet and dried for two days in ambient condition. The images were taken using tapping mode (AAC mode). A Si_3N_4 tip was used for the imaging. The rheological studies were carried out by using a Rheometer (Anton Paar, MCR102, USA). The cone and plate method was used for the viscosity measurements (CP25). The zero gap was 0.1 mm. The shear rate used was in the range of 0.1 to 2000 s^{-1}. The microstructure of the carbon composite foams was observed using a SEM (FEI Quanta FEG200). The cell size was measured using ImageJ software from the SEM microstructure. The compressive strength of the carbon composite foams was measured using a universal testing machine (Instron 5050, Instron USA) at a crosshead speed of 0.5 mm/min with 25 mm x 25 mm x 12 mm samples (ASTM standard C365/C365M-05). The load cell used was 5 kN. The maximum stress in the stress-strain graph was noted as the compressive strength. The reported compressive strength values are average of six measurements. The textural properties of the carbon composite foams were analyzed using the volumetric N_2 adsorption-desorption at -196 ^{o}C using a surface area analyzer (Micromeritics Tristar II, USA). The CO_2 adsorption of the carbon composite foams was evaluated at 0 ^{o}C by volumetric gas adsorption studies using the surface area analyzer. Prior to the measurements, the samples were crushed using an agate and mortar and degassed overnight at 300 ^{o}C. The electrical conductivity of the carbon composite foams was measured using a four probe technique. A constant current (*I*) was supplied from a programmable source (Keithley 6221) and the voltage drop (*V*) was measured between two pins separated by the distance of 2 mm using a digital nano-voltmeter. The current and voltage data were used for calculation of bulk

electrical resistivity of the carbon composite foams using the equation (7.1), where ρ is electrical resistivity and s is the distance between the pins.

$$\rho = 2\pi s(\frac{V}{I}) \quad (7.1)$$

The EMI shielding properties of the carbon composite foam were measured using a vector network analyzer (E5071C) by fixing the carbon composite foam in the cavity of a wave guide. The rectangular carbon foam samples of dimensions 22.7 mm X 10.2 mm X 5 mm were used for the measurement. The EMI shielding was measured for the X band (8.2 – 12.4 GHz) in the microwave region using the corresponding waveguides. The shielding effectiveness was used as the measure of shielding efficiency.

7.3 Results and Discussion

7.3.1 Characterization of GO

Figure 7.1 (a) shows the FTIR spectrum of GO showing the presence of various functional groups. The peaks at 3394, 1717, 1232 and 1028 cm^{-1} are corresponding to –OH stretching vibrations, -C=O stretching vibrations, -C-OH stretching vibrations and -C-O-C- stretching vibrations, respectively (Paredes et al., 2008). The thermal analysis shows that the main weight loss of GO happens in the temperature range of 150 to 200 ^{o}C due to the decomposition of the liable oxygen functional groups introduced during oxidation of graphite (Figure 7(b)) (Paredes et al., 2008). The XRD spectra of graphite and GO are shown in Figure 7(c). The XRD pattern of graphite shows a sharp peak at 26.2^{o}, which is due to the reflection from (002) plane. Whereasthe sharp peak in the XRD pattern of graphite vanishes after the oxidation treatment and a broad peak observed at a 2θ value of 12^{o}, corresponding to a d-spacing of 7.4 Å. This d-spacing represents, approximately, one-molecular layer thick water trapped between the GO layers (Aboutalebi et al., 2011b). Figure 7(d) shows the Raman spectra of the graphite and GO. The graphite shows sharp peaks at 1582 and 2745 cm^{-1} corresponding to

G band and 2D band, respectively. On the other hand, Raman spectrum of GO shows peaks at 1368 and 1617 cm^{-1} corresponding to the D and G bands, respectively. The G-band is due to Raman active sp^2 hybridized carbon atoms, and D-band is due to the defect that causes double resonance Raman scattering. The shift in G band from 1581 to 1617 cm^{-1} is because the isolated double bonds in GO resonate at higher frequencies than that of graphite (Aboutalebi et al., 2011b). The AFM image of the GO sheets and the height-profile are shown in Figure 7.1 (e). The AFM image clearly reveals the single layer GO. The height-profile shows the thickness of GO sheet as approximately 0.9 nm. The thickness obtained is corresponding to the single layer graphene oxide as reported in the literature (Aboutalebi et al., 2011b).

7.3.2 Dispersion of GO in the Molten Sucrose

The melting point of sucrose reported in the literature is in the range of 169-185 ^oC. Figure 7.2 (a and b) shows the DSC plot and melting point of the sucrose-GO mixtures prepared by ball-milling at GO concentrations in the range of 0 to 1.25 wt.%. The DSC shows the melting point of sucrose without GO as 190^oC. The melting point drastically decreases to 148 ^oC with the addition of 0.15 wt.% of GO. Further increase in the GO concentration from 0.15 to 1.25 wt.% decreases the melting point of the mixture from 148 to 120.7 ^oC. The depression in freezing point of polyethylene glycol by GO incorporation is reported by Wang et al. (2012a); Zhang et al. (2012). In this, the mechanism of freezing point depression is due to hydrogen bonding interactions between GO and polyethylene glycol. The sharp decrease in melting point of sucrose with GO concentration is due to the hydrogen bonding interactions between the sucrose hydroxyls and surface functional groups present on GO sheets.

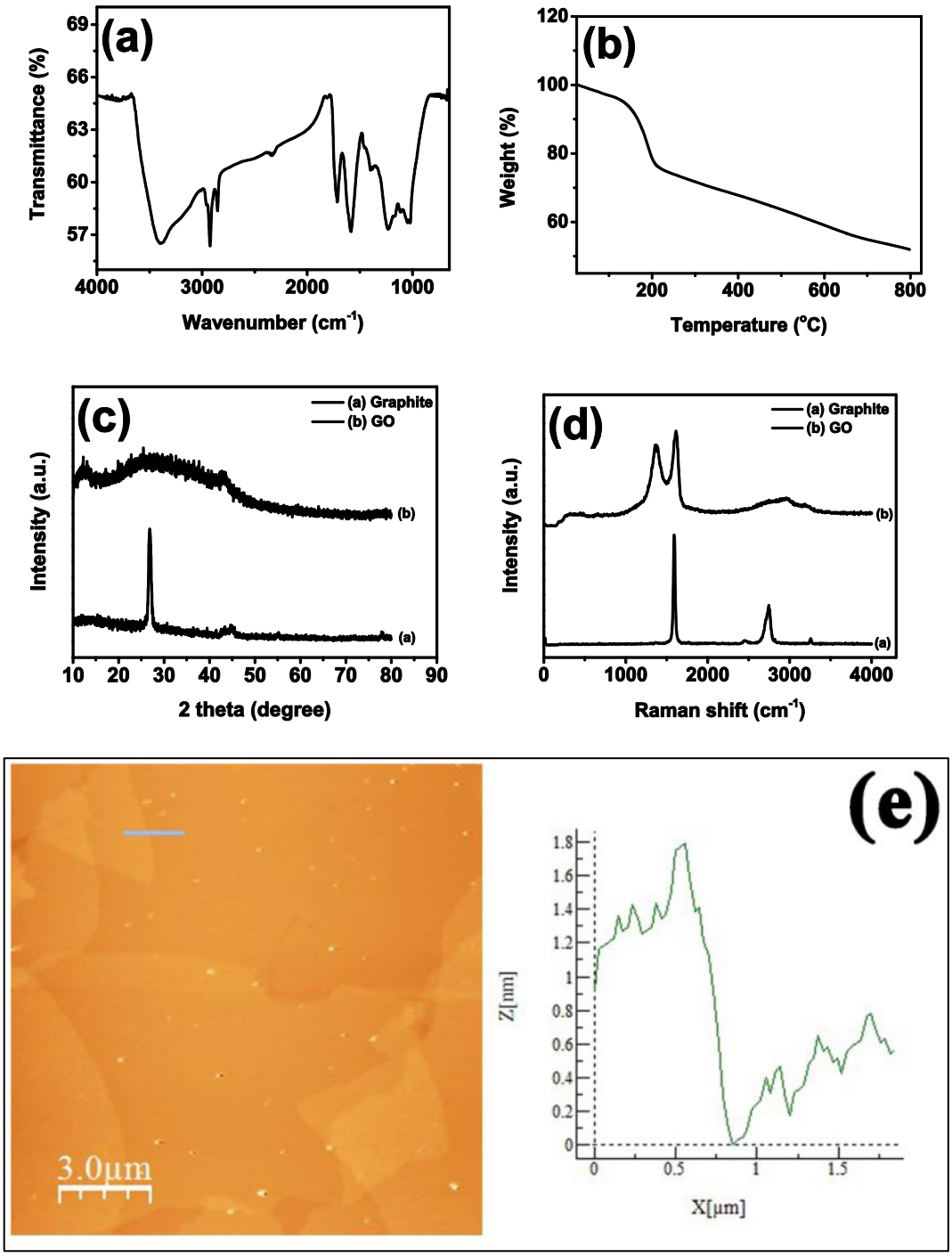

Figure 7.1: (a) FTIR and (b) TGA of the GO (c) XRD spectra and (d) Raman spectra of the graphite and GO and (e) AFM of the GO

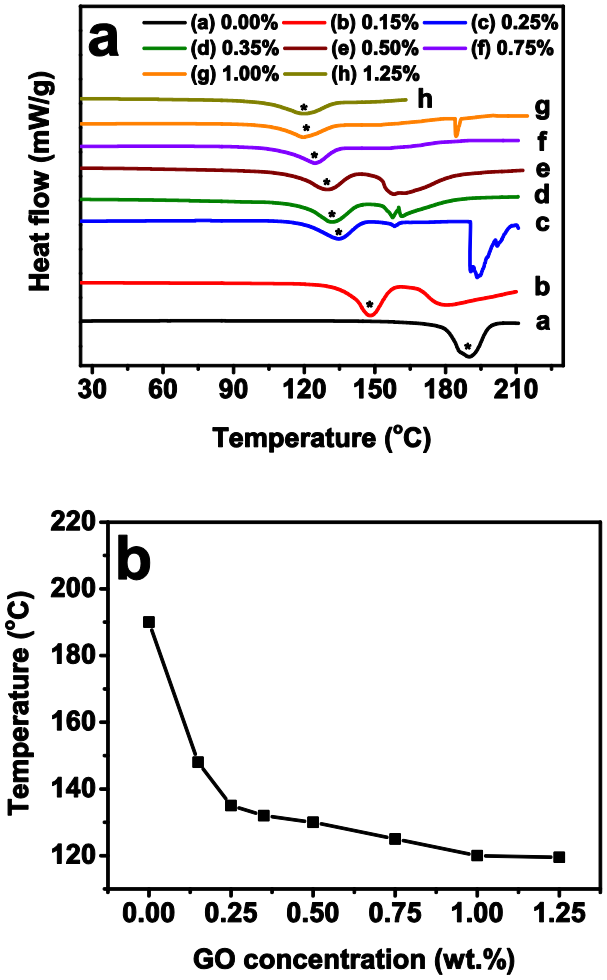

Figure 7.2: (a) DSC plot and (b) melting point of the sucrose-GO mixtures prepared by ball-milling at various GO concentrations

The sucrose-GO mixtures obtained by ball milling are melted in glass trays at a temperature slightly higher than the melting point determined from DSC. The GO disperses in the molten sucrose during melting of sucrose-GO mixtures. The rheological studies are carried out to understand the dispersion of the GO in the molten sucrose. Figure 7.3 shows the shear rate versus viscosity plots of the GO dispersions in molten sucrose at various GO concentrations measured at 120 ^{o}C (foaming temperature). The viscosity of the molten sucrose without GO is in the range of 17.6 to 13.4 Pa.s at shear rates in the range of 0.1 to 2000 s^{-1}. The GO dispersions in molten sucrose show shear thinning flow behavior and the shear thinning nature increases with an increase in the GO concentration. At the low shear rates, the GO dispersions show viscosity higher

than that of molten sucrose. However, at the higher shear rates the viscosity of GO dispersions with GO concentrations in the range of 0.15 to 1 wt.% fall below that of molten sucrose. The viscosity of GO dispersions in molten sucrose measured at a shear rate of 10 s^{-1} increases gradually from 13.7 to 38 Pa.s when the GO concentration increases from 0 to 0.75 wt.% (Inset of the Figure 7.3). After that, the viscosity of the dispersions increases rapidly from 38 to 179 Pa.s when the GO concentration increases from 0.75 to 1.25 wt.%. The hydrogen bonding interactions between the GO surface functional groups and sucrose hydroxyls promote the dispersion of GO in molten sucrose. The slow viscosity increase up to 0.75 wt.% of GO indicates its uniform dispersion. The rapid increase in viscosity beyond 0.75 wt.% shows the agglomeration of GO due to the hydrogen bonding interactions between the GO. It appears that, at higher shear rates, the sucrose to GO and GO to GO hydrogen bonding interactions break resulting in a decrease of viscosity below that of bare molten sucrose.

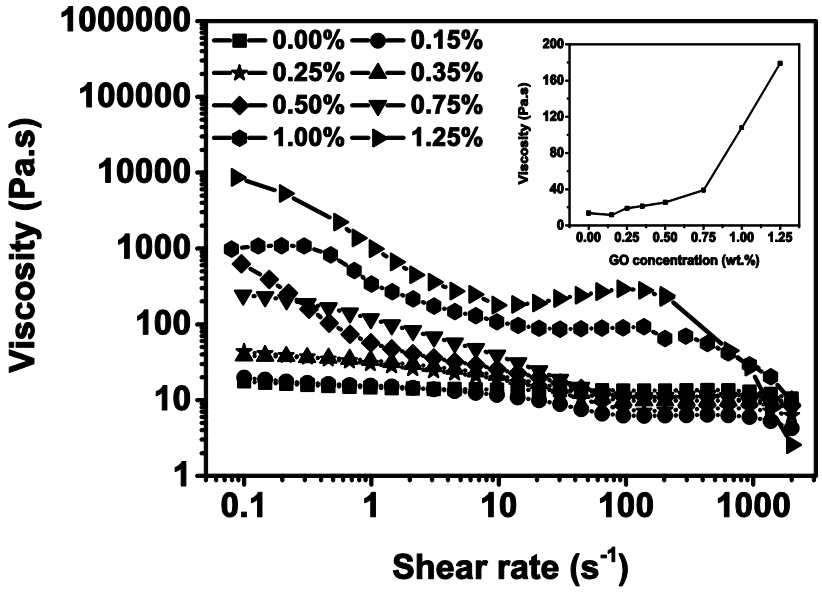

Figure 7.3: Shear rate versus viscosity plot of the GO dispersions in molten sucrose prepared at various GO concentrations at 120 ^{o}C (Inset shows the GO concentration versus viscosity plot)

7.3.3 Foaming and Setting Characteristics

The GO dispersions in molten sucrose undergo foaming and setting at 120 ^{o}C in an air oven. However, the neat molten sucrose is not foaming at 120 ^{o}C even after 120 h. Thus, the carbon foam without GO, for comparison, is prepared by foaming molten sucrose at 130 ^{o}C. The molten sucrose without GO takes nearly 72 h for foaming and 120 h for the foam setting at 130 ^{o}C. Figure 7.4 shows the foaming time, foam setting time, and foam rise of GO dispersions in molten sucrose at various GO concentrations. The foaming time of GO dispersions in molten sucrose decreases from 48 to 1.5 h when the GO concentration increases from 0.15 to 1.25 wt.%. On the other hand, the total time for foaming and setting decreases from 72 to 12 h when the GO concentration increases from 0.15 to 1.25 wt.%. Though faster foaming and foam setting of GO dispersions is possible at higher temperatures, the solid organic foams produced at temperature higher than 120 ^{o}C have large and non-uniform cells. The time for foaming and foam setting is lower in the case of sucrose-GO system when compared to the MWNT-sucrose and AC powder-sucrose systems, even though, the foaming temperature is lower. This is due to the higher catalytic activity of GO because of the presence of a large number of acidic functional groups.

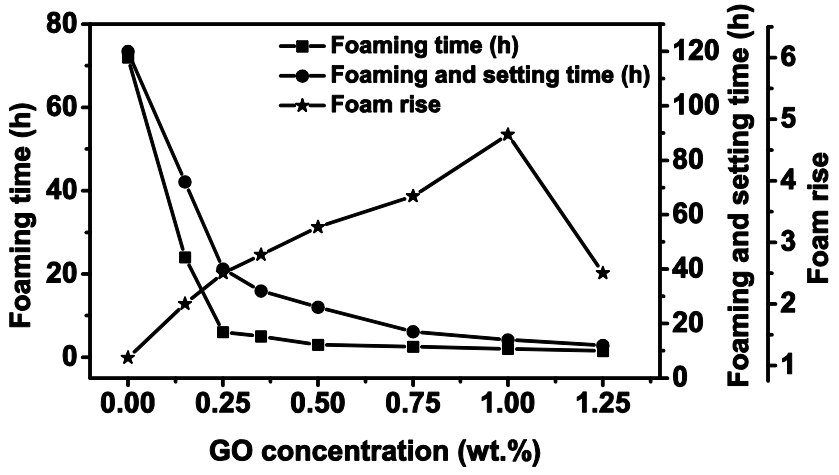

Figure 7.4: Foaming time, foam setting time and foam rise of the GO dispersions in molten sucrose at various GO concentrations at 120 ^{o}C (Foaming temperature for molten sucrose without GO is 130 ^{o}C)

The decrease in foaming time and foam setting time with an increase in GO concentration indicates that the GO catalyzes the –OH to –OH condensation reactions responsible for the foaming and setting of molten sucrose. This is supported by the measurement of variation of viscosity with time of GO dispersions at the foaming temperature (120 ^{o}C). Figure 7.5 shows the viscosity variation with time of the GO dispersions in molten sucrose measured at 120 ^{o}C at a constant shear rate of 10 s^{-1}. The viscosity of the molten sucrose without the GO remains more or less constant for a period of six hours. On the other hand, the GO dispersions in molten sucrose show a gradual increase in viscosity up to a certain time and then a rapid increase with time. The time at which the rapid increase in viscosity observed decreases with an increase in GO concentration. The rapid increase in viscosity is observed at 2 and 0.5 h, respectively, for GO dispersions at GO concentrations of 0.15 and 0.75 wt.%. At GO concentrations beyond 0.75 wt.%, viscosity measurement with time is difficult due to its rapid foaming. In addition to the –OH condensation between sucrose molecules, the condensation of sucrose hydroxyl with –OH and –COOH groups of GO is also expected. The faster –OH condensation results in the formation of large volume of water vapour that creates a large number of bubbles in the GO dispersions. These bubbles are stabilized by the increase in viscosity of the GO dispersions resulting in faster foaming. The GO catalyzed –OH condensations continue after the foaming. The continued GO catalyzed –OH condensation reactions are responsible for the decrease in foam setting time with an increase in GO concentrations.

Figure 7.6 (a and b) shows the TG and DTG in an argon atmosphere of solid organic foams prepared at various GO concentrations. The solid organic foam without GO shows a single stage thermal decomposition with a peak at 276 ^{o}C in the DTG. On the other hand, the solid organic foams prepared from GO dispersions decompose in two steps, a low-temperature step, and a high-temperature step. The DTG peak corresponding to the low-temperature decomposition shifts to lower temperatures with an increase in GO concentration. On the other hand, DTG peak corresponding to the high-temperature decomposition shifts to higher temperatures with an increase in GO concentration.

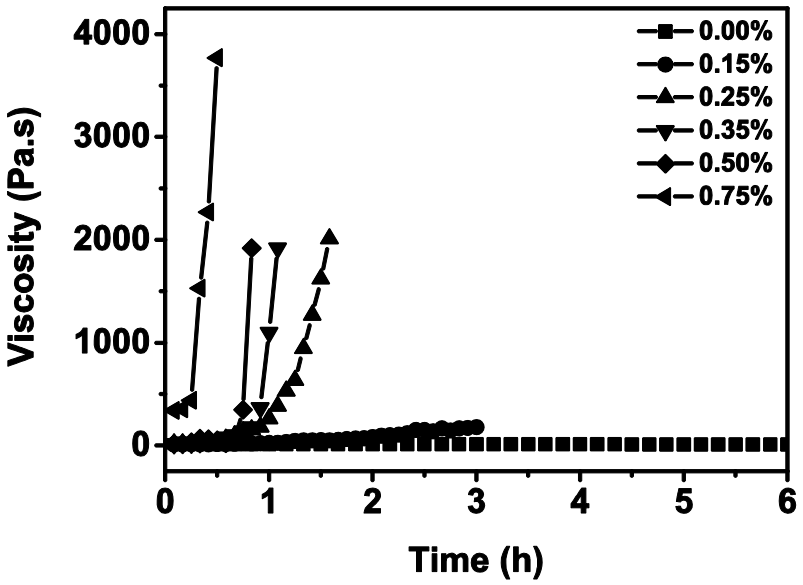

Figure 7.5: Time versus viscosity of the GO dispersions in molten sucrose at various GO concentrations measured at a shear rate of 10 s^{-1} at 120 ^{o}C

The solid organic foam without GO leaves a char residue of 24 wt.% at 900 ^{o}C. The char residue at 900 ^{o}C increases from 24 to 30 wt.% when the GO concentration increases from 0 to 1.25 wt.%. The low-temperature decomposition of the solid organic foams is due to the continued –OH condensations. The shift in the low-temperature DTG peak to lower temperatures with an increase in GO concentration is due to the catalytic activity of GO towards the –OH condensation. The low-temperature decomposition results in the formation of highly cross-linked thermally stable carbon-rich structures containing C-O-C linkages. These C-O-C linkages are formed by the condensation between sucrose hydroxyls, sucrose hydroxyl and GO hydroxyls and between GO hydroxyls. It appears that the C-O-C linkages involving the GO are more thermally stable due to its aromatic nature (Pohjanlehto et al., 2014). The high-temperature decomposition is due to the formation of CO from the cross-linked carbon-rich structure containing the C-O-C linkages. The shift in DTG peak corresponding to the high-temperature decomposition to higher temperatures with an increase in GO concentration is due to the increase in the number of C-O-C linkages involving GO. During the dehydration and carbonization of the solid organic

foams, the GO undergoes reduction to form graphene (McAllister et al., 2007; Schniepp et al., 2006).

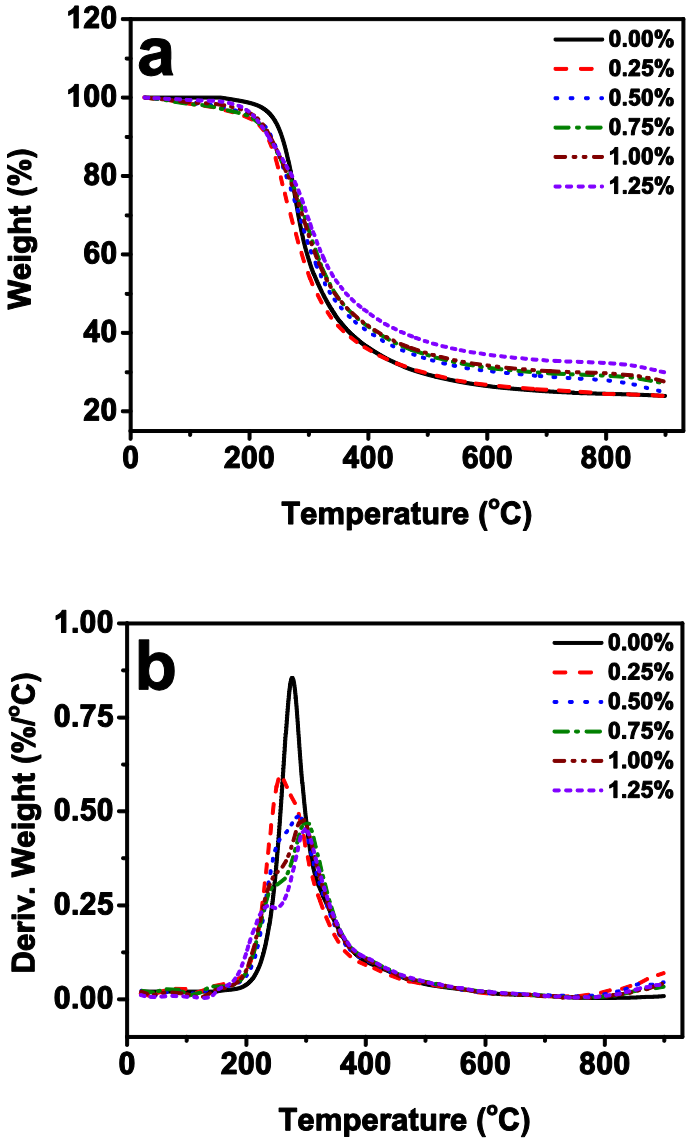

Figure 7.6: (a) TGA and (b) DTG of the solid organic foams prepared at various GO concentrations

The thermal decomposition of GO produces nearly 52 wt.% of graphene as evidenced from the TGA as shown in Figure 7.1 (b). The solid organic foams without GO yield 24 wt.% carbon at 900 °C. Calculations based on the carbon yield from solid organic foam without GO and graphene yield from GO show that the carbon composite foams prepared at GO concentrations in the range of 0.25 to

1.25 wt.% of sucrose contain graphene concentrations in the range of 0.54 to 2.71 wt.%.

7.3.4 Density and Microstructure

The solid organic foams obtained after foaming and setting are dehydrated and carbonized at 200 and 900 ^{o}C, respectively. Figure 7.7 shows the density of the graphene reinforced carbon composite foams prepared at various GO concentrations. The bulk density of the carbon foam prepared without GO is 0.22 g/cm^3 (foaming temperature is 130 ^{o}C). The bulk density of the carbon composite foams decreases from 0.25 to 0.13 g/cm^3 when the GO concentration increases from 0.15 to 1 wt.% of sucrose. Further, increase in GO concentration to 1.25 wt.% results in an increase in bulk density to 0.28 g/cm^3.

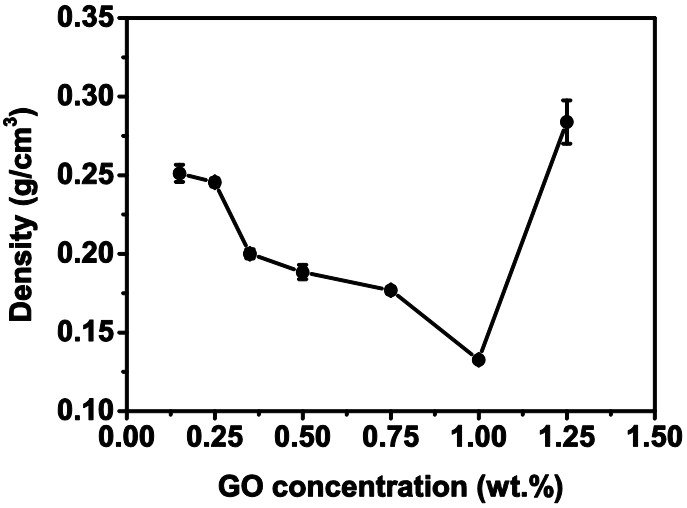

Figure 7.7: Density of the graphene reinforced carbon composite foams prepared at various GO concentrations

Figure 7.8 shows the SEM microstructures of carbon composite foams prepared at various GO concentrations. The carbon composite foam at GO concentrations in the range of 0.15 to 1 wt.% shows cellular structure with nearly spherical cells. The cells are interconnected through circular or oval shaped pores. The size and number of interconnecting pores increase with an increase in GO

concentration. On the other hand, the carbon composite foam prepared at 1.25 wt.% GO shows highly irregular shaped cells. The irregular cells are due to bubble collapse as evidenced from the decrease in foam rise. The cell size measured from the SEM images using the ImageJ software is shown in Figure 7.9. The cell size of the carbon foam prepared without GO is 0.895 mm. The cell size of carbon composite foam increases from 0.35 to 0.86 mm when the GO concentration increases from 0.15 to 1 wt.%. The accurate measurement of cell size of the composite foam prepared at a GO concentration of 1.25 wt.% is difficult due to its highly irregular shape.

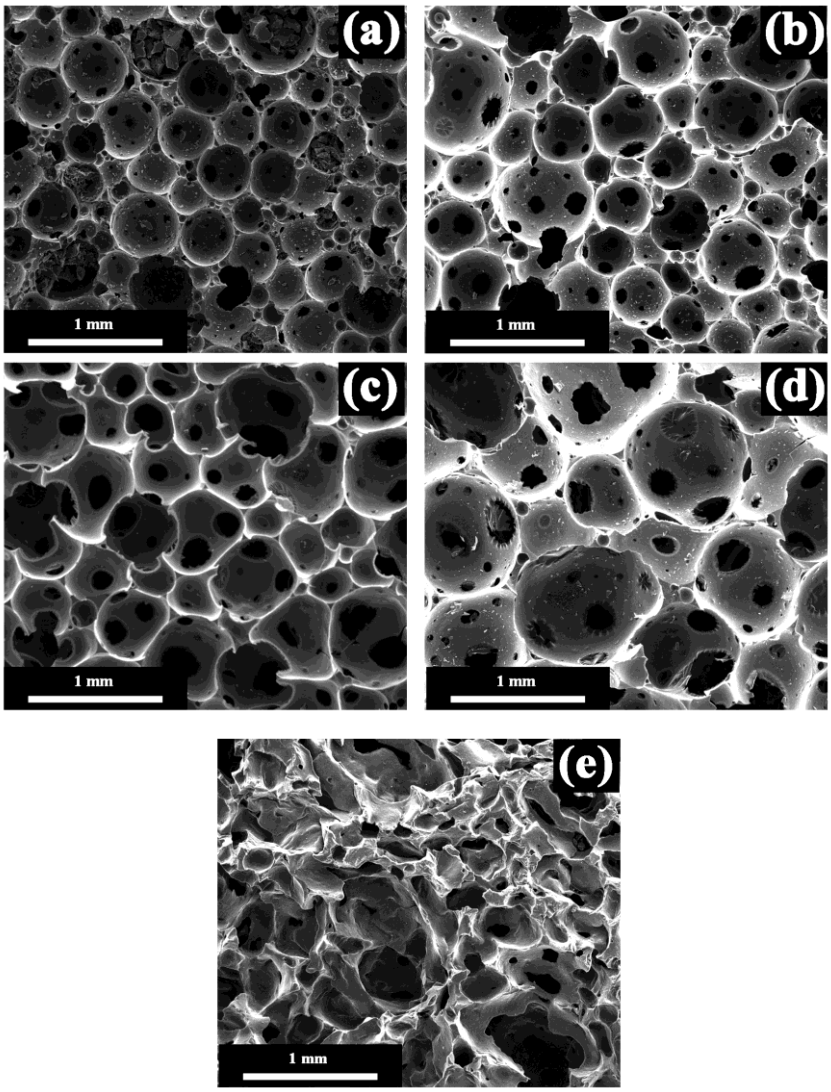

Figure 7.8: SEM micrographs of the graphene reinforced carbon composite foams prepared at various GO concentrations (a) 0.25 wt.% (b) 0.5 wt.% (c) 0.75 wt.% (d) 1.00 wt.% and (e) 1.25 wt.%

The increase in cell size of carbon foams with an increase in GO concentration from 0.15 to 1 wt.% is due to the rapid growth of bubbles as a result of the faster production of water vapour by enhanced –OH to –OH condensation. However, at the GO concentration of 1.25 wt.%, the bubbles collapse as the pressure developed inside the bubbles is higher than the strength of the cell walls (Wang et al., 2009a). The decrease in density with an increase in GO concentration up to 1 wt.% is due to the observed increase in the cell size. The increase in foam density observed at a GO concentration from 1 to 1.25 wt.% is due to the densification by foam collapse.

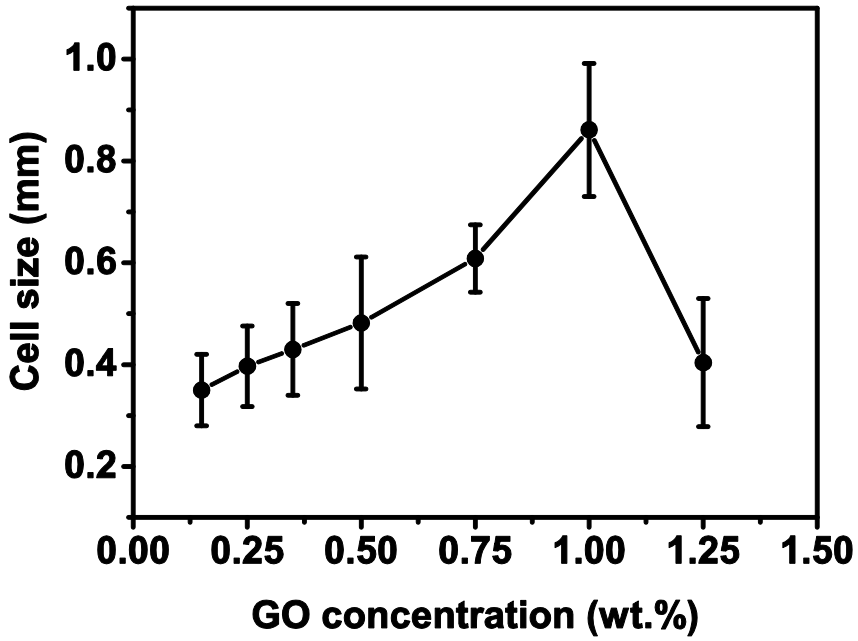

Figure 7.9: Cell size of the graphene reinforced carbon composite foams prepared at various GO concentrations

7.3.5 Textural Properties

Figure 7.10 (a) shows the nitrogen adsorption-desorption isotherms of the carbon foams prepared at various GO concentrations. The carbon foam prepared without GO shows a narrow adsorption at $p/p_o < 0.02$ which corresponds to type I isotherm, according to IUPAC classification. The narrow adsorption is due to the

intrinsic micropores in the cell walls and struts of the carbon foam. Figure 7.10 (b) shows the DFT PSD of the carbon composite foams prepared at various GO concentrations. The DFT PSD plots show that the micropores present in the carbon composite foams is in the size range of 11 to 15 Å. Figure 7.11 shows the specific surface area and total pore volume of the carbon composite foams prepared at various GO concentrations. The surface area of the carbon composite foams increases from 367 to 520 m^2/g when the GO concentration increases from 0 to 0.25 wt.%. Further increase in GO concentration decreases the surface area. On the other hand, the total pore volume increases from 0.18 to 0.25 cm^3/g when the GO concentration increases from 0 to 0.5 wt.%. Further increase in GO concentration results in a decrease of pore volume. However, the microporosity increases with GO concentrations up to 0.25 wt.% and then remains more or less constant. The mechanism of the micropore formation in the cell walls and struts of carbon foams is due to the *in situ* activation as discussed in Chapter 2. That is, the micropores are produced by the reaction of oxygen, retains as a result of –OH to –OH condensation, with the carbon at higher temperatures to form CO. It appears that the high catalytic activity of GO promotes–OH to –OH condensation that retain more amount of oxygen as C-O-C linkages at temperature less than 400 ^oC. The increase in pore volume, microporosity and surface area up to a GO concentration of 0.25 wt.% is due to the removal of this oxygen as CO at higher temperatures. The decrease in surface area and pore volume at higher GO concentrations is due to the agglomeration by stacking of GO layers in molten sucrose. The carbon composite foams prepared at GO concentrations in the range of 0 to 1.25 wt.% show the CO_2 adsorption capacity in the range of 2.4 to 3.34 mmol/g.

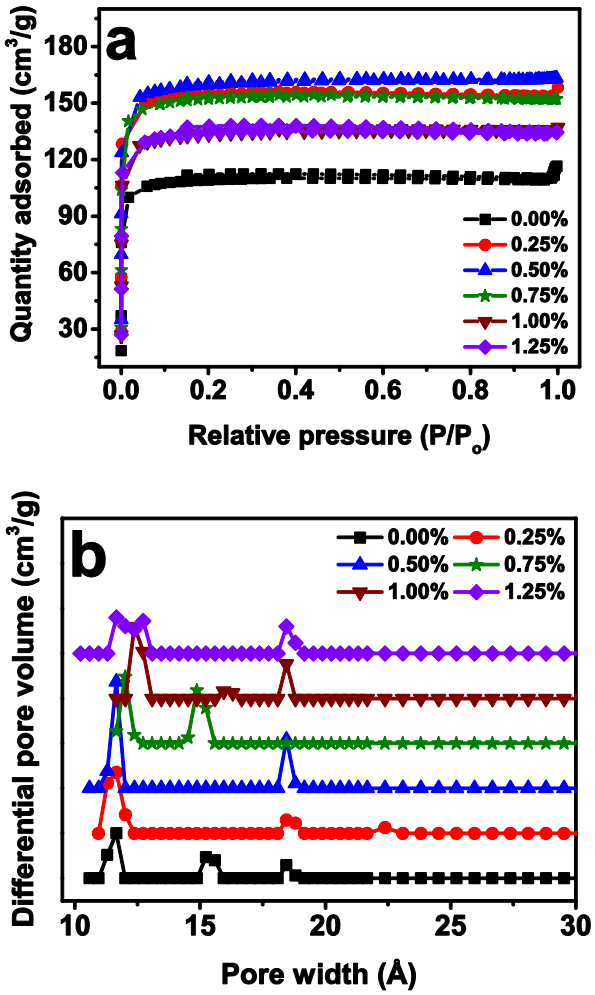

Figure 7.10: (a) Nitrogen adsorption-desorption isotherms and (b) DFT PSD of the graphene reinforced carbon foams prepared at various GO concentrations

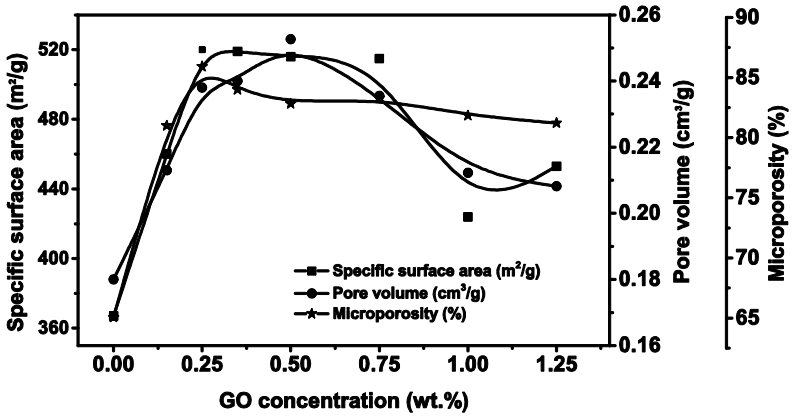

Figure 7.11: Specific surface area, pore volume and microporosity of the graphene reinforced carbon composite foams prepared at various GO concentrations

7.3.6 Compressive Strength

Figure 7.12 shows the stress-strain graphs of carbon composite foams prepared at various GO concentrations. The stress-strain graphs show a typical behavior of the elastic, rigid, solid foam with an initial linear elastic region followed by a stress maximum and finally a densification region. Figure 7.13 shows the compressive strength and specific compressive strength of the carbon composite foams at various GO concentrations. The compressive strength increases from 1.3 to 5.2 MPa when the GO concentration increases from 0 to 0.25 wt.%. Further increase in GO concentration to 1 wt.% results in the decrease of compressive strength to 0.97 MPa. After that, the compressive strength shows a slight increase to 1.5 MPa when the GO concentration increases to 1.25 wt.%. Similarly, the Young's modulus increases from 30 to 92.4 MPa when the GO concentration increases from 0 to 0.25 wt.%. Further increase in GO concentration to 1.25 wt.% results in the decrease of Young's modulus to 26.4 MPa. The graphene reinforced carbon composite foams shows a maximum specific compressive strength of 21.3 MPa/g/cm/^{3} at 0.25 wt.% of GO. That is, the maximum compressive strength and specific compressive strength observed is at a graphene concentration of 0.54 wt.% of the carbon matrix. The increase in the compressive strength with the incorporation of GO is due to the reinforcement effect of the graphene produced by the *in situ* reduction of GO. The compressive strength maximum indicates uniform dispersion of GO in the molten sucrose up to a GO concentration of 0.25 wt.%.The uniform dispersion of GO creates maximum graphene-carbon matrix interface that facilitates effective matrix to reinforcement stress transfer. The decrease in compressive strength at GO concentrations above 0.25 wt.% is due to the agglomeration of GO in molten sucrose. The agglomeration of GO at concentrations above 0.25 wt.% is clearly evidenced from the high magnification SEM of the strut region of the carbon composite foams. Figure 7.14 shows the SEM micrographs of the fractured strut region of the graphene reinforced carbon composite foams. The uniform distribution of graphene can be seen up to a GO concentration of 0.25 wt.%. On the other hand, graphene agglomerates are clearly visible at the GO concentrations above 0.25

wt.%. The extent of agglomeration increases with an increase in GO concentration. The increase in compressive strength observed at a GO concentration of 1.25 wt.% is due to the higher density and smaller cell size of the carbon composite foam.

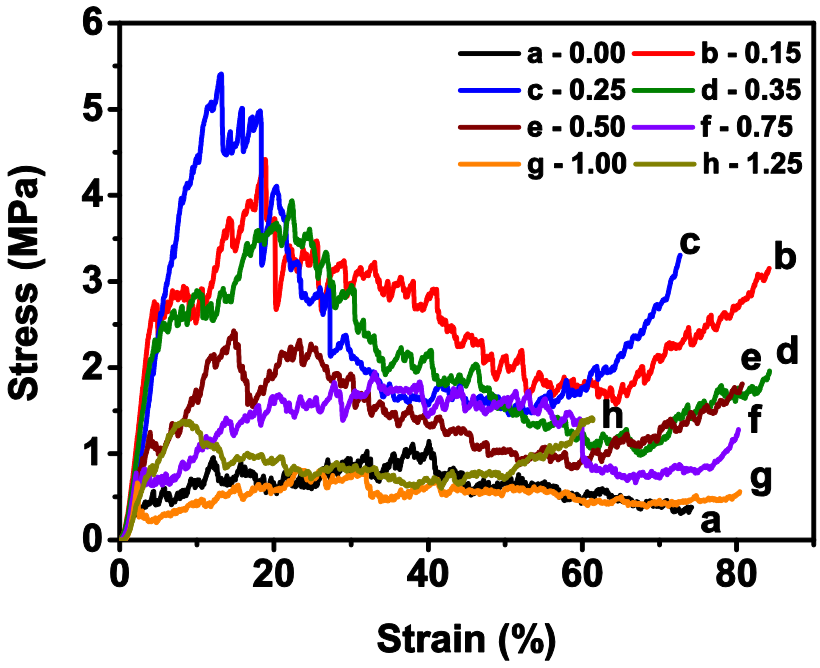

Figure 7.12: Stress-strain plots of the graphene reinforced carbon composite foams prepared at various GO concentrations

The maximum percentage improvement in the specific compressive strength achieved is 133. The maximum specific compressive strength obtained for graphene reinforced carbon composite foam is more or less same as that obtained for MWNT reinforced carbon composite foam reported in chapter 6. On the other hand, the maximum specific compressive strength of graphene reinforced carbon composite foam is higher than that of (17 MPa/g/cm^3) carbon fiber reinforced carbon composite foam reported in Chapter 5.The maximum specific strength observed is at a lower reinforcement concentration in the case of GO when compared to MWNT (0.5 wt.%) and carbon fiber (2 wt.%). This indicates that GO is a more effective reinforcement than MWNT and carbon fiber because of its high surface area.

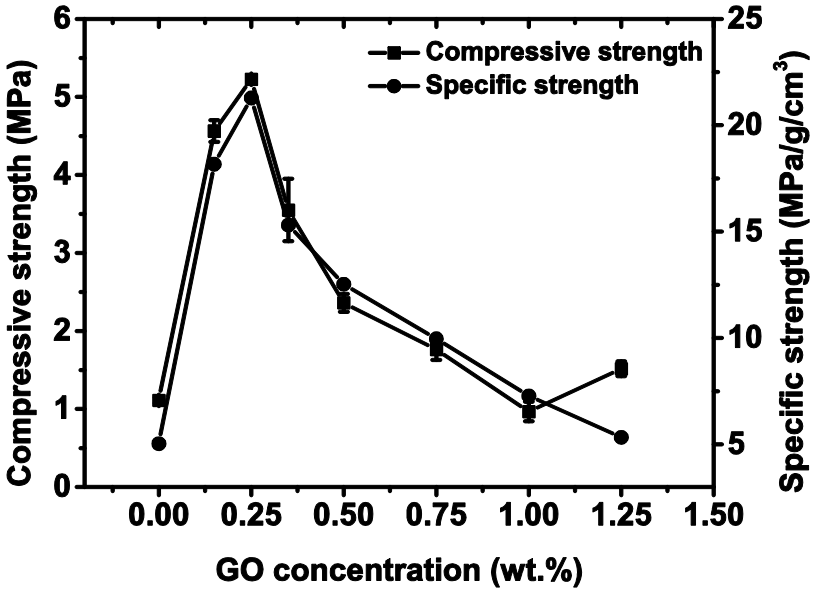

Figure 7.13: Compressive strength and specific strength of the graphene reinforced carbon composite foams prepared at various GO concentrations

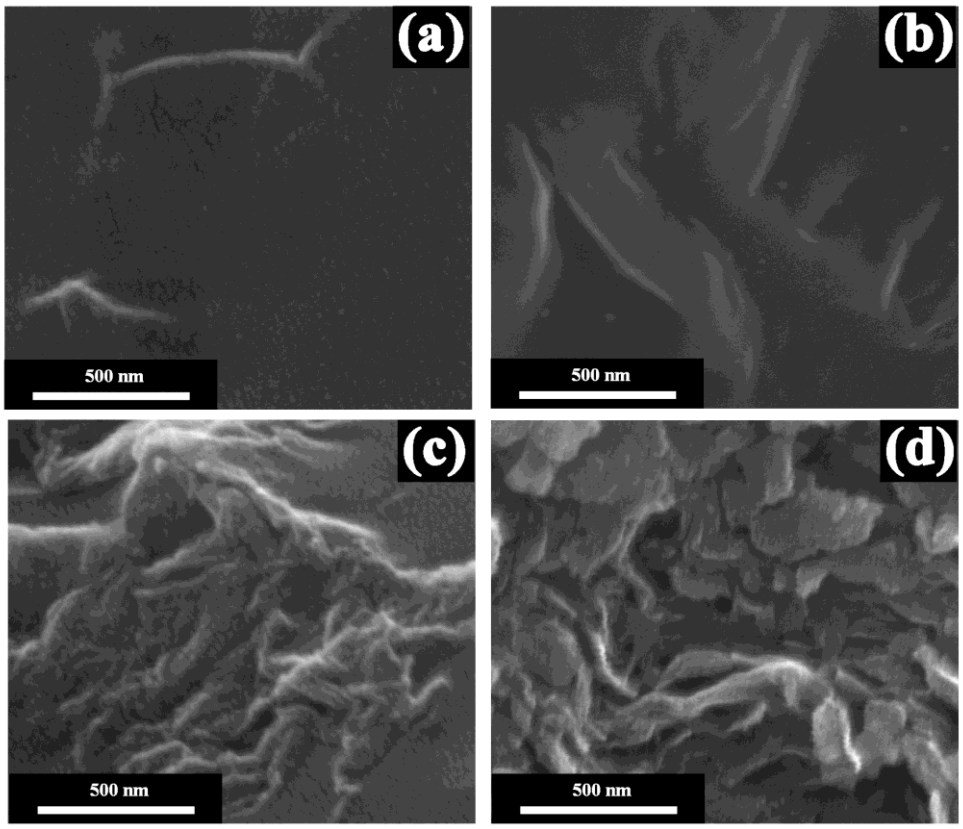

Figure 7.14: Fractured strut region of the graphene reinforced carbon composite foam with various GO concentrations (a – 0.25 wt.%; b – 0.5 wt.%; c – 0.75 wt.%; d – 1.25 wt.%)

7.3.7 Electrical Conductivity and EMI Shielding Properties

Figure 7.15 shows the electrical conductivity of the carbon composite foams. The electrical conductivity of carbon foam without GO is 3.5 S/cm. The electrical conductivity increases from 3.5 to 14 S/cm when the GO concentration increases from 0 to 0.15 wt.%. Further increase in GO concentration up to 1 wt.% results in a decrease in the electrical conductivity to 3.1 S/cm. After that, the electrical conductivity increases to 4.8 S/cm when the GO concentration increases to 1.25 wt.%. This indicates that the percolation of graphene in the carbon matrix takes place at a GO concentration of 0.15 wt.%. The decrease in electrical conductivity at GO concentrations higher than 0.15 wt.% is attributed to the agglomeration of the graphene in the carbon matrix. Various authors reported the decline of electrical conductivity at higher graphene concentrations in the graphene reinforced polymer matrix composites due to agglomeration of graphene (Chen et al., 2003a). The increase in electrical conductivity observed at GO concentration of 1.25 wt.% is due to the increase in carbon foam density.

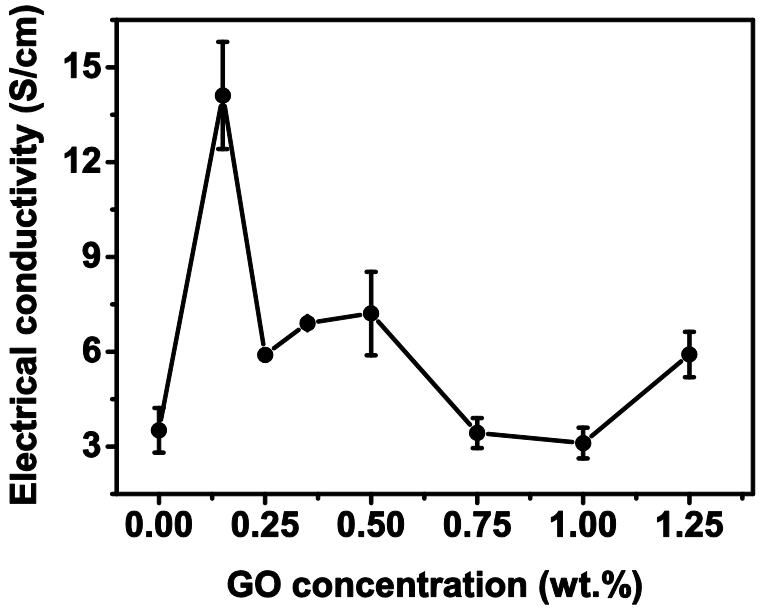

Figure 7.15: Electrical conductivity of the carbon composite foams prepared at various GO concentrations

Figure 7.16 (a) is a typical graph showing the shielding effectiveness (SE) of graphene reinforced carbon composite foam in X-band region (8.2 – 12.4 GHz). The SE is almost constant in the entire X-band region for the carbon composite foams at a particular GO concentration. The total SE has contributions from absorption, reflection, and multiple reflections (Kumar et al., 2013a). All the graphene reinforced carbon composite foams show SE greater than 10 dB and thus ignored the loss associated with the multiple reflections (Kumar et al., 2013a). The absorption loss is dominating the reflection loss at all GO concentrations. Figure 7.16 (b) shows the effect of GO concentration on the total, absorption and reflection SE of carbon composite foams. The variation in reflection contribution with GO concentration is marginal (8.3 to 10.3 dB). On the other hand, the absorption contribution increases from 20.6 to 28.3 dB when the GO concentration increases from 0 to 0.15 wt.%. After that the absorption contribution decreases to 12.5 dB when the GO concentration increases to 1.0 wt.%. Further increase in GO concentration to 1.25 wt.% produces a marginal increase in the EM absorption. The trend in total SE follows the trend in the absorption contribution. The total SE increases from 30 to 38.6 dB when the GO concentration increases from 0 to 0.15 wt.%. After that, the total SE gradually decreases to 21.2 dB when the GO concentration increases to 1 wt.%. Further increase in GO concentration to 1.25 wt.% increases the total SE to 23.1 dB. The trend in variation of SE of the carbon composite foams observed with GO concentrations is same as the trend in variation of electrical conductivity. Therefore, variation in SE of carbon composite foams with GO concentration is mainly due to the variation in their electrical conductivity (Kumar et al., 2013a; Kumar et al., 2013b; Kumar et al., 2014a; Kumar et al., 2014b).

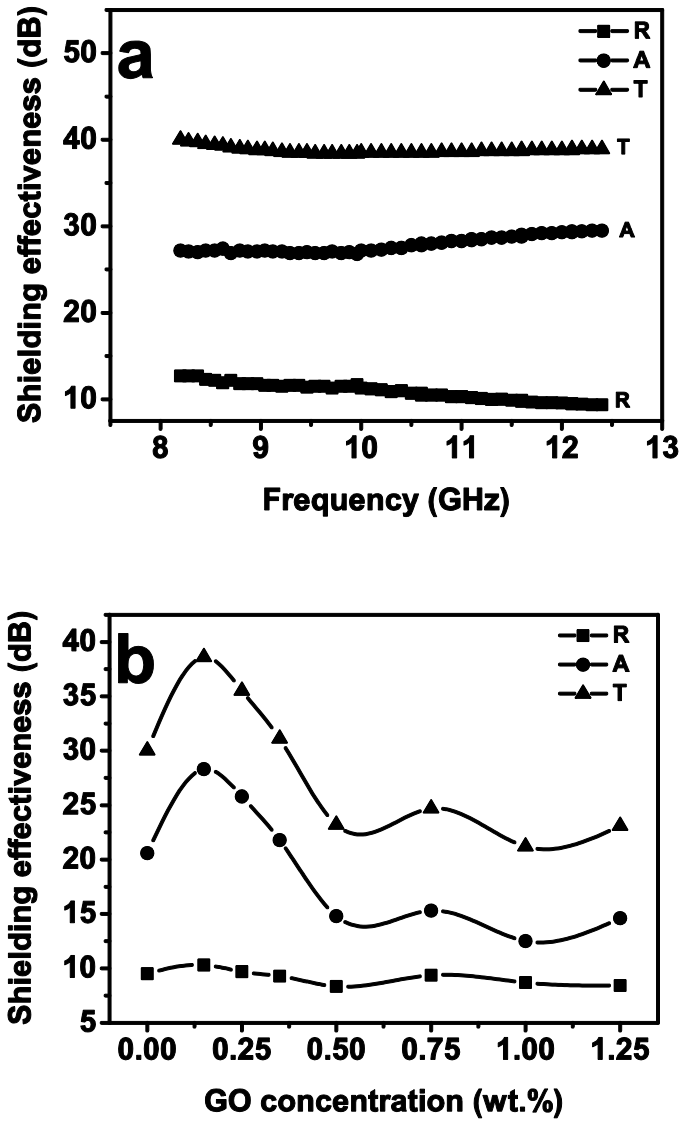

Figure 7.16: (a) EMI SE of the carbon composite foam at GO concentration of 0.15 wt.% in X-band region and (b) Reflection, absorption and total SE of the carbon composite foams prepared at various GO concentrations at 11 GHz

The specific shielding effectiveness (SSE), the attenuation of EM per unit density, is an important parameter, especially for EMI shielding materials used in aerospace applications. Figure 7.17 shows the SSE of graphene reinforced carbon composite foams as a function of GO concentration. The carbon foam without GO shows a SSE of 136 dB/g/cm^3. A maximum SSE of 160 dB/g/cm^3 is observed at a GO concentration of 1 wt.%. A drastic decrease in SSE with GO concentration from 1 to 1.25 wt.% is due to the rapid increase in foam density due to foam

collapse. The observed SSE of graphene reinforced carbon composite foams is much higher than that of (10 dB/g/cm^3) copper and the highest reported SSE (130 dB/g/cm^3) of carbon foams (Kumar et al., 2013a; Saini et al., 2012; Saini et al., 2013). On the other hand, the maximum SSE of graphene reinforced carbon composite foam is lower than that of (166 dB/g/cm^3) MWNT reinforced carbon composite foams.

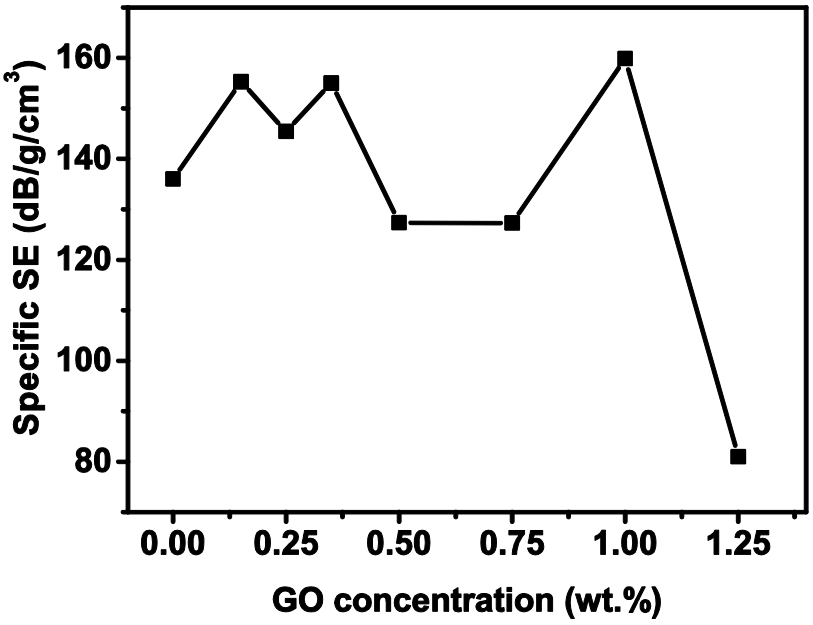

Figure 7.17: SSE of graphene reinforced carbon composite foams as a function of GO concentration

7.5 Conclusions

Graphene reinforced carbon composite foams are prepared by the thermo-foaming of GO dispersions in molten sucrose followed by dehydration and carbonization. The melting point of the sucrose in sucrose-GO mixtures decreases from 190 to 120 ^{o}C when the GO concentration increases from 0 to 1.25 wt.% due to the hydrogen bonding interactions of sucrose with GO surface functional groups. The foaming time and foam setting time decrease with an increase in GO concentration as the acidic functional groups present in GO catalyzed the –OH to –OH condensation which is responsible for the foaming and

setting of molten sucrose.The density of the graphene reinforced carbon composite foams decreases from 0.25 to 0.13 g/cm^3 and cell size increases from 0.35 to 0.86 mm when the GO concentration increases from 0.15 to 1 wt.%. Further increase in GO concentration to 1.25 wt.% results in the increase of foam density and decrease in cell size due to foam collapse. The compressive strength and specific compressive strength increase with an increase in the GO concentration up to 0.25 wt.% and then decrease. The decrease in compressive strength observed at GO concentration beyond 0.25 wt.% is due to the agglomeration of graphene as evidenced from SEM micrographs. The maximum compressive strength and specific compressive strength observed are 5.2 MPa and 21.3 MPa/g/cm^3, respectively. The electrical conductivity and EMI SE of the graphene reinforced carbon composite foams increase with an increase in the GO concentration up to 0.15 wt.% and then decrease due to graphene agglomeration. The maximum SE achieved is 38.6 dB at a GO concentration of 0.15 wt.%. The maximum SSE of the graphene reinforced carbon composite foam obtained is 160 dB/g/cm^3.

CHAPTER 8

PROCESSING AND CHARACTERIZATION OF CARBON COMPOSITE FOAMS FROM AQUEOUS SUCROSE RESIN AND ACTIVATED CARBON POWDER

8.1 Introduction

The carbon foam from sucrose is originally prepared by an aqueous sucrose resin-based method (Prabhakaran et al., 2007). In this, a resin obtained by acid catalyzed polymerization of sucrose in an aqueous solution is foamed and set at 120 ºC to produce the solid organic foams. The carbon foams are prepared by carbonization of the solid organic foams at 1400 ºC. The carbon foams produced by this process have low density and poor mechanical strength. The low density and poor mechanical strength are due to the relatively low carbon yield. Moreover, the solid organic foams undergo large shrinkage (~70%) during carbonization that results in warping or cracking during carbonization of large solid organic foam bodies. The mechanical strength of the carbon foams can be improved by incorporating reinforcing carbon additives such as carbon powder, carbon short fiber, MWNT and graphene (Amini et al., 2011; Fawcett and Shetty, 2010; Harikrishnan et al., 2007; Leroy et al., 2007; Li et al., 2007b; Li et al., 2010a, 2011c; Wang et al., 2009b; Wu et al., 2009; Zhu et al., 2007). In addition to the reinforcement effect, the additives increase the carbon yield and thereby decrease the volume shrinkage during carbonization. This may facilitate the preparation of large carbon foam bodies from aqueous sucrose resin.

Various reinforcing additives such as AC powder, milled carbon fiber, MWNT and GO are incorporated in aqueous sucrose resin with a view to increase the mechanical strength of carbon foams. The success was limited only to the

preparation of reinforced carbon foam from AC powder incorporated aqueous sucrose resin. The problems observed with the other reinforcing additives are summarized in Table 8.1

Table 8.1: Observations with various reinforcing carbon additives in aqueous sucrose resin

S.No.	Reinforcing additive	Observations	Suitable/not suitable for carbon foam preparation
1	Milled carbon fiber	The sedimentation of carbon fiber during foaming leads to the non-homogenous foam structure. A dense layer was formed in the bottom of the glass tray	Not suitable
2	MWNT	Non homogenous foam structure. A dense layer was observed at the bottom of the glass tray	Not suitable
3	GO	Local gelation of the sucrose polymer due to the reaction with the graphene oxide. Large and non-uniform bubbles in the solid organic foam	Not suitable
4	AC powder	Uniform foaming and foam setting	Suitable

The present chapter reports preparation and characterization of carbon composite foams from AC powder dispersions in aqueous sucrose resin. The effect of AC powder particle size and AC powder concentration on dispersion, foaming characteristics and properties of the carbon composite foams are investigated.

8.2 Experimental

8.2.1 Preparation of AC Powder with Different Particle Sizes

The wood-derived amorphous AC powder contained particles in the size range of few micrometers to few hundred micrometers. The powders of different average particle sizes were prepared by ball milling the as received AC powder for various time periods in the acetone medium using a high energy planetary ball mill (Pulveritz, Germany). The ball milling was performed in zirconia bowls using zirconia grinding media of 10 mm diameter at 300 RPM. The AC powder to ball weight ratio used was 1:6. The ball milled AC powder was dried in an air oven at 120 ^{o}C. The particle size measurement of the ball milled AC powder was carried out by laser diffraction using helium-neon laser in a particle size analyzer (Mastersizer 2000, Malvern, UK). The particle size of AC powder after ball milling for various time periods is shown in Figure 8.1. The corresponding particle size data is given in Table 8.2.

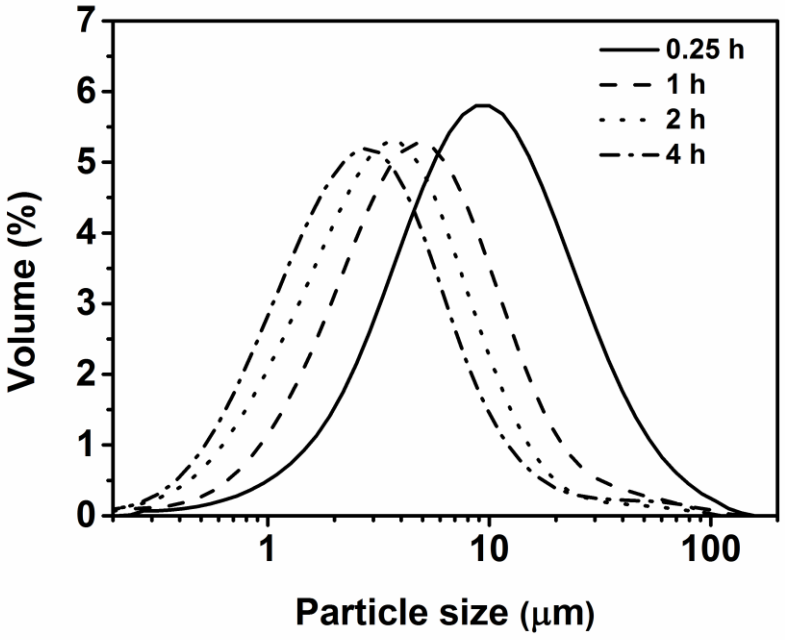

Figure 8.1: Particle size distribution plot of AC powders

Table 8.2: Particle size data of AC powders

Ball milling time (h)	Volume weighed mean (μm)	d-10 (%) (μm)	d-50 (%) (μm)	d-90 (%) (μm)
0.25	15.0	2.78	9.84	32.87
1.00	7.8	1.54	4.96	15.45
2.00	5.4	1.05	3.53	10.49
4.00	4.9	0.89	2.83	9.06

8.2.2 Preparation of the Carbon Composite Foams

An aqueous solution containing 200 g sucrose in 200 ml water was acidified with 2 ml concentrated nitric acid and heated on a hot plate to form a dark honey-like viscous resin. The final volume of the resin was 240 ml. That is, the resin used throughout the work reported in the present chapter contained the organic content equivalent to 200 g sucrose in 240 ml. The flow chart for the preparation of carbon composite foams is shown in Figure 8.2. The dispersions with AC powder to sucrose weight ratios in the range of 0 to 0.40 were prepared by mixing the aqueous sucrose resin with various amounts of AC powder of different particle sizes using a mechanical stirrer for 2 h. The dispersions were transferred to 1.5 liter borosilicate glass trays and heated in an air oven at 120 ºC for 72 h for foaming and setting. The sucrose polymer – AC powder composite foams (solid organic foams) obtained were cut into rectangular bodies of 8 cm x 5 cm x 2 cm size and dehydrated by heating in a muffle furnace at the rate of 2 ºC/h up to 200 ^{o}C. A holding time of 3 h was given at 200 ^{o}C. The dehydrated samples were carbonized at 900 ^{o}C for 2 h in an ultra-high pure argon atmosphere in a tubular furnace. The heating rate used was 2 ^{o}C/min. The samples were unloaded from the furnace after cooling it to room temperature. The same inert atmosphere was maintained throughout the cooling of the furnace. The shrinkage of the samples was calculated from their initial and final dimensions. The density of the carbon composite foams was calculated from their weight and dimensions.

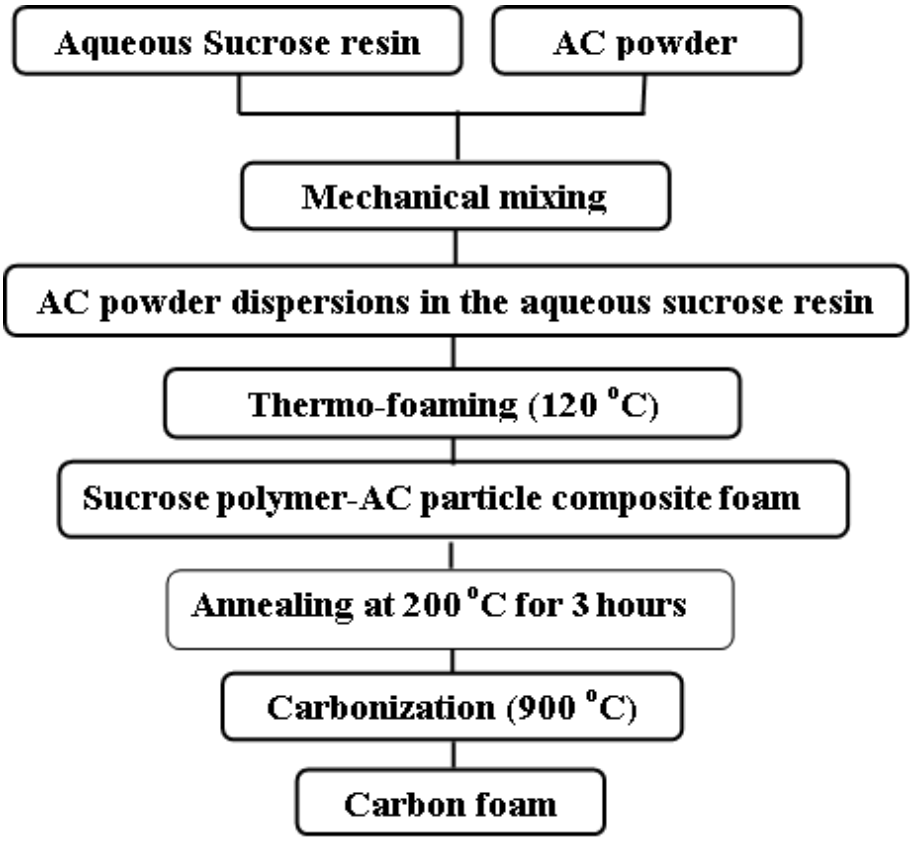

Figure 8.2: Flow chart for the preparation of carbon composite foams

8.2.3 Characterization

The viscosity of the dispersions was measured using an RVT model Brookfield viscometer (Brookfield Engineering Inc. USA). All measurements were taken in the increasing order of the shear rate. The temperature of the dispersions was maintained at 120 ^{o}C during the viscosity measurements with the help of a Thermosel accessory. The foam rise (a measure of foam volume) was calculated as the ratio of the initial height of the AC powder dispersion and the final height of the foam. The samples were physically inspected during foaming and foam setting at an interval of one hour to determine the approximate foaming time and foam setting time. The char yield was taken as the weight retained after dehydration and carbonization of the large (8 cm x 5 cm x 2 cm) solid organic foams. The densities were calculated from the weight and dimension of rectangular carbon composite foam bodies. The microstructure of the carbon composite foams was observed using a Scanning Electron Microscope (SEM, FEI

Quanta FEG200). The cell size of the carbon composite foams was measured using ImageJ software from the SEM microstructure. The compressive strength of the carbon composite foams was measured using a universal testing machine (Instron 5050, Instron USA) at a crosshead speed of 0.5 mm/min with 25 mm x 25 mm x 12 mm samples (ASTM standard C365/C365M-05). The maximum stress in the stress-strain graph was noted as the compressive strength. The thermal conductivity of the carbon composite foam samples was measured using modified transient plane source method (MTPS) at room temperature. The 20 mm x 20 mm x 6 mm samples were used for the thermal conductivity measurements. The reported thermal conductivity is the average of four measurements.

8.2.3.1 Immersion Test and Contact Angle Measurements

The immersion test of the AC powders was conducted to understand the relative wettability of the particles (Binks and Lumsdon, 2000). In this, 50 mg of the AC powder was carefully and evenly dropped on the surface of 20 ml aqueous sucrose resin solution taken in a 30 ml cylindrical glass vial. The time taken for all the powder particles to disappear from the surface by sinking into the resin solution was measured as the immersion time. The immersion times reported were the average of five measurements. The sucrose resin diluted to ten times was used for the immersion time measurement. The contact angle of aqueous sucrose resin on the surface of a monolithic carbon obtained by carbonization of wood was measured using a Goniometer (OCA 20, Dataphysics, Germany). The monolithic carbon surface was thoroughly cleaned with acetone and dried prior to the measurement. The static contact angle was measured by placing the aqueous sucrose resin on the monolithic carbon surface.

8.2.3.2 Machinability and Fire Resistance

Machinability of the carbon composite foams was checked by cutting slots using a universal milling machine (Bharat Fritz Werner Ltd, Bangalore, India) and drilling holes using a drilling machine on the carbon composite foam

bodies of 15 cm x 10 cm x 1.5 cm size. The slots were made using a high speed steel end mill cutter with a diameter of 10 mm at a feed rate of 125 mm/min and at 700 RPM. The holes were made using a drill bit of 8 mm diameter. The evenness of the machined surfaces was observed using a vision inspection system with a CCD colour camera (Vision 300 GL, TESA Technologies, Switzerland) at a magnification of 30x. Fire resistance and ablative property of the carbon composite foams were tested by exposing the carbon composite foam samples of 15 cm x 10 cm x 2 cm size to an oxyacetylene ablation torch. The inner diameter of the nozzle and flow rate of acetylene was 2 mm and 500 L/h, respectively. The distance between the nozzle tip and specimen surface was 10 mm.

8.3 Results and Discussion

8.3.1 Mechanism of AC powder Dispersion in Aqueous Sucrose Resin

The chemistry of formation of the aqueous sucrose resin from sucrose solution containing nitric acid is reported in the literature (Jana and Ganesan, 2009; Prabhakaran et al., 2007). This involves acid catalyzed hydrolysis of sucrose to form glucose and fructose followed by partial oxidation to form hydroxyl carboxylic acids. These molecules are polymerized through –OH to –OH and –COOH to –OH condensation reactions to form the sucrose resin. As the amount of nitric acid used in our study, 1 ml/100g sucrose, is sufficient to oxidize less than 2% glucose and fructose produced from sucrose, the majority of polymerizations are through the –OH to –OH condensation. The polymer obtained is called as sucrose polymer for convenience. The AC powder disperses in the aqueous sucrose resin to form stable dispersions. This is due to the adsorption of sucrose polymer containing large numbers of hydroxyl functional groups on the AC powder particles. It is well-known that hydrophilic colloids like starch and poly (vinyl alcohol) are used for the stabilization of hydrophobic particles in the aqueous medium (Bromley, 1986; Nakamae et al., 1999). In this approach, the hydrophilic colloids adsorb over the hydrophobic particles which increase their interaction with the aqueous medium. In the present case, the hydroxyl groups

present in the sucrose polymer molecules adsorb on the AC particle surface interact strongly with the water medium, promoting their dispersion.

Generally, submicron powders and nanopowders produce stable dispersions in the aqueous medium. As particle size increases the tendency for sedimentation increases. Figure 8.3 is a photograph showing the sedimentation behaviour of the AC powder (15 μm) dispersions in the aqueous sucrose resin and in an aqueous ammonium polyacrylate solution (commonly used dispersant in an aqueous medium). The ammonium polyacrylate used is 1 wt.% of the AC powder. In the case of AC powder dispersions in the aqueous sucrose resin, though the average particle size of the ball milled AC powder is 15 μm, no phase separation by particle settling is observed for the first 6 h. After 6 h, phase separation starts due to slow settling of the AC particles. However, no stable sediment is observed even after ageing the dispersions for one week. On the other hand, the AC powder dispersion in an aqueous ammonium polyacrylate solution undergoes phase separation in 30 min. It appears that both the higher viscosity of the medium (sucrose resin) and the adsorbed sucrose polymer layer on the particle surface contribute to the decrease in the settling rate of the AC powder dispersions. The adsorbed polymer layer with a large number of hydroxyl groups interacts strongly with the water molecules and the un-adsorbed sucrose polymer molecules present in the aqueous medium through hydrogen bonding. These hydrogen bonding interactions hold the large AC particles in the resin medium and slow down its sedimentation. A schematic showing the stabilization of the AC powder particles in the aqueous sucrose resin medium is shown in Figure 8.4.

Figure 8.3: Photograph showing the sedimentation behaviour of AC powder dispersions (A) in the ammonium polyacrylate solution after 30 min; (B) in the aqueous sucrose resin after 24 h; (C) in the aqueous sucrose resin after 6 h (AC powder to sucrose weight ratio is 0.1)

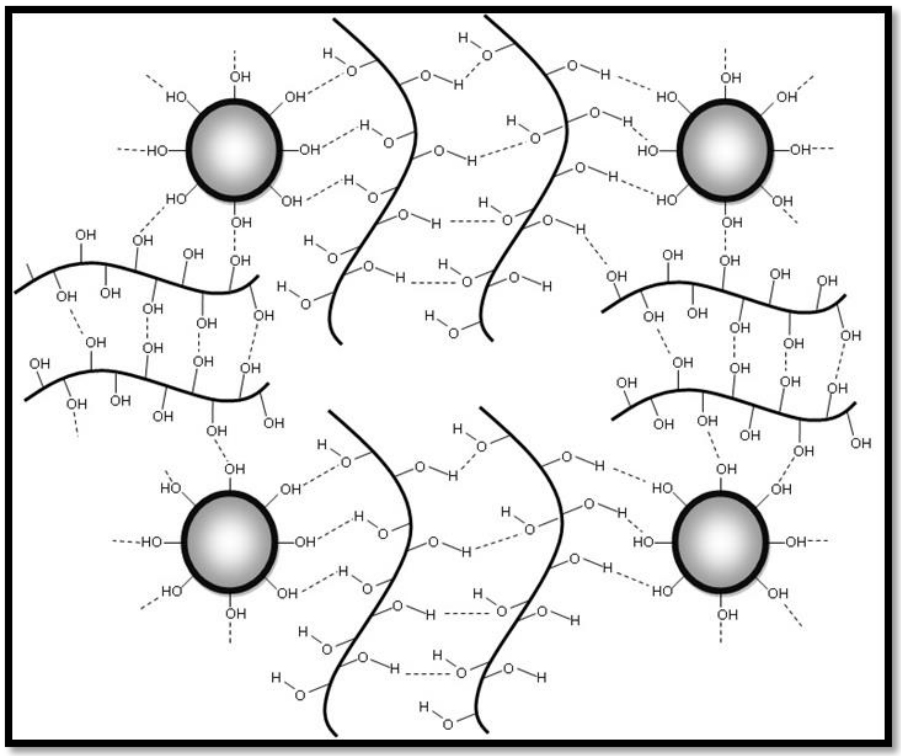

Figure 8.4: Schematic showing the stabilization of the AC powder particles in the aqueous sucrose resin medium

It is well-known that the interparticle Van der Waals interactions leading to the agglomeration of particles in the suspension medium increases with an increase in powder loading and the decrease in particle size (G.D.Parfitt, 1981). Figure 8.5 shows the viscosity versus shear rate plots of AC powder dispersions at an AC powder to sucrose weight ratio of 0.2 prepared using AC powders of various particle sizes. The dispersions, in general, show shear thinning flow behavior. The viscosity and shear thinning flow behavior of the dispersions increase with a decrease in particle size. This is due to the increase in interparticle Van der Waals interactions with a decrease in particle size. The effect of AC powder loading and AC particle size on the viscosity of the AC powder dispersions measured at a shear rate of 9.3 s^{-1} is shown in Figure 8.6. In all the studied particle sizes, the viscosity of dispersions increases gradually up to a certain AC powder loading and then rapidly. The rapid increase in viscosity is due to the particle agglomeration by the increased interparticle Van der Waals interactions. The AC powders of lower particle size show a rapid increase in viscosity at lower AC powder to sucrose weight ratios. Thus, the particle agglomeration in finer AC powders limits their loading in the sucrose resin for the preparation of carbon foams.

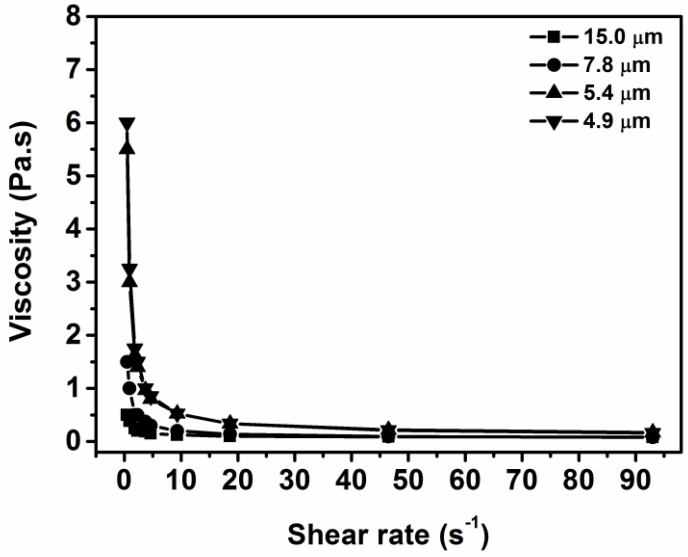

Figure 8.5: Effect of particle size on the viscosity versus shear rate plots of AC powder dispersions (AC powder to sucrose weight ratio - 0.2)

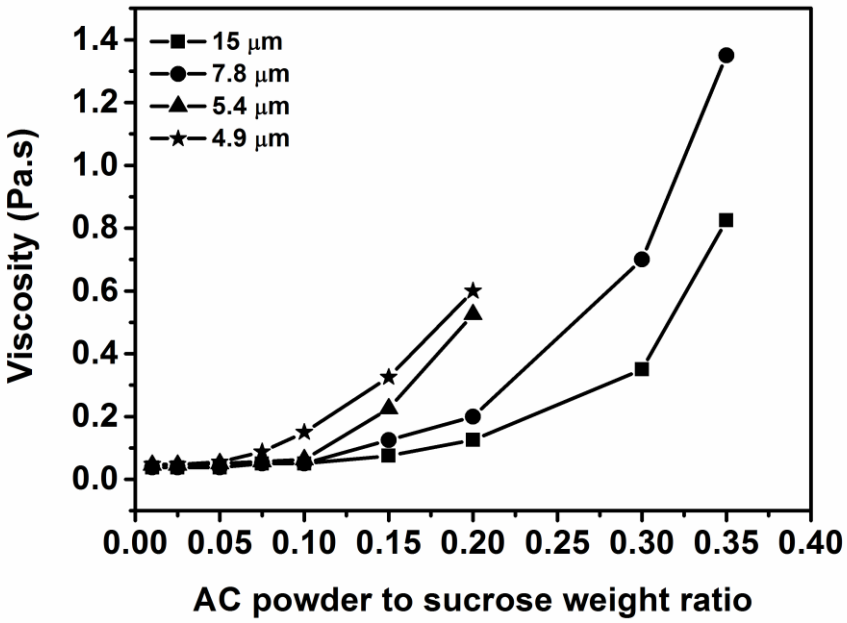

Figure 8.6: Effect of particle size and powder loading on the viscosity of the AC powder dispersions measured at a shear rate of 9.3 s^{-1}

8.3.2 Foaming of the AC Powder Dispersions in the Aqueous Sucrose Resin

The AC powder dispersions in aqueous sucrose resin undergo foaming and setting when heated in a glass tray at 120 ^{o}C in an air oven. The effect of AC powder to sucrose weight ratio (AC particle size - 15 μm) on the foaming and foam setting time is shown in Figure 8.7. The aqueous sucrose resin without the AC powder completes its foaming in 6.5 h and setting in 24 h. The foaming time decreases to 1.5 h and foam setting time decreases to 4 h when the AC powder to sucrose weight ratio increases to 0.35. The mechanism of foaming of aqueous sucrose resin without AC powder is due to the stabilization of bubbles produced by water vapour by increase in viscosity of the resin due to –OH to –OH condensation. Figure 8.8 shows the viscosity variation at 120 ^{o}C with time of AC powder dispersions at various AC powder to sucrose weight ratios (AC particle size - 15 μm). The samples for the viscosity measurements are collected while heating the dispersions for foaming, and the respective measurements are made at 120 ^{o}C with the help of a thermosel accessory. The viscosity of the sucrose resin

for the case without AC powder shows a rapid increase at 1.5 h due to the cross-linking of the sucrose polymer. On the other hand, the AC powder dispersions show rapid increase in viscosity after 3 h of heating. The delay in a rapid increase in viscosity of the dispersions indicates that the incorporation of the AC powder retards the –OH to –OH condensation reactions which are leading to the cross-linking of the sucrose polymer. It suggests that the observed rapid increase in viscosity after 3 h of heating the AC powder dispersions has a major contribution from the increase in solid content by the evaporation of water.

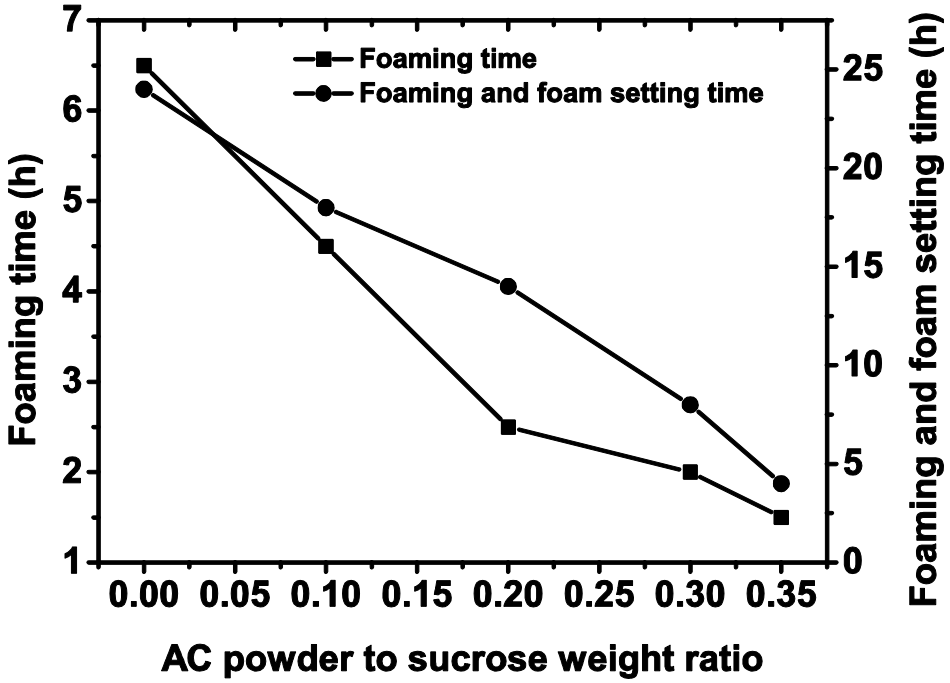

Figure 8.7: Effect of AC powder to sucrose weight ratio on the foaming and foam setting time of AC powder dispersions in aqueous sucrose resin (AC particle size - 15 μm)

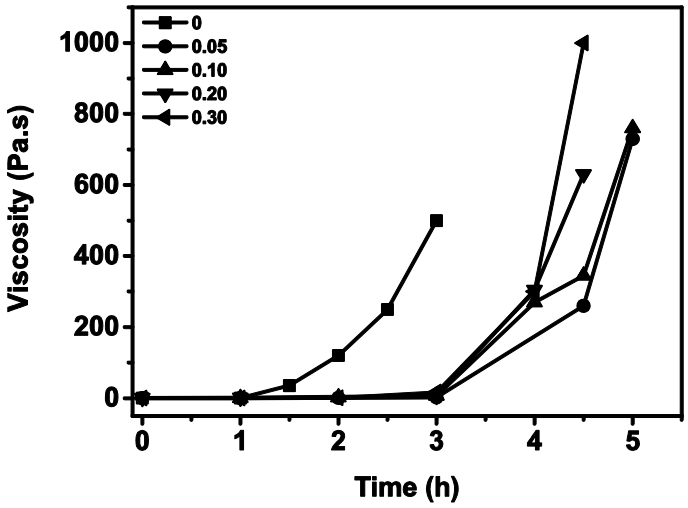

Figure 8.8: Viscosity variations at 120 ^{o}C with time of AC powder dispersions at various AC powder to sucrose weight ratios (AC particle size - 15 μm)

Faster foaming of AC powder dispersions in spite of the slow viscosity increase suggests a bubble stabilization mechanism other than the viscosity increase. It appears that the AC particles stabilize the bubbles created in the AC powder dispersions by adsorbing on the air-sucrose resin interface. This is supported by the fact that the aqueous sucrose resin showed a contact angle of 68^{o} on the carbon surface (produced by carbonization of wood). This contact angle is within the ideal range (60 to 80^{o}) for foam stabilization by particles (Gonzenbach et al., 2006a, b, c). Figure 8.9 shows a photograph of contact angle between aqueous sucrose resin and wood derived carbon surface.

Figure 8.9: Photograph of contact angle between aqueous sucrose resin and wood derived carbon surface

The effect of AC particle size and AC powder to sucrose weight ratio on the foam rise is shown in Figure 8.10. In all the studied particle sizes, the foam rise decreases to a minimum when the AC powder to sucrose weight ratio increases from 0 to 0.025. Thereafter, the foam rise increases to a maximum and then decreases with the further increase in AC powder to sucrose weight ratio. Hereafter, the AC powder to sucrose weight ratio at which maximum foam rise observed is called as the threshold AC powder to sucrose weight ratio. In all the studied AC powder to sucrose weight ratios, foam rise increases with a decrease in particle size. The increase in the foam rise with a decrease in AC particle size indicates that the finer particles are better for the stabilization of bubbles. The threshold AC powder to sucrose weight ratio decreases with a decrease in the particle size. It appears that the finer AC powder could form complete particle coverage on the liquid–vapour interface at lower AC powder to sucrose weight ratio. That is, AC powder with finer particle size could form stable foams at lower AC powder to sucrose weight ratio.

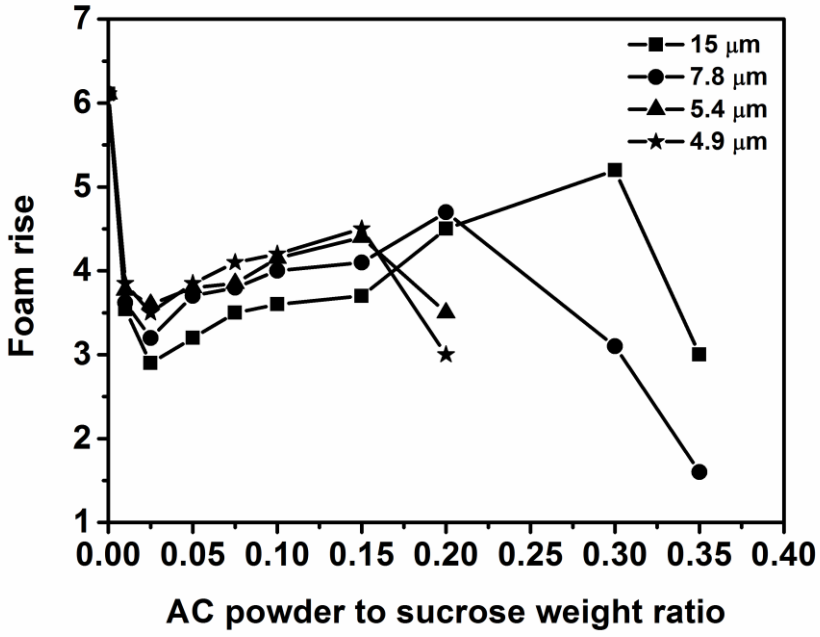

Figure 8.10: Effect of particle size on the foam rise of AC powder dispersions at various powder loadings

It is well-known that the wettability of a powder with a liquid depends on its particle size (Binks and Horozov, 2005; Dickinson et al., 2004; Gonzenbach et al., 2006b). As the contact angle measurement on AC particle is not possible with the available facility, the immersion test is used as a qualitative measure of relative wetting characteristics as the sinking of particles in a liquid involves the replacement of the solid-gas interface with a solid-liquid interface. Figure 8.11 shows the immersion time of the AC powder as a function of the particle size. The increase in the wettability with a decrease in the particle size of AC powders is clearly evidenced from the decrease in immersion time. The increase in foam rise with a decrease in AC particle size is due to the increase in foam stability achieved by the increase in the wettability.

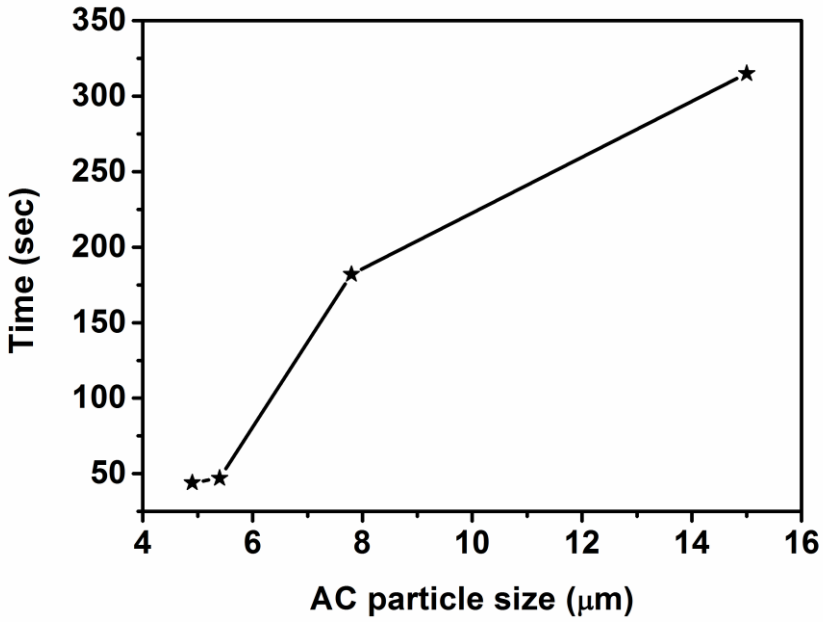

Figure 8.11: The effect of AC particle size on the immersion time

The aqueous sucrose resin without the AC powder starts foaming in 2.5 h at 120 ^{o}C. In this, bubbles generated by the water vapour are stabilized due to high viscosity (~ 250 Pa.s) of the highly cross-linked sucrose polymer resin. On the other hand, the poor cross-linking of the sucrose polymer in the presence of the AC powder unable to stabilize the bubbles due to its low viscosity. This is evidenced from the poor foamability of the AC powder dispersion at an AC

powder to sucrose weight ratio of 0.025. It suggests that the AC particle coverage in the gas-liquid interface at an AC powder to sucrose weight ratio of 0.025 is not sufficient to stabilize the bubble. However, at the higher AC powder concentrations, AC particle coverage on the air-resin interface is sufficient to stabilize the bubbles. That is, foaming of dispersions with the AC powder to sucrose weight ratios beyond 0.025 is due to the stabilization of the bubbles by the AC particles. We have observed that the time required for initiating the foaming decreases with an increase in the AC powder to sucrose weight ratio. The early foaming of the AC powder dispersions at higher AC powder to sucrose weight ratio indicates that the stability of the bubbles increases by increase in the AC particle concentration. The decrease in the foam rise after the threshold AC powder to sucrose weight ratio is explained as follows: In the AC powder dispersions, the AC particles are separated by a thin layer of the aqueous sucrose resin. As the AC particles concentration increases, the thickness of the resin layer between the particles decreases. When the resin layer thickness is less than a certain value, the particle to particle contact establishes that act as a weak point which results in the rupture of the bubbles before setting. The addition of AC powder beyond the threshold AC powder to sucrose weight ratio results in foam collapse due to the agglomeration of the AC particles.

8.3.3 Dehydration and Carbonization of the Sucrose Polymer-AC Particle Composite Foams

The sucrose polymer-AC particle composite foam bodies of 8 cm x 5 cm x 2 cm size prepared at all AC powder to sucrose weight ratios when dehydrated by heating from 100 to 200 ^{o}C at the rate of 0.5 ^{o}C/h do not produce any crack or deformation. On the other hand, attempts made at a higher heating rate of 2 ^{o}C/min result in swelling of samples prepared at the AC powder to sucrose weight ratios in the range of 0.025 to 0.1. The foam structure collapses due to this swelling. As the AC powder retards the –OH to –OH condensation reactions, the sucrose polymer present in the composite foams has low molecular weight and fewer numbers of cross-links. The swelling is due to the melting of the poorly

cross-linked low molecular weight sucrose polymer formed in the presence of AC powder. The swelling is not observed in samples without AC powder as well as in samples with the AC powder at AC powder to sucrose weight ratio of more than 0.1. At higher AC powder to sucrose weight ratios, the deformation due to the melting of the low molecular weight sucrose polymer is resisted by the network of the AC particles. Annealing at temperatures in the range of 200 to 250 ^{o}C in air atmosphere is a common practice to stabilize the precursors in the preparation of many carbon based materials (Savage, 1993). The slow heating of sucrose polymer-AC particle composite foam in air atmosphere enhances the cross-linking between the sucrose polymer molecules that increases the carbon yield and decreases the possibility of warping during carbonization (Savage, 1993). Figure 8.12 shows the FTIR spectra of the composite foams prepared at an AC powder to sucrose weight ratio of 0.1 before and after dehydration at 200 ^{o}C. The sample dehydrated at 200 ^{o}C shows a decrease in the intensity of the peak at 1660 cm^{-1} corresponding to the C=C stretching vibration. In addition to that the composite foams show very small weight loss (~1.5 wt.%) during the dehydration at 200 ^{o}C. These two observations indicate that the cross linking of the sucrose polymer chains by the H^{+} catalyzed reaction between the C=C and the –OH groups. The proposed mechanism of the cross-linking reaction is shown in Figure 8.13. The formation of cross-links during annealing at 200 ^{o}C increases the thermal stability and the carbon yield of the sucrose polymer. Figure 8.14 shows the TGA in the nitrogen atmosphere of the sucrose polymer-AC particle composite foam before and after dehydration at 200 ^{o}C. The carbon yield at 900 ^{o}C obtained from the samples before and after dehydration are 31.99 wt.% and 36.55 wt.%, respectively.

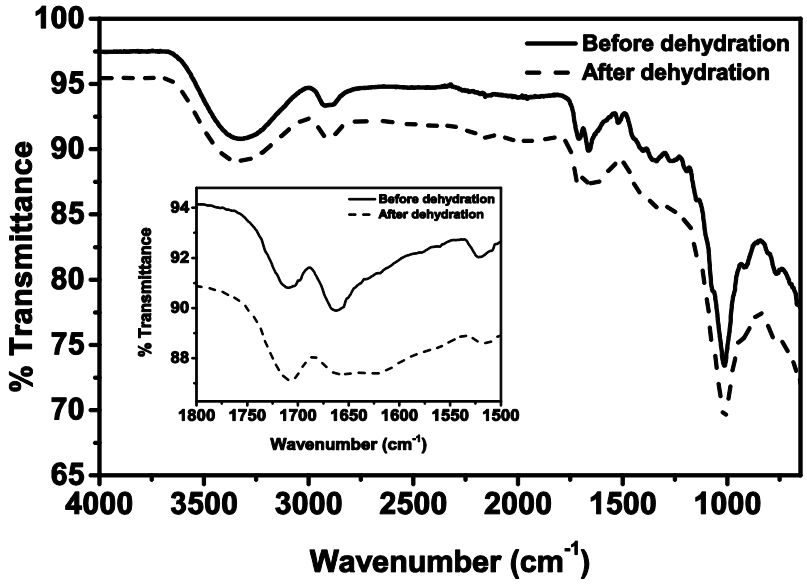

Figure 8.12: FTIR spectra of sucrose polymer-AC particle composite foam before and after dehydration at 200 ^{o}C. Enlarged view of the C=O and C=C peaks are given as an inset (AC powder to sucrose weight ratio is 0.1)

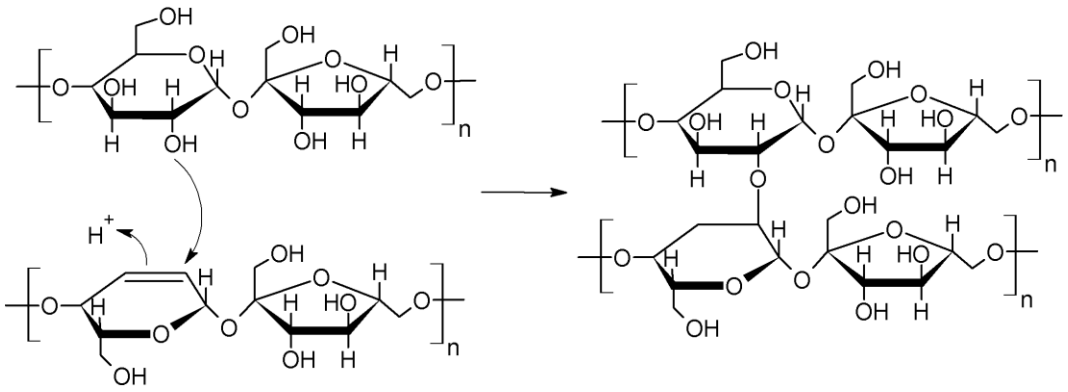

Figure 8.13: The proposed mechanism of cross-linking of sucrose polymer during annealing

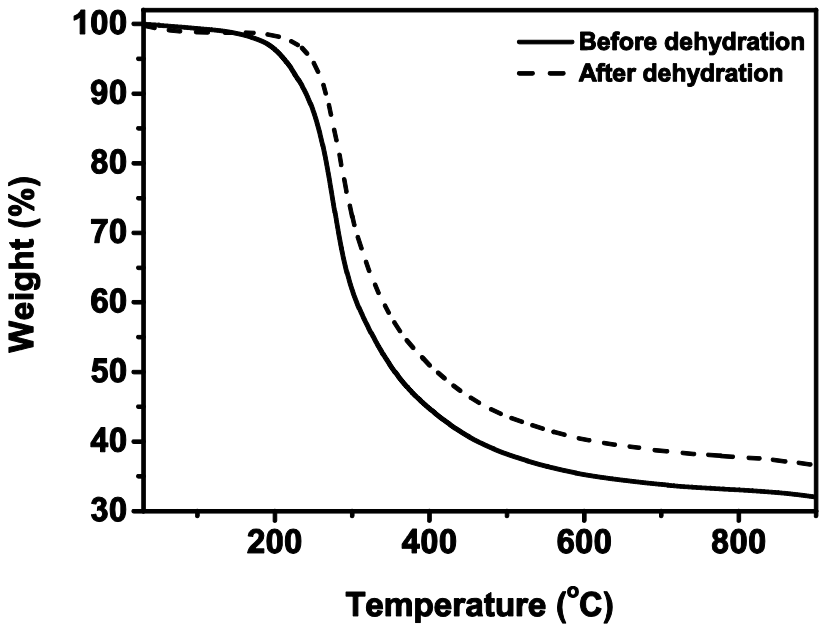

Figure 8.14: TGA of the organic and dehydrated sucrose polymer-AC particle composite foam samples. AC powder to sucrose weight ratio is 0.1

8.3.4 Microstructure of Carbon Composite Foams

Figure 8.15 shows the SEM photomicrographs of the carbon composite foams prepared using AC powders of various average particle sizes at AC powder to sucrose weight ratios of 0.025 and 0.15. The carbon composite foams have interconnected cellular structure. The cells have spherical or near spherical morphology. The high magnification images of the cell wall surfaces show an increased adsorption of the AC particles with an increase in the AC powder loading. At the threshold AC powder to sucrose weight ratios, the AC particles form complete coverage on the cell wall surfaces. This confirms the bubble stabilization by the adsorption of AC particles on the sucrose resin-air interface.

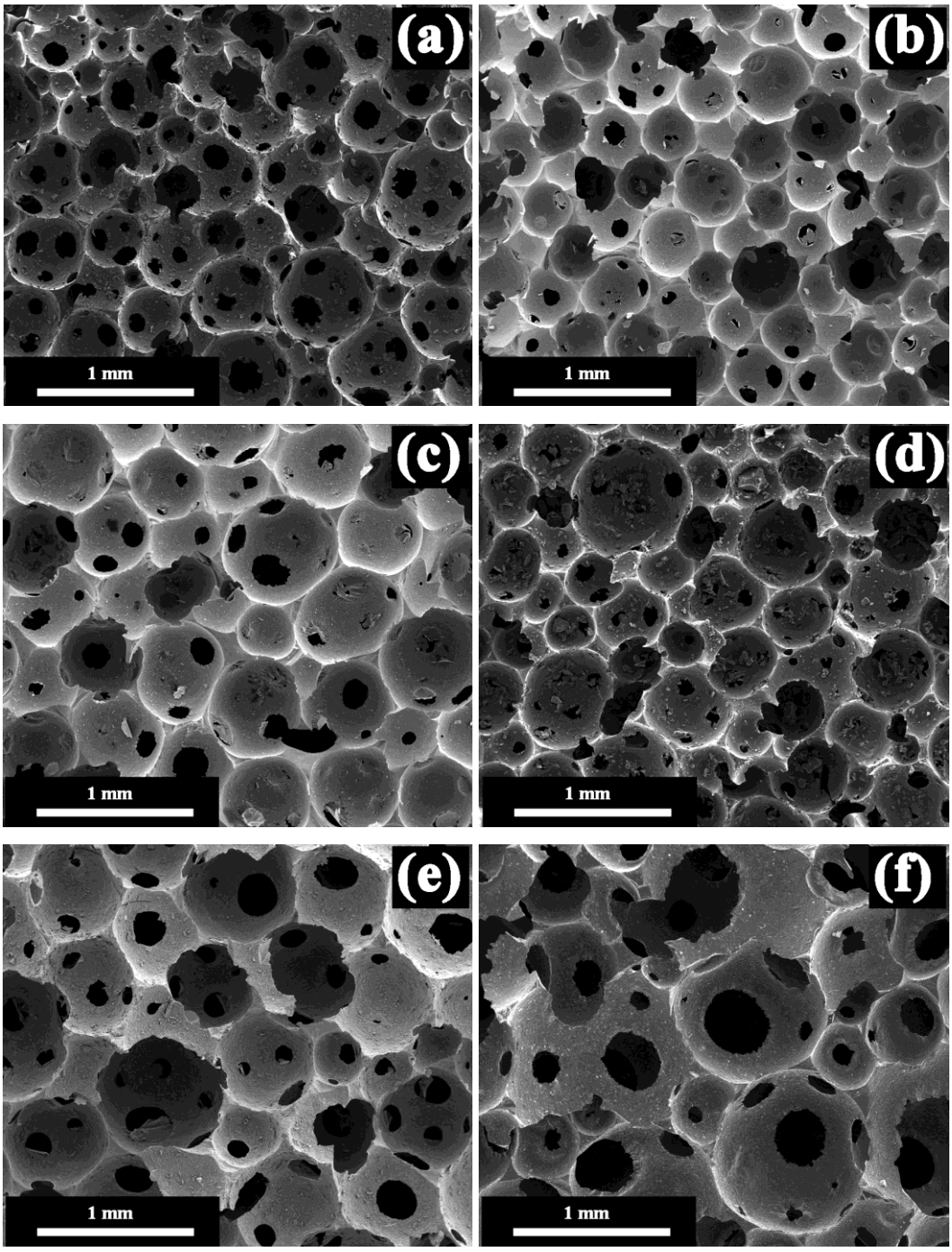
(a)
1 mm
(b)
1 mm
(c)
1 mm
(d)
1 mm
(e)
1 mm
(f)
1 mm

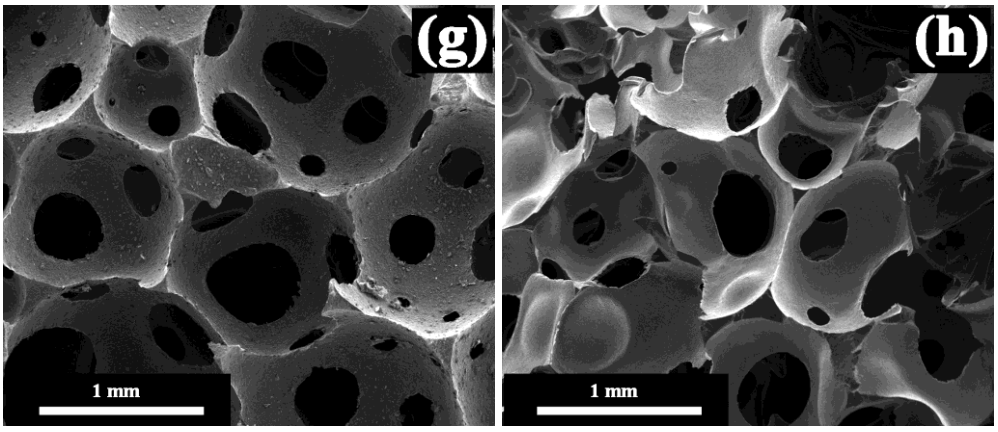

Figure 8.15: SEM photomicrographs of carbon composite foams prepared using AC powder of various particle sizes at AC powder to sucrose weight ratios of 0.025 and 0.15. a) 0.025, 15 μm; b) 0.025, 7.8 μm; c) 0.025, 5.4 μm; d) 0.025, 4.9 μm, e) 0.15, 15 μm, f) 0.15, 7.8 μm; g) 0.15, 5.4 μm and h) 0.15, 4.9 μm

Uniform spherical morphology of the cells is observed below the threshold AC powder to sucrose weight ratio. A large distortion of the cells from spherical morphology is observed in the bottom portion of the carbon foams obtained at the threshold AC powder to sucrose weight ratio. The deviation from spherical morphology is attributed to the collapse of bubbles in the bottom due to the sedimentation of agglomerated AC particles. The SEM microstructures of the bottom portion of the carbon foam body prepared using 4.9 μm AC powder at AC powder to sucrose weight ratios of 0.1 and 0.15 are shown in Figure 8.16. The carbon foams prepared above the threshold AC powder to sucrose weight ratio have the distorted cell morphology throughout due to extensive particle agglomeration.

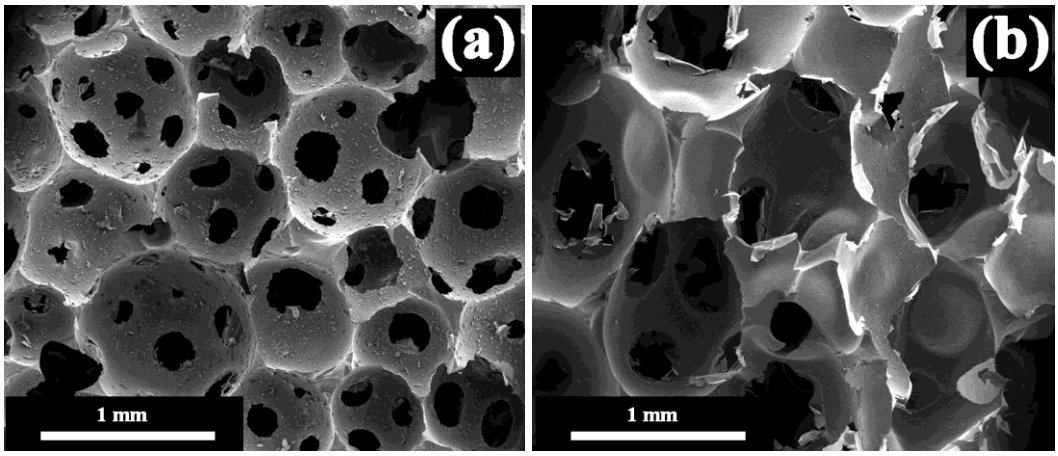

Figure 8.16: SEM photomicrographs of the bottom portion of the carbon composite foam bodies prepared using 4.9 μm AC powder at the AC powder to sucrose weight ratios of (a) 0.10 and (b) 0.15 (0.15 is the threshold AC powder to sucrose weight ratio)

Figure 8.17 shows the effect of average particle size of AC powder on average cell size of the carbon composite foams prepared at various AC powder to sucrose weight ratios. The average cell size of the carbon composite foams increases considerably with the AC powder to sucrose weight ratios in all the studied particle sizes. On the other hand, the cell size shows a marginal increase with a decrease in the AC particle size at all the studied AC powder to sucrose weight ratios. This confirms that the finer AC particles are more effective in stabilizing the bubbles. It is further evidenced from the high magnification SEM images showing the preferential adsorption of the finer fraction of the AC powders on the bubble surfaces. Figure 8.18 shows the high magnification SEM photomicrographs of the cell wall surface of carbon foams prepared at an AC powder to sucrose weight ratio of 0.15 using AC powders of average particle sizes 4.9 and 7.8 μm. The approximate estimation of the average size of AC particles on the cell wall surface of carbon foams prepared using AC powder of average particle sizes 4.9 and 7.8 μm are 1.84 and 3.41 μm, respectively. The size of cell windows connecting the cells also increases with an increase in the AC powder to sucrose weight ratio.

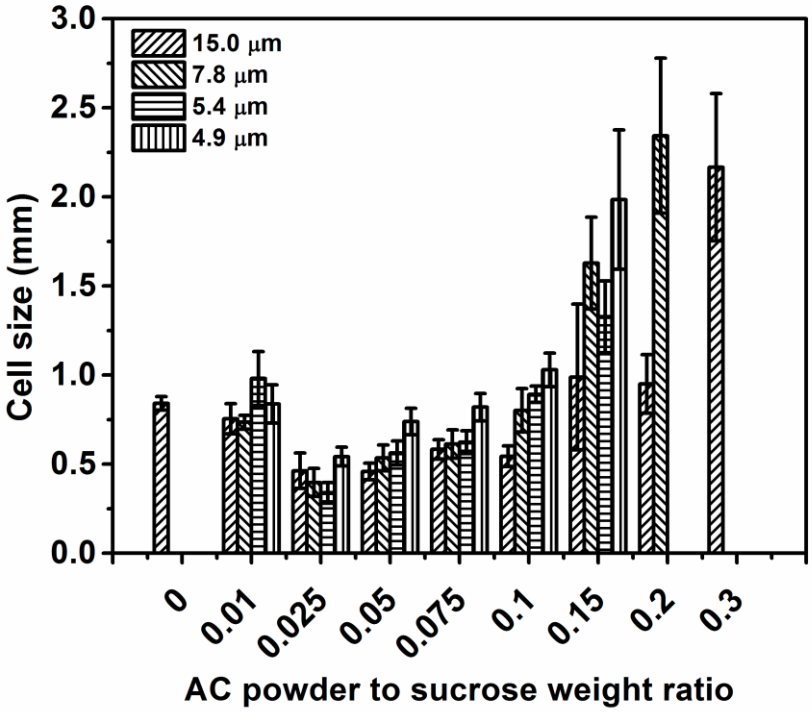

Figure 8.17: Effect of the AC particle size and powder loading on cell size of the carbon composite foams

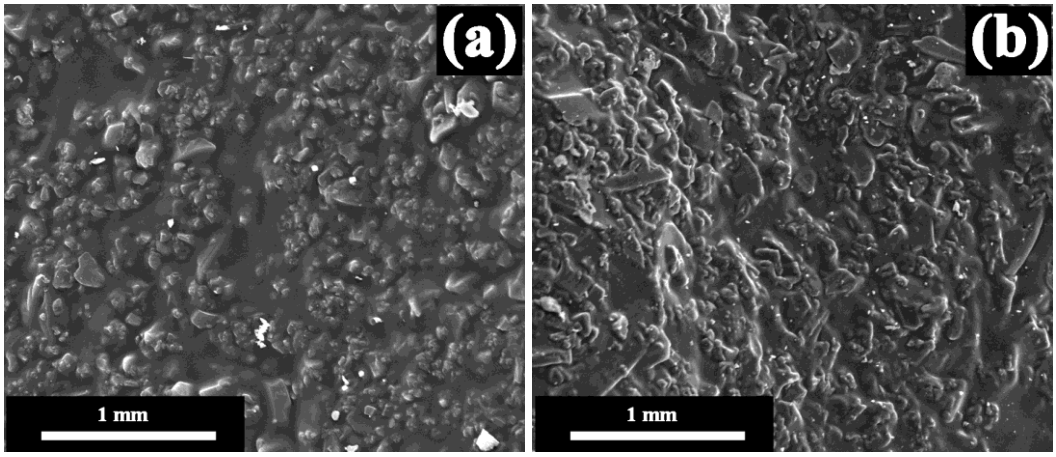

Figure 8.18: SEM photomicrographs of cell wall surfaces of carbon composite foams prepared at an AC powder to sucrose weight ratio of 0.15 using powders of (a) 4.9 μm and (b) 7.8 μm

8.3.5 Density and Compressive Strength

The density variation of the carbon composite foams with the AC particle size and AC powder to sucrose weight ratio is shown in Figure 8.19. The addition of AC powder into the sucrose resin up to AC powder to sucrose weight ratio of 0.01 shows a slight increase in carbon composite foam density. A further increase in the AC powder to sucrose weight ratio to 0.025 increases the carbon composite foam density considerably and to a maximum. The density remains a plateau at AC powder to sucrose weight ratios in the range of 0.025 to 0.075 and then decreases. At each AC powder to sucrose weight ratio, the difference in density due to the difference in AC particle size is only marginal. The considerable increase in density observed from the AC powder to sucrose weight ratio from 0.01 to 0.025 is due to the change in the mechanism of the bubble stabilization. That is, up to the AC powder to sucrose weight ratio of 0.01 the foaming is mainly by the stabilization of bubbles due to the increase in viscosity by polymerization through –OH to –OH condensation. On the other hand, at AC powder to sucrose weight ratio of above 0.01 the foaming is mainly by the stabilization of bubbles by the adsorption of AC particles on the air-liquid interface. A simultaneous increase in cell size and foam density from AC powder to sucrose weight ratios of 0.01 to 0.075 indicates that the bubble stabilization by the AC particles produce carbon foams with thick struts and cell walls compared to the bubble stabilization by viscosity increase through –OH to –OH condensation.

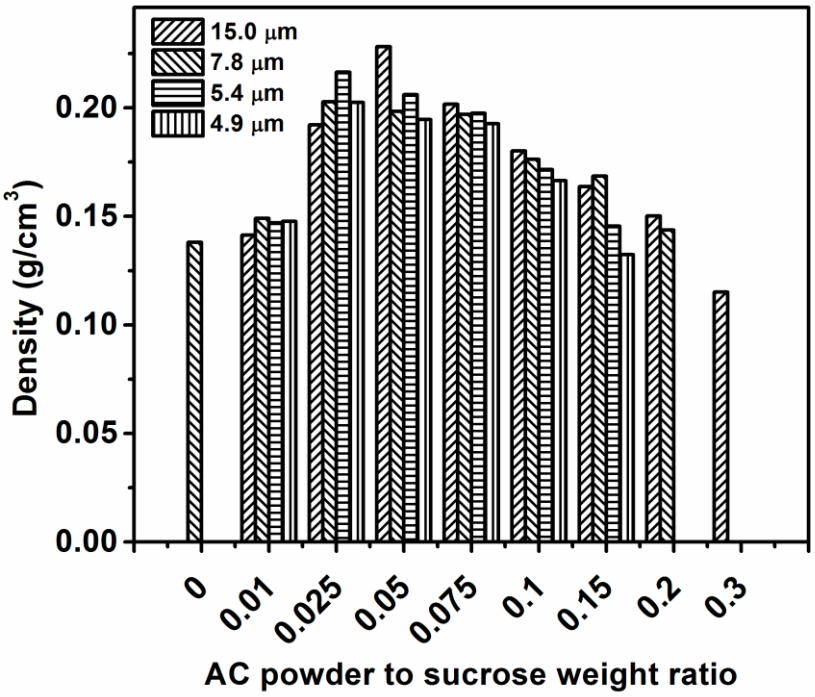

Figure 8.19: Density variations of carbon composite foams with the AC particle size and powder loading

The carbon composite foams prepared at various AC powder to sucrose weight ratios using AC particles with different particle sizes show typical elastic-brittle behaviour during compression loading as evidenced from the stress-strain graphs shown in Figure 8.20. An elastic region followed by a yield point, a plateau region and a region of densification are observed in the stress–strain graphs. The foams start their failure due to the fracture of ligaments after reaching the plateau stress. The debris formed by the fracture of the ligaments fill the cells in the carbon foam body resulting in the densification of the foams. The densification of the foam is observed at strain values in the range of 60 to 80 %. The foams with higher density and lower cell size start densification at lower strain values.

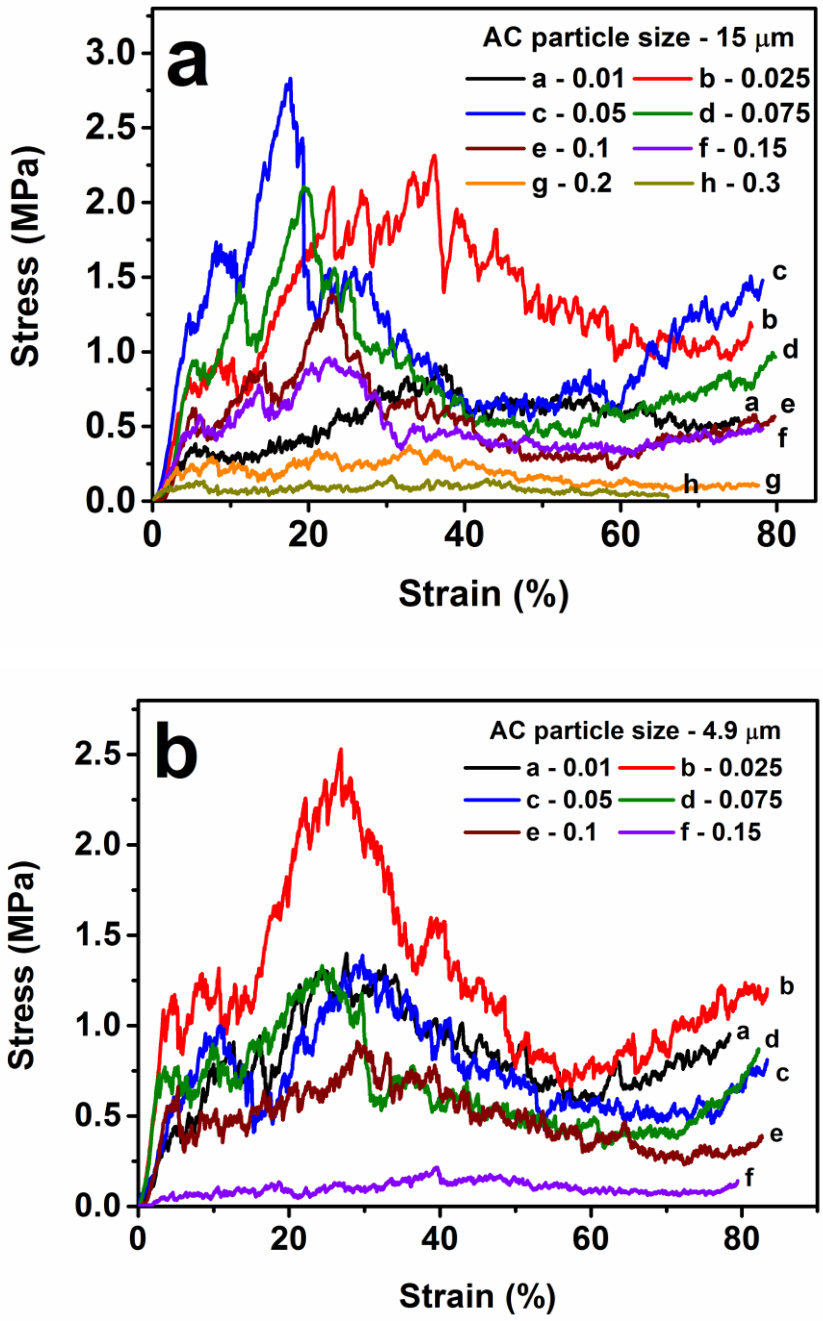

Figure 8.20: Stress-strain graphs of the carbon foams prepared at various AC powder to sucrose weight ratios using AC powder of average particle sizes (a) 15.0 μm and (b) 4.9 μm

The compressive strength of foam materials generally increases with an increase in foam density and decrease in the cell size (Gibson and Ashby, 1997; Li et al., 2012). The reinforcement by the AC particles is evidenced from the plot of specific compressive strength as a function of AC particle size and AC powder

loading as shown in Figure 8.21. Irrespective of the AC particle size, the carbon foams show maximum specific compressive strength at the AC powder to sucrose weight ratio of 0.025 even though they have the highest density. At this AC powder to sucrose weight ratio, the carbon foams show a marginal increase in the specific compressive strength with a decrease in AC particle size. On the other hand, at higher AC powder to sucrose weight ratios, the specific compressive strength decreases with a decrease in AC particle size. It is well-known that well-dispersed finer particles in the matrix provide better reinforcement by creating more matrix–reinforcement interfaces. It appears that the AC powder disperses without agglomeration at AC powder to sucrose weight ratio up to 0.025 irrespective of the particle size. The particle agglomeration starts at AC powder to sucrose weight ratio above 0.025 and increases with an increase in AC powder to sucrose weight ratio. This results in the decrease of specific compressive strength at AC powder to sucrose weight ratio beyond 0.025. The particle agglomeration is severe in finer AC powders as evidenced from the decrease of specific compressive strength with a decrease of average AC particle size at AC powder to sucrose weight ratios above 0.025. That is, these particle agglomerates decrease the compressive strength by acting as strength limiting flaws. It is interesting to note that the maximum specific strength obtained in carbon composite foams prepared from AC powder dispersions in aqueous sucrose resin (11.3 MPa/g/cm^3) is higher than that obtained for carbon composite foams prepared from AC powder dispersions in molten sucrose (8.3 MPa/g/cm^3). This is attributed to the better dispersion of AC powder in low viscous aqueous sucrose resin compared to the high viscous molten sucrose.

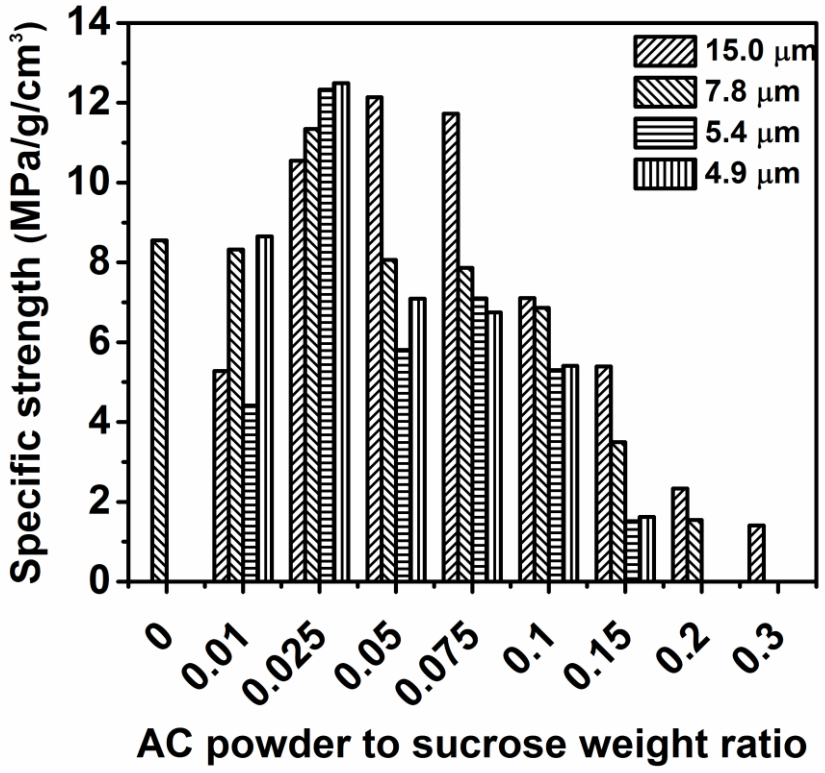

Figure 8.21: Effect of the AC particle size and AC powder to sucrose weight ratio on the specific compressive strength of carbon composite foams

8.3.6 Thermal Conductivity

Figure 8.22 shows the variation in thermal conductivity of the carbon composite foams with the AC particle size and AC powder to sucrose weight ratio. The thermal conductivity of carbon foams depends on the bulk density, cell size and thickness of the cell wall and strut (Gibson and Ashby, 1997; Li et al., 2012). The effect of AC particle size on the thermal conductivity of the carbon composite foams is insignificant. However, the thermal conductivity of carbon composite foams increases marginally with an increase in AC powder to sucrose weight ratio up to 0.025. A further increase in the AC powder concentration marginally decreases the thermal conductivity. The variation in thermal conductivity with the AC powder to sucrose weight ratio is in line with the variation of density and cell size. The thermal conductivity values obtained are in the range of 0.026 to 0.063 W/m/K. The thermal conductivity values are lower

than that reported for the vitreous carbon foams of similar densities prepared from other precursor materials (Li et al., 2012; Tondi et al., 2009).

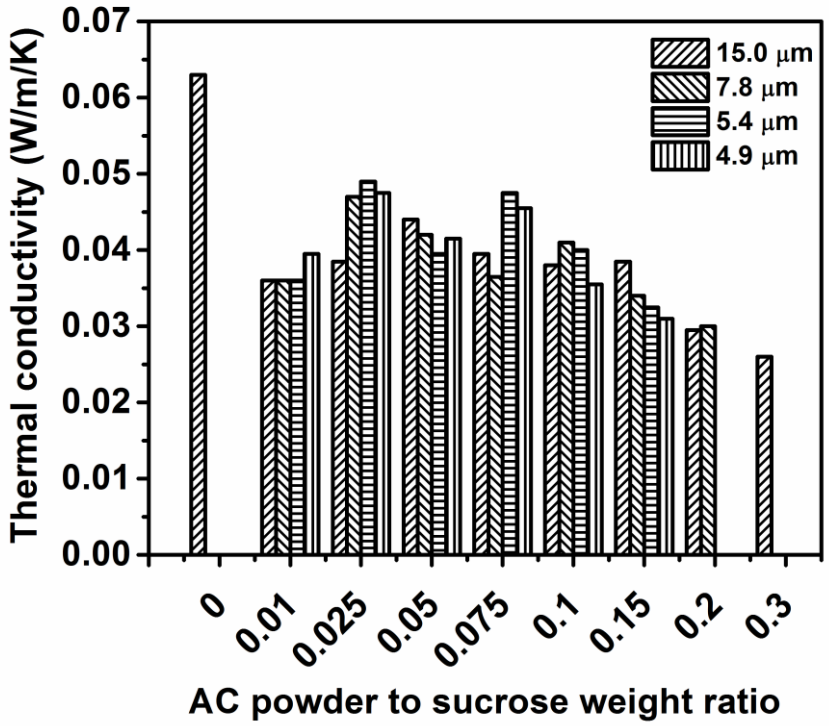

Figure 8.22: Effect of the AC particle size and AC powder to sucrose weight ratio on the thermal conductivity of carbon composite foams

8.3.7 Machinability and Fire Resistance

The materials intended for structural applications need to be configured to the required size and shape. The machinability of carbon composite foams depends on the AC powder to sucrose weight ratio and AC particle size. The carbon composite foams prepared using AC powders of average particle size 4.9, 5.4, 7.8 and 15 μm show good machinability characteristics with respect to the evenness of the machined surfaces and edges up to the AC powder to sucrose weight ratios of 0.075, 0.1, 0.15, and 0.2, respectively. The poor machinability at the higher AC powder to sucrose weight ratios is because of the low strength due to low density, large cell size and heavy agglomeration of the AC particles. Figure

8.23 is the photograph of a rectangular carbon composite foam body showing slots made by milling and holes by drilling with conventional machines and tools.

Figure 8.23: Photograph of a rectangular carbon composite foam body showing slots made by milling and holes made by drilling

Carbon foams are proposed to be used in fire resistant structures and thermal protection systems based on their excellent fire resistance and ablative property coupled with low thermal conductivity. The carbon composite foams prepared from sucrose resin and activated carbon powder does not contain sufficient volatile matter to support combustion when exposed to the oxyacetylene flame irrespective of the AC particle size and AC powder to sucrose weight ratios. There are no hazardous fumes or smoke produced. Photograph of the carbon composite foam during and after exposure to oxyacetylene flame is shown in Figure 8.24. Though the carbon composite foam does not catch fire, the oxyacetylene flame pierces through the carbon composite foam on prolonged exposure. The oxyacetylene flame took 60 to 70 sec to penetrate 15 mm thick carbon composite foam. The time required for the penetration of flame is much higher than that reported for tannin based and bituminous coals' extracts based carbon foams (Stansberry et al., 2000; Tondi et al., 2009). That is, the carbon composite foams prepared from sucrose resin and AC powder have superior flame resistance and ablative property.

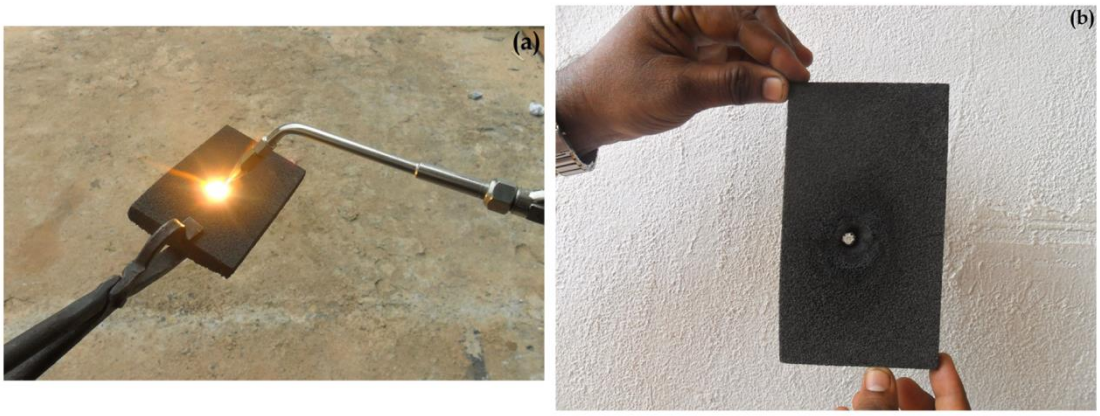

Figure 8.24: Photograph of carbon composite foam (a) during and (b) after exposure to oxyacetylene flame

8.4 Conclusions

Planetary ball milling is used to reduce the particle size of as received AC powder to prepare powders of various average particle sizes. The AC powder disperses in aqueous sucrose resin due to the adsorption of sucrose polymer molecules. The AC particles in the resin medium are stabilized against sedimentation due to the hydrogen bonding interactions between the sucrose polymer molecules adsorbed on the AC particle surface and the un-adsorbed sucrose polymer molecules present in the medium. The AC powder retards the –OH to –OH condensation reactions responsible for the cross-linking of the sucrose polymer. The thermo-foaming of AC powder dispersions in aqueous sucrose resin is by the stabilization of the bubbles produced due to water vapour by the adsorption of AC particles on the gas-resin interface. The foamed AC powder dispersions set into solid organic foams due to the continued polymerization through –OH to –OH condensation reactions. The wettability of the AC particles increases with a decrease of particle size. The foam volume increases with a decrease in the AC particle size due to the better stabilization of bubbles by the finer particles**.** At each average particle size, there is a threshold AC powder to sucrose weight ratio beyond which the foam collapses due to the agglomeration of the AC particles. The threshold AC powder to sucrose weight ratio decreases with a decrease in the average particle size of AC powder. The cell size of the carbon

foams prepared by dehydration followed by carbonization of solid organic foams increases with a decrease in AC particle size and an increase in AC powder to sucrose weight ratio. The AC particle size has a marginal effect on the density and thermal conductivity of the carbon foams. On the other hand, the density, the compressive strength, and the thermal conductivity of the carbon foams increase with an increase in AC powder to sucrose weight ratio up to 0.025 and then decrease. The thermal conductivity values are lower than that of the vitreous carbon foams of similar densities reported in the literature. The carbon foams show very good machinability characteristics and fire resistance.

CHAPTER 9

CONCLUSIONS AND FUTURE WORK

9.1 Conclusions

Carbon foam is a three-dimensional, cellular, macroporous carbon material with low density, tunable thermal and electrical conductivity, very good fire resistance and relatively high mechanical strength. They find applications in light-weight fire resistant structures, thermal protection systems, heat exchangers, radiators, electrodes in batteries, EMI shielding, etc. Currently, carbon foams are mainly prepared from non-renewable resources such as petroleum and coal-tar pitches and some of the synthetic polymers which leave large amount of carbon residue on pyrolysis. The depletion of fossil fuels and other environmental concerns demand a shift from non-renewable precursors to naturally renewable precursors for the preparation of carbon foam. Sucrose is a widely available naturally renewable material used as precursor for carbon foam. However, the carbon foam prepared from sucrose has low density and compressive strength. This thesis investigates on the novel processing of carbon foams from sucrose and reinforcing carbon additives such as AC powder, short carbon fiber, MWNT and graphene. Two novel blowing agents such as aluminium nitrate and boric acid are investigated for the foaming of molten sucrose and the effect of these blowing agents on the properties of the carbon foams is also studied. The carbon foams are characterized for various applications such as thermal insulation, CO_2 adsorption, oil absorption and EMI shielding.

A brief review of the preparation of carbon foams from various precursors and their properties and applications is given in chapter 1. A review of various reinforcements used in carbon foams is also provided in chapter 1. Processing of carbon foams by thermo-foaming of molten sucrose using an

aluminium nitrate blowing agent is described in chapter 2. The aluminium nitrate contributes to the foaming and setting of molten sucrose as the H^+ generated by its hydrolysis catalyzes the –OH to –OH condensation responsible for foaming and foam setting. The total time for foaming and setting of molten sucrose at 150 ^oC decreases from 48 to 4 h when the aluminum nitrate concentration increases from 0 to 4 wt.% of sucrose. The carbon foams contain near spherical cells connected through oval shaped cell windows. The cell size (1.62 to 0.83 mm) and density (0.053 to 0.15 g/cm^3) of the carbon foams decrease with an increase in aluminium nitrate concentration. The alumina formed from the aluminium nitrate blowing agent concentrates more on the surface of the cell walls, ligaments and struts of the carbon foam. The compressive strength (0.06 to 0.64 MPa), Young's modulus (2.9 to 22 MPa) and thermal conductivity (0.04 to 0.07 W/m/K) of the carbon foams depend on the aluminium nitrate concentration. The surface area and pore volume of the carbon foams increase with an increase in aluminum nitrate concentration. The mechanism of formation of micropore due to *in situ* activation and alumina pillaring is established. The CO_2 adsorption capacity (2.87 to 3.37 mmol/g at 0 ^oC and 760 mmHg) of the carbon foams increases with an increase in aluminium nitrate concentration. The CO_2 adsorption in carbon foams shows very good selectivity over N_2 adsorption and the adsorbent is easily regenerated by heating at 50 ^oC. On the other hand, the oxidation resistance of the carbon foam prepared from aluminium nitrate blowing agent decreases with an increase in aluminium nitrate concentration due to the catalytic effect of alumina formed towards the carbon oxidation reaction.

Processing of carbon foams by thermo-foaming of molten sucrose using a boric acid blowing agent is described in chapter 3. The boric acid acts not only as a blowing agent but also as the source of boron which improves the oxidation resistance of carbon. The H^+ ions produced from boric acid due to the formation of complex with sucrose catalyzes the –OH to –OH condensation reactions in the molten sucrose which results in its faster foaming and setting. The char yield from the solid organic foams increases from 24 to 37.4 wt.% when boric acid concentration increases from 0 to 8 wt.% of sucrose due to the formation of the B-

O-C cross-links between sucrose polymers by B-OH to C-OH condensations. The density and compressive strength decrease and the cell size increases with an increase in boric acid concentration. The room temperature thermal conductivity of the boron-doped carbon foams is in the range of 0.057 to 0.043 W/m/K. The surface area and pore volume increase with an increase in the boric acid concentration up to 6 wt.% and then decrease. The boron present (0.44 to 3.4 wt.%) retards the oxidation of carbon foams as evidenced from the increase in the oxidation onset temperature and char residue at 900 ^{o}C with an increase in boric acid concentration.

Out of the two studied blowing agents, the foaming and foam setting of molten sucrose are achieved faster with the boric acid than with the aluminium nitrate. Though foaming of the boric acid based system occurs at a lower temperature, the aluminium nitrate based system produces foams with uniform cells. Moreover, rapid foaming and foam collapse are observed in the case of boric acid blowing agent at foaming temperature higher than 120 ^{o}C. In general, the char yield is higher in the boric acid blowing agent system compared to the aluminium nitrate blowing agent system. The major difference between the aluminum nitrate and boric acid systems is in the variation of cell size with the blowing agent concentration. In the case of aluminum nitrate blowing agent, the cell size decreases with an increase in aluminium nitrate concentration, whereas in the case of boric acid blowing agent, the cell size increases with an increase in boric concentration. The aluminium nitrate blowing agent produces carbon foam with lower density (0.15 to 0.053 g/cm^3) compared to that produced using boric acid blowing agent (0.103 to 0.16 g/cm^3). The carbon foams produced using aluminium nitrate and boric acid blowing agents contain microporous cell walls and strut. The maximum surface area achieved is higher for boric acid system (570 m^2/g) than with the aluminium nitrate system (540 m^2/g). It is interesting to note that the oxidation resistance of carbon foam decreases with an increase in aluminium nitrate blowing agent concentration, whereas the same increases with an increase in boric acid blowing agent concentration.

In chapter 4, the processing of carbon composite foams by thermo-foaming of activated carbon (AC) powder dispersions in molten sucrose is described. The rheological studies show a decrease in viscosity with an increase in AC powder to sucrose weight ratio up to 0.1 due to the interruption of the intermolecular hydrogen bonding in the molten sucrose by the AC particles. The AC powder stabilizes the bubbles by adsorbing on the molten sucrose-gas interface. The acidic surface functional groups present on the AC powder act as a catalyst for the –OH to –OH condensation. The volume shrinkage (46 – 68 %), char yield (33.2 – 47.2 %), density (0.16 – 0.22 g/cm^3), and cell size (0.65 – 1.76 mm) depend on the AC powder to sucrose weight ratio. The maximum compressive strength of the carbon composite foam achieved is 1.36 MPa at an AC powder to sucrose weight ratio of 0.05. Thermal conductivity of the carbon composite foams marginally decreases from 0.07 to 0.067 W/m/K when the AC powder to sucrose weight ratio increases from 0 to 0.25. The carbon composite foams have a hierarchical pore structure with interconnected cells made up of carbon containing micropores. The carbon composite foams show relatively high (2.59 to 3.04 mmol/g) CO_2 adsorption capacity with very good CO_2/N_2 selectivity and excellent recyclability. The carbon composite foams show oil absorption from the oil-water mixtures and surfactant stabilized oil-in-water emulsion.

Processing of carbon composite foams by thermo-foaming of milled carbon fiber dispersions in molten sucrose is described in chapter 5. In the case of longer carbon fibers (average fiber length 300 μm), the density and compressive strength of the carbon composite foams decrease with an increase in fiber concentration due to agglomeration by fiber bridging. The planetary ball milling of sucrose-carbon fiber mixture decreases the fiber length. The fiber length of 33 μm for optimum compressive strength of carbon composite foam is achieved by planetary ball milling of sucrose-carbon fiber mixture for 1.5 h. The maximum compressive strength and specific compressive strength of 3.86 MPa and 17.3 MPa/g/cm^3, respectively, are achieved at a fiber concentration 2 wt.% of sucrose .

In chapter 6, processing of carbon composite foams by thermo-foaming of MWNT dispersions in molten sucrose is described. Viscosity of the dispersions shows a gradual increase up to a MWNT concentration of 1.5 wt.% and then a rapid increase up to 2.5 wt.%. The foaming time and foam setting time decrease with an increase in the MWNT concentration due to the catalytic effect of MWNT towards –OH to –OH condensation. The MWNT acts as a heterogeneous site for the nucleation of bubbles in molten sucrose. The maximum compressive strength and specific compressive strength of 4.9 MPa and 21 MPa/g/cm^3, respectively, are achieved at a MWNT concentration of 0.5 wt.%.The decrease in d-spacing of (002) planes with an increase in MWNT concentration indicates the stress induced crystallization of carbon along the axis of the MWNT. The electrical conductivity of the carbon composite foams increases with an increase in MWNT concentration up to 1.5 wt.% and then slightly decreases due to the MWNT agglomeration. The EMI SE of the carbon composite foams increases gradually with an increase in MWNT concentration up to 1.5 wt.% and then rapidly up to 2.5 wt.%. The highest SE and specific SE achieved are 39 dB and 166 dB/g/cm^3, respectively. The contribution of absorption loss dominates the reflection loss in the total SE. The rapid increase in SE at higher MWNT concentrations is due to the absorption of EM internally reflected from the additional interfaces created by the pores formed within the MWNT agglomerates.

Processing of graphene reinforced carbon composite foams by thermo-foaming of graphene oxide (GO) dispersions in molten sucrose is described in chapter 7. The melting point of the sucrose decreases from 190 to 120 ^{o}C with an increase in the GO concentration from 0 to 1.25 wt.% of sucrose. The viscosity of GO dispersions in molten sucrose increases gradually with GO concentration up to 0.75 and then rapidly with further increase in GO concentration. The foaming time and foam setting time decrease drastically from 48 to 1.5 h and 72 to 12 h, respectively, when the GO concentration increases from 0.15 to 1.25 wt.% due to the catalytic effect of GO towards –OH to –OH condensation reactions. The density and cell size of the carbon composite foams depend on the GO concentration. A maximum compressive strength and specific compressive

strength of 5.2 MPa and 21.3 MPa/g/cm^3, respectively, are achieved at a very low GO concentration of 0.25 wt.%. The electrical conductivity and EMI SE of the graphene reinforced carbon composite foams increase with an increase in the GO concentration up to 0.15 wt.% and then decrease due to graphene agglomeration. The maximum SE achieved is 38.6 dB at a GO concentration of 0.15 wt.%. The maximum SSE of the graphene reinforced carbon composite foam obtained is 160 dB/g/cm^3.

Processing of carbon composite foams by thermo-foaming of AC powder dispersions in aqueous sucrose resin is described in Chapter 8. The AC powders with average particle sizes in the range of 4.9 to 15 μm are stabilized in the aqueous sucrose resin by the adsorption of sucrose polymer molecules and relatively high viscosity of the medium. Unlike in molten sucrose, the AC powder retards the –OH to –OH condensation reactions in aqueous sucrose resin. The foaming of the AC powder dispersions in aqueous sucrose resin is due to the stabilization of bubbles by the adsorption of AC particles on the gas-resin interface. The finer AC particles offer better foam stability by preferentially adsorbing on the gas-resin interface. A threshold AC powder to sucrose weight ratio is observed for each AC particle size beyond which the foam collapses due to the agglomeration of the AC particles. The threshold AC powder to sucrose weight ratio decreases with a decrease in the average particle size of AC powder. The cell size of the carbon composite foams increases with both the AC particle size and AC powder to sucrose weight ratio. The density, the compressive strength and the thermal conductivity of the carbon composite foams increase with an increase in AC powder to sucrose weight ratio up to 0.025 and then decrease. The AC particle size has a marginal effect on the thermal conductivity of the carbon composite foams. The carbon composite foams show very good fire resistance and machinability characteristics.

Among the studied reinforcing additives, AC particle, MWNT and GO assist the foaming and foam setting process by catalyzing the –OH to –OH condensation, whereas the carbon short fiber remains inert towards the foaming

and foam setting of molten sucrose. The catalytic activity of the reinforcing additives towards foaming and foam setting is in the order GO > AC powder > MWNT. In the case of carbon short fiber, the uniformity of the cells depends on the fiber length. In all other reinforcing additives, uniform cells are achieved at lower reinforcement concentrations. At reinforcement concentration beyond a certain limit, non-uniform and distorted cells are observed due to foam collapse by agglomeration of the reinforcing additives. The concentrations at which the foam collapse observed are decreases with a decrease in the size of the reinforcing additive. That is, the concentration at which the foam collapse observed is highest in the case of AC powder (30 wt.%) and lowest in the case of GO (1.25 wt.%). The compressive strength of carbon foams increases with an increase in concentration of reinforcing additives, reaches a maximum and then decreases. The concentration at which the maximum strength obtained is decreased with a decrease in the size of the reinforcing additives. The concentration at which the compressive strength maximum obtained are 5 wt.%, 2 wt.%, 0.5 wt.% and 0.25 wt.% for AC powder, carbon fiber, MWNT and GO, respectively. The maximum compressive strength obtained also increases with a decrease in the size of the reinforcing agent. That is, the maximum compressive strength achieved for carbon foam prepared from molten sucrose is highest for GO (5.2 MPa) and lowest for AC powder (1.36 MPa) reinforcement. In the case of AC powder reinforced carbon foams, the carbon foams prepared from aqueous sucrose resin shows higher density and compressive strength than the one prepared from molten sucrose.

9.2 Future Work

The carbon foams prepared from molten sucrose using aluminium nitrate blowing agent show a very good CO_2 adsorption capacity with high CO_2/N_2 selectivity and easy regeneration. The highly interconnected macroporous structure of the carbon foam allows the flow of the flue gases without much pressure drop. There are possibilities to further improve the CO_2 adsorption capacity by modifying the cell wall surface by functionalization. The study on the

fabrication of carbon foam-based CO_2 scrubber system is proposed as one of the future works.

Low density carbon foams prepared from sucrose and various reinforcing additives show relatively high mechanical strength and very good fire resistance. These carbon foams can be used in light-weight fire resistant structural applications. Fabrication of sandwich composite structures using carbon foam as a core material is essential to realize the light-weight structural components. Therefore, it is proposed to study the fabrication of sandwich composite structures using the carbon composite foams and evaluation of their mechanical properties.

The MWNT and graphene reinforced carbon composite foams are having a relatively high electrical conductivity. The electrical conductivity coupled with the observed high surface area of the carbon composite foams makes them good candidates for electrode materials in batteries. A study on the electrochemical properties of the carbon composite foams can also be done in future. In addition, these composite foams show relatively high EMI shielding effectiveness of ~ 40 dB. Future studies are required to further improve the EMI shielding effectiveness by incorporating metallic, dielectric and magnetic particles in the carbon foams. The thermal conductivity measurements of MWNT and graphene reinforced carbon composite foams are also to be conducted for finding their suitability in thermal insulation application.

REFERENCES

1. Aboutalebi, S. H., Chidembo, A. T., Salari, M., Konstantinov, K., Wexler, D., Liu, H. K., & Dou, S. X. (2011a). Comparison of GO, GO/MWCNTs composite and MWCNTs as potential electrode materials for supercapacitors. *Energy & Environmental Science,* 4(5): 1855-1865.

2. Aboutalebi, S. H., Gudarzi, M. M., Zheng, Q. B., & Kim, J.-K. (2011b). Spontaneous Formation of Liquid Crystals in Ultralarge Graphene Oxide Dispersions. *Advanced Functional Materials,* 21(15): 2978-2988.

3. Agarwal, A., Bakshi, S. R., & Lahiri, D. (2010). *Carbon nanotubes: reinforced metal matrix composites*. CRC press.

4. Ahmadpour, A., & Do, D. D. (1996). The preparation of active carbons from coal by chemical and physical activation. *Carbon,* 34(4): 471-479.

5. Amaral-Labat, G., Gourdon, E., Fierro, V., Pizzi, A., & Celzard, A. (2013). Acoustic properties of cellular vitreous carbon foams. *Carbon,* 58: 76-86.

6. Amini, N., Aguey-Zinsou, K.-F., & Guo, Z.-X. (2011). Processing of strong and highly conductive carbon foams as electrode. *Carbon,* 49(12): 3857-3864.

7. Anantram, M. P., & Léonard, F. (2006). Physics of carbon nanotube electronic devices. *Reports on Progress in Physics,* 69(3): 507.

8. Atkins, P., & DE Paula, J. (2007). *Physical Chemistry*. Delhi: Oxford university press.

9. Balasubramanian, K., & Burghard, M. (2006). Biosensors based on carbon nanotubes. *Analytical and Bioanalytical Chemistry,* 385(3): 452-468.

10. Bao, Y., Zhan, L., Wang, C.-x., Wang, Y.-l., Yang, G.-z., Yang, J.-h., Qiao, W.-m., & Ling, L.-c. (2011). Synthesis of carbon nanofiber/carbon-foam composite for catalyst support in gas-phase catalytic reactions. *New Carbon Materials,* 26(5): 341-346.

11. Baumann, T. F., & Satcher, J. H. (2003). Homogeneous Incorporation of Metal Nanoparticles into Ordered Macroporous Carbons. *Chemistry of Materials,* 15(20): 3745-3747.

12. Becerril, H. A., Mao, J., Liu, Z., Stoltenberg, R. M., Bao, Z., & Chen, Y. (2008). Evaluation of Solution-Processed Reduced Graphene Oxide Films as Transparent Conductors. *ACS Nano,* 2(3): 463-470.

13. Binks, B. P., & Horozov, T. S. (2005). Aqueous Foams Stabilized Solely by Silica Nanoparticles. *Angewandte Chemie International Edition,* 44(24): 3722-3725.

14. Binks, B. P., & Lumsdon, S. O. (2000). Influence of Particle Wettability on the Type and Stability of Surfactant-Free Emulsions†. *Langmuir,* 16(23): 8622-8631.

15. Blanco, C., Bermejo, J., Marsh, H., & Menendez, R. (1997). Chemical and physical properties of carbon as related to brake performance. *Wear,* 213(1–2): 1-12.

16. Boehm, H. P. (1994). Some aspects of the surface chemistry of carbon blacks and other carbons. *Carbon,* 32(5): 759-769.

17. Bonzom, A., Crepaux, A. P., & Moutard, A. M. E. J. Expansion by thermal decomposition of blowing agent. US patent 4276246, 1981.

18. Brazel, J. P. Tri-element carbon based heat shield US patent 4892783, 1990.

19. Bromley, C. W. A. (1986). The preparation of sterically stabilised aqueous latices using polyethylene oxide. *Colloids and Surfaces,* 17(1): 1-11.

20. Brown, J. D., & Simandl, R. F. Microcellular carbon foam and method. US patent 5300272, 1994.

21. Calvo, M., García, R., Arenillas, A., Suárez, I., & Moinelo, S. R. (2005). Carbon foams from coals. A preliminary study. *Fuel,* 84(17): 2184-2189.

22. Carhart Homer, W., & Thompson Joseph, K. (1975). Removal of Contaminants from Submarine Atmospheres. *Removal of Trace Contaminants from the Air* (Vol. 17, pp. 1-16): AMERICAN CHEMICAL SOCIETY.

23. Caturla, F., Molina-Sabio, M., & Rodríguez-Reinoso, F. (1991). Preparation of activated carbon by chemical activation with ZnCl2. *Carbon,* 29(7): 999-1007.

24. Cfoam. (2004). http://www.cfoam.com/thermalprotection.htm

25. Che, S., Garcia-Bennett, A. E., Liu, X., Hodgkins, R. P., Wright, P. A., Zhao, D., Terasaki, O., & Tatsumi, T. (2003). Synthesis of Large-Pore Ia$\bar 3$d Mesoporous Silica and Its Tubelike Carbon Replica. *Angewandte Chemie International Edition,* 42(33): 3930-3934.

26. Chen, C., Kennel, E. B., Stiller, A. H., Stansberry, P. G., & Zondlo, J. W. (2006). Carbon foam derived from various precursors. *Carbon,* 44(8): 1535-1543.

27. Chen, G., Weng, W., Wu, D., & Wu, C. (2003a). PMMA/graphite nanosheets composite and its conducting properties. *European Polymer Journal,* 39(12): 2329-2335.

28. Chen, W., Peng, J., Su, Y., Zheng, L., Wang, L., & Jiang, Z. (2009). Separation of oil/water emulsion using Pluronic F127 modified polyethersulfone ultrafiltration membranes. *Separation and Purification Technology,* 66(3): 591-597.

29. Chen, W. X., Tu, J. P., Wang, L. Y., Gan, H. Y., Xu, Z. D., & Zhang, X. B. (2003b). Tribological application of carbon nanotubes in a metal-based composite coating and composites. *Carbon,* 41(2): 215-222.

30. Chen, Y., Chen, B., Shi, X., Xu, H., Hu, Y., Yuan, Y., & Shen, N. (2007). Preparation of pitch-based carbon foam using polyurethane foam template. *Carbon,* 45(10): 2132-2134.

31. Chung, D. D. L. (2000). Materials for electromagnetic interference shielding. *Journal of Materials Engineering and Performance,* 9(3): 350-354.

32. Chung, D. D. L. (2001). Electromagnetic interference shielding effectiveness of carbon materials. *Carbon,* 39(2): 279-285.

33. Coleman, J. N., Khan, U., Blau, W. J., & Gun'ko, Y. K. (2006). Small but strong: A review of the mechanical properties of carbon nanotube–polymer composites. *Carbon,* 44(9): 1624-1652.

34. Cuong, T. V., Pham, V. H., Chung, J. S., Shin, E. W., Yoo, D. H., Hahn, S. H., Huh, J. S., Rue, G. H., Kim, E. J., Hur, S. H., & Kohl, P. A. (2010). Solution-processed ZnO-chemically converted graphene gas sensor. *Materials Letters,* 64(22): 2479-2482.

35. Dalmolin, C., Biaggio, S. R., Rocha-Filho, R. C., & Bocchi, N. (2009). Preparation, electrochemical characterization and charge–discharge of reticulated vitreous carbon/polyaniline composite electrodes. *Electrochimica Acta,* 55(1): 227-233.

36. Dalmolin, C., Biaggio, S. R., Rocha-Filho, R. C., & Bocchi, N. (2010). Reticulated vitreous carbon/polypyrrole composites as electrodes for lithium batteries: Preparation, electrochemical characterization and charge–discharge performance. *Synthetic Metals,* 160(1-2): 173-179.

37. Danckwerts, P. V. (1979). The reaction of CO2 with ethanolamines. *Chemical Engineering Science,* 34(4): 443-446.

38. Darder, M., & Ruiz-Hitzky, E. (2005). Caramel-clay nanocomposites. *Journal of Materials Chemistry,* 15(35-36): 3913-3918.

39. deMan, J. M. (1999). *Principle of food chemistry*. Maryland: Chapman & Hall.

40. Deqing, W., & Ziyuan, S. (2003). Effect of ceramic particles on cell size and wall thickness of aluminum foam. *Materials Science and Engineering: A,* 361(1–2): 45-49.

41. Dickinson, E., Ettelaie, R., Kostakis, T., & Murray, B. S. (2004). Factors Controlling the Formation and Stability of Air Bubbles Stabilized by Partially Hydrophobic Silica Nanoparticles. *Langmuir,* 20(20): 8517-8525.

42. Dreyer, D. R., Park, S., Bielawski, C. W., & Ruoff, R. S. (2010). The chemistry of graphene oxide. *Chemical Society Reviews,* 39(1): 228-240.

43. Dubinin, M. (1966). *Chemistry and physics of carbon*. New York: Marcel Dekker.

44. Fang, Z., Li, C., Sun, J., Zhang, H., & Zhang, J. (2007). The electromagnetic characteristics of carbon foams. *Carbon,* 45(15): 2873-2879.

45. Fathollahi, B., & Zimmer, J. (2007). Microstructure of mesophase-based carbon foam. *Carbon,* 45(15): 3057-3059.

46. Fawcett, W., & Shetty, D. K. (2010). Effects of carbon nanofibers on cell morphology, thermal conductivity and crush strength of carbon foam. *Carbon,* 48(1): 68-80.

47. Finar, I. L. (2007a). *Organic Chemistry*. Delhi: Pearson Education.

48. Finar, I. L. (2007b). *Organic Chemistry*. Delhi: Pearson Education.

49. Ford Walter, D. Method of making cellular refractory thermal insulating material. US patent 3121050, 1964.

50. Franklin, R. (1951). The structure of graphitic carbons. *Acta Crystallographica,* 4(3): 253-261.

51. Friedrich, J. M., Ponce-de-León, C., Reade, G. W., & Walsh, F. C. (2004). Reticulated vitreous carbon as an electrode material. *Journal of Electroanalytical Chemistry,* 561: 203-217.

52. G.D.Parfitt (Ed.) (1981). *Dispersion of powders in liquid*. NJ: Applied Science.

53. Gaies, D., & Faber, K. T. (2002). Thermal properties of pitch-derived graphite foam. *Carbon,* 40(7): 1137-1140.

54. Gallego, N. C., & Klett, J. W. (2003). Carbon foams for thermal management. *Carbon,* 41(7): 1461-1466.

55. Gibson, L. J., & Ashby, M. F. (1997). *Cellular solids: structure and properties*. Cambridge University Press: Cambridge Solid State Press.

56. Glover, A. J., Cai, M., Overdeep, K. R., Kranbuehl, D. E., & Schniepp, H. C. (2011). In Situ Reduction of Graphene Oxide in Polymers. *Macromolecules,* 44(24): 9821-9829.

57. Goertzen, S. L., Thériault, K. D., Oickle, A. M., Tarasuk, A. C., & Andreas, H. A. (2010). Standardization of the Boehm titration. Part I. CO2 expulsion and endpoint determination. *Carbon,* 48(4): 1252-1261.

58. Gonzenbach, U. T., Studart, A. R., Tervoort, E., & Gauckler, L. J. (2006a). Stabilization of Foams with Inorganic Colloidal Particles. *Langmuir,* 22(26): 10983-10988.

59. Gonzenbach, U. T., Studart, A. R., Tervoort, E., & Gauckler, L. J. (2006b). Tailoring the Microstructure of Particle-Stabilized Wet Foams. *Langmuir,* 23(3): 1025-1032.

60. Gonzenbach, U. T., Studart, A. R., Tervoort, E., & Gauckler, L. J. (2006c). Ultrastable Particle-Stabilized Foams. *Angewandte Chemie International Edition,* 45(21): 3526-3530.

61. Googin, J. M., Napier, J. M., & Scrivner, M. E. Method for manufacturing foam carbon products. US patent 3345440, 1967.

62. Gui, X., Zeng, Z., Lin, Z., Gan, Q., Xiang, R., Zhu, Y., Cao, A., & Tang, Z. (2013). Magnetic and Highly Recyclable Macroporous Carbon Nanotubes for Spilled Oil Sorption and Separation. *ACS Applied Materials & Interfaces,* 5(12): 5845-5850.

63. Han, S., & Hyeon, T. (1999). Simple silica-particle template synthesis of mesoporous carbons. *Chemical Communications*(19): 1955-1956.

64. Hao, G.-P., Li, W.-C., Qian, D., Wang, G.-H., Zhang, W.-P., Zhang, T., Wang, A.-Q., Schüth, F., Bongard, H.-J., & Lu, A.-H. (2011). Structurally Designed Synthesis of Mechanically Stable Poly(benzoxazine-co-resol)-Based Porous Carbon Monoliths and Their Application as High-Performance CO2 Capture Sorbents. *Journal of the American Chemical Society,* 133(29): 11378-11388.

65. Hao, G.-P., Li, W.-C., Wang, S., Zhang, S., & Lu, A.-H. (2010). Tubular structured ordered mesoporous carbon as an efficient sorbent for the removal of dyes from aqueous solutions. *Carbon,* 48(12): 3330-3339.

66. Harikrishnan, G., Umasankar Patro, T., & Khakhar, D. V. (2007). Reticulated vitreous carbon from polyurethane foam–clay composites. *Carbon,* 45(3): 531-535.

67. Hopper, R. W., & Pekala, R. W. Low density microcellular carbon or catalytically impregnated carbon forms and process for their preparation. US patent 4806290, 1989.

68. Hu, R., & Chung, T. C. (1996). Poly(acrylonitrile-co-vinylcatecholborane): A new precursor for carbon containing B/C, B/N and B/O species. *Carbon,* 34(5): 595-600.

69. Iijima, S. (1991). Helical microtubules of graphitic carbon. *Nature,* 354(6348): 56-58.

70. Inagaki, M., Morishita, T., Kuno, A., Kito, T., Hirano, M., Suwa, T., & Kusakawa, K. (2004). Carbon foams prepared from polyimide using urethane foam template. *Carbon,* 42(3): 497-502.

71. Inayat, A., Schwerdtfeger, J., Freund, H., Körner, C., Singer, R. F., & Schwieger, W. (2011). Periodic open-cell foams: Pressure drop measurements and modeling of an ideal tetrakaidecahedra packing. *Chemical Engineering Science,* 66(12): 2758-2763.

72. Iten, M., & Liu, S. (2014). A work procedure of utilising PCMs as thermal storage systems based on air-TES systems. *Energy Conversion and Management,* 77: 608-627.

73. Jana, P., Fierro, V., Pizzi, A., & Celzard, A. (2014). Biomass-derived, thermally conducting, carbon foams for seasonal thermal storage. *Biomass and Bioenergy,* 67: 312-318.

74. Jana, P., & Ganesan, V. (2009). Synthesis, characterization and radionuclide (^{137}Cs) trapping properties of a carbon foam. *Carbon,* 47(13): 3001-3009.

75. Jana, P., & Ganesan, V. (2011). The production of a carbon-coated alumina foam. *Carbon,* 49(10): 3292-3298.

76. Ji, K., Zhao, H., Zhang, J., Chen, J., & Dai, Z. (2014). Fabrication and electromagnetic interference shielding performance of open-cell foam of a Cu–Ni alloy integrated with CNTs. *Applied Surface Science,* 311(0): 351-356.

77. Job, N., Théry, A., Pirard, R., Marien, J., Kocon, L., Rouzaud, J.-N., Béguin, F., & Pirard, J.-P. (2005). Carbon aerogels, cryogels and xerogels: Influence of the drying method on the textural properties of porous carbon materials. *Carbon,* 43(12): 2481-2494.

78. Jones, L. E., & Thrower, P. A. (1987). The effect of boron on carbon fiber microstructure and reactivity. *Journal de Chimie Physique,* 84: 1431-1438.

79. Jun, S., Joo, S. H., Ryoo, R., Kruk, M., Jaroniec, M., Liu, Z., Ohsuna, T., & Terasaki, O. (2000). Synthesis of New, Nanoporous Carbon with

Hexagonally Ordered Mesostructure. *Journal of the American Chemical Society,* 122(43): 10712-10713.

80. Kang, S., Yu, J.-S., Kruk, M., & Jaroniec, M. (2002). Synthesis of an ordered macroporous carbon with 62 nm spherical pores that exhibit unique gas adsorption properties. *Chemical Communications*(16): 1670-1671.

81. Kearns, K. M. Process for preparing pitch foams. US patent 5868974, 1999.

82. Kershaw, J. R., & Black, K. J. T. (1993). Structural characterization of coal-tar and petroleum pitches. *Energy & Fuels,* 7(3): 420-425.

83. Kierzek, K., Frackowiak, E., Lota, G., Gryglewicz, G., & Machnikowski, J. (2004). Electrochemical capacitors based on highly porous carbons prepared by KOH activation. *Electrochimica Acta,* 49(4): 515-523.

84. Kim, T.-W., Park, I.-S., & Ryoo, R. (2003). A Synthetic Route to Ordered Mesoporous Carbon Materials with Graphitic Pore Walls. *Angewandte Chemie,* 115(36): 4511-4515.

85. Kim, T., France, D. M., Yu, W., Zhao, W., & Singh, D. (2014). Heat transfer analysis of a latent heat thermal energy storage system using graphite foam for concentrated solar power. *Solar Energy,* 103: 438-447.

86. Kleitz, F., Hei Choi, S., & Ryoo, R. (2003). Cubic Ia3d large mesoporous silica: synthesis and replication to platinum nanowires, carbon nanorods and carbon nanotubes. *Chemical Communications*(17): 2136-2137.

87. Klett, J., & Conway, B. (2000). Thermal management solutions utilizing high thermal conductivity graphite foams. *Society for the Advancement of Material and Process Engineering, Bridging the Centuries with SAMPE's Materials and Processes Technology,* 45: 1933-1943.

88. Klett, J., Hardy, R., Romine, E., Walls, C., & Burchell, T. (2000). High-thermal-conductivity, mesophase-pitch-derived carbon foams: effect of precursor on structure and properties. *Carbon,* 38(7): 953-973.

89. Klett, J. W., & Burchell, T. D. Pitch-based carbon foam heat sink with phase change material. US patent 6780505, 2004.

90. Klett, R. D. High temperature insulating carbonaceous material. US patent 3914392, 1975.

91. Knippenberg, W., & Lersmacher, B. (1976). Carbon foam. *Philips Technical Review,* 36(4): 93-103.

92. Koh, C., Tahir, S., Sen, A., Pathak, A., & Pramanik, P. (2002). Preparation of nanosized mixed oxide ceramic powders using polyvinyl alcohol and

polyhydroxy organic compounds. *British Ceramic Transactions,* 101(3): 114-119.

93. Kowbel, W., Huang, Y., & Tsou, H. (1993). Effect of boron ion implantation on the oxidation behavior of three-dimensional carbon-carbon composite. *Carbon,* 31(2): 355-363.

94. Kroto, H. W., Heath, J. R., O'Brien, S. C., Curl, R. F., & Smalley, R. E. (1985). C60: Buckminsterfullerene. *Nature,* 318(6042): 162-163.

95. Kumar, R., Dhakate, S. R., Gupta, T., Saini, P., Singh, B. P., & Mathur, R. B. (2013a). Effective improvement of the properties of light weight carbon foam by decoration with multi-wall carbon nanotubes. *Journal of Materials Chemistry A,* 1(18): 5727-5735.

96. Kumar, R., Dhakate, S. R., & Mathur, R. B. (2013b). The role of ferrocene on the enhancement of the mechanical and electrochemical properties of coal tar pitch-based carbon foams. *Journal of Materials Science,* 48(20): 7071-7080.

97. Kumar, R., Kumari, S., & Dhakate, S. R. (2014a). Nickel nanoparticles embedded in carbon foam for improving electromagnetic shielding effectiveness. *Applied Nanoscience,* 5(5): 553-561.

98. Kumar, R., Kumari, S., Mathur, R. B., & Dhakate, S. R. (2014b). Nanostructuring effect of multi-walled carbon nanotubes on electrochemical properties of carbon foam as constructive electrode for lead acid battery. *Applied Nanoscience,* 5(1): 53-61.

99. Kumar, R., Singh, A. P., Chand, M., Pant, R. P., Kotnala, R. K., Dhawan, S. K., Mathur, R. B., & Dhakate, S. R. (2014c). Improved microwave absorption in lightweight resin-based carbon foam by decorating with magnetic and dielectric nanoparticles. *RSC Advances,* 4(45): 23476-23484.

100. Kwon, Y. W., Yoon, S. H., & Sistare, P. J. (1997). Compressive failure of carbon-foam sandwich composites with holes and/or partial delamination. *Composite Structures,* 38(1–4): 573-580.

101. Kyotani, T. (2000). Control of pore structure in carbon. *Carbon,* 38(2): 269-286.

102. Kyotani, T., Nagai, T., Inoue, S., & Tomita, A. (1997). Formation of New Type of Porous Carbon by Carbonization in Zeolite Nanochannels. *Chemistry of Materials,* 9(2): 609-615.

103. Lafdi, K., Mesalhy, O., & Elgafy, A. (2008). Graphite foams infiltrated with phase change materials as alternative materials for space and terrestrial thermal energy storage applications. *Carbon,* 46(1): 159-168.

104. Lastoskie, C., Gubbins, K. E., & Quirke, N. (1993). Pore size distribution analysis of microporous carbons: a density functional theory approach. *The Journal of Physical Chemistry,* 97(18): 4786-4796.

105. Lee, J., Yoon, S., Hyeon, T., M. Oh, S., & Bum Kim, K. (1999a). Synthesis of a new mesoporous carbon and its application to electrochemical double-layer capacitors. *Chemical Communications*(21): 2177-2178.

106. Lee, J., Yoon, S., Hyeon, T., Oh, S. M., & Kim, K. B. (1999b). Synthesis of a new mesoporous carbon and its application to electrochemical double-layer capacitors. *Chemical Communications*(21): 2177-2178.

107. Lei, S., Guo, Q., Shi, J., & Liu, L. (2010). Preparation of phenolic-based carbon foam with controllable pore structure and high compressive strength. *Carbon,* 48(9): 2644-2646.

108. Leroy, C., Carn, F., Backov, R., Trinquecoste, M., & Delhaes, P. (2007). Multiwalled-carbon-nanotube-based carbon foams. *Carbon,* 45(11): 2317-2320.

109. Li, J. F., Lu, W., Zeng, Y. B., & Luo, Z. P. (2014). Simultaneous enhancement of latent heat and thermal conductivity of docosane-based phase change material in the presence of spongy graphene. *Solar Energy Materials and Solar Cells,* 128: 48-51.

110. Li, S., Guo, Q., Song, Y., Liu, Z., Shi, J., Liu, L., & Yan, X. (2007a). Carbon foams with high compressive strength derived from mesophase pitch treated by toluene extraction. *Carbon,* 45(14): 2843-2845.

111. Li, S., Song, Y., Song, Y., Shi, J., Liu, L., Wei, X., & Guo, Q. (2007b). Carbon foams with high compressive strength derived from mixtures of mesocarbon microbeads and mesophase pitch. *Carbon,* 45(10): 2092-2097.

112. Li, S., Tian, Y., Zhong, Y., Yan, X., Song, Y., Guo, Q., Shi, J., & Liu, L. (2011a). Formation mechanism of carbon foams derived from mesophase pitch. *Carbon,* 49(2): 618-624.

113. Li, T.-Q., Wang, C.-Y., An, B.-X., & Wang, H. (2005). Preparation of graphitic carbon foam using size-restriction method under atmospheric pressure. *Carbon,* 43(9): 2030-2032.

114. Li, W., Zhang, H., & Xiong, X. (2011b). Properties of multi-walled carbon nanotube reinforced carbon foam composites. *Journal of Materials Science,* 46(4): 1143-1146.

115. Li, W. Q., Qu, Z. G., Zhang, B. L., Zhao, K., & Tao, W. Q. (2013). Thermal behavior of porous stainless-steel fiber felt saturated with phase change material. *Energy,* 55: 846-852.

116. Li, W. Q., Zhang, H. B., Xiong, X., & Xiao, F. (2010a). Effect of zirconium addition on the microstructure and performance of carbon foam. *Materials Science and Engineering: A,* 527(12): 2993-2997.

117. Li, W. Q., Zhang, H. B., Xiong, X., & Xiao, F. (2010b). Influence of fiber content on the structure and properties of short carbon fiber reinforced carbon foam. *Materials Science and Engineering: A,* 527(27-28): 7274-7278.

118. Li, W. Q., Zhang, H. B., Xiong, X., & Xiao, F. (2010c). Influence of fiber content on the structure and properties of short carbon fiber reinforced carbon foam. *Materials Science and Engineering: A,* 527(27–28): 7274-7278.

119. Li, W. Q., Zhang, H. B., Xiong, X., & Xiao, F. (2011c). A study of the properties of mesophase-pitch-based foam/graphitized carbon black composites. *Materials Science and Engineering: A,* 528(6): 2999-3002.

120. Li, X., Basso, M. C., Braghiroli, F. L., Fierro, V., Pizzi, A., & Celzard, A. (2012). Tailoring the structure of cellular vitreous carbon foams. *Carbon,* 50(5): 2026-2036.

121. Lin, D., Wu, J., Ju, H., & Yan, F. (2014a). Nanogold/mesoporous carbon foam-mediated silver enhancement for graphene-enhanced electrochemical immunosensing of carcinoembryonic antigen. *Biosensors & bioelectronics,* 52: 153-158.

122. Lin, Q., Qu, L., Luo, B., Fang, C., & Luo, K. (2014b). Preparation and properties of multiwall carbon nanotubes/carbon foam composites. *Journal of Analytical and Applied Pyrolysis,* 105: 177-182.

123. Lin, W., Sundén, B., & Yuan, J. (2013). A performance analysis of porous graphite foam heat exchangers in vehicles. *Applied Thermal Engineering,* 50(1): 1201-1210.

124. Liu, K., Chen, L., Chen, Y., Wu, J., Zhang, W., Chen, F., & Fu, Q. (2011). Preparation of polyester/reduced graphene oxide composites via in situ melt polycondensation and simultaneous thermo-reduction of graphene oxide. *Journal of Materials Chemistry,* 21(24): 8612-8617.

125. Liu, M., Gan, L., Zhao, F., Fan, X., Xu, H., Wu, F., Xu, Z., Hao, Z., & Chen, L. (2007a). Carbon foams with high compressive strength derived from polyarylacetylene resin. *Carbon,* 45(15): 3055-3057.

126. Liu, M., Gan, L., Zhao, F., Xu, H., Fan, X., Tian, C., Wang, X., Xu, Z., Hao, Z., & Chen, L. (2007b). Carbon foams prepared by an oil-in-water emulsion method. *Carbon,* 45(13): 2710-2712.

127. Liu, S., Huang, Z., & Wang, R. (2013). A carbon foam with a bimodal micro–mesoporous structure prepared from larch sawdust for the gas-phase toluene adsorption. *Materials Research Bulletin,* 48(7): 2437-2441.

128. Loh, K. P., Bao, Q., Ang, P. K., & Yang, J. (2010). The chemistry of graphene. *Journal of Materials Chemistry,* 20(12): 2277-2289.

129. Lorjai, P., Wongkasemjit, S., & Chaisuwan, T. (2009). Preparation of polybenzoxazine foam and its transformation to carbon foam. *Materials Science and Engineering: A,* 527(1–2): 77-84.

130. Luo, R., Ni, Y., Li, J., Yang, C., & Wang, S. (2011a). The mechanical and thermal insulating properties of resin-derived carbon foams reinforced by K2Ti6O13 whiskers. *Materials Science and Engineering: A,* 528(4–5): 2023-2027.

131. Luo, R., Ni, Y., Li, J., Yang, C., & Wang, S. (2011b). The mechanical and thermal insulating properties of resin-derived carbon foams reinforced by K2Ti6O13 whiskers. *Materials Science and Engineering: A,* 528(4-5): 2023-2027.

132. Ma, Z., Kyotani, T., Liu, Z., Terasaki, O., & Tomita, A. (2001). Very High Surface Area Microporous Carbon with a Three-Dimensional Nano-Array Structure: Synthesis and Its Molecular Structure. *Chemistry of Materials,* 13(12): 4413-4415.

133. Ma, Z., Kyotani, T., & Tomita, A. (2000). Preparation of a high surface area microporous carbon having the structural regularity of Y zeolite. *Chemical Communications*(23): 2365-2366.

134. Marinković, S., Sužnjević, Č., & Dežarov, I. (1969). Simultaneous pyrolytic deposition of carbon and boron. *Carbon,* 7(1): 185-193.

135. Marsh, H. (1991). A tribute to Philip L. Walker. *Carbon,* 29(6): 703-704.

136. Marsh, H., & Reinoso, F. R. (2006). *Activated Carbon*. Elsevier.

137. Mathieu, B., Blacher, S., Pirard, R., Pirard, J. P., Sahouli, B., & Brouers, F. (1997). Freeze-dried resorcinol-formaldehyde gels. *Journal of Non-Crystalline Solids,* 212(2-3): 250-261.

138. McAllister, M. J., Li, J.-L., Adamson, D. H., Schniepp, H. C., Abdala, A. A., Liu, J., Herrera-Alonso, M., Milius, D. L., Car, R., Prud'homme, R. K., & Aksay, I. A. (2007). Single Sheet Functionalized Graphene by Oxidation and Thermal Expansion of Graphite. *Chemistry of Materials,* 19(18): 4396-4404.

139. McEnaney, B., & Rand, B. (1985). Carbon binders from polymeric resins and pitch: II, Structure and properties of the carbons. *British Ceramic Transactions and Journal,* 84(6): 193-198.

140. McKee, D. W. (1991). Oxidation protection of carbon materials. In P. A. Thrower (Ed.). *Chemistry and Physics of Carbon* (Vol. 23, pp. 173-232). New York: Dekker.

141. Mesalhy, O., Lafdi, K., & Elgafy, A. (2006). Carbon foam matrices saturated with PCM for thermal protection purposes. *Carbon,* 44(10): 2080-2088.

142. Miller, D. J., Lewis, I. C., & Mercuri, R. A. Carbon foam structural insulated panel. US patent 7785712, 2010a.

143. Miller, D. J., Lewis, I. C., & Mercuri, R. A. High strength monolithic carbon foam. US patent 8372510, 2013.

144. Miller, D. J., Lewis, I. C., Shao, R. L., & Yazici, M. S. (2010b). Foaming a carbon fiber-phenolic resin mixture and carbonizing the foam to form a material with a compressive strength of at least 2000 psi; at least 90% of the pores have a diameter of 10-95 microns and at least 1% of the pores have a diameter of 0.8-3.5 m; liquid permeability of no greater than 3. Google Patents.

145. Miura, K., Hayashi, J., & Hashimoto, K. (1991). Production of molecular sieving carbon through carbonization of coal modified by organic additives. *Carbon,* 29(4-5): 653-660.

146. Moeini Sedeh, M., & Khodadadi, J. M. (2013). Thermal conductivity improvement of phase change materials/graphite foam composites. *Carbon,* 60: 117-128.

147. Moglie, F., Micheli, D., Laurenzi, S., Marchetti, M., & Mariani Primiani, V. (2012). Electromagnetic shielding performance of carbon foams. *Carbon,* 50(5): 1972-1980.

148. Mondal, S., & Banthia, A. K. (2005). Low-temperature synthetic route for boron carbide. *Journal of the European Ceramic Society,* 25(2–3): 287-291.

149. Morgan, P. (2005). *Carbon fibers and their composites*. CRC PressI Llc.

150. Nakagawa, H., Watanabe, K., Harada, Y., & Miura, K. (1999). Control of micropore formation in the carbonized ion exchange resin by utilizing pillar effect. *Carbon,* 37(9): 1455-1461.

151. Nakamae, M., Yuki, K., Sato, T., & Maruyama, H. (1999). Preparation of polymer emulsions using a poly(vinyl alcohol) as protective colloid. *Colloids and Surfaces A: Physicochemical and Engineering Aspects,* 153(1–3): 367-372.

152. Ning, G., Fan, Z., Wang, G., Gao, J., Qian, W., & Wei, F. (2011). Gram-scale synthesis of nanomesh graphene with high surface area and its

application in supercapacitor electrodes. *Chemical Communications,* 47(21): 5976-5978.

153. Novoselov, K. S., Geim, A. K., Morozov, S. V., Jiang, D., Zhang, Y., Dubonos, S. V., Grigorieva, I. V., & Firsov, A. A. (2004). Electric field effect in atomically thin carbon films. *Science (New York, N.Y.),* 306(5696): 666-669.

154. Oganov, A. R., Hemley, R. J., Hazen, R. M., & Jones, A. P. (2013). Structure, Bonding, and Mineralogy of Carbon at Extreme Conditions. *Reviews in Mineralogy and Geochemistry,* 75(1): 47-77.

155. Pacewska, B., & Keshr, M. (2002). Thermal transformations of aluminium nitrate hydrate. *Thermochimica Acta,* 385(1–2): 73-80.

156. Paredes, J. I., Villar-Rodil, S., Martínez-Alonso, A., & Tascón, J. M. D. (2008). Graphene Oxide Dispersions in Organic Solvents. *Langmuir,* 24(19): 10560-10564.

157. Park, O.-K., Hahm, M. G., Lee, S., Joh, H.-I., Na, S.-I., Vajtai, R., Lee, J. H., Ku, B.-C., & Ajayan, P. M. (2012). In Situ Synthesis of Thermochemically Reduced Graphene Oxide Conducting Nanocomposites. *Nano Letters,* 12(4): 1789-1793.

158. Park, S., An, J., Jung, I., Piner, R. D., An, S. J., Li, X., Velamakanni, A., & Ruoff, R. S. (2009). Colloidal Suspensions of Highly Reduced Graphene Oxide in a Wide Variety of Organic Solvents. *Nano Letters,* 9(4): 1593-1597.

159. Pekala, R. W. (1989). Organic aerogels from the polycondensation of resorcinol with formaldehyde. *Journal of Materials Science,* 24(9): 3221-3227.

160. Pekala, R. W., & Alviso, C. T. (2011). Carbon Aerogels and Xerogels. *MRS Proceedings,* 270: 3-3.

161. Pereira, M. F. R., Figueiredo, J. L., Órfão, J. J. M., Serp, P., Kalck, P., & Kihn, Y. (2004). Catalytic activity of carbon nanotubes in the oxidative dehydrogenation of ethylbenzene. *Carbon,* 42(14): 2807-2813.

162. Pielichowska, K., & Pielichowski, K. (2014). Phase change materials for thermal energy storage. *Progress in Materials Science,* 65: 67-123.

163. Pierson, H. O. (1993). *Handbook of Carbon, Graphite, Diamond, and Fullerenes: Properties, Processing, and Applications*. Noyes Publications.

164. Pohjanlehto, H., Setälä, H. M., Kiely, D. E., & McDonald, A. G. (2014). Lignin-xylaric acid-polyurethane-based polymer network systems: Preparation and characterization. *Journal of Applied Polymer Science,* 131(1): 39714.

165. Potts, J. R., Dreyer, D. R., Bielawski, C. W., & Ruoff, R. S. (2011). Graphene-based polymer nanocomposites. *Polymer,* 52(1): 5-25.

166. Prabhakaran, K., Singh, P., Gokhale, N., & Sharma, S. (2007). Processing of sucrose to low density carbon foams. *Journal of Materials Science,* 42(11): 3894-3900.

167. Prieto, R., Louis, E., & Molina, J. M. (2012). Fabrication of mesophase pitch-derived open-pore carbon foams by replication processing. *Carbon,* 50(5): 1904-1912.

168. Pulci, G., Tirillò, J., Marra, F., Fossati, F., Bartuli, C., & Valente, T. (2010). Carbon–phenolic ablative materials for re-entry space vehicles: Manufacturing and properties. *Composites Part A: Applied Science and Manufacturing,* 41(10): 1483-1490.

169. Rawal, S. P., Thornton, J. M., & Willcockson, W. H. Insulated reentry heat shield. US patent 6558785, 2003.

170. Reyes, G., & Rangaraj, S. (2011). Fracture properties of high performance carbon foam sandwich structures. *Composites Part A: Applied Science and Manufacturing,* 42(1): 1-7.

171. Rios, R. V. R. A., Martínez-Escandell, M., Molina-Sabio, M., & Rodríguez-Reinoso, F. (2006). Carbon foam prepared by pyrolysis of olive stones under steam. *Carbon,* 44(8): 1448-1454.

172. Rogers, D. K., & Plucinski, J. W. Electrochemical cell electrodes comprising coal-based carbon foam. US patent 6899970, 2005.

173. Rosebrock, G., Elgafy, A., Beechem, T., & Lafdi, K. (2005). Study of the growth and motion of graphitic foam bubbles. *Carbon,* 43(15): 3075-3087.

174. Rouquerol, J., Rouquerol, F., Llewellyn, P., Maurin, G., & Sing, K. S. (2013). *Adsorption by powders and porous solids: principles, methodology and applications*. Academic press.

175. Ryoo, R., Joo, S. H., Kruk, M., & Jaroniec, M. (2001). Ordered Mesoporous Carbons. *Advanced Materials,* 13(9): 677-681.

176. Sahoo, N. G., Rana, S., Cho, J. W., Li, L., & Chan, S. H. (2010). Polymer nanocomposites based on functionalized carbon nanotubes. *Progress in Polymer Science,* 35(7): 837-867.

177. Saini, P., Choudhary, V., Vijayan, N., & Kotnala, R. K. (2012). Improved electromagnetic interference shielding response of poly(aniline)-coated fabrics containing dielectric and magnetic nanoparticles. *The Journal of Physical Chemistry C,* 116(24): 13403-13412.

178. Saini, V. K., Pinto, M. L., & Pires, J. (2013). Synthesis and adsorption properties of micro/mesoporous carbon-foams prepared from foam-shaped sacrificial templates. *Materials Chemistry and Physics,* 138(2-3): 877-885.

179. Sanchez-Coronado, J., & Chung, D. D. L. (2003). Thermomechanical behavior of a graphite foam. *Carbon,* 41(6): 1175-1180.

180. Savage, G. (1993). *Carbon-Carbon Composites*. London: Chapman & Hall.

181. Schadler, L. S., Giannaris, S. C., & Ajayan, P. M. (1998). Load transfer in carbon nanotube epoxy composites. *Applied Physics Letters,* 73(26): 3842-3844.

182. Scheffler, M., & Colombo, P. (2006). *Cellular ceramics: structure, manufacturing, properties and applications*. John Wiley & Sons.

183. Schniepp, H. C., Li, J.-L., McAllister, M. J., Sai, H., Herrera-Alonso, M., Adamson, D. H., Prud'homme, R. K., Car, R., Saville, D. A., & Aksay, I. A. (2006). Functionalized Single Graphene Sheets Derived from Splitting Graphite Oxide. *Journal of Physical Chemistry B,* 110(17): 8535-8539.

184. Seo, J., Park, H., Shin, K., Baeck, S. H., Rhym, Y., & Shim, S. E. (2014). Lignin-derived macroporous carbon foams prepared by using poly(methyl methacrylate) particles as the template. *Carbon,* 76: 357-367.

185. Sevilla, M., & Fuertes, A. B. (2011). Sustainable porous carbons with a superior performance for CO2 capture. *Energy & Environmental Science,* 4(5): 1765-1771.

186. Shafi, M. A., & Flumerfelt, R. W. (1997). Initial bubble growth in polymer foam processes. *Chemical Engineering Science,* 52(4): 627-633.

187. Shalaby, S. M., Bek, M. A., & El-Sebaii, A. A. (2014). Solar dryers with PCM as energy storage medium: A review. *Renewable and Sustainable Energy Reviews,* 33: 110-116.

188. Shearer, C. J., Cherevan, A., & Eder, D. (2014). Application and Future Challenges of Functional Nanocarbon Hybrids. *Advanced Materials,* 26(15): 2295-2318.

189. Sheehan, J. E. (1989). Oxidation protection for carbon fiber composites. *Carbon,* 27(5): 709-715.

190. Shi, Z., Zhang, W., Zhang, F., Liu, X., Wang, D., Jin, J., & Jiang, L. (2013). Ultrafast Separation of Emulsified Oil/Water Mixtures by Ultrathin Free-Standing Single-Walled Carbon Nanotube Network Films. *Advanced Materials,* 25(17): 2422-2427.

191. Sihn, S., Ganguli, S., Anderson, D. P., & Roy, A. K. (2012). Enhancement of through-thickness thermal conductivity of sandwich construction using carbon foam. *Composites Science and Technology,* 72(7): 767-773.

192. Silvestre-Albero, J., Wahby, A., Sepulveda-Escribano, A., Martinez-Escandell, M., Kaneko, K., & Rodriguez-Reinoso, F. (2011). Ultrahigh CO2 adsorption capacity on carbon molecular sieves at room temperature. *Chemical Communications,* 47(24): 6840-6842.

193. Sing, K. S. (1985). Reporting physisorption data for gas/solid systems with special reference to the determination of surface area and porosity (Recommendations 1984). *Pure and applied chemistry,* 57(4): 603-619.

194. Sing, K. S. W. (1998). Adsorption methods for the characterization of porous materials. *Advances in Colloid and Interface Science,* 76–77(0): 3-11.

195. Sircar, S., Golden, T. C., & Rao, M. B. (1996). Activated carbon for gas separation and storage. *Carbon,* 34(1): 1-12.

196. Socher, R., Krause, B., Boldt, R., Hermasch, S., Wursche, R., & Pötschke, P. (2011). Melt mixed nano composites of PA12 with MWNTs: Influence of MWNT and matrix properties on macrodispersion and electrical properties. *Composites Science and Technology,* 71(3): 306-314.

197. Stansberry, P. G., Stiller, A. H., & Zondlo, J. W. (2000). Low-cost carbon foams for thermal protection and reinforcement applications. *Bridging the Centuries with SAMPE's Materials and Processes Technology: Long Beach Convention Center, Long Beach California, May 21-25, 2000* (Vol. 1): Taylor & Francis US.

198. Su, D. S., Maksimova, N., Delgado, J. J., Keller, N., Mestl, G., Ledoux, M. J., & Schlögl, R. (2005a). Nanocarbons in selective oxidative dehydrogenation reaction. *Catalysis Today,* 102–103(0): 110-114.

199. Su, F., Zeng, J., Bao, X., Yu, Y., Lee, J. Y., & Zhao, X. S. (2005b). Preparation and Characterization of Highly Ordered Graphitic Mesoporous Carbon as a Pt Catalyst Support for Direct Methanol Fuel Cells. *Chemistry of Materials,* 17(15): 3960-3967.

200. Subramaniam, A. B., Mejean, C., Abkarian, M., & Stone, H. A. (2006). Microstructure, Morphology, and Lifetime of Armored Bubbles Exposed to Surfactants. *Langmuir,* 22(14): 5986-5990.

201. Suehiro, J., Zhou, G., Imakiire, H., Ding, W., & Hara, M. (2005). Controlled fabrication of carbon nanotube NO_2 gas sensor using dielectrophoretic impedance measurement. *Sensors and Actuators B: Chemical,* 108(1–2): 398-403.

202. Sun, X., Liu, Z., Welsher, K., Robinson, J., Goodwin, A., Zaric, S., & Dai, H. (2008). Nano-graphene oxide for cellular imaging and drug delivery. *Nano Research,* 1(3): 203-212.

203. Tamon, H., Ishizaka, H., Yamamoto, T., & Suzuki, T. (1999). Preparation of mesoporous carbon by freeze drying. *Carbon,* 37(12): 2049-2055.

204. Tamon, H., Ishizaka, H., Yamamoto, T., & Suzuki, T. (2000). Influence of freeze-drying conditions on the mesoporosity of organic gels as carbon precursors. *Carbon,* 38(7): 1099-1105.

205. Tasis, D., Tagmatarchis, N., Bianco, A., & Prato, M. (2006). Chemistry of Carbon Nanotubes. *Chemical Reviews,* 106(3): 1105-1136.

206. Teng, H., Yeh, T.-S., & Hsu, L.-Y. (1998). Preparation of activated carbon from bituminous coal with phosphoric acid activation. *Carbon,* 36(9): 1387-1395.

207. Thareja, P., Ising, B. P., Kingston, S. J., & Velankar, S. S. (2008). Polymer Foams Stabilized by Particles Adsorbed at the Air/Polymer Interface. *Macromolecular Rapid Communications,* 29(15): 1329-1334.

208. Thostenson, E. T., Ren, Z., & Chou, T.-W. (2001). Advances in the science and technology of carbon nanotubes and their composites: a review. *Composites Science and Technology,* 61(13): 1899-1912.

209. Tondi, G., Fierro, V., Pizzi, A., & Celzard, A. (2009). Tannin-based carbon foams. *Carbon,* 47(6): 1480-1492.

210. Tseng, R.-L. (2007). Physical and chemical properties and adsorption type of activated carbon prepared from plum kernels by NaOH activation. *Journal of hazardous materials,* 147(3): 1020-1027.

211. Vilatela, J. J., & Eder, D. (2012). Nanocarbon Composites and Hybrids in Sustainability: A Review. *ChemSusChem,* 5(3): 456-478.

212. Walker Jr, P. L., Taylor, R. L., & Ranish, J. M. (1991). An update on the carbon-oxygen reaction. *Carbon,* 29(3): 411-421.

213. Walker, L. S., Marotto, V. R., Rafiee, M. A., Koratkar, N., & Corral, E. L. (2011). Toughening in Graphene Ceramic Composites. *ACS Nano,* 5(4): 3182-3190.

214. Wang, C., Feng, L., Yang, H., Xin, G., Li, W., Zheng, J., Tian, W., & Li, X. (2012a). Graphene oxide stabilized polyethylene glycol for heat storage. *Physical Chemistry Chemical Physics,* 14(38): 13233-13238.

215. Wang, J., Li, Z., Fan, G., Pan, H., Chen, Z., & Zhang, D. (2012b). Reinforcement with graphene nanosheets in aluminum matrix composites. *Scripta Materialia,* 66(8): 594-597.

216. Wang, M.-x., Wang, C.-y., Chen, M.-m., Li, T.-q., & Hu, Z.-j. (2009a). Bubble growth in the preparation of mesophase-pitch-based carbon foams. *New Carbon Materials,* 24(1): 61-66.

217. Wang, M.-x., Wang, C.-Y., Li, T.-Q., & Hu, Z.-J. (2008a). Preparation and characterization of mesophase-pitch-based foam/natural graphite composites. *Composites Science and Technology,* 68(10–11): 2220-2223.

218. Wang, M.-x., Wang, C.-Y., Li, T.-Q., & Hu, Z.-J. (2008b). Preparation of mesophase-pitch-based carbon foams at low pressures. *Carbon,* 46(1): 84-91.

219. Wang, M., Wang, C., Li, T., & Hu, Z. (2008c). Preparation and characterization of mesophase-pitch-based foam/natural graphite composites. *Composites Science and Technology,* 68(10-11): 2220-2223.

220. Wang, Q., Han, X. H., Sommers, A., Park, Y., T' Joen, C., & Jacobi, A. (2012c). A review on application of carbonaceous materials and carbon matrix composites for heat exchangers and heat sinks. *International Journal of Refrigeration,* 35(1): 7-26.

221. Wang, R., Li, W., & Liu, S. (2011). A porous carbon foam prepared from liquefied birch sawdust. *Journal of Materials Science,* 47(4): 1977-1984.

222. Wang, S., Luo, R., & Ni, Y. (2010). Preparation and characterization of resin-derived carbon foams reinforced by hollow ceramic microspheres. *Materials Science and Engineering: A,* 527(15): 3392-3395.

223. Wang, X., Luo, R., Ni, Y., Zhang, R., & Wang, S. (2009b). Properties of chopped carbon fiber reinforced carbon foam composites. *Materials Letters,* 63(1): 25-27.

224. Wang, X., Zhong, J., Wang, Y., & Yu, M. (2006). A study of the properties of carbon foam reinforced by clay. *Carbon,* 44(8): 1560-1564.

225. Wang, Y., Tao, S., & An, Y. (2013). A reverse membrane emulsification process based on a hierarchically porous monolith for high efficiency water-oil separation. *Journal of Materials Chemistry A,* 1(5): 1701-1708.

226. Wenmakers, P. W. a. M., van der Schaaf, J., Kuster, B. F. M., & Schouten, J. C. (2008). "Hairy Foam": carbon nanofibers grown on solid carbon foam. A fully accessible, high surface area, graphitic catalyst support. *Journal of Materials Chemistry,* 18(21): 2426-2426.

227. Wenmakers, P. W. A. M., van der Schaaf, J., Kuster, B. F. M., & Schouten, J. C. (2010). Comparative Modeling Study on the Performance of Solid Foam as a Structured Catalyst Support in Multiphase Reactors. *Industrial & Engineering Chemistry Research,* 49(11): 5353-5366.

228. Wong, J. C. H., Tervoort, E., Busato, S., Gonzenbach, U. T., Studart, A. R., Ermanni, P., & Gauckler, L. J. (2010). Designing macroporous polymers from particle-stabilized foams. *Journal of Materials Chemistry,* 20(27): 5628-5640.

229. Wu, X., Fang, M., Mei, L., & Luo, B. (2012). Effect of final pyrolysis temperature on the mechanical and thermal properties of carbon foams reinforced by aluminosilicate. *Materials Science and Engineering: A,* 558: 446-450.

230. Wu, X., Liu, Y. g., Fang, M., Mei, L., & Luo, B. (2011). Preparation and characterization of carbon foams derived from aluminosilicate and phenolic resin. *Carbon,* 49(5): 1782-1786.

231. Wu, X., Luo, R., Ni, Y., & Xiang, Q. (2009). Microstructure and mechanical properties of carbon foams and fibers reinforced carbon composites densified by CLVI and pitch impregnation. *Composites Part A: Applied Science and Manufacturing,* 40(2): 225-231.

232. Xia, Z., Riester, L., Curtin, W. A., Li, H., Sheldon, B. W., Liang, J., Chang, B., & Xu, J. M. (2004). Direct observation of toughening mechanisms in carbon nanotube ceramic matrix composites. *Acta Materialia,* 52(4): 931-944.

233. Xiao, X., & Zhang, P. (2013). Morphologies and thermal characterization of paraffin/carbon foam composite phase change material. *Solar Energy Materials and Solar Cells,* 117: 451-461.

234. Xiao, X., Zhang, P., & Li, M. (2014). Effective thermal conductivity of open-cell metal foams impregnated with pure paraffin for latent heat storage. *International Journal of Thermal Sciences,* 81: 94-105.

235. Xu, Z., Zheng, Q.-S., & Chen, G. (2007). Elementary building blocks of graphene-nanoribbon-based electronic devices. *Applied Physics Letters,* 90(22): 223115.

236. Yadav, A., Kumar, R., Bhatia, G., & Verma, G. L. (2011). Development of mesophase pitch derived high thermal conductivity graphite foam using a template method. *Carbon,* 49(11): 3622-3630.

237. Yamaguchi, A., Zhang, S., & Yu, J. (1996). Effect of Refractory Oxides on the Oxidation of Graphite and Amorphous Carbon. *Journal of the American Ceramic Society,* 79(9): 2509-2511.

238. Yang, H., Shi, Q., Liu, X., Xie, S., Jiang, D., Zhang, F., Yu, C., Tu, B., & Zhao, D. (2002). Synthesis of ordered mesoporous carbon monoliths with bicontinuous cubic pore structure of Ia3d symmetry. *Chemical Communications*(23): 2842-2843.

239. Yang, J., Shen, Z.-m., & Hao, Z.-b. (2004). Microwave characteristics of sandwich composites with mesophase pitch carbon foams as core. *Carbon,* 42(8-9): 1882-1885.

240. Yang, Y., Wei, Z., Wang, C., & Tong, Z. (2013). Lignin-based Pickering HIPEs for macroporous foams and their enhanced adsorption of copper(II) ions. *Chemical Communications*.

241. Yu, J.-S., Kang, S., Yoon, S. B., & Chai, G. (2002). Fabrication of Ordered Uniform Porous Carbon Networks and Their Application to a Catalyst Supporter. *Journal of the American Chemical Society,* 124(32): 9382-9383.

242. Yu, J.-S., Yoon, S. B., & Chai, G. S. (2001). Ordered uniform porous carbon by carbonization of sugars. *Carbon,* 39(9): 1442-1446.

243. Yu, Q., Straatman, A. G., & Thompson, B. E. (2006). Carbon-foam finned tubes in air–water heat exchangers. *Applied Thermal Engineering,* 26(2–3): 131-143.

244. Zakhidov, A. A. (1998). Carbon Structures with Three-Dimensional Periodicity at Optical Wavelengths. *Science,* 282(5390): 897-901.

245. Zaldivar, R. J., Kobayashi, R. W., Rellick, G. S., & Yang, J. M. (1991). Carborane-catalyzed graphitization in polyarylacetylene-derived carbon-carbon composites. *Carbon,* 29(8): 1145-1153.

246. Zeng, C., Hossieny, N., Zhang, C., & Wang, B. (2010). Synthesis and processing of PMMA carbon nanotube nanocomposite foams. *Polymer,* 51(3): 655-664.

247. Zeng, Y., Wang, K., Yao, J., & Wang, H. (2014). Hollow carbon beads fabricated by phase inversion method for efficient oil sorption. *Carbon,* 69(0): 25-31.

248. Zhan, G.-D., Kuntz, J. D., Wan, J., & Mukherjee, A. K. (2003). Single-wall carbon nanotubes as attractive toughening agents in alumina-based nanocomposites. *Nature Materials,* 2(1): 38-42.

249. Zhang, A., Chen, M., Du, C., Guo, H., Bai, H., & Li, L. (2013). Poly(dimethylsiloxane) Oil Absorbent with a Three-Dimensionally Interconnected Porous Structure and Swellable Skeleton. *ACS Applied Materials & Interfaces,* 5(20): 10201-10206.

250. Zhang, C., Wang, C., Zhan, L., Wang, C., Wang, Y., & Ling, L. (2011). Synthesis of carbon foam covered with carbon nanofibers as catalyst support for gas phase catalytic reactions. *Materials Letters,* 65(12): 1889-1891.

251. Zhang, S.-p., Liu, M.-x., Gan, L.-h., Wu, F.-r., Xu, Z.-j., Hao, Z.-x., & Chen, L.-w. (2010). Synthesis of carbon foams with a high compressive strength from arylacetylene. *New Carbon Materials,* 25(1): 9-14.

252. Zhang, S., Tao, Q., Wang, Z., & Zhang, Z. (2012). Controlled heat release of new thermal storage materials: the case of polyethylene glycol intercalated into graphene oxide paper. *Journal of Materials Chemistry,* 22(38): 20166-20169.

253. Zhao, W., France, D. M., Yu, W., Kim, T., & Singh, D. (2014). Phase change material with graphite foam for applications in high-temperature latent heat storage systems of concentrated solar power plants. *Renewable Energy,* 69: 134-146.

254. Zhong, D. H., Sano, H., Uchiyama, Y., & Kobayashi, K. (2000). Effect of low-level boron doping on oxidation behavior of polyimide-derived carbon films. *Carbon,* 38(8): 1199-1206.

255. Zhong, Y., Guo, Q., Li, S., Shi, J., & Liu, L. (2010). Heat transfer enhancement of paraffin wax using graphite foam for thermal energy storage. *Solar Energy Materials and Solar Cells,* 94(6): 1011-1014.

256. Zhong, Y., Zhou, M., Huang, F., Lin, T., & Wan, D. (2013). Effect of graphene aerogel on thermal behavior of phase change materials for thermal management. *Solar Energy Materials and Solar Cells,* 113: 195-200.

257. Zhou, X., Yu, Q., Zhang, S., Zhang, C., & Feng, J. (2013). Porous silica matrices infiltrated with PCM for thermal protection purposes. *Ceramics International,* 39(5): 5247-5253.

258. Zhu, J., Wang, X., Guo, L., Wang, Y., Wang, Y., Yu, M., & Lau, K.-t. (2007). A graphite foam reinforced by graphite particles. *Carbon,* 45(13): 2547-2550.

259. Zhu, Y., Murali, S., Cai, W., Li, X., Suk, J. W., Potts, J. R., & Ruoff, R. S. (2010). Graphene and Graphene Oxide: Synthesis, Properties, and Applications. *Advanced Materials,* 22(35): 3906-3924.

260. Zukal, A., Mayerová, J., & Čejka, J. (2010). Alkali metal cation doped Al-SBA-15 for carbon dioxide adsorption. *Physical chemistry chemical physics : PCCP,* 12(20): 5240-5247.